WARSAW UNIVERSITY OF TECHNOLOGY

Faculty of Physics

Ph.D. Thesis

Leszek Krzysztof Kosarzewski, M.Sc. Eng

Study of quarkonium production in relativistic proton-proton collisions in the STAR experiment

Supervisor

Professor Jan Pluta, Ph.D.

Co-supervisor

Daniel Kikoła, Ph.D., D.Sc.

Warsaw 2017

Acknowledgments / Podziękowania

Po polsku

Pragnę poświęcić tą pracę mojej ukochanej Babuni, która zawsze motywowała mnie w postępach naukowych. Jest mi bardzo przykro, że nie doczekałaś ukończenia tej pracy. Wiem, że ucieszyłabyś się.

Chciałem też wyrazić swoje podziękowania dla mojej Mamy i Taty. Dziękuję wam za cierpliwość, pomoc w trudnych sytuacjach i wsparcie. Również bardzo doceniam rady, które otrzymałem od moich Promotorów Prof. Jana Pluty i Dr Daniela Kikoły. W dodatku, dziekuję Prof. Manuelowi Calderonowi de la Barca Sanchezowi za owocną współpracę i opiekę w czasie wizyt w UC Davis.

Autor uzyskał środki finansowe na przygotowanie rozprawy doktorskiej z Narodowego Centrum Nauki w ramach finansowania stypendium doktorskiego na podstawie decyzji numer: DEC-2015/16/T/ST2/00524. Praca ta była również wspierana ze środków Europejskiego Funduszu Socjalnego (Program Operacyjny Kapitał Ludzki) otrzymanego poprzez stypendium Centrum Studiów Zaawansowanych PW.

In English

I would like to dedicate this thesis to my beloved Grandma, who always motivated me in my scientific progress. I am deeply saddened that you could not see the completion of this thesis. I know you would be happy.

I would like to express my thanks to my Mother and Father. Thank you for your patience, help in difficult situations and support. I also very much appreciate the advise, I received from my Supervisors Prof. Jan Pluta and Dr Daniel Kikoła. In addition, I thank Prof. Manuel Calderon de la Barca Sanchez for a fruitful collaboration and care during my visits in UC Davis.

The author has received financial support for the preparation of doctoral thesis from the National Science Centre of Poland based on the decision number: DEC-2015/16/T/ST2/00524. This work was also supported by the European Union in the framework of European Social Fund (Human Capital Operational Programme) received as a scholarship WUT Center for Advanced Studies.

Abstract

This thesis summarizes measurements of J/ψ and Υ meson production in high energy proton-proton collisions in the STAR (Solenoidal Tracker at RHIC) experiment at the Relativistic Heavy Ion Collider (RHIC). The Υ, a bound state of $b\bar{b}$ quarks, and the J/ψ, which is made of $c\bar{c}$ pair are examples of quarkonium mesons. Studies of transverse momentum (p_T) or rapidity (y) dependence of their production cross section can provide constraints for the quarkonium production models. In addition, the production studies in $p + p$ collisions may be used as a reference for the Quark-Gluon Plasma (QGP) studies in heavy-ion collisions ($A + A$). Quark-gluon Plasma is a state of matter with quark and gluon degrees of freedom, that can be formed at high temperature or density. It existed in the Universe shortly after the Big Bang and can be recreated in high-energy $A + A$ collisions.

Recently, there are indications, that the QGP may also be created in small collision systems like $p + A$ or even $p + p$, as both feature collective effects just as in $A + A$. These effects are acknowledged as one of the signatures of the QGP. Studies of quarkonium production as a function of charged particle multiplicity, which is a measure of event activity, show a strong enhancement with multiplicity at Large Hadron Collider (LHC). The String Percolation Model, which predicts collective interaction of strings of color field, describes the observed dependence. In this thesis, it is investigated if such a trend is also present at RHIC energies.

Interpretation of world data on quarkonium production in $A+A$ and $p+A$ is complicated by lack of information about the quarkonium breakup in interactions with hadrons. The interaction probability increases with number of hadrons produced in an event. It also increases with the radius and decreasing binding energy for excited Υ states. A study of $\frac{\Upsilon(nS)}{\Upsilon(1S)}$ ratios as a function of multiplicity may provide information about such interaction.

In this thesis, the results of Υ production measurements in $p + p$ collisions at center-of-mass energy $\sqrt{s} = 500$ GeV in the STAR experiment are reported. Also, the results of J/ψ production in $p + p$ at $\sqrt{s} = 200$ GeV are presented.

This is the first measurement of Υ cross section as a function of transverse momentum at RHIC energies. The data allowed separation of $\Upsilon(1S)$ from $\Upsilon(2S + 3S)$. In addition, the rapidity dependence of Υ was obtained. The data are compared to the Υ production models. An integrated cross section was measured and compared to the world data vs. $\sqrt{s}$ and Color

Evaporation Model.

Furthermore, the $\frac{\Upsilon(nS)}{\Upsilon(1S)}$ ratios were obtained and are compared to the world data. The ratios are also investigated as a function of event multiplicity.

A dependence of normalized Υ yield on normalized multiplicity was also studied. It is consistent with data reported by other experiments and models, which indicate a strong rise at high multiplicity. This could be an indication of collective effects or Υ production in multiple parton interactions.

The J/ψ invariant cross section was measured and compared to the other RHIC data and models. It is consistent both with data and theory predictions. Also, an integrated cross section was calculated as well as mean p_T^2.

Keywords: particle physics, high energy physics, proton-proton collisions, strong interaction, quarkonium

Streszczenie

Badanie produkcji kwarkonium w relatywistycznych zderzeniach proton-proton w eksperymencie STAR

Rozprawa ta podsumowuje pomiary produkcji mezonów J/ψ i Υ w zderzeniach proton-proton wysokich energii w eksperymencie STAR (Solenoidal Tracker at RHIC) przy zderzaczu Relativistic Heavy Ion Collider (RHIC). Υ, stan związany kwarków $b\bar{b}$ i J/ψ, składające się z pary $c\bar{c}$ są przykładami kwarkonium, czyli stanu związanego pary kwark i anty-kwark. Badania zależności przekroju czynnego na produkcję tych mezonów od pędu poprzecznego p_T lub pospieszności y mogą pozwolić na weryfikację i usprawnienie modeli produkcji kwarkonium. Ponadto wyniki pomiarów produkcji w zderzeniach $p + p$ mogą zostać użyte jako punkt odniesienia dla badań właściwości Plazmy Kwarkowo-Gluonowej (QGP) w zderzeniach ciężkich jonów ($A + A$). Plazma Kwarkowo-Gluonowa to stan materii charakteryzującym się kwarkowymi i gluonowymi stopniami swobody, który może zostać utworzony w warunkach wysokiej temperatury lub gęstości. Istniał on we Wszechświecie we wczesnych fazach po Wielkim Wybuchu i może zostać odtworzony w wysokoenergetycznych zderzeniach $A + A$.

Ostatnio pojawiły się wskazówki, że QGP może również zostać wytworzona w reakcjach małych systemów takich jak $p + A$ lub nawet $p + p$, jako że w obu z nich widać efekty kolektywne tak jak w $A + A$. Efekty te są uznawane za przesłankę na powstanie QGP. Badania produkcji kwarkonium w Wielkim Zderzaczu Hadronów (LHC) w funkcji krotności cząstek naładowanych, która jest miarą aktywności w zdarzeniu, wykazują silny wzrost wraz z krotnością. Model Perkolacji Strun (ang. String Percolation Model), który przewiduje kolektywne oddziaływania strun pola kolorowego, opisuje zaobserwowaną zależność. Badania, czy podobne zjawisko jest obserwowane dla niższych energii, sa również elementem tej pracy.

Interpretacja danych dotyczących produkcji kwarkonium w zderzeniach $A + A$ i $p + A$ jest skomplikowana między innymi z powodu braku informacji o rozbijaniu kwarkonium w oddziaływaniach z hadronami. Prawdopodobieństwo oddziaływania rośnie wraz z liczbą hadronów wyprodukowanych w zdarzeniu. Zwiększa się ono również wraz z rosnącym promieniem i malejącą energia wiązania dla stanów wzbudzonych Υ. Badanie stosunków $\frac{\Upsilon(nS)}{\Upsilon(1S)}$ w funkcji krotności może dostarczyć informacji o tym oddziaływaniu.

W tej pracy prezentowane są wyniki pomiarów produkcji Υ w zderzeniach $p+p$ o energii w układzie środka masy $\sqrt{s} = 500\ \mathrm{GeV}$ w eksperymencie STAR. Prezentowane również są wyniki dla produkcji J/ψ w zderzeniach $p+p$ o energii $\sqrt{s} = 200\ \mathrm{GeV}$.

Jest to pierwszy pomiar przekroju czynnego Υ w funkcji pędu poprzecznego przy energiach dostępnych dla RHIC. Dane pozwoliły na rozdzielenie $\Upsilon(1S)$ od $\Upsilon(2S+3S)$. W dodatku, otrzymana została zależność od pospieszności. Przekrój czynny został zmierzony i porównany z innymi dostępnymi danymi w zależności od $\sqrt{s}$ oraz z modelem Color Evaporation Model.

Co więcej, stosunki $\frac{\Upsilon(nS)}{\Upsilon(1S)}$ zostały otrzymane i porównane z danymi uzyskanymi w innych eksperymentach. Stosunki te są także badane w funkcji krotności cząstek w zdarzeniu.

Zależność znormalizowanego sygnału Υ od znormalizowanej krotności także została zbadana. Jest ona spójna z danymi z innych eksperymentów i modelami, które wykazują silny wzrost dla dużych krotności. Może to wskazywać na efekty kolektywne albo produkcję Υ w oddziaływaniach wielopartonowych.

Przekrój czynny na produkcję J/ψ został zmierzony i porównany z danymi RHIC oraz modelami. Jest on zgodny z danymi oraz przewidywaniami teoretycznymi. Został także policzony całkowity przekrój czynny dla $y = 0$ oraz średni p_T^2.

Słowa kluczowe: fizyka cząstek elementarnych, fizyka wysokich energii, zderzenia proton-proton, oddziaływania silne, kwarkonium

Contents

List of Figures

List of Tables

Chapter 1

Introduction

1.1 Motivation

The most general goal of this thesis was the experimental study of the strong force by investigation of charmonium (a bound state of a pair of charm+anti-charm quark) and bottomonium (made up with a bottom+anti-bottom pair) production in high-energy proton-proton collisions. Since the 99% of all the mass of all nucleons originates from the strong interaction, it is essential to understand its properties.

This thesis is a study of J/ψ ($c\bar{c}$) and Υ ($b\bar{b}$) meson production vs. rapidity and transverse momentum p_T in proton-proton collisions in the STAR experiment at the Relativistic Heavy Ion Collider (RHIC). These data may be used to constrain charmonium and bottomonium production models and provide a reference for Υ measurements in heavy-ion collisions, which is a part of the study of the Quark-Gluon Plasma (QGP) properties. Such knowledge is essential for understanding and modeling the evolution of Early Universe because the QGP is predicted to exist up to 1 μs after the Big Bang. For these purposes, it is crucial to measure production of the $\Upsilon(1S)$, $\Upsilon(2S)$ and $\Upsilon(3S)$ states separately and extract their ratios. It is worth noting that the results presented in this thesis are the first measurements of the p_T spectrum of the Υ states at RHIC energy.

Furthermore, investigation of charged particle multiplicity (event activity) dependence of bottomonium production might provide information about the underlying particle production mechanism. Recent results [1–4] show that there is a connection between light and heavy particle production in $p+p$ collisions. Such measurements allow the study of collective effects [5, 6] and may shed some light on possible QGP formation in small colliding systems. Hints of such processes have been observed both at Large Hadron Collider (LHC) and RHIC [7–10]. The study of Υ production vs. event activity at RHIC energy may provide additional insight into collective effects and constraints for the models.

Finally, studies of $\frac{\Upsilon(nS)}{\Upsilon(1S)}$ vs. particle multiplicity may allow us to understand Υ interaction with hadrons [4, 11]. Excited Υ states, due to the larger radius and lower binding energy than $\Upsilon(1S)$ are expected to have a larger cross section for a breakup due to interactions with hadrons. Information about the modification of the observed yields due to hadronic interactions is necessary for correct interpretation of measurements of the bottomonium production in heavy-ion collisions.

1.2 Particle physics

The branch of physics that focuses on studies of particles which form matter or radiation is called particle physics. Basic properties of particles are studied by observing the outcome of particle interactions, which are influenced by these properties. Interactions are studied in laboratory conditions by colliding various types of particles at high energies. This allows studies of phenomena at subatomic scales. Such collisions are performed with particle accelerators and the results are measured by sophisticated particle detectors. A beam of particles is accelerated and collided with a stationary target or with another beam in a collider machine.

High-energy interactions are described using a set of variables introduced below, which simplify the description. A center-of-mass reference frame is used within a cylindrical coordinate system.

- $\sqrt{s}$ is the center-of-mass energy for a collision of particles
- $\sqrt{s_{NN}}$ is the center-of-mass energy per nucleon pair for a collision of ions
- p_T is the transverse momentum of a particle with respect to the beam axis
- p_z,p_L is the longitudinal momentum of a particle with respect to the beam axis (along the beam axis)
- θ (polar angle) is the angle between particle's momentum and the beam axis
- ϕ (azimuthal angle) is the angle between particle's transverse momentum and the direction to the center of a collider ring
- $y = \frac{1}{2}\ln(\frac{E+p_z c}{E-p_z c})$ (rapidity) is a measure of particle velocity along the beam axis, redefined in such a way that it is additive under the Lorentz transformation. Here, E is the particle energy, while c is the speed of light in a vacuum.

- $\eta \equiv -\ln(\tan(\frac{\theta}{2}))$ (pseudorapidity) is an approximation of rapidity for high energy particles, does not need measurements of particle energy and momentum as it is related to the polar angle

- $\beta = \frac{v}{c}$ is the particle velocity $v = |\vec{v}|$ normalized to the speed of light c.

1.3 Quantum chromodynamics

Quantum chromodynamics (QCD) is a quantum field theory describing the strong interaction of quarks and gluons. The strong interaction is one of the fundamental forces within the Standard Model. In this theory, a degree of freedom called color is a property of both quarks and gluons. It is an equivalent of electric charge in the electromagnetic interaction. A quark can have one of 3 types of color: red, green or blue (R, G, B in order), while an anti-quark has anti-color: anti-red, ant-green and anti-blue ($\bar{R}, \bar{G}, \bar{B}$). The gluon, which is the mediator of the strong interaction carries both color and anti-color. This makes the theory non-abelian and causes the gluons to interact with each other and form strings. There are 8 types of gluons (octet) predicted by the theory. The quarks can form hadrons made of either 3 quarks (baryons) or a quark and anti-quark pair (meson). An example of these particles connected by color fields is shown in a schematic in Figure 1.1a.

An important feature of the strong interaction is confinement of quarks in hadrons, and it is reflected in the QCD theory. In QCD, the potential $V_{q\bar{q}}$ for a pair of heavy quark and anti-quark has the form presented in Equation 1.1 [14]. The first term in the equation is the Coulomb-like part and the second term is called the confining term.

$$V_{q\bar{q}} = -\frac{4}{3}\frac{\alpha_s(q^2)}{r} + kr \tag{1.1}$$

Here, the $\alpha_s(q^2)$ is the running coupling constant of the strong interaction, which changes with the square of the 4-momentum transfer q^2 and r is the distance between $q\bar{q}$. The linear term kr, with parameter $k \approx 1\ \mathrm{GeV/fm}$ [14], describes the potential energy stored in a string formed by gluons as the $q\bar{q}$ pair is being pulled apart. If the potential energy of the color field reaches a sufficient value, another $q\bar{q}$ pair is created. At this point the string brakes and forms 2 strings as shown in the example in Figure 1.1b [13]. This causes the quarks to be confined in hadrons and prevents the separation of a single quark.

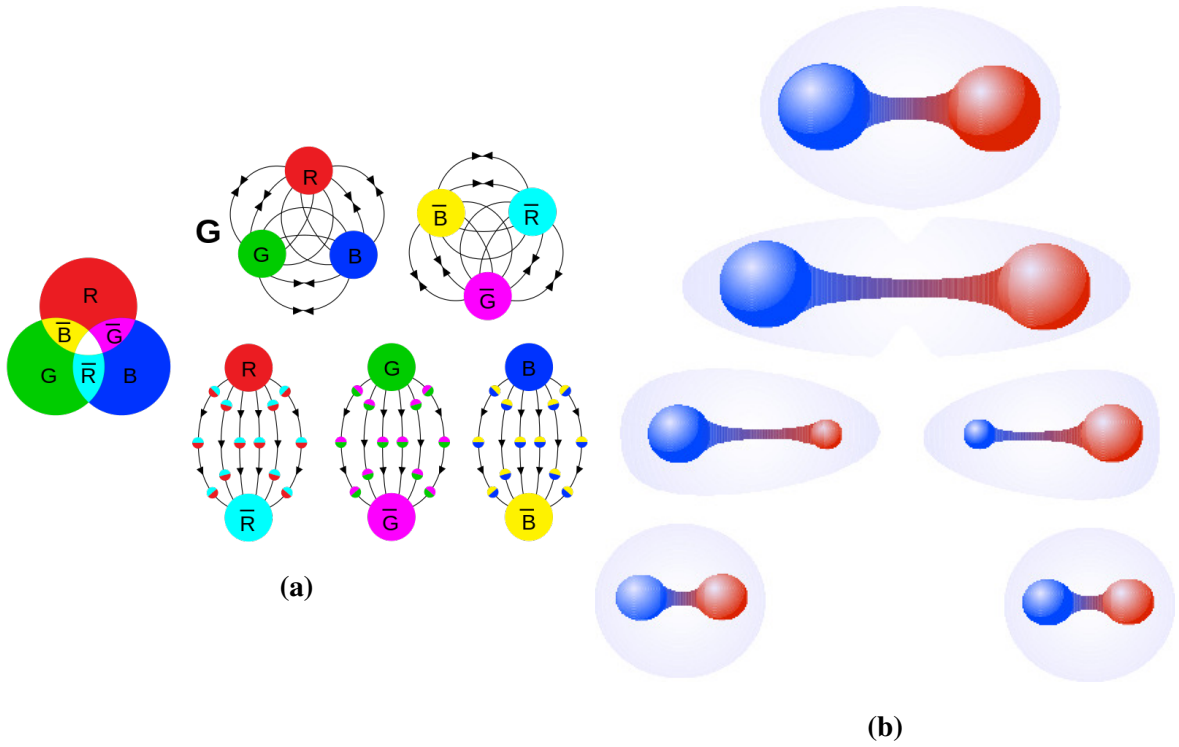

Figure 1.1: Figure 1.1a: Schematic of color fields for baryons and mesons [12]. Figure 1.1b: Schematic of color string breaking [13].

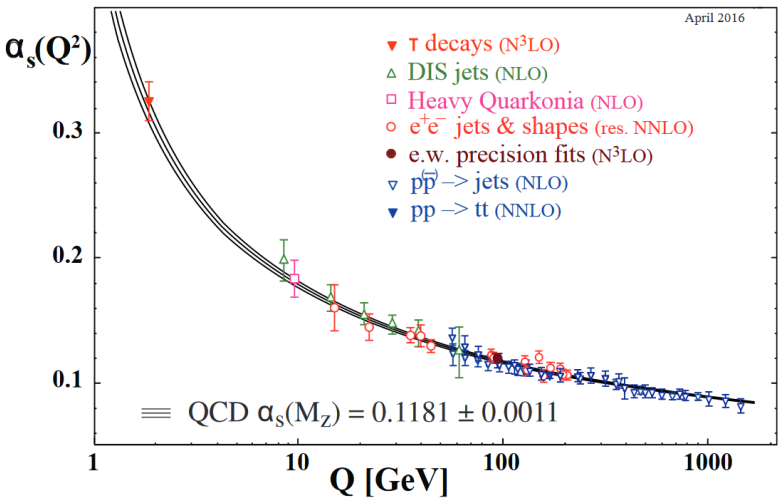

Figure 1.2: α_s dependence on Q, a summary of measurements [15].

Another important feature of QCD is Asymptotic Freedom predicted by D.J. Gross and F. Wilczek [16] and independently by H.D. Politzer [17] for witch they received a Nobel Prize in 2004. For high values of the 4-momentum transfer squared q^2, the coupling constant $\alpha_s(q^2)$ becomes very small and $\alpha_s(q^2) \to 0$ as $q^2 \to \infty$. This is due to running of the coupling constant

shown in the Figure 1.2 and described by the Equation 1.2.

$$\alpha_s(q^2) \equiv \frac{g_s^2(q^2)}{4\pi} \approx \frac{1}{\beta_0 \ln\left(\frac{q^2}{\Lambda_{QCD}}\right)} \tag{1.2}$$

In the equation above, the β_0 is the first order coefficient originating from renormalization group equation, in which $\alpha_s(q^2)$ is expanded into power series in $\ln(\frac{q^2}{\mu^2})$ [14]. The β_0 depends on the number of quark flavors. The $\Lambda_{QCD} = 217^{+25}_{-23}\mathrm{MeV}$ [18] parameter is the characteristic QCD scale, which is the infrared cutoff for the theory. This is a consequence of the application of perturbation theory, which is valid only for $q^2 \gg \Lambda_{QCD}$. Because of this distinction, the interactions described by QCD are divided into 2 categories: hard processes, which are described by Perturbative QCD (See Section 1.3.2), and soft processes. The former are connected with large momentum transfers, while the latter originate from small momentum transfers.

The running of the coupling constant is caused by the vacuum polarization effect. In QCD, the virtual $q\bar{q}$ pairs are polarized, so that the color charges of interacting particles are amplified at small values of q^2 and long distances. On the other hand, due to this anti-screening effect, the color charges are decreased at short distances or large q^2.

1.3.1 Quark-Gluon Plasma

A consequence of asymptotic freedom is the possibility of Quark-Gluon Plasma (QGP) [19–21] formation. It is a state of matter which features quark and gluon degrees of freedom. If the temperature of nuclear matter is high enough, around $T_c \approx 150\ \mathrm{MeV}$ (this implies large q^2 between partons), the interaction of quarks and gluons within hadrons may be very weak, so they behave like quasi-free particles. On the other hand, if the density of nuclear matter is very high ($\epsilon_c \approx 1\ \mathrm{GeV/fm^3}$ [22]), the hadrons start to overlap. When quarks are in close proximity to each other, their color charges are screened.

QGP is studied in relativistic heavy-ion ($A + A$) collisions, which may provide high density or temperature required for its formation. Such studies are important for understanding of the Early Universe [23], in which the QGP may also have formed.

1.3.2 Perturbative QCD

Perturbative QCD (pQCD) is the method of calculating various physical quantities (eg. cross sections) for hard QCD processes on the parton level, by taking advantage of the small value

of $\alpha_s \ll 1$ at high energy scale. This allows the expansion of cross section for a given process in powers of $\alpha_s^{n+2}(q^2)$. Thanks to the fact that $\alpha_s \ll 1$, the lowest order terms have the largest contribution. Increasing the power n allows for more precise n-th order calculation involving sums over sets of more complicated Feynman diagrams. The types of calculations are:

- $n = 0$ - Leading order (LO)
- $n = 1$ - Next-to-leading order (NLO)
- $n = 2$ - Next-to-next-to-leading order (NNLO) etc.

In order to calculate cross section $\sigma_{AB\to C}$ for a process $A + B \to C$, where A, B, C are hadrons, it is assumed that the cross section factorizes into 3 parts as shown in the Equation 1.3 [24].

$$\sigma_{AB\to C} = f_{a/A}(x_a, \mu_F^2) f_{b/B}(x_b, \mu_F^2) \otimes \sigma_{ab\to c}(s, \mu_F^2, \mu_R^2, \alpha_s) \otimes D_{c\to C}(z, \mu_F^2) \tag{1.3}$$

The first one is the parton level cross section $\sigma_{ab\to c}(s, \mu_F^2, \mu_R^2, \alpha_s)$ for short distance interaction, which can be calculated with pQCD. Here, s is the square of the center-of-mass energy, μ_F is the factorization scale used to evaluate parton densities, μ_R is the renormalization scale used to avoid ultraviolet divergence. The second part is the long distance, non-perturbative part, which includes parton distribution functions (PDF) $f_{a/A}(x_a, \mu_F^2)$, $f_{b/B}(x_b, \mu_F^2)$ for both hadrons A and B and a fragmentation function (FF) $D_{c\to C}(z, \mu_F^2)$. The former describes the distribution of parton a (b) in hadron A (B) with longitudinal momentum fraction x_a (x_b) at factorization scale μ_F. The latter describes the hadronization of parton c into a final state hadron C. Parton distribution functions are determined by deep inelastic scattering experiments, while fragmentation functions can be measured in e^+e^- collisions.

1.4 Relativistic proton-proton collisions

Proton-proton collisions at relativistic energies allow experimental studies of QCD and basic constituents of matter. They also provide a reference for heavy-ion collision studies. Protons are, however, complex objects, which are made of 3 valence quarks uud and a "sea" of quarks and gluons. The latter are either forming strings connecting the valence quarks or spontaneously appear due to vacuum fluctuations. This is schematically illustrated in Figure 1.3.

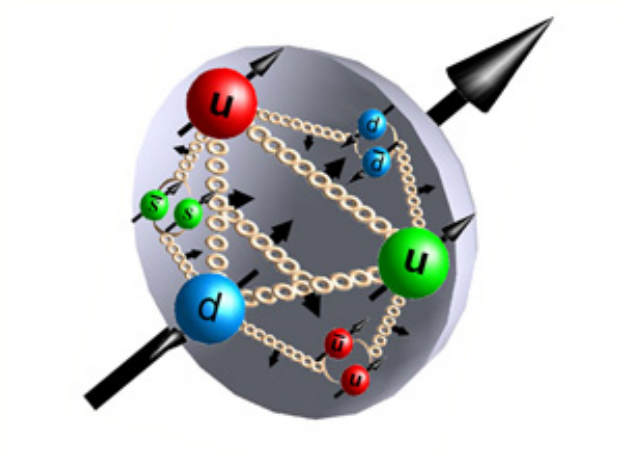

Figure 1.3: Schematic illustration of the proton structure. The arrows indicate spin direction, while color corresponds to color charge for quarks or anti-color charge for anti-quarks [25].

Furthermore, the structure of the proton depends on the scale q^2 at which it is probed. The higher the momentum transfer, the greater the parton density. This effect is reflected in the experimentally-determined parton distribution function (PDF). An example PDF is presented in Figure 1.4 [26] and shows the increasing parton density with q^2. In fact, at high values of q^2, the proton is dominated by small-x gluons.

Recent developments also include transverse momentum dependent parton distributions (TMD) [28] and generalized parton distributions (GPD) [29].

The manner in which quarks, gluons and their orbital momenta contribute to proton's spin of $1/2$ is still an open question.

1.4.1 Multiple parton interactions

Since protons are such complex objects, the $p + p$ collisions are also complicated. In reality, multiple parton collisions may happen in a single $p + p$ collision [30–32]. Such a collision is shown in an example in Figure 1.5. The multiple parton interactions (MPI) can be either hard or soft processes. It has to be noted, that MPI are responsible for bulk particle production in $p + p$ collisions. In the most extreme collisions, lots of particles are produced through MPI reflecting a high activity in the event.

The PYTHIA8 event generator is one of the models used in this thesis and implements MPI.

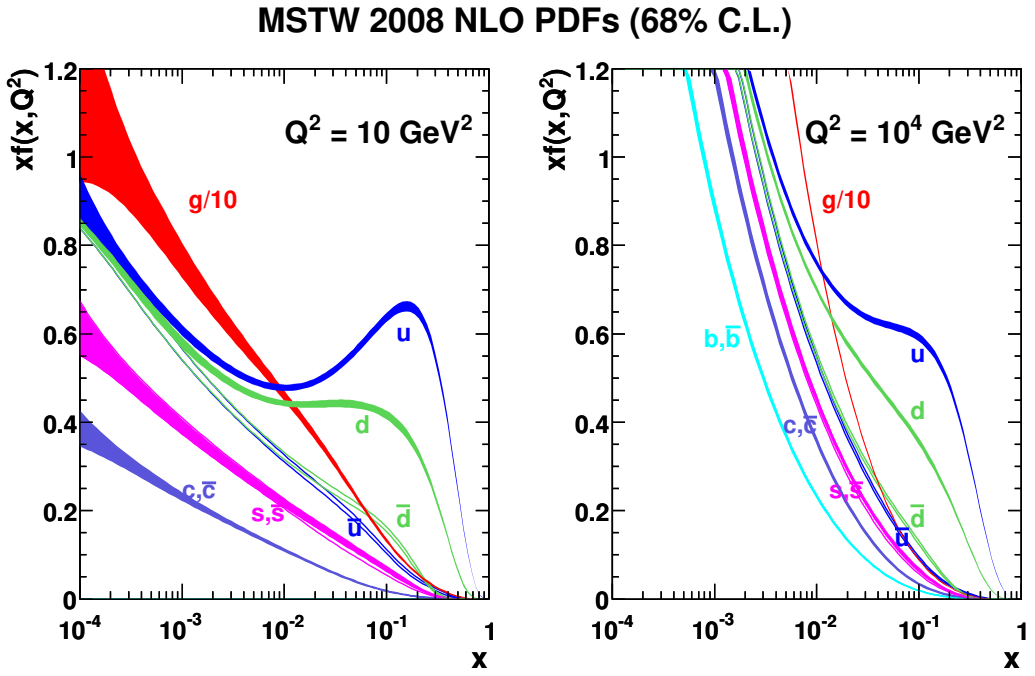

Figure 1.4: Parton distribution functions for various types of partons at $q^2 = 10\ \mathrm{GeV}^2$ (left) and $q^2 = 10^4\ \mathrm{GeV}^2$ (right) [27]. They indicate the probability of finding a parton with proton momentum fraction x at a given scale.

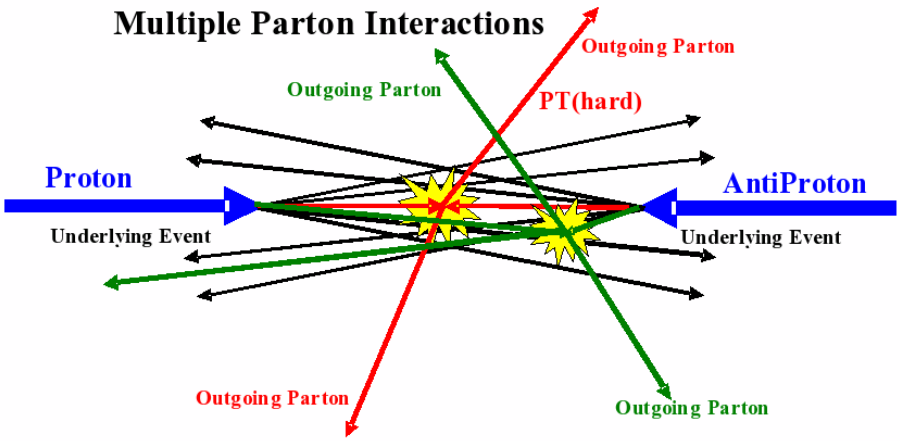

Figure 1.5: Schematic of a $p + \bar{p}$ collision with the main hard process (red) and a parallel process in MPI (green) [33].

1.4.2 Color Glass Condensate

The Color Glass Condensate (CGC) [34] is a state of matter that may exist in an $A + A$ or $p + p$ collision. The colliding ions or protons are Lorentz-contracted and are subjected to time

dilation, thus the gluons are squeezed together and interact weakly with each other. Moreover, the gluon density ρ_g at high energy scale and low x increases very fast as can be seen in Figure 1.6 [35]. It saturates, however, due to the competition between gluon radiation ($\propto \rho_g$) and fusion ($\propto \rho_g^2$). This is represented by the saturation scale Q_s parameter.

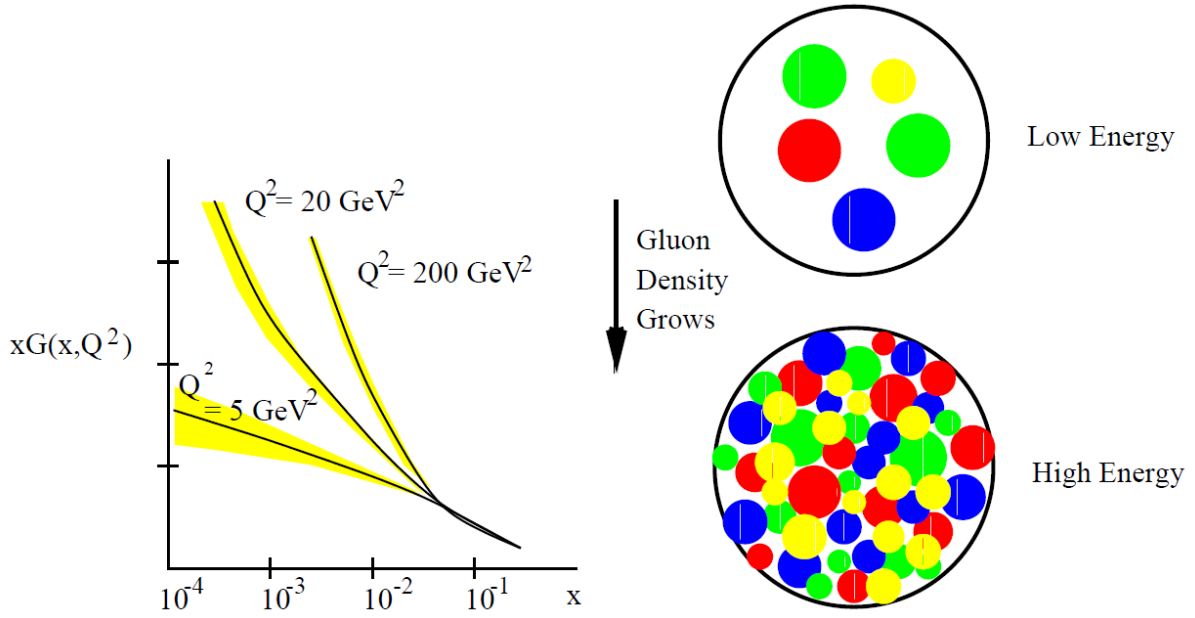

Figure 1.6: Left: Density of gluons vs. x for $Q^2 = -q^2 = 5, 20, 200$ GeV^2. Right: Illustration of increasing gluon density and Color Glass Condensate formation [35].

In the CGC framework, an $A + A$ collision may be modeled as a collision of classical fields corresponding to the gluon condensates. It can also be applied to $p + A$ collisions [36] with the proton being represented as a dilute projectile colliding with a dense nucleus. This picture can be extended to $p + p$ collisions at forward rapidity, where one proton is dilute (large $x \approx 1/3$) and the other one is dense (small $x \ll 1/3$).

1.4.3 Hints of possible Quark-Gluon Plasma formation in small systems

In high energy $p + p$ collisions, the basic requirements for QGP creation can be met, if the parton density is high enough. Recent measurements at RHIC [7, 8] and LHC [37] suggest presence of collective effects in small systems like those produced in $d+Au$ and $p+p$ collisions. These effects are similar to the ones observed in $A + A$ collisions, which had been assumed as signatures of QGP.

In $A + A$ collisions, the charged particle multiplicity is connected to the centrality of the

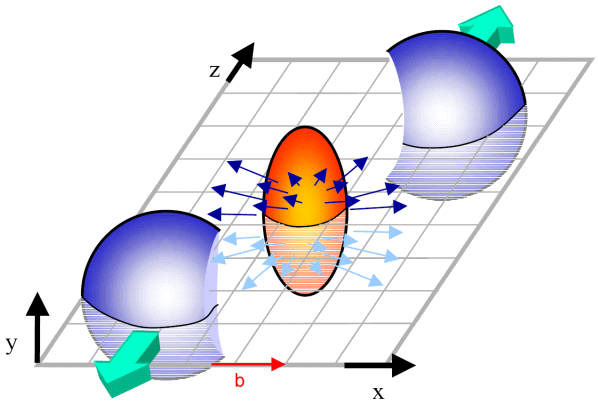

Figure 1.7: Illustration of a mid-central $A + A$ collision [38].

collision, measured by impact parameter $\vec{b}$. The impact parameter is a vector originating in the center of the projectile and pointing to the center of the target. In mid-central collisions, the overlap region, in which the QGP forms, has an elliptical "almond"-like shape. This produces pressure gradients, which cause a collective motion of produced particles, that also has an elliptic pattern. More particles flow along the axis of the impact parameter than along the axis of the "almond". This elliptic flow is measured by v_2, the second coefficient in a Fourier decomposition of the $\Delta\phi$ angle distribution, which is the angle between $\vec{p_T}$ and the event plane (the plane defined by the beam axis and impact parameter $\vec{b}$). Such a case is presented in a schematic in Figure 1.7.

While the impact parameter decreases, the volume (system size) and charged particle multiplicity in an event increase. In summary, multiplicity can be a measure of event activity, however for $p+p$ collisions it is not directly proportional to the impact parameter. The underlying event activity [40, 41] in $p+p$ collisions is defined as all processes additional to the hard scattering of interest. These include MPI, initial (ISR) and final-state radiation (FSR) and proton remnants. All of these increase charged particle multiplicity of a $p+p$ event.

The Figure 1.8 shows elliptic v_2 and triangular v_3 (3rd coefficient in the Fourier decomposition mentioned above) flow coefficients vs. multiplicity measured by CMS [39]. There is an evidence of collective effects in all types of collision systems, which may indicate QGP formation even in small systems. A review of recent results from LHC is made in Reference [10] and both RHIC and LHC in Reference [9].

Collective effects are also a possible explanation of a strong dependence of J/ψ [1, 2], D meson [3] and Υ production [4] on event activity, which is measured by the normalized charged

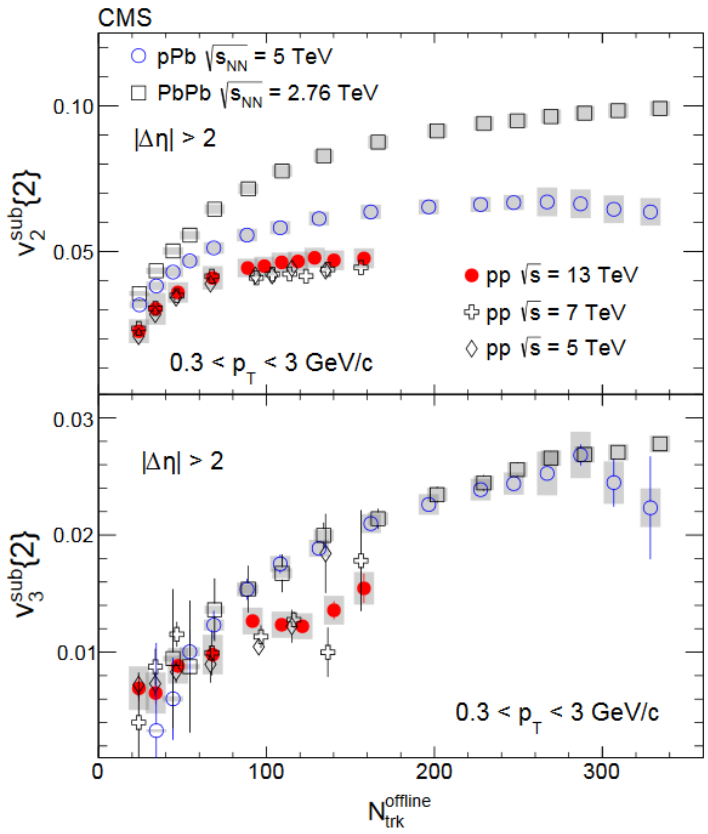

Figure 1.8: Elliptic v_2 and triangular v_3 flow coefficients vs. multiplicity measured by CMS [39].

particle multiplicity. These results are well described by the String Percolation Model [6, 42], which assumes collective interaction between strings of color field.

1.5 Quarkonium

The general name of quarkonium is used for a meson made of heavy quark and anti-quark of the same type. A Cornell potential of the form shown in Equation 1.4 is used to describe the interaction between $q\bar{q}$ pair in a quarkonium.

$$V(r) = -\frac{\alpha}{r} + \sigma r \tag{1.4}$$

Where the parameters $\alpha = \frac{4}{3}\alpha_s$ and σ is the string tension. The Cornell potential is in agreement with the lattice QCD calculations [43].

An important feature of heavy quarkonium states like charmonium and bottomonium is that their mass is largely determined by the bare charm (c) or bottom (b) quark mass, so relativistic effects can be neglected.

At high temperature or density the color charges are screened due to the phenomenon similar to Debye screening. It has been predicted to cause a suppression of J/ψ production induced by the QGP [44]. In the QGP, the Cornell potential is modified and the new potential for $q\bar{q}$ takes the form in Equation 1.5.

$$V(r) = -\frac{\alpha}{r} e^{\frac{-r}{r_D(T)}} \tag{1.5}$$

Here, r_D is the Debye screening radius.

The suppression of both charmonium and bottomonium production in heavy-ion collisions relative to the yields expected from baseline measurements in $p + p$ has been observed at SPS, RHIC and LHC [45]. Moreover, a sequential suppression has been observed [46], which is expected due to the larger radius of excited quarkonium states and are thus more easily dissociated in the QGP. The studies are still ongoing, because the interpretation of the heavy-ion results is affected by the cold cold nuclear matter (CNM) effects. CNM effects include interaction with co-moving hadrons and influence of modified PDFs in a nucleus [47] and they are not well understood. These may modify quarkonium production for reasons unrelated to the QGP, diluting the picture. In addition, feed-down from excited states complicates the interpretation.

1.5.1 Charmonium

Charmonium is a bound state of $c\bar{c}$ (charm) quarks. Most notable charmonium is the J/ψ particle, which was independently discovered by experiments led by Samuel Ting [48] and Burton Richter [49] in 1974. It confirmed the existence of the charm quark. Both won Nobel Prize in 1976 for their discoveries. The event sparked a rapid progress in high energy physics, named "November Revolution".

Indeed, there is an entire family of charmonium particles, which are listed in the Table 1.1. Each of the states has different mass, binding energy, radius, and quantum numbers: n - principal quantum number, L - orbital quantum number, S - spin quantum number, J - total angular momentum, P - parity, C - charge conjugation. The higher, the mass, the larger the radius and the lower the binding energy.

Also, the excited states may decay to the lower mass states like $\psi(2S) \rightarrow J/\psi + X$, which contribute to the directly produced J/ψ. This is called feed-down. A schematic of the feed-down pattern of charmonium states is shown in Figure 1.9. In addition, the charmonium states above the $D\bar{D}$ threshold can decay into $D\bar{D}$ mesons. $B \rightarrow J/\psi + X$ meson decays also

Charmonium	$n^{2S+1}L_J$	J^{PC}	Mass [MeV]
$\eta_c(1S)$	1^1S_0	0^{-+}	2983.4 ± 0.5
$J/\psi(1S)$	1^3S_1	1^{--}	3096.900 ± 0.006
$\chi_{c0}(1P)$	1^3P_0	0^{++}	3414.75 ± 0.31
$\chi_{c1}(1P)$	1^3P_1	1^{++}	3510.66 ± 0.07
$h_c(1P)$	1^1P_0	1^{+-}	3525.38 ± 0.11
$\chi_{c2}(1P)$	1^3P_2	2^{++}	3556.20 ± 0.09
$\eta_c(2S)$	2^1S_0	0^{-+}	3639.2 ± 1.2
$\psi(2S)$	2^3S_1	1^{--}	$3986.0.97 \pm 0.025$

Table 1.1: Table of charmonium states [15].

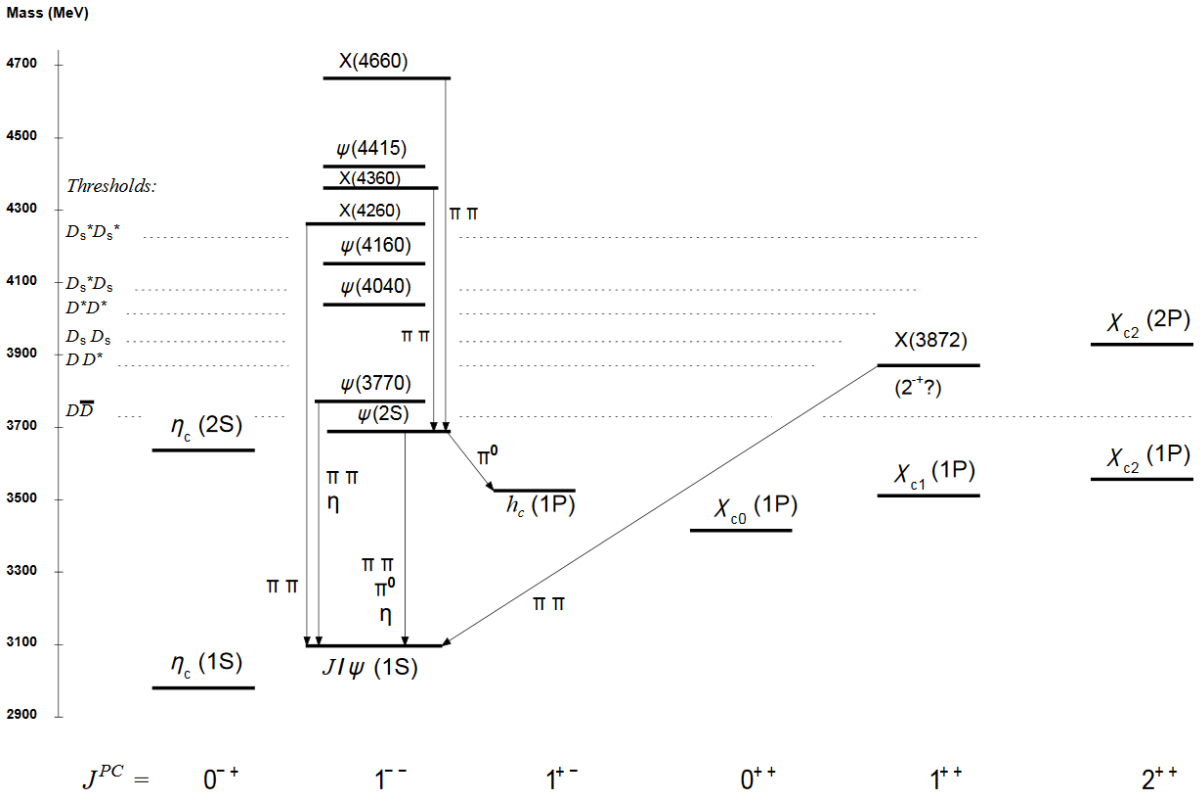

Figure 1.9: Schematic of charmonium feed-down pattern [15].

contribute to the observed yield.

In this thesis, the J/ψ are studied via $J/\psi \to e^+e^-$, a process with branching ratio $B_{ee} = (5.971 \pm 0.032)\%$.

1.5.2 Bottomonium

The first particle of the bottomonium family, the $\Upsilon(1S)$, was discovered by a group under leadership of Leon Lederman [50] in 1977. Bottomonium states are bound states of $b\bar{b}$ quarks. They are similar to charmonium states, but their masses are much larger and are more rarely produced. Selected bottomonium states are summarized in Table 1.2.

Bottomonium	$n^{2S+1}L_J$	J^{PC}	Mass [MeV]
$\eta_b(1S)$	1^1S_0	0^{-+}	9399.0 ± 2.3
$\Upsilon(1S)$	1^3S_1	1^{--}	9460.30 ± 0.26
$\chi_{b0}(1P)$	1^3P_0	0^{++}	$9859.44 \pm 0.42 \pm 0.31$ (PDG evaluation)
$\chi_{b1}(1P)$	1^3P_1	1^{++}	$9892.78 \pm 0.26 \pm 0.31$ (PDG evaluation)
$h_b(1P)$	1^1P_0	1^{+-}	9899.3 ± 0.8
$\chi_{b2}(1P)$	1^3P_2	2^{++}	$9912.21 \pm 0.26 \pm 0.31$ (PDG evaluation)
$\eta_b(2S)$	2^1S_0	0^{-+}	$9999.0 \pm 3.5^{+2.8}_{-1.9}$
$\Upsilon(2S)$	2^3S_1	1^{--}	10023.26 ± 0.31
$\Upsilon(1D)$	1^3D_2	2^{--}	10163.7 ± 1.4
$\chi_{b0}(2P)$	2^3P_0	0^{++}	$10232.5 \pm 0.4 \pm 0.5$ (PDG evaluation)
$\chi_{b1}(2P)$	2^3P_1	1^{++}	$10255.46 \pm 0.22 \pm 0.50$ (PDG evaluation)
$h_b(2P)$	2^1P_0	1^{+-}	$10259.8 \pm 0.5 \pm 1.1$
$\chi_{b2}(2P)$	2^3P_2	2^{++}	$10268.65 \pm 0.22 \pm 0.50$ (PDG evaluation)
$\Upsilon(3S)$	3^3S_1	1^{--}	10355.2 ± 0.5
$\chi_{b1}(3P)$	3^3P_1	1^{++}	$10512.1 \pm 2.1 \pm 0.9$ (PDG evaluation)

Table 1.2: Table of bottomonium states [15]. The second uncertainty on the mass of some states (PDG evaluation) is from additional Particle Data Group evaluation.

Feed-down also affects bottomonium states. A schematic of feed-down is shown in Figure 1.10. A large contribution to $\Upsilon(nS)$ is from the $\chi_{bJ}(nL)$ states, which are not shown in the Figure.

In this thesis, the Υ states are measured in dielectron channel. The branching ratios are:

- $\Upsilon(1S) \to e^+e^-$ $B_{ee} = (2.38 \pm 0.11)\%$
- $\Upsilon(2S) \to e^+e^-$ $B_{ee} = (1.91 \pm 0.16)\%$

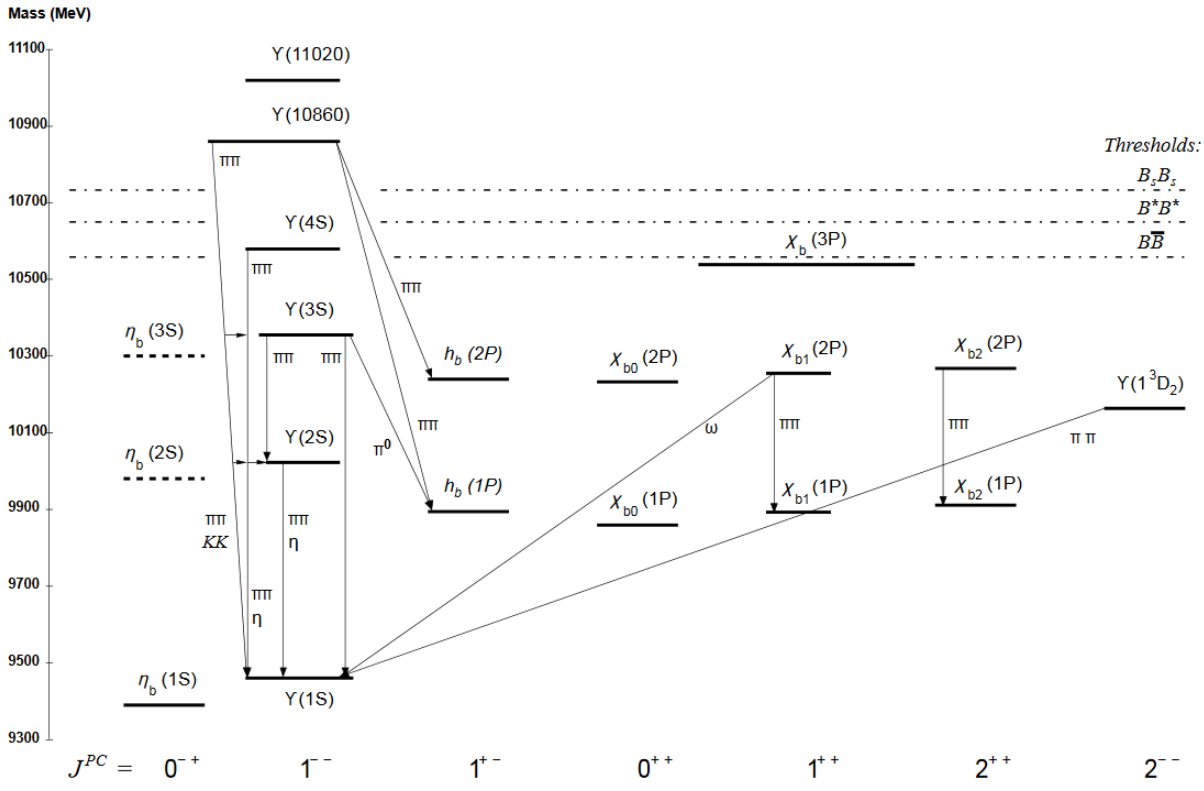

Figure 1.10: Schematic of bottomonium feed-down pattern [15].

- $\Upsilon(3S) \to e^+e^-$ $B_{ee} = (2.18 \pm 0.20)\%$

Chapter 2

Quarkonium production

2.1 Quarkonium production models

The quarkonium production mechanism is still not fully understood. This is because the it is influenced by both perturbative and non-perturbative processes in QCD. The c or b quarks, which form the quarkonium have a high mass ($m_c = 1.28 \pm 0.03 \mathrm{GeV/c^2}$, $m_b = 4.18^{+0.04}_{-0.03} \mathrm{GeV/c^2}$) [15], thus they have to be produced in pairs in a hard process. This part can be calculated in pQCD. The second part is the formation of a bound state, which is non-perturbative and has to be modeled. This phenomenon can be divided into 2 cases, depending on the quantum numbers of the $Q\bar{Q}$ pair. It can be produced in color singlet (CS), colorless, state with quantum numbers being the same as those of the final state quarkonium ($^3S_1$ in case of J/ψ or Υ). On the other hand, it can be produced in color octet (CO) state with any possible quantum numbers $^{+1}L_J$ and color. Both these cases are shown in an example in Figure 2.1.

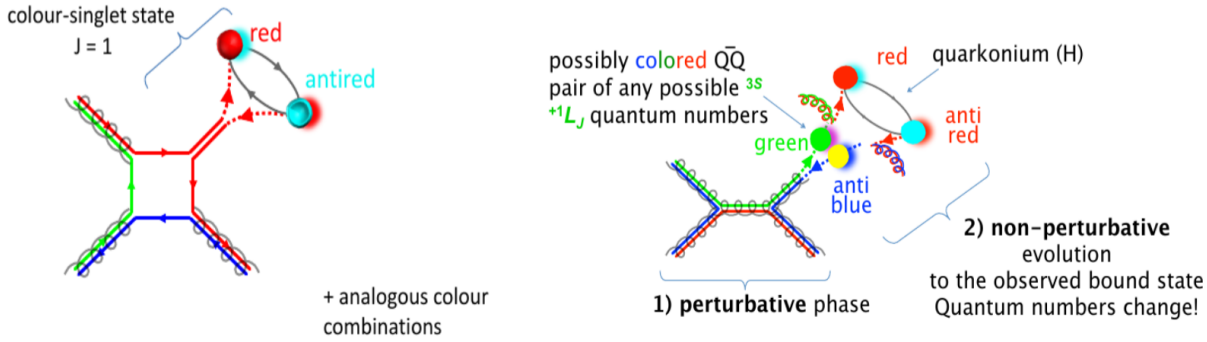

Figure 2.1: Illustration of quarkonium production in color singlet (CS, left) and color octet (CO, right) models [51].

2.1.1 Color Singlet Model

The color singlet model [52–54] is based on the assumption that the $Q\bar{Q}$ pair is produced directly in a colorless state and that the subsequent evolution can be neglected. The cross section for quarkonium production $d\sigma_{Q_{Q\bar{Q}}+X}$ can be calculated with the formula in Equation 2.1.

$$d\sigma_{Q_{Q\bar{Q}}+X} = \sum_{a,b} \int f_{a/A}(x_a, \mu_F) f_{b/B}(x_b, \mu_F) d\sigma_{ab\to(Q\bar{Q})+X}(s, \mu_F, \mu_R, \alpha_s) |\psi(0)|^2 \tag{2.1}$$

The only input to the model are the PDFs $f_{a/A}$, $f_{b/B}$, factorization μ_F and renormalization μ_R scales and wave function $|\psi(0)|^2$, but the latter can be obtained from data or calculated.

The CS describes a large fraction of the quarkonium cross section in RHIC and LHC data [55], but there are some issues, especially with Tevatron data [56]. This points to the conclusion that large fraction of high-p_T quarkonium production is through the CS channel, however, this is not enough to describe the entire production. In addition, the higher order corrections (NLO, approximate NNLO) are not negligible and thus are needed.

The CS model is limited to $p_T > m_{Q_{Q\bar{Q}}}$, where $m_{Q_{Q\bar{Q}}}$ is the mass of the quarkonium.

2.1.2 Color Octet Model

The Color Octet Model [57] is an attempt to take into account all possible states of $Q\bar{Q}$ pair during the formation of the bound state. It is implemented in the Non-relativistic QCD (NRQCD) framework [58, 59]. This is possible, thanks to the fact, that heavy quarks are massive and move slowly, so a non-relativistic treatment is feasible. Furthermore, since their velocity $v \ll c$, an expansion in powers of v of the non-perturbative part can be made. A leading contribution in v corresponds to the CS model. The cross section for quarkonium production can be calculated with the Equation 2.2.

$$d\sigma_{Q_{Q\bar{Q}}+X} = \sum_{a,b,n} \int f_{a/A}(x_a, \mu_F) f_{b/B}(x_b, \mu_F) d\sigma_{ab\to(Q\bar{Q})_n+X}(s, \mu_F, \mu_R, \mu_\Lambda, \alpha_s) \left\langle O^n_{Q_{Q\bar{Q}}} \right\rangle \tag{2.2}$$

The $\left\langle O^n_{Q_{Q\bar{Q}}} \right\rangle$ are the long-distance matrix elements (LDMEs), which describe the bound state formation. These LDMEs are assumed to be universal, but have to be extracted from fits to the data. However, there was a need to introduce an additional scale μ_Λ to avoid divergence.

The CO model is limited to $p_T > m_{Q_{Q\bar{Q}}}$, but it describes the quarkonium production at Tevatron [60, 61], LHC [62], RHIC [63] and other experiments [64].

2.1.3 CGC+NRQCD model

In order to extend the NRQCD framework to $p_T < m_{Q_{Q\bar{Q}}}$, it was combined with CGC model [65]. It uses the dense proton+dilute proton picture of a $p + p$ collision, which is mostly valid at forward rapidity. The perturbative part in Equation 2.2 is replaced with CGC calculation. In conjunction with NLO NRQCD, the CGC+NRQCD allows a comprehensive description of J/ψ production at RHIC and LHC [66].

2.1.4 Color Evaporation Model

The Color Evaporation Model (CEM) is based on a principle of quark-hadron duality [67–69]. This makes the quarkonium production directly connected to the $Q\bar{Q}$ production if an invariant mass of the pair satisfies $2m_Q < m_{Q\bar{Q}} < 2m_H$. Where, the m_Q is the mass of a heavy quark and m_H is the mass of a lightest open heavy-flavor hadron (D or B meson). The Equation 2.3 is used to calculate the cross section.

$$d\sigma_{Q_{Q\bar{Q}}} = F_{Q_{Q\bar{Q}}} \int_{2m_Q}^{2m_H} \frac{d\sigma_{Q\bar{Q}}}{dm_{Q\bar{Q}}} dm_{Q\bar{Q}} \tag{2.3}$$

The coefficient $F_{Q_{Q\bar{Q}}}$ represents the probability of a particular bound state formation. It is extracted from the fits to the world data.

A main drawback of the CEM is that the color of the $Q\bar{Q}$ pair and other quantum numbers are neglected. It could however describe the world data well [70, 71]. Recently, an Improved CEM (ICEM) was developed [72], which introduces a p_T dependence in quarkonium ratios. These are otherwise constant vs. p_T by definition in CEM.

2.1.5 String Percolation Model

In the extreme $p + p$ collisions, where a large number of charged particles is produced, the density of produced strings may be so high that they start overlapping [73]. An example is shown in Figure 2.2. This leads to the String Percolation Model, which describes the interaction between strings and its effects on particle production. It assumes collective interaction between strings of color field. The number of hard processes is proportional to the number of strings N_s.

While the charged particle multiplicity $\frac{dN_{ch}}{d\eta}$ (reflecting event activity) is calculated according to Equation 2.4 [6].

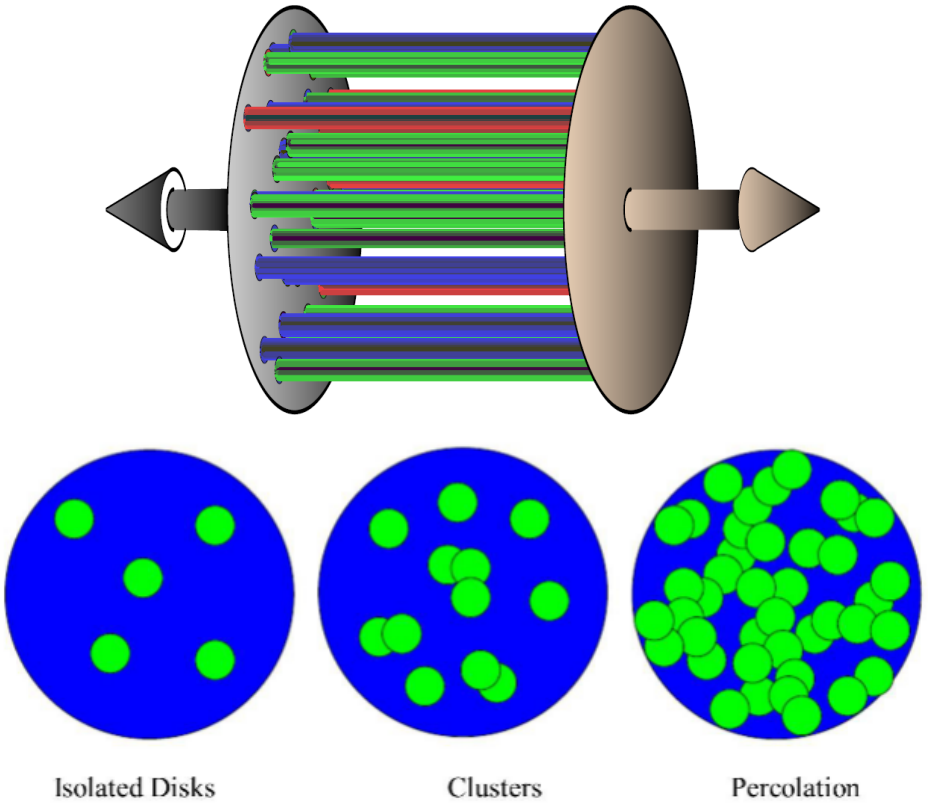

Figure 2.2: Illustration of string percolation as the event activity increases in a collision [36, 74].

$$\frac{dN_{ch}}{d\eta} = F(\rho)N_s\mu_1 \tag{2.4}$$

In the formula above, the $F(\rho)$ is the string density-dependent damping factor, which reflects the damping of particle production caused by the overlap of strings. The coefficient μ_1 is the multiplicity produced by a single string. Furthermore, the transverse radius of the strings r_T is inversely proportional to the transverse mass $r_T \propto 1/m_T$ [42]. The overlap is stronger then, for many strings originating from soft interactions. These effects produce a relation between hard and soft particle production as reflected in Equation 2.5 [6].

$$\frac{\frac{dN_{ch}}{d\eta}}{\left\langle \frac{dN_{ch}}{d\eta} \right\rangle} = \left(\frac{N_{hard}}{\langle N_{hard} \rangle} \right)^{\frac{1}{2}} \left[\frac{1 - e^{-\frac{N_{hard}}{\langle N_{hard} \rangle}\langle\rho\rangle}}{1 - e^{-\langle\rho\rangle}} \right]^{\frac{1}{2}} \tag{2.5}$$

It leads to the quadratic dependence of normalized yield from hard processes on normalized

multiplicity at high multiplicity as presented in Equation 2.6 [6].

$$\frac{N_{hard}}{\langle N_{hard} \rangle} = \langle \rho \rangle \left(\frac{\frac{dN_{ch}}{d\eta}}{\left\langle \frac{dN_{ch}}{d\eta} \right\rangle} \right)^2 \tag{2.6}$$

The String Percolation Model successfully explains the ALICE J/ψ [6] and D meson results [42].

2.2 Quarkonium production in proton-proton collisions

2.2.1 Overview of recent Υ results in proton-proton collisions

Recent results at LHC energy include separated $\Upsilon(1S)$, $\Upsilon(2S)$ and $\Upsilon(3S)$ cross section measurements by CMS [75] and ATLAS [76]. The p_T dependence of the cross section is shown in Figure 2.3a, while the y dependence is presented in Figure 2.3b.

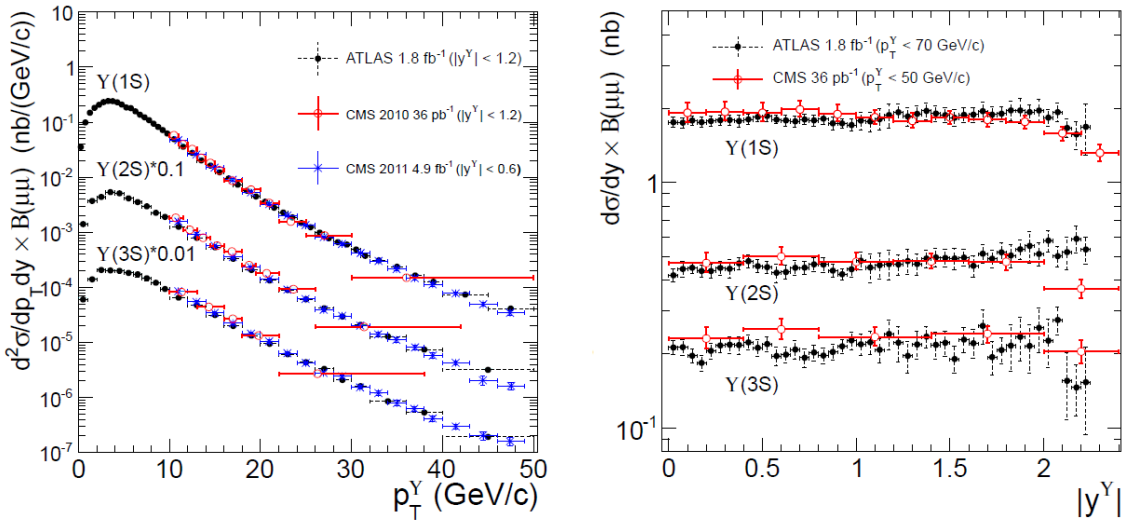

(a) **(b)**

Figure 2.3: Figure 2.3a: Cross section vs. p_T for $\Upsilon(1S)$, $\Upsilon(2S)$ and $\Upsilon(3S)$ for ATLAS (black closed circles) and CMS for $|y| < 1.2$ (red open circles) and $|y| < 0.6$ (blue crosses) [75]. Figure 2.3b: Cross section vs. y for $\Upsilon(1S)$, $\Upsilon(2S)$ and $\Upsilon(3S)$ measured by ATLAS (black closed circles) and CMS (red open circles) [75].

CMS has also measured $\Upsilon(1S)$, $\Upsilon(2S)$ and $\Upsilon(3S)$ cross sections up to $p_T < 100\mathrm{GeV/c}$ [77]. These are well described by the NLO CS+CO calculation [78].

In addition to the precise data at LHC, there are Υ measurements at ISR [79] and Tevatron [80]. Figure 2.4 shows the invariant cross section for $\Upsilon(1S)$ production at ISR. There are no p_T-dependent studies at RHIC energy, which motivates this research.

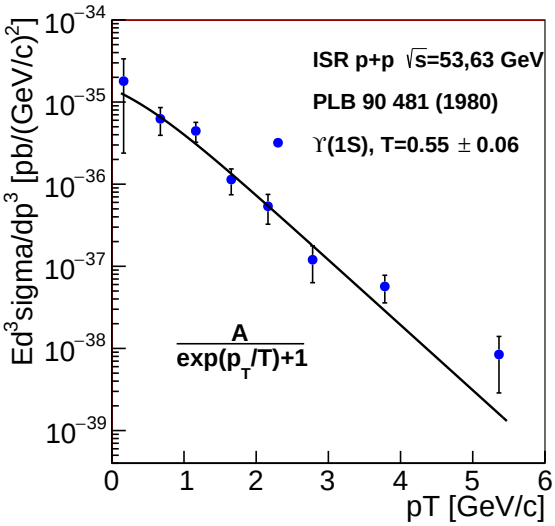

Figure 2.4: Cross section of $\Upsilon(1S)$ vs. p_T measured by ISR (blue circles) fitted with an exponential function (black line) [79, 81].

Figure 2.5a shows the p_T dependence of $\frac{\Upsilon(2S)}{\Upsilon(1S)}$ and $\frac{\Upsilon(3S)}{\Upsilon(1S)}$ ratios for world data [82]. The ratios increase with p_T above $p_T > 10\ \mathrm{GeV/c}$. The rapidity dependence of the ratios is presented in Figure 2.5b. The data trend is consistent with a flat dependence.

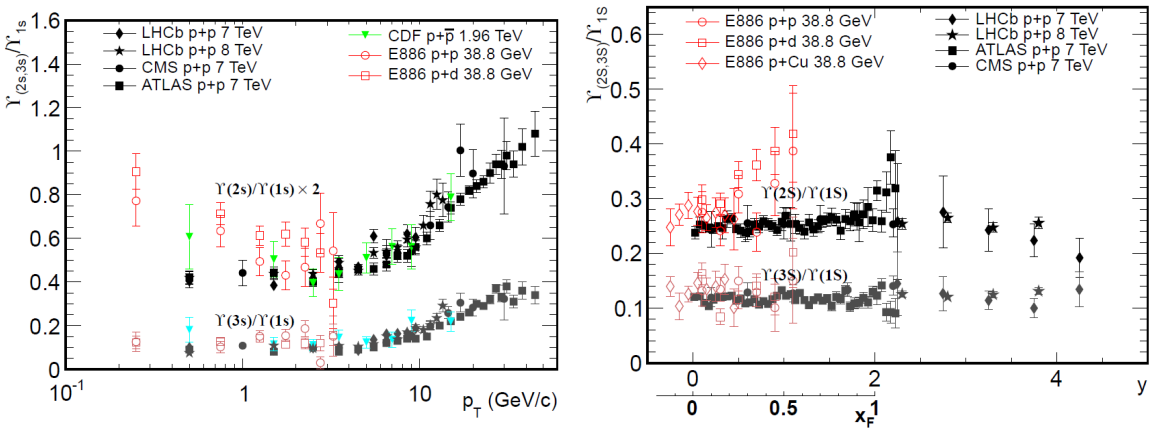

(a) **(b)**

Figure 2.5: Figure 2.5a: Upsilon ratios vs. p_T [82]. Figure 2.5b: Upsilon ratios vs. y [82].

In addition, ATLAS observed a new bottomonium state $\chi_b(3P)$ [83]. LHCb on the other hand, measured precise feed-down fraction to the $\Upsilon(1S)$, which is 30% at most [84].

2.2.2 Quarkonium in high multiplicity proton-proton collisions

Measurements of quarkonium production in high multiplicity $p + p$ collisions show a strong dependence of normalized yield on normalized multiplicity N_{ch}. The N_{ch} is a measure of event activity and high multiplicity collisions correspond to the extreme, high event activity, collisions. Moreover, in high multiplicity events a CGC may be created or perhaps a small-system QGP. This may be investigated by studying quarkonium production in such events.

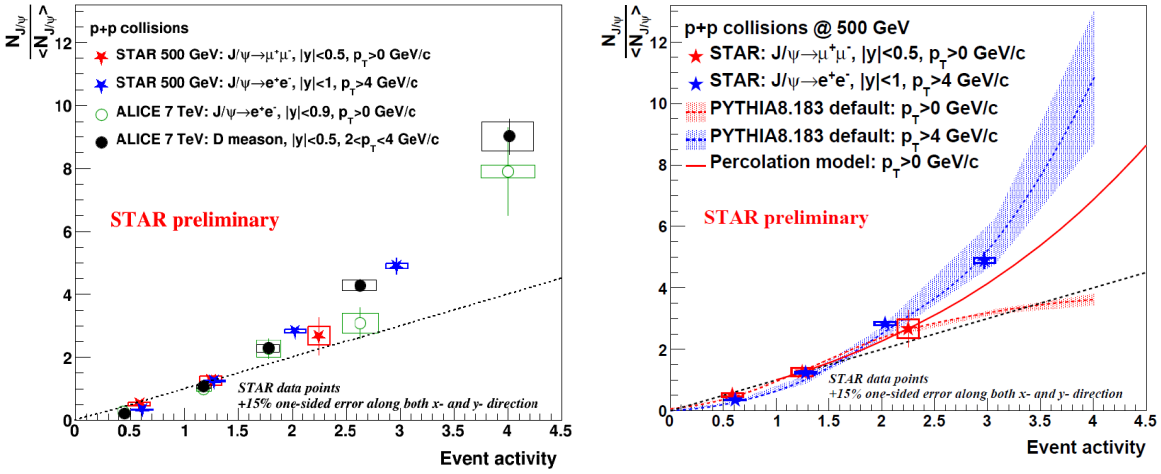

(a) **(b)**

Figure 2.6: Figure 2.6a: J/ψ normalized yield vs. normalized multiplicity. STAR $J/\psi \to \mu^+\mu^-$ (red stars) and $J/\psi \to e^+e^-$ (blue stars) results [1] are compared to ALICE J/ψ (green open circles) [2] and D (black closed circles) meson data [3]. Figure 2.6b: J/ψ normalized yield vs. normalized multiplicity from STAR $J/\psi \to \mu^+\mu^-$ (red stars) and $J/\psi \to e^+e^-$ (blue stars) results [1]. The data are compared to the String Percolation Model (red line) [5, 6] and PYTHIA8 calculation for $p_T > 0\,\mathrm{GeV/c}$ (red dashed line) and $p_T > 4$ GeV/c (blue dashed line) [85].

A similar trend is observed when comparing J/ψ production measured by STAR [1] and ALICE [2] despite a large difference in collision energy. This is shown in Figure 2.6a. However, a linear dependence is observed for $J/\psi \to \mu^+\mu^-$ with $p_T > 0$ GeV/c measured with the new Muon Telescope Detector (MTD) [86]. It is interesting that D mesons follow a similar trend as J/ψ. The STAR data are compared to models in Figure 2.6b. PYTHIA8 calculation with a description of MPI is in agreement with the data. This points to the J/ψ being produced in hard processes in MPI. The String Percolation Model reproduces the trend observed in the data [5, 6].

Event activity dependence is investigated for Υ states by CMS and is shown in Figure 2.7 [4].

Both $\Upsilon(1S)$ and $\Upsilon(2S)$ in $p+p$ collisions exhibit a strong rise with the normalized multiplicity. No strong dependence is observed in $p + Pb$ collisions. Moreover, CMS has observed a production of $\Upsilon(1S)$ pairs in a single event [87]. This may also point to $\Upsilon(1S)$ production in MPI or a similar process to double D meson and $D + J/\psi$ production measured by LHCb [88, 89].

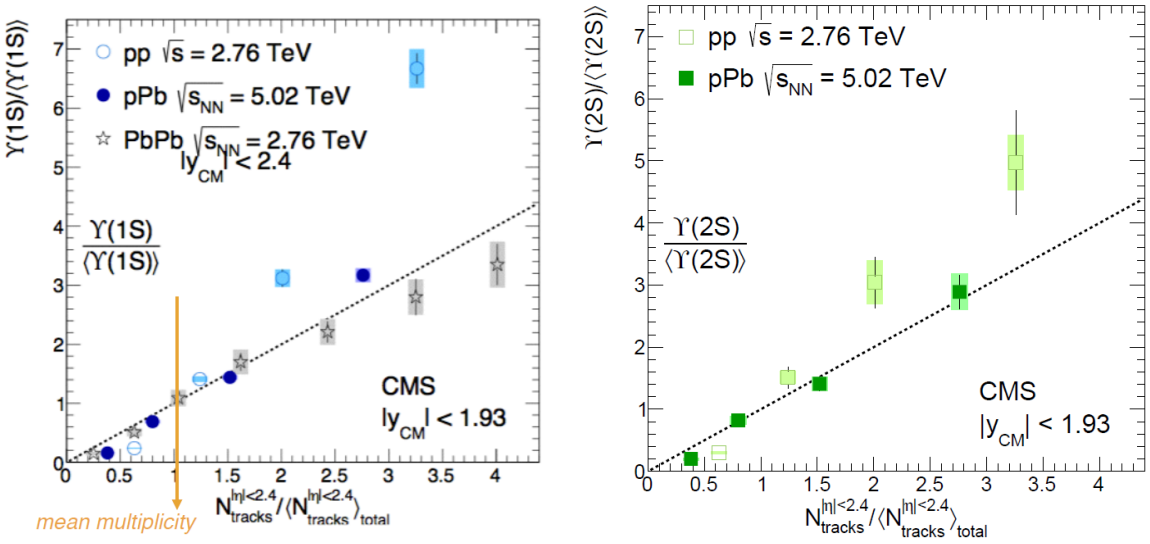

(a) **(b)**

Figure 2.7: Figure 2.7a: Normalized $\Upsilon(1S)$ yield vs. normalized multiplicity in $p + p$ (light blue open circles), $p + Pb$ (dark blue closed circles) and $Pb + Pb$ collisions (black open stars) [4]. Figure 2.7b: Normalized $\Upsilon(2S)$ yield vs. normalized multiplicity in $p+p$ (light green open squares) and $p+Pb$ (dark green closed squares) [4].

Chapter 3

Thesis goals

The aim of this thesis is to investigate Υ production vs. p_T and rapidity in $p+p$ collisions at $\sqrt{s} = 500$ GeV. Such data will provide constraints for the quarkonium production models and may provide reference for heavy-ion data after extrapolation to $\sqrt{s} = 200$ GeV. Since the Υ cross section is larger at $\sqrt{s} = 500$ GeV than at $\sqrt{s} = 200$ GeV, these data should provide a better statistical precision. Similar aim motivated the J/ψ studies at $\sqrt{s} = 200$ GeV.

In order to investigate the interplay between hard and soft QCD processes, a study of Υ normalized yield vs. charged particle multiplicity is needed. The CMS data at LHC [4] show a strong increase of the Υ yield with charged particle multiplicity. It is important to check if a similar behavior is found at RHIC. This will provide information about fundamental processes and critical checks for the event generators and particle production models. Also, a strong dependence of Υ production vs. multiplicity may be a sign of collective effects, as predicted by the String Percolation Model, which could be a signature of the QGP formation in high energy proton-proton collisions at RHIC. Such study is a part of this thesis.

Finally, a study of the dependence of the ratio of Υ states $\frac{\Upsilon(nS)}{\Upsilon(1S)}$ vs. charged particle multiplicity in $p+p$ collisions is also a goal of this thesis. Since the radii of excited $\Upsilon(nS)$ ($n = 2, 3$) states are larger than $\Upsilon(1S)$ and their binding energies smaller than $\Upsilon(1S)$, they should more easily break up by collisions with comoving hadrons. Experimental data at RHIC will provide an input for model calculations to constrain the cross section for quarkonium-hadron interactions and a breakup probability. Such information is necessary for the interpretation of the results of the quarkonium measurements in heavy-ion collisions and investigation of the properties of the QGP.

Chapter 4

Experiment

4.1 The STAR experiment

The Solenoidal Tracker At RHIC (STAR) [90] is a multipurpose, complex detector dedicated to heavy ion physics. It is located in the southern interaction region of the Relativistic Heavy Ion Collider (RHIC). RHIC, which became operational in 2000, is a versatile collider built in Brookhaven National Laboratory, Upton, NY, USA. RHIC is made of 2 independent storage rings, which are capable of accelerating and colliding beams of heavy ions ($A + A$): $Au + Au$, $U + U$, light ions $Cu + Cu$, $p + p$ and even $d + Au$. Other colliding systems are also possible. These beams can be accelerated to energies in a wide range, resulting in a collision energy per nucleon pair in the center of mass starting from $\sqrt{s_{NN}} = 7.7\,\mathrm{GeV}$ up to $\sqrt{s_{NN}} = 200\,\mathrm{GeV}$ for $Au+Au$. Because RHIC is focused on colliding heavy ions, it is the world's highest luminosity heavy ion collider with peak luminosity $\mathcal{L} = 1.55{\cdot}10^{28}\mathrm{cm}^{-2}\mathrm{s}^{-1}$ [91]. This allows studies of rare processes. The $p+p$ collisions are available at the energy up to $\sqrt{s} = 510\,\mathrm{GeV}$. The Figure 4.1 shows the schematic of the RHIC complex, along with a chain of smaller accelerators, which fill the RHIC with ion bunches. Heavy ions originate in the Electron Beam Ion Source [92] and are accelerated first by a linear accelerator, before being injected into the Booster synchrotron. Next, they are injected into the Alternating Gradient Synchrotron(AGS), which finally feeds them into RHIC. In fact, it takes many cycles of operation of the pre-accelerators to completely fill RHIC. In the case of protons, the procedure is similar, but the beam originates in the LINAC.

In addition to STAR, there are many scientific projects related to RHIC:

- PHENIX [93] - A rare physics experiment with tracking chambers [94], particle identification detectors [95], calorimeters [96], and muon arms [97]. Soon to be replaced with sPHENIX [98].

- pp2pp [99] - Experiment focused on studies of elastic $p + p$ collisions. At the moment,

part of STAR.

- Beam Energy Scan (BES) phase II [100] - Project to collect large amounts of data at low collision energy of $\sqrt{s_{NN}} = 7.7, 11.5, 14.6, 19.6\ \mathrm{GeV}$. Takes advantage of electron cooling to reduce beam spread, which reduces collision rate especially at low $\sqrt{s_{NN}}$. It is a continuation of the Beam Energy Scan. The main goals are the study of the onset of the QGP, search for the critical point in the QCD phase diagram and study a possible first-order phase transition.

- Fixed target mode [101]- Part of STAR. Records data from collisions between Au beam and a thin foil Au target. This program's aims are similar to the BES, but it will extend the energy range to even lower values of $\sqrt{s_{NN}} = 7.7 - 3.0\ \mathrm{GeV}$. It will allow collection of large amounts of data at these energies, when running concurrently with BES II.

- Electron-Ion Collider - In conceptual design phase [102]. It is an effort to build a collider and specialized detectors in order to study electron-ion collisions. Such collisions will provide information about the 3D structure and spin of a nucleon as well as allow the studies of QCD at extreme parton densities.

The main focus of the STAR experiment is to study the QGP and gluon contribution to the proton's spin. In order to achieve these goals, STAR measures particles produced in heavy ion ($A + A$) or $p + p$ collisions. The particles are measured by various detectors, shown in Figure 4.2, which are described in the next subsections. To allow the determination of particle's momenta, the detector is placed in an uniform, solenoidal magnetic field of $B = 0.5\ \mathrm{T}$ [103]. The magnetic field is generated by a large solenoid magnet surrounding the central barrel and 2 magnets located in the endcaps.

STAR was designed with a large acceptance in mind, thus the main detectors cover $|\eta| < 1$ and full azimtuhal angle $0 < \phi < 2\pi$. It is also well suited to recording almost all information about the event, as it is capable of detecting a large number (a few thousand) of ionization tracks left by charged particles. The detectors used in this analysis are described in the next subsections.

4.1.1 Time Projection Chamber

The main tracking detector of the STAR experiment is the Time Projection Chamber (TPC) [106] shown in Figure 4.3. It is designed to measure a large number of charged-particle tracks,

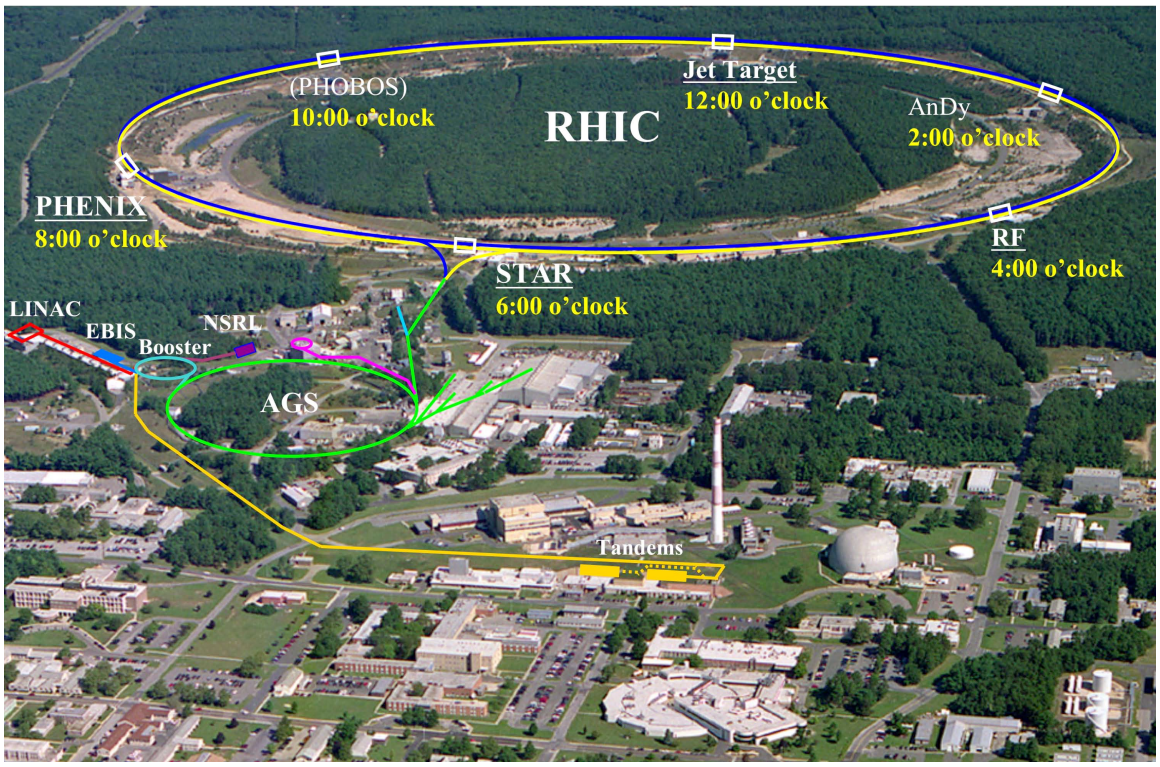

Figure 4.1: A picture of the main part of the Brookhaven National Laboratory [104]. It includes a schematic of the RHIC accelerator and pre-accelerator Complex as well as the experiments. The accelerated ions are produced in EBIS and are further accelerated by the Booster and AGS before being injected into RHIC. Protons, however, are first injected into Booster by the LINAC.

including their momenta and energy loss, in a high track-density environment.

The TPC can record thousands of particle tracks and measure their momenta from the curvature of a track. It has a large acceptance of $0 < \phi < 2\pi$ and $|\eta| < 1.8$ [106], but to achieve a high track reconstruction quality, efficiency and good particle identification, a pseudorapidity range of $|\eta| < 1$ is usually used in the analysis. It can measure momenta in the range $0.1 < p < 30$ GeV/c with good resolution. It can also identify particles in the momentum range $0.1 < p < 1$ GeV/c or more, depending on their type. The particles can be identified by measuring their energy loss $\frac{dE}{dx}$ from ionization of the gas, as they traverse the TPC.

The TPC consists of a large, cylindrical chamber filled with P10 gas (a mixture of 10% of methane and 90% argon) [107] and 24 Multi-Wire Proportional Chambers (MWPC) at the cylinder's endcaps. The outer radius of this cylinder is $R = 2$ m and the inner radius is $r = 0.5$ m, while the length along the beam axis is $L = 4.2$ m [106]. Lightweight and resistant materials like aluminium, Kapton and NOMEX arranged in a honeycomb pattern were used for

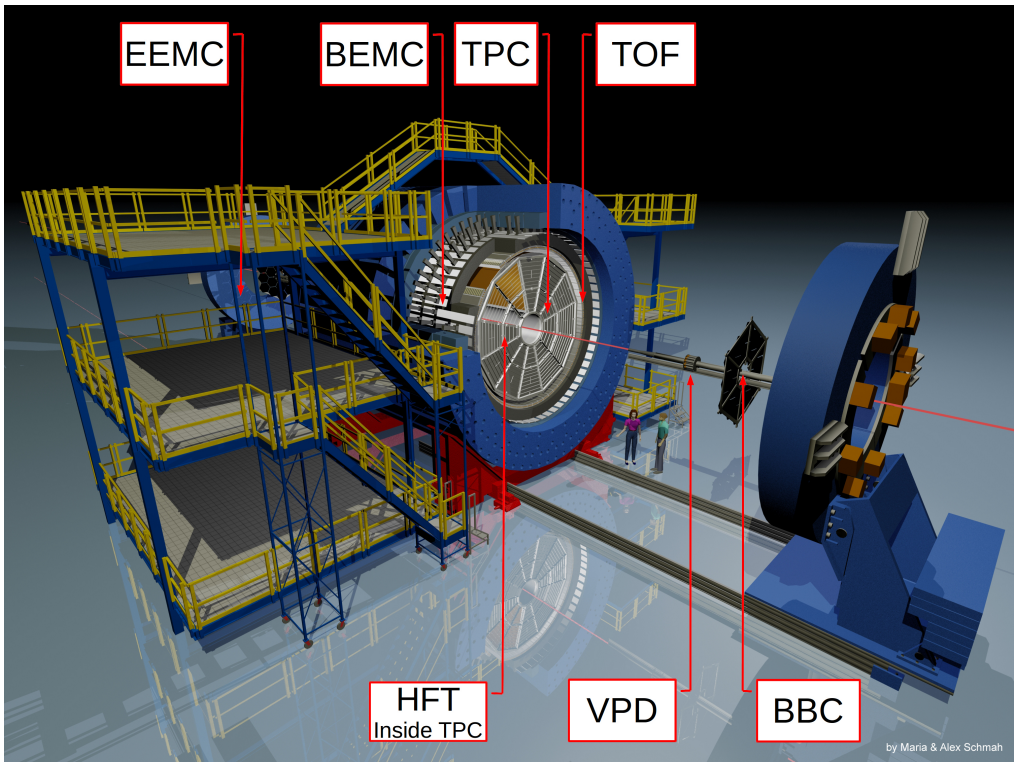

Figure 4.2: A 3D rendering of the STAR experiment with a cut out view of the TPC [105].

the construction. This also keeps the radiation length low, which reduces secondary scatterings and knockout particles from the detector material. A thin central membrane is used to establish a high voltage of $28\ \mathrm{kV}$ between it and the endcaps. This causes the electrons, produced from ionizations of the gas by the measured particles, to drift to the MWPCs in the endcaps. The drift velocity is around $u = 5.45\ \mathrm{cm}/\mu\mathrm{s}$. It depends on the running conditions (gas pressure, charge accumulation, etc.), so it has to be monitored during the run using ultraviolet lasers for calibration [108]. Ionization electrons are detected in the MWPCs, which determine the position of the original track in the x, y plane. The z coordinate is determined from the drift time t by a simple relation $z = ut$. Signal in the MWPCs is recorded in one of a maximum of 512 timebins, which allows the determination of the drift time t.

Figure 4.4 shows a schematic of the MWPCs of the inner and outer parts of the TPC sectors. Each MWPC is made of 3 planes of wires and a pad plane for readout shown in Figure 4.5. In order to control the flow of electrons into the MWPCs, the gating grid is used. It is the outermost plane of wires. Next there is a shield grid, which provides ground to the final plane of anode wires. These wires produce a local electric field ($1170\ \mathrm{V}$ for inner and $1390\ \mathrm{V}$ [106] for outer sectors), which causes the ionization electrons to produce an avalanche. This amplifies the

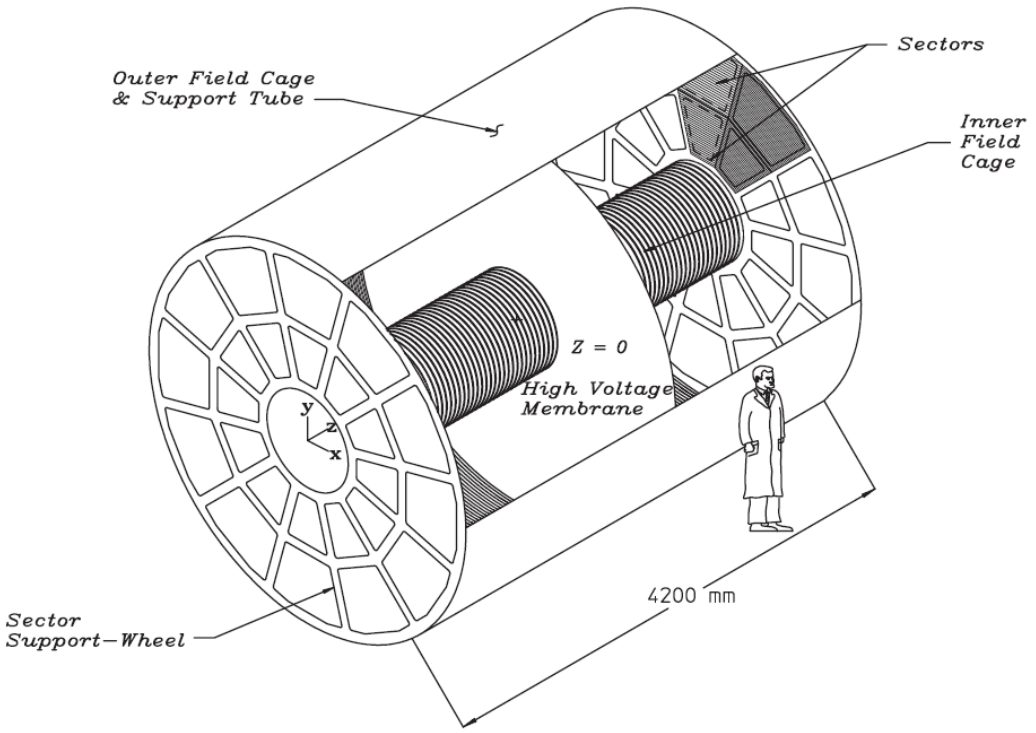

Figure 4.3: Schematic of the STAR TPC design. It is a barrel-shaped chamber filled with P10 gas suspended in the magnetic field of $B = 0.5$ T. In addition to the magnetic field, there is an electric field of $V = 28$ kV produced between the central membrane and the endcaps. Both the E and B field are parallel to the beam axis, which causes the ionization electrons to drift to the endcaps in straight lines. The MWPCs in the endcaps are used to measure the (x, y) coordinates of an ionization track. In order to determine the z coordinate, the drift time of ionization electrons is measured [106].

signal by a factor of $1000 - 3000$. The avalanche, in turn, induces a charge on a few pads on the pad plane, producing an electric signal. Next, the signal is processed by the readout electronics and digitized. During event reconstruction, the signal from the nearby pads can be combined into clusters, which form TPC hits. This allows more precise hit position determination than when using a single pad. In addition, the magnitude of collected charge can be used for $\frac{dE}{dx}$ calculation.

As described above, the TPC can measure ionization tracks of charged particles and their energy loss. In total, it has $136,608$ pads, which combined with 512 time bins creates 70 M [110] voxels for a 3D picture of the recorded event. The transverse momentum resolution determined from Monte Carlo (MC) simulations is $\frac{\sigma_{p_T}}{p_T} = 0.02$ for pions at $p_T = 0.5$ GeV/c [106], which is the average momentum for produced particles at $\sqrt{s_{NN}} = 200$ GeV [110].

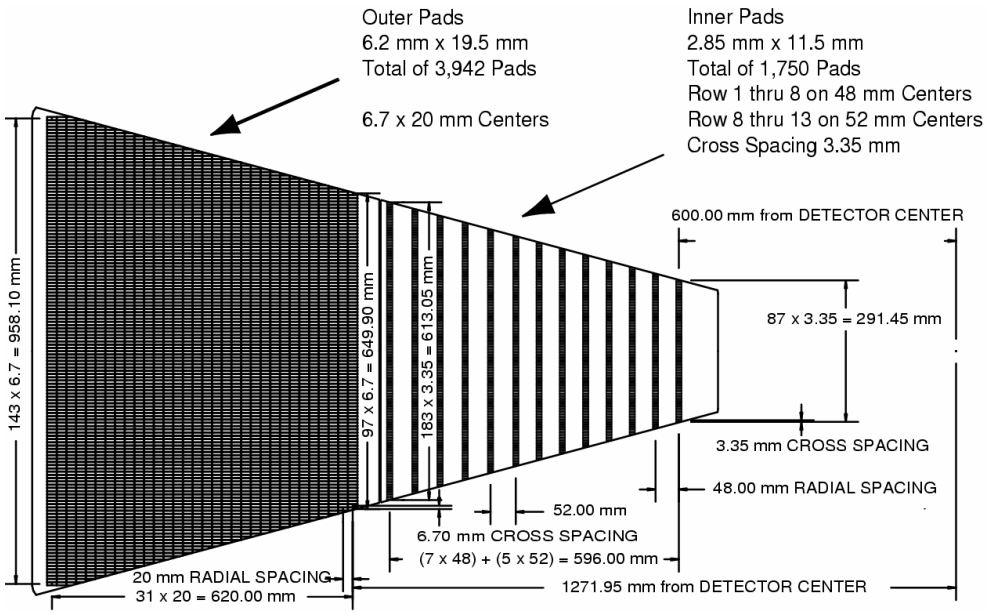

Figure 4.4: Schematic of the TPC sector showing pad arrangement in the inner and outer parts of the sector as well as the sector construction [106].

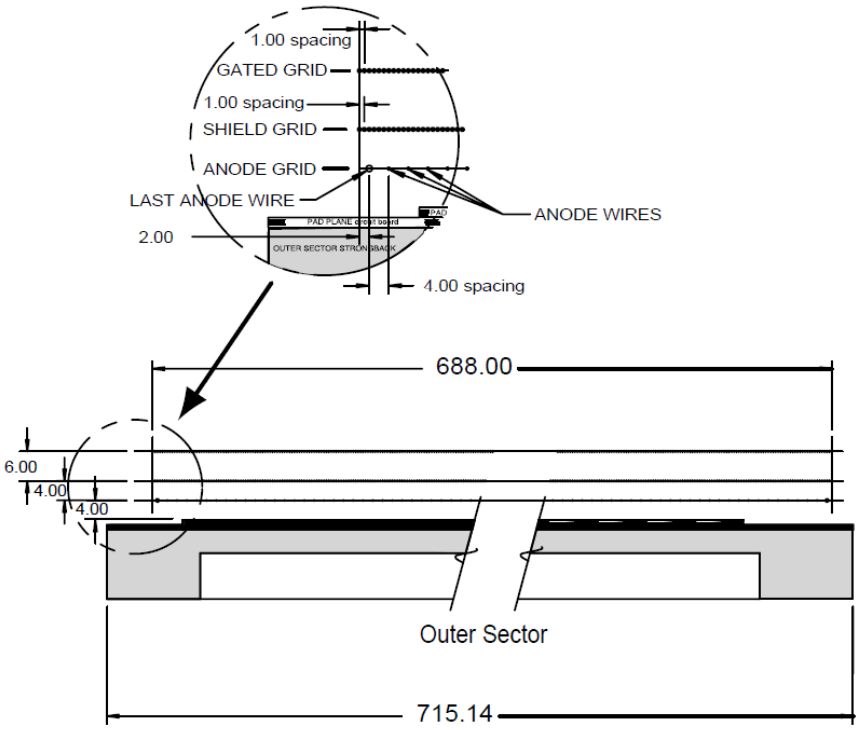

Figure 4.5: Schematic of the wire arrangement in the Multi-Wire Proportional Chambers of inner and outer sectors of the STAR TPC [109].

4.1.2 Heavy Flavor Tracker

The Heavy Flavor Tracker (HFT) [111] was developed to allow direct reconstruction of secondary vertices of heavy flavor decays [112] by providing precision tracking. It is a state of the art vertex detector with 4 layers of silicon detectors. Figure 4.6 shows the structure of the HFT with it's 3 subsystems: Pixel (PXL), Intermediate Silicon Tracker (IST) and Silicon Strip Detector (SSD), listed starting from the center. The HFT was designed with a low material budget in mind to reduce scatterings and knockout particles as well. Thus, the sensors are mounted on very thin carbon fiber ladders. The total thickness of the HFT in terms of radiation length is $3.5\%X_0$ [113], including the SSD.

All the subsystems of the HFT are silicon based detectors. A silicon detector uses the effect of formation of a p-n junction on a boundary between a p-doped and n-doped silicon crystals. Such a p-n junction is subjected to a voltage, which causes a reverse bias. An incident charged particle creates free electrons and holes through ionization. These drift to the corresponding electrodes and produce a signal.

The acceptance of the HFT covers full azimuthal angle and $|\eta| < 1$. The most important parameter of the HFT is the resolution of the distance of closest approach (DCA) of a track to the primary collision vertex. This is important for distinguishing secondary vertices of heavy flavor decays from the primary vertex. For reconstructed TPC tracks with hits in both layers of the PXL and IST, the DCA resolution is better than the design goal. The design DCA resolution was $60\,\mu\mathrm{m}$ [114] for kaons with $p_T = 0.75\,GeV/c$, while a value of $46\,\mu\mathrm{m}$ was achieved [115]. This underlines the very successful construction of the HFT.

4.1.2.1 Silicon Pixel Detector

The Silicon Pixel Detector (PXL) or Pixel consists of 2 layers of very thin silicon pixel sensors. Figure 4.7 shows a schematic of the Pixel detector. The Pixel is divided into 10 trapezoid-shaped sectors with each sector containing one ladder of the inner layer and 3 ladders of the outer layer. The layers are located at a radius $2.8\ \mathrm{cm}$ and $8\ \mathrm{cm}$ [114] from the center of the beampipe. A ladder contains 10 silicon sensors arranged in a row with a readout chip located at the end. A zero suppression algorithm is implemented in the readout chip, which significantly reduces the data output.

The sensors are made using Monolithic Active Pixel Sensor (MAPS) [116] technology, which is applied here for the first time in a collider experiment. Each sensor covers an area of

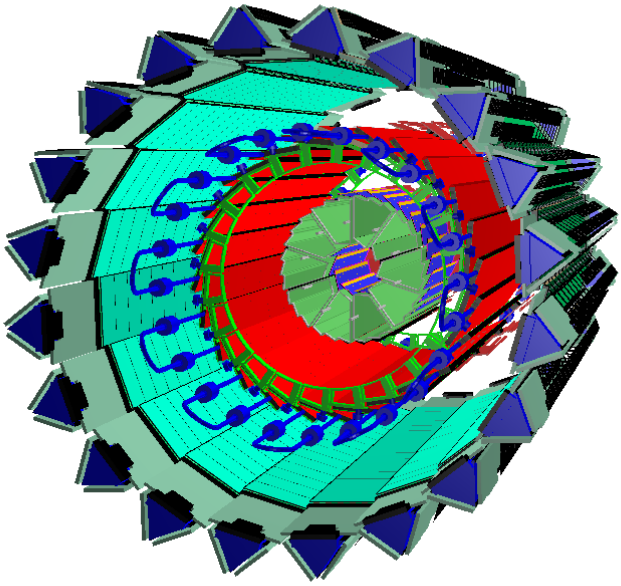

Figure 4.6: A 3D rendering of the Heavy Flavor Tracker geometry model. This model is the exact version used in STAR simulation package. Beginning from the center, it shows PXL, IST and SSD.

$20.22\,mm$ by $22.71\,mm$ and is $50\,\mu$m thick. This yields a very low radiation length of $0.5\%X_0$. A sensor contains 928 rows and 960 columns of square-shaped silicon pixels of $20.7\,\mu$m [116] size.

Charged particles crossing the sensor volume produce a charge, which diffuses to the nearby pixels. This allows a more precise determination of a hit position, giving a better resolution of $18\,\mu$m [114] compared to the pixel size.

In total, the Pixel contains $356\,M$ pixels in 400 sensors. The integrated radiation length is around $1\%X_0$. An important feature of the Pixel support structure is that the detector can be quickly removed and replaced with a spare one. The whole operation takes only a few hours and does not introduce any significant shift in the positioning of the Pixel with respect to the rest of the STAR experiment.

4.1.2.2 Intermediate Silicon Tracker

The Intermediate Silicon Tracker (IST) [113] is a single-sided silicon pad detector located at a radius of 14cm from the center of the beampipe. It is made of 144 sensors mounted in 24 ladders

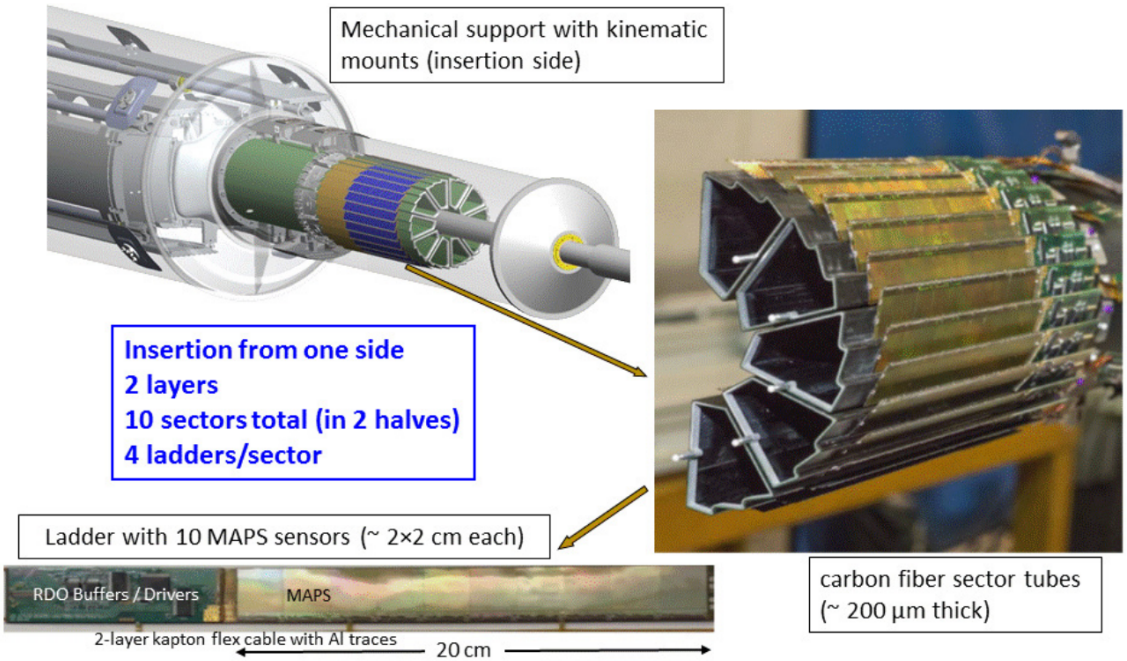

Figure 4.7: Left: A schematic of the Pixel detector showing the detector and it's support structure. Right: A picture of a single Pixel module composed of 5 trapezoidal sectors. Bottom: A picture of a Pixel ladder, containing 10 MAPS sensors. [114].

of 6 sensors each. The ladders are arranged in such a way that 2 IST ladders overlap with one of the 12 TPC sectors. This is important, as the IST serves as an intermediate tracker, providing a bridge between high precision PXL and the TPC. In addition, there is a small overlap between sensor active areas of neighbouring ladders. An IST ladder is shown in Figure 4.8. It contains 6 silicon sensors and 36 readout chips. A sensor covers an area of $7.7\,cm \times 4\,\mathrm{cm}$ and is $300\,\mu\mathrm{m}$ thick. It is divided into 12 columns and 64 rows of pads. Each pad is $600\,\mu m \times 6000\,\mu\mathrm{m}$.

In summary, the IST has 110592 readout channels corresponding to pads and the integrated radiation length is $1.5\%X_0$. The hit position resolution is on the order of the pad size, as the effect of charge sharing between neighboring pads is small.

4.1.2.3 Silicon Strip Detector

The Silicon Strip Detector (SSD) [118] is located at a radius $22\,\mathrm{cm}$ from the beampipe. It is a double-sided silicon strip detector with strips on the N and P sides of a silicon wafer. These strips are separated with $95\,\mu\mathrm{m}$ pitch and are oriented at $35\,mrad$ angle between them. Such a design reduces ambiguity of double hit resolution in 2D. The dimensions of the wafer are

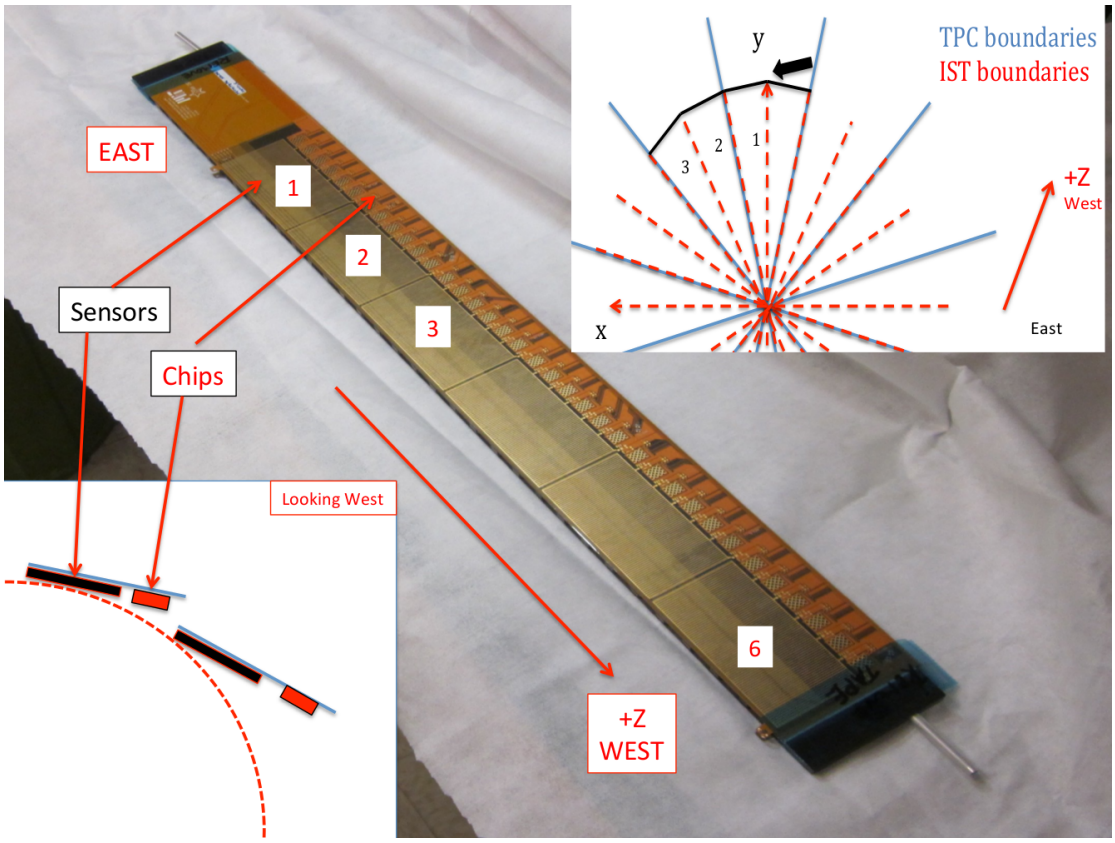

Figure 4.8: A picture of IST ladder including 6 silicon pad sensors and 36 readout chips. Left inset: A schematic of the ladder positioning in the IST. In fact, the sensor active areas overlap at the edges, which is not shown here. Right inset: A schematic of IST ladder positioning with respect to TPC sector boundaries [117].

$75\ mm \times 42\ mm$ with $300\ \mu$m thickness. A wafer contains 768 on each side and 12 readout modules.

The wafers are installed on a carbon fiber ladders with each ladder supporting 16 modules as shown in Figure 4.9. There are 20 ladders in the entire detector.

The total number of channels is 491520 and the number of wafers is 320. After including SSD in tracking with the TPC, the position resolution is $300\ \mu$m [119].

The SSD received a readout electronics upgrade as part of the HFT project [113] in order to meet the requirement for readout frequency of at least 1 kHz.

4.1.3 Barrel Electromagnetic Calorimeter

The STAR Barrel Electromagnetic Calorimeter (BEMC) [120] is designed to study rare processes (jets, electrons from heavy quark decays, direct γ, π^0, etc.). It is designed to measure

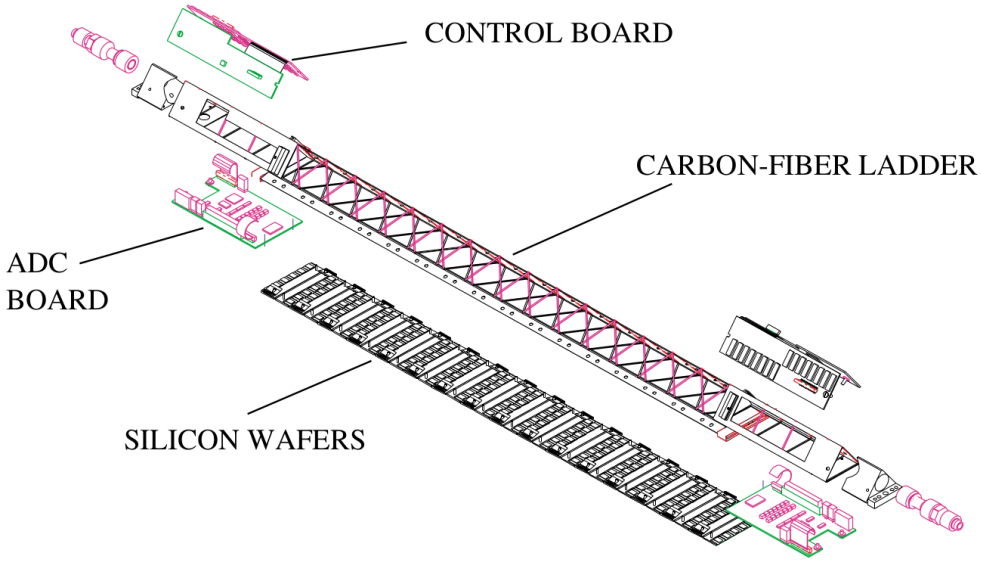

Figure 4.9: A schematic of the Silicon Strip Detector ladder. The ladder mounts 16 modules. [118].

the energy deposited by electrons or photons as they produce an electromagnetic shower while traversing the BEMC active volume. It is a Shashlik type sampling calorimeter, which is built of alternating layers of lead and plastic scintillator. In STAR, the BEMC also serves as a trigger for rare processes. A good example of such trigger is a High Tower trigger, which records the event if a shower with sufficient energy, as defined by an energy threshold, is deposited in one of the BEMC cells called towers. The data used for Υ analysis were collected with High Tower trigger.

The BEMC, shown in Figure 4.10, covers an acceptance of $0 < \phi < 2\pi$ and $|\eta| < 1$ and is made of 4800 towers divided into 120 modules of dimensions $\Delta\phi \times \Delta\eta = 0.1 \times 1$ each containing 40 towers [120]. The modules are installed between the TPC and the magnet at a radius of $R \approx 2.2$ m. A module is shown in Figure 4.11. In order to provide a uniform acceptance of $\Delta\phi \times \Delta\eta = 0.05 \times 0.05$ for each tower, their size increases with $|\eta|$, with the towers at $\eta = 0$ measuring $10 \times 10\ \mathrm{cm}^2$. Furthermore, the towers are aligned in such a way that they point to the center of the detector. An individual tower is shown in Figure 4.12. A tower is made of alternating layers of lead and plastic scintillator tiles. There are 20 lead tiles and 21 plastic scintillator tiles in a tower. Lead is a high Z-number element, which increases the interaction cross section for electromagnetic interaction and reduces the radiation length $X_0 \propto Z^{-2}$ of the material. In total, a tower has a thickness of $20X_0$ at $\eta = 0$. A Shower Maximum Detector (SMD) is placed at $\approx 5.6X_0$ at $\eta = 0$, which is used for a fine spatial

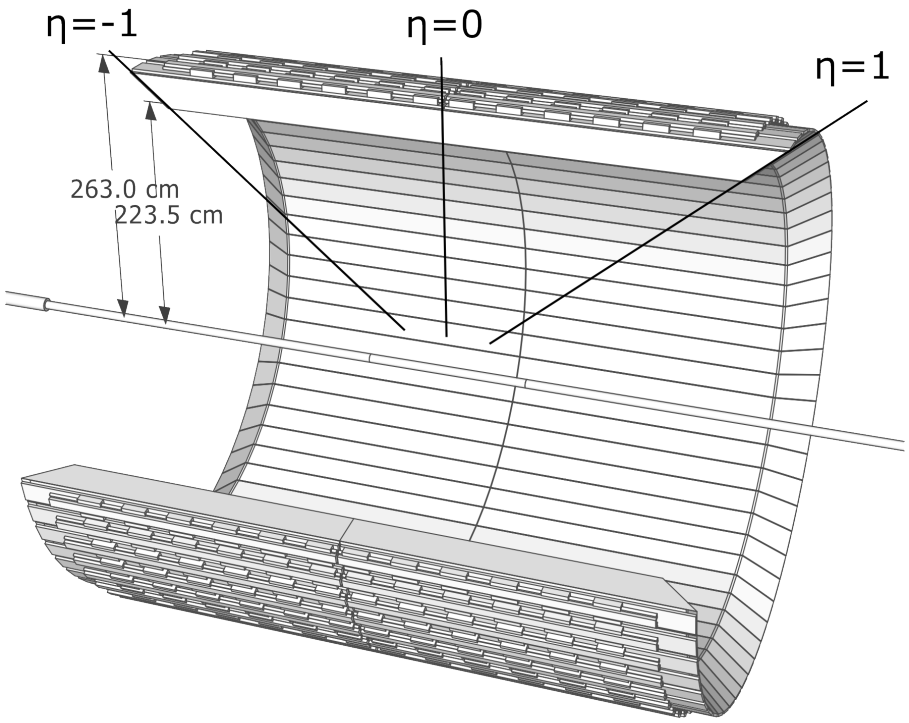

Figure 4.10: Schematic of the BEMC module arrangement [121].

position determination of a shower. The SMD is a proportional gas chamber with anode wires and two layers of perpendicular cathode strips in η and ϕ directions respectively.

A plastic scintillator is used to sample the energy of the produced shower and convert it to the light pulses. The light is then shifted in wavelength with wavelength shifting (WLS) grooves attached to the scintillator tile. Next, the light pulses are sent via optical fibers to the photomultiplier tubes (PMT) located outside the STAR magnet. This simplifies the design of PMTs, as they don't have to be shielded from high magnetic field. The readout electronics are also located outside the magnet.

The energy E resolution σ_E of BEMC is estimated to be $\left(\frac{\sigma_E}{E}\right)^2 = \frac{0.14^2\,\mathrm{GeV}}{E} + 0.015^2$ [120]. However, this does not include possible variation in the light yield from different towers (coming from tower non-uniformities and cross talk, for example), which was measured to be 8.1%.

Electrons are expected to deposit most of their energy in a single tower, with some leakage to the neighboring towers due to electromagnetic shower transverse radius. The radius is characteristic for a material of the calorimeter and is called the Molière radius. Furthermore, electrons are expected to deposit almost all of their energy in the BEMC.

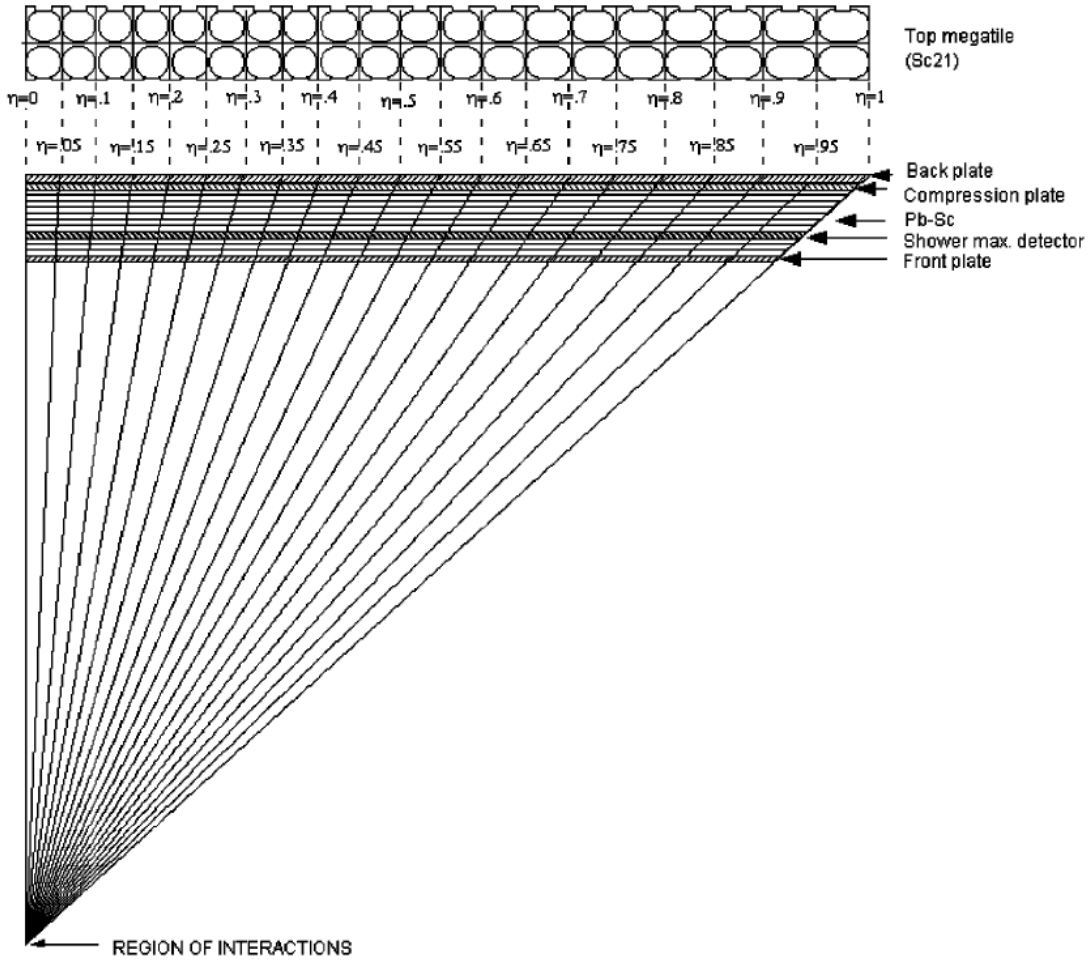

Figure 4.11: Schematic of the tower arrangement in the BEMC module. Each module contains 2 rows of towers in ϕ direction and 20 towers in each row in η direction. The towers dimensions vary, so that each one covers $\delta\eta = 0.05$ and $\delta\phi = 0.05$, with the size increasing for $|\eta|$ increases. In addition the towers point to the center of the detector [120].

4.1.4 Endcap Electromagnetic Calorimeter

Similar to the BEMC is the Endcap Electromagnetic Calorimeter, which extends STAR's calorimetry to include $1 < |\eta| < 2$ and $0 < \phi < 2\pi$. It is also used to measure energy of photons, electrons and positrons in the energy range $0.2 < E < 150\ \mathrm{GeV}$. Like the BEMC, with which it shares many design features, the EEMC is a Shashlik type sampling calorimeter made of Pb and plastic scintillator.

The EEMC consists of 720 towers of size $\Delta\phi = 0.1$ and ranging in $0.057 < \Delta\eta < 0.099$, with $\Delta\eta$ decreasing as η increases. These towers are arranged in rings of constant η as shown in Figure 4.13. In addition to towers, the EEMC features a Shower Maximum Detector as well

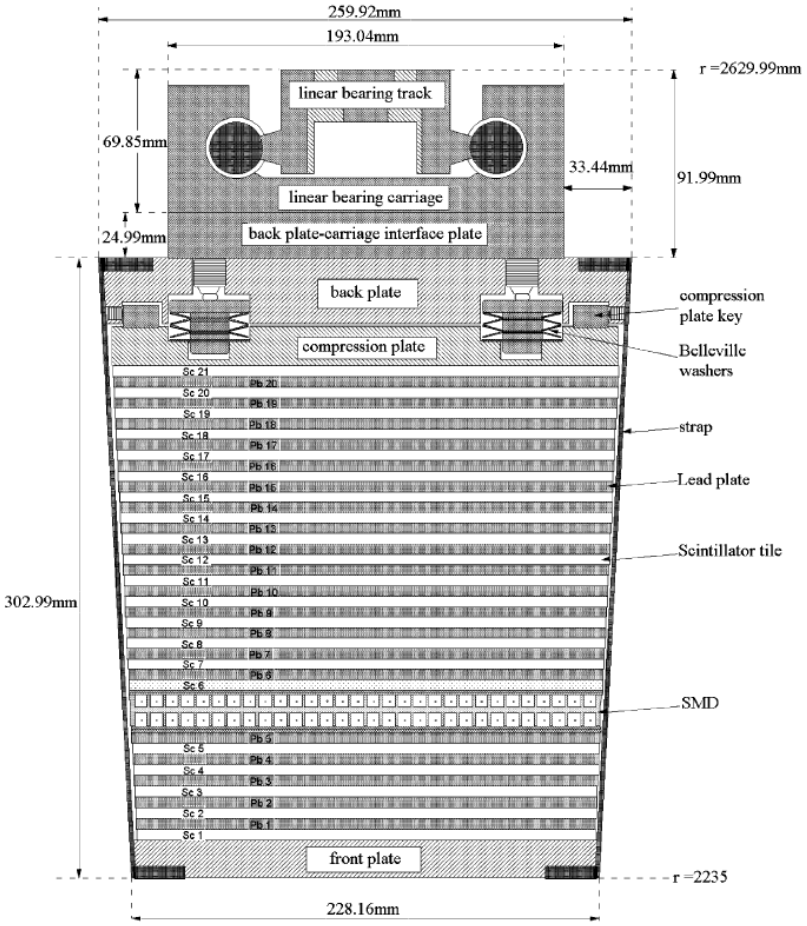

Figure 4.12: Schematic of the BEMC tower construction. A tower is made of 20 lead tiles and 21 plastic scintillator tiles. Such a design of sampling calorimeter, with alternating layers is called Shashlik type [120].

as a pre-shower and post-shower detectors.

The energy resolution of the EEMC is $\left(\frac{\sigma_E}{E}\right) \leq \frac{0.16\,\mathrm{GeV}}{\sqrt{E}} + 0.02$ [122].

4.1.5 Time of Flight detector

The Time of Flight (TOF) detector [123] improves the particle identification capabilities of STAR. It measures the time of flight of particles using modules of Multi-gap Resistive Plate Chambers (MRPC) [124, 125]. These modules register the time when particles pass through the detector, while the Vertex Position Detector provides the start time.

A TOF module schematic is presented in Figure 4.14. It is made of alternating high resistivity ($5 \cdot 10^{12}$) glass plates and 220 μm gas-filled gaps. A high voltage is applied, so that a

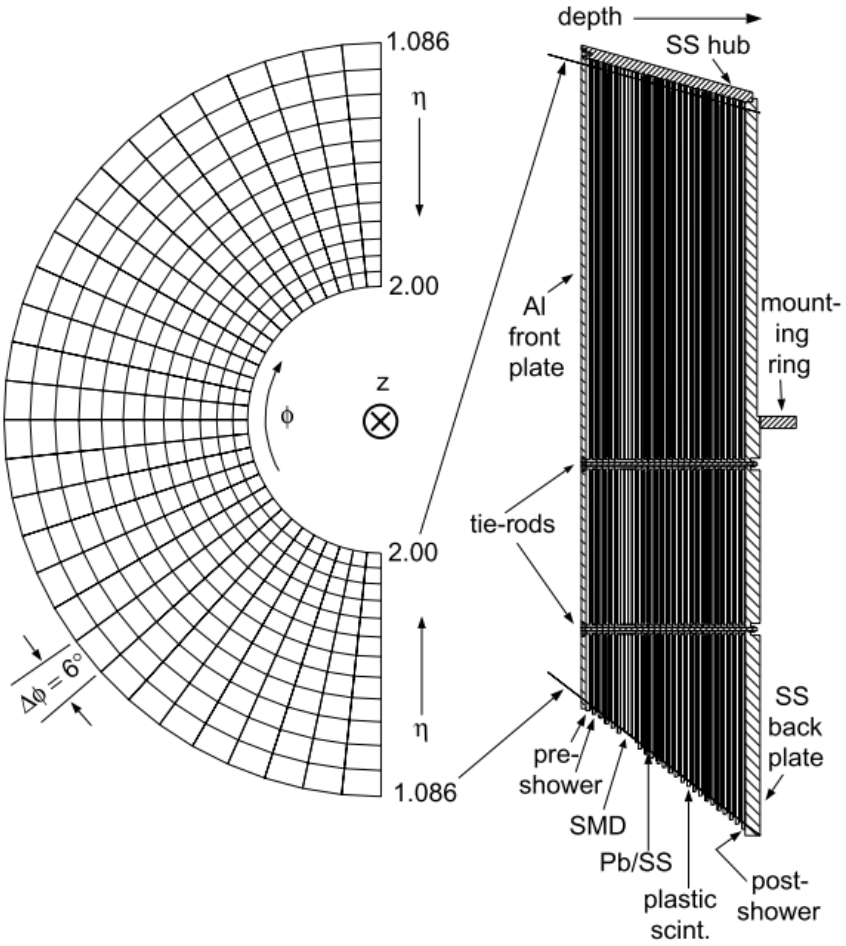

Figure 4.13: Layout of EEMC towers and a cross-section of the calorimeter along phi and z directions [122].

passing charged particle produces an avalanche in the gas. The plates are designed to quench an avalanche, while letting the produced charge through to the readout pads. A mixture of 90% tetrafluoroethane ($C_2H_2F_4$), 5% of isobutane and 5% of sulfur hexafluoride SF_6 is used to fill the gaps.

The TOF is made of 120 trays, which cover an acceptance of $0 < \phi < 2\pi$ and $|\eta| < 1$ [123]. A TOF tray is shown in Figure 4.15. It is designed in such a way that the detector modules in a tray point to the center of the STAR experiment. The detector timing resolution is around $120\ ps$ in $p + p$ collisions.

$$\beta = \frac{l}{ct} \tag{4.1}$$

A particle's velocity β can be determined using Eq. 4.1 by taking a path length l of a recon-

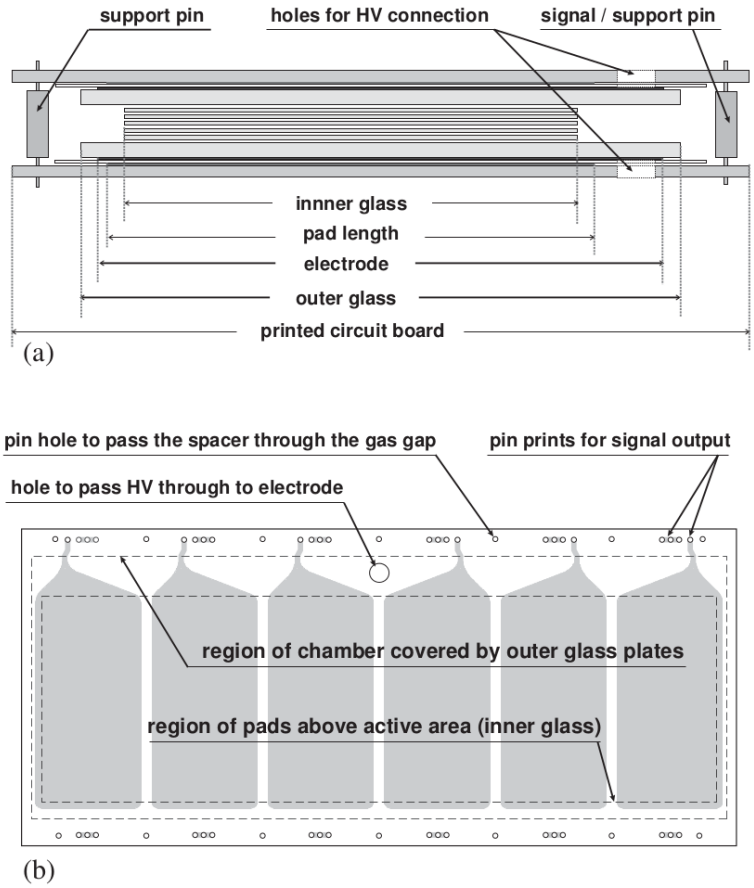

Figure 4.14: (a) A side cross section of the MRPC TOF module. (b) A top view of the module. The readout pads are shown in gray [124].

structed track and time of flight t, and speed of light c.

During the 2009 run, 72% of TOF trays were installed, while during the 2011 run it was already fully installed.

4.1.6 Vertex Position Detector

Vertex Position Detector (VPD) [126] is made of 2 sets of 19 scintillators with Pb and photo-multiplier tubes, which are shown in Figure 4.16. Each set is located around a beampipe on either east or west side of the interaction region at a distance $z = \pm 540$ cm [127]. VPD's are used to detect forward-going photons produced by a collision. The detector serves as a minimum-bias trigger and provides a start time for the TOF. It is also used for primary vertex z position determination calculated from a time difference between hits in the east and west modules.

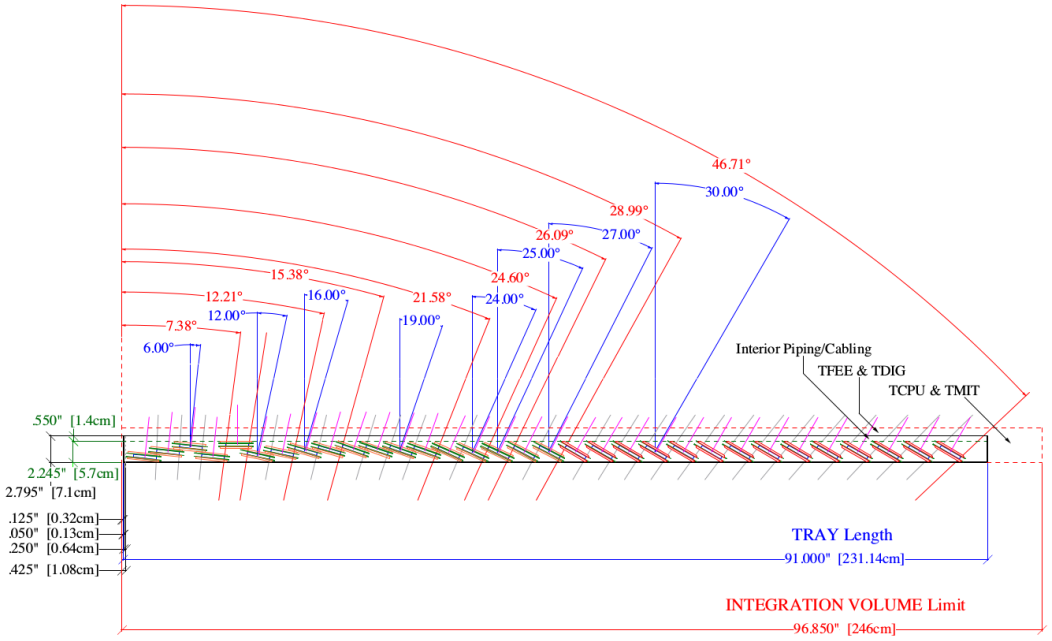

Figure 4.15: Schematic of TOF modules arrangement in a tray. The trays are tilted, so that they point to the center of the detector [123].

The start time resolution is 54 ps [126], while the position resolution is 3 cm.

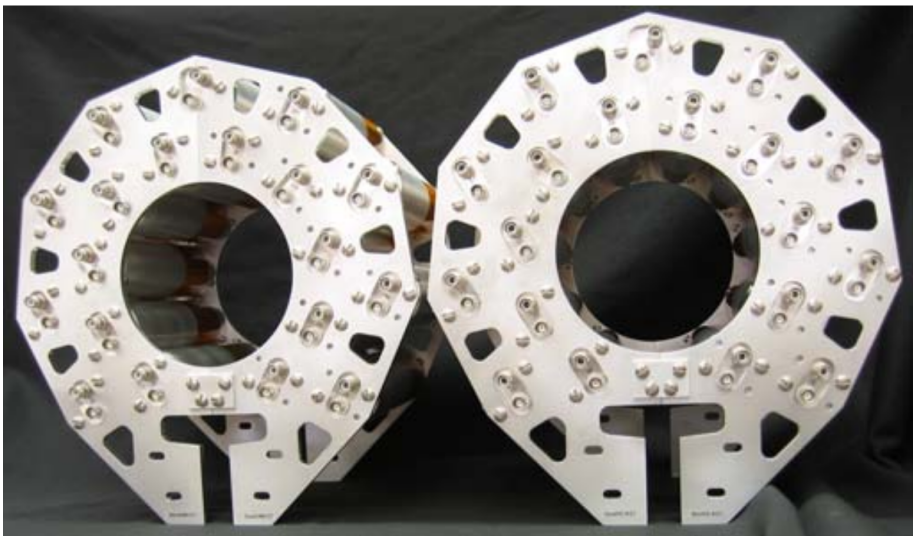

Figure 4.16: Picture of disassembled VPD modules [126].

4.1.7 Beam-Beam Counter

The Beam-Beam Counter (BBC) is a set of 2 identical detectors, each made of 36 scintillating tiles. The BBC is located along the beampipe, with both tile planes placed at ± 374 cm [128] from the interaction region as shown in Figure 4.17. Each plane is either called BBC east or BBC west, based on its location. The tiles that comprise the detector are arranged in 4 rings around the beampipe. The 2 inner rings are made of smaller tiles. A tile is hexagonally shaped and is 1 cm thick [129]. In total, the acceptance of the BBC is $2.1 < |\eta| < 3.6$ for rings containing large tiles and $3.3 < |\eta| < 5.0$ for rings with small tiles [130].

The BBC is used for luminosity monitoring and triggering. The coincidence of hits in both east and west BBC planes indicates a collision event, which is easily distinguishable from background. Beam-gas and beam halo collisions constitute background and produce hits in only one of the BBC's.

In the Υ studies, the BBC is used along with BEMC to form a High Tower trigger, which is described in Section 5.2.

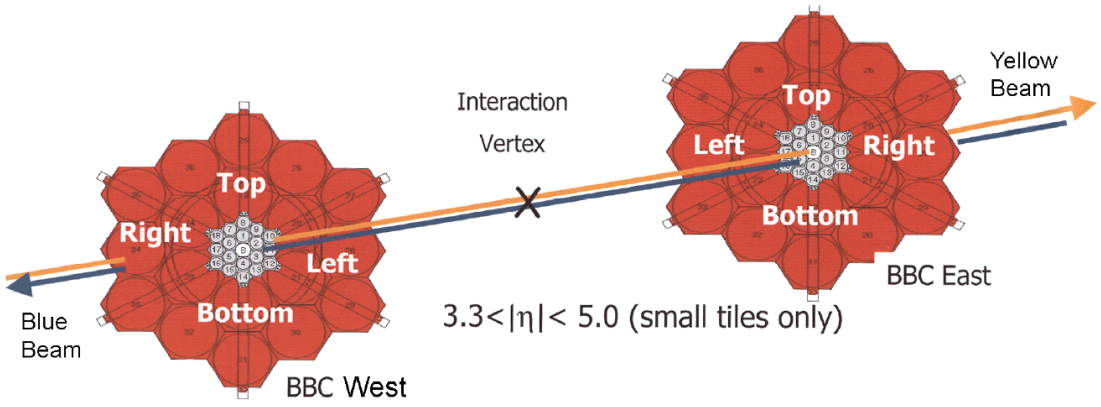

Figure 4.17: BBC setup along the beam axis. [128]

4.2 Event reconstruction in STAR

The purpose of event reconstruction is to transform raw data into physics analysis-ready format. It produces tracks using a helix model for the particles trajectories inside STAR's magnetic field. Each track is characterized by $\vec{p}$, distance of closest approach to the primary vertex (DCA), number of points used in the helix fitting (nFitPts) etc.

STAR uses a Big Full Chain [131, 132] (BFC) software for a full reconstruction using multiple (≈ 100) components called makers, corresponding to various steps of reconstruction for each individual detector. The STAR reconstruction procedure is illustrated in Figure 4.18 with the example of IST. The first step consists of applying calibrations to raw data, which had been collected either in normal or zero-suppression mode. This produces ADC from rawADC for each hit in a particular detector. Next, the clustering algorithms combine the adjacent hits into clusters, from which the final hits used for reconstruction are produced. The Kalman filter-based [133] tracking algorithms then look for tracks among the final hits. First, the track seeds are found in the outer parts of the detector and extended to inner parts by including more points step-by-step. This yields a collection of the so-called global tracks.

Finally a vertex finding algorithm is run in order to find primary collision vertices. Since the TPC readout time is $\approx 40\ \mu\mathrm{s}$ compared to $107\ \mathrm{ns}$ [134], there may be multiple vertices in a single event. Once vertices are found, a secondary refit is done for the tracks assigned to a primary vertex with it as a constraint. This yields a collection of the so-called primary tracks, separate for each vertex, with an improved momentum resolution.

Such reconstructed data are stored in MuDst format ROOT [135] files and are ready for physics analysis.

4.3 Detector simulation

Simulation-based detector efficiency studies are an important part of almost every analysis. These simulations use Monte Carlo (MC) methods to simulate particle transport through the material of various detectors. For this purpose, STAR uses GEANT3 [137]. The detector description is stored in AgML [138–140] format, which has an XML-like structure. The AgML geometry is converted to GEANT3 format for simulations and to Sti [141] tracking algorithm for reconstruction. Such a solution provides a unified geometry description. In order to produce a realistic detector response, the output of GEANT3 simulations is supplied to the detector response simulators for each subsystem. However, to make a full study of efficiencies, detector and reconstruction effects, simulations embedded into real data are needed.

Such a a procedure is called embedding, and consists of combining real data in a raw format with simulation and performing reconstruction on such a combined data set. Simulation is done using particles of interest for a particular analysis. In this way, the simulated data are embedded

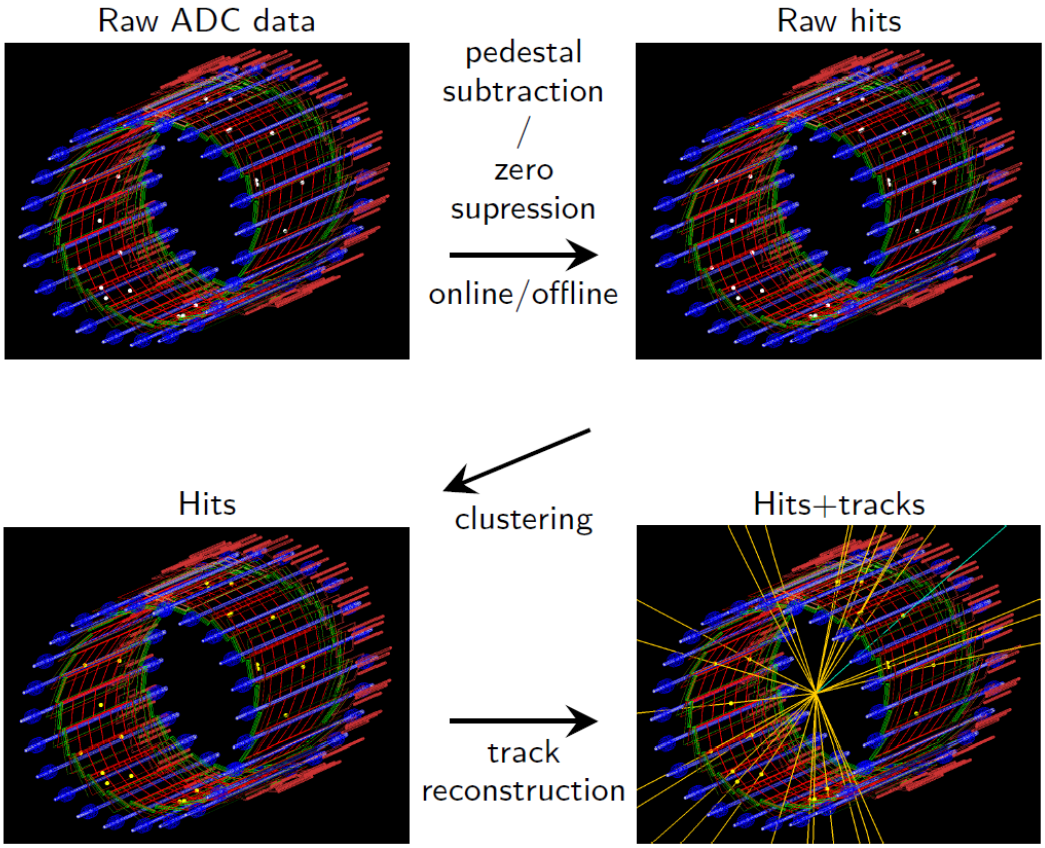

Figure 4.18: Example of reconstruction steps with the IST [136]. The wireframe model corresponds to the IST geometry. Raw hits are shown as white dots, while reconstructed hits are shown as yellow dots. The reconstructed tracks are drawn as lines.

into the real data. This takes into account the running conditions of the detector during the data recording in order to produce as much realistic response as possible.

4.4 Author's contribution to STAR

The STAR experiment is a complex apparatus, made of many different subsystems. These require maintenance, supervision and in some cases even upgrades. As a member of the international STAR Collaboration, the author participated in various service work tasks for the experiment. Such a technical contribution of a graduate student is required by the STAR collaboration and is a good technical experience. More importantly, this work is a crucial part of experiment preparation and operation. It consists of:

- Data taking shifts

- Experiment calibration
- Software development
- Detector development

4.4.1 Data-taking shifts

During author's work in the STAR Collaboration, he participated in data-taking shifts. The purpose of this work is to take data during the running of the RHIC collider, when collisions take place inside the STAR experiment. A crew of a few collaboration members (typically 4 or 5) supervises and operates the detectors from the STAR Control Room. They also ensure that the detector operates properly and that necessary calibration data are recorded. It is a huge responsibility. They take shifts (day, evening and night) to man the detector 24h a day. The crew is also supported by on-call detector experts.

The author participated in data taking shifts as:

- 2010 - Shift crew, 2 weeks. I was responsible for recording of data and subsystem monitoring.
- 2014 - Shift crew, 1 week.
- 2014 - Detector operator trainee, 1 week. I took training for the detector operator post. It is required as a detector operator needs to understand the details of control interfaces and operation of each detector.
- 2015 - Detector operator, 1 week. As a detector operator I was responsible for bringing the detectors online, offline and responding to detector-related issues.
- 2015 - Shift leader trainee, 1 week. As a shift leader trainee, I was training to become a shift leader, who commands the entire crew. It is the task with highest level of responsibility for the shift crew and requires deep knowledge of the detector and accelerator operation. The shift leader takes all the decisions and instructs the crew to ready the detector for data recording or to keep it on standby. He is also responsible for communication with the RHIC Main Control Room.

This was a good chance to familiarize with operation of the entire STAR detector and its subsystems. Thus, the author is experienced with the technical aspects of the detector operation

as well as leadership of an international team. Author's contribution to STAR also included supervising students.

4.4.2 Development of a detector response simulator for the Intermediate Silicon Tracker

Another part of involvement in the service work for STAR was the development of the response simulator for the Intermediate Silicon Tracker (IST), a so called IST Slow Simulator (StIstSlowSimMaker) [142]. This is part of the HFT project, which is an important upgrade of the STAR tracking capabilities. The requirements for the IST Slow Simulator were as follows. First it had to be integrated with the IST offline reconstruction chain software. Second, it had to be integrated into STAR simulation package Starsim (an interface to GEANT3). Figure 4.19 shows the structure of the IST offline reconstruction chain, including the IST Slow Simulator.

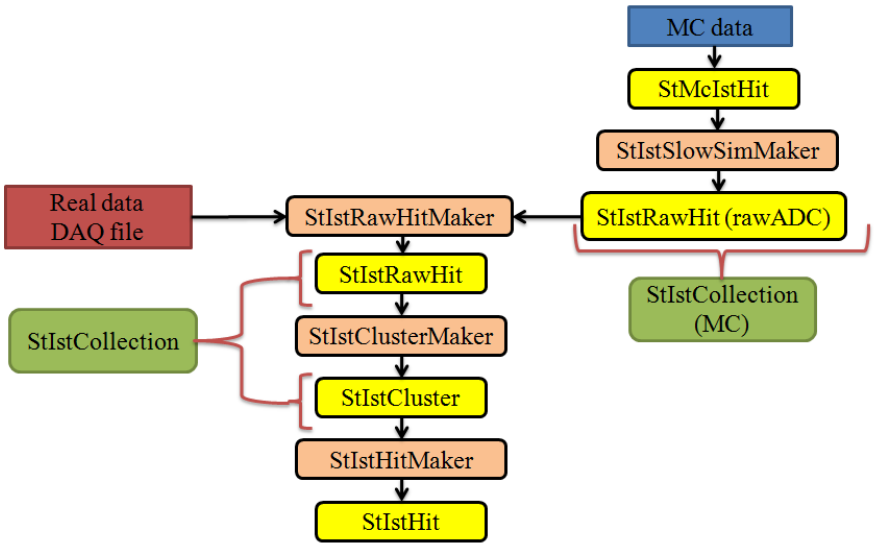

Figure 4.19: The structure of the IST offline reconstruction chain. After addition of the IST Slow Simulator, the StIstRawHitMaker had to be modified to include both raw real data and simulated raw hits by the StIstSlowSimMaker.

The integration of the IST Slow Simulator was done by creating interfaces to the existing IST data structures for both pure simulation and embedding mode. An important feature of the simulator is that it can access IST calibration database to get information about individual channel's gains, pedestal values and status (good or masked out).

The main purpose of the detector response simulator is to read the ionization charge produced by particles in the GEANT simulation and distribute it among the IST pads. In order to complete this task the simulator reads Monte Carlo (MC) hits from GEANT tables, which are the output of the GEANT simulation. Next the simulated charge is distributed among the pads, whose volume was traversed by the incident particle. The Figure 4.20 shows the principle of the IST Slow Simulator charge distribution alorithm. A straight line model was assumed for the particle trajectory, because of very small thickness $300\ \mu\mathrm{m}$ of a silicon sensor. A MC hit contains information about the deposited energy dE, the distance traveled in the sensor active volume dS, local position $\vec{X}$ and local momentum $\vec{p}$ in the coordinate system of the sensor. MC Hits are always placed in the middle of the sensor's height. For a passing particle the entrance $\vec{A}_1$ and exit $\vec{A}_2$ points can be found by moving half the traveled distance from the local position of the hit, eg:

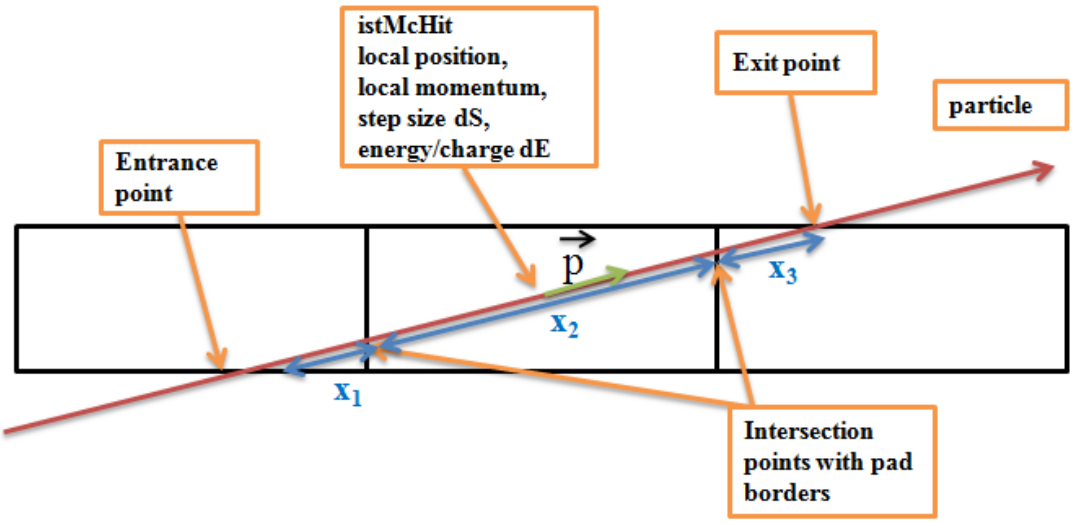

Figure 4.20: An illustration of the principle of charge distribution in IST Slow Simulator. Particles are assumed to travel in a straight line through the silicon sensors along the local momentum vector $\vec{p}$. The ionization energy assigned to a pad is the fraction of the total energy dE. The fraction is calculated by dividing the distance traveled in a pad by the entire path length $\frac{x_i}{dS}$.

$$\vec{A}_{1,2} = \vec{X} \pm \frac{\vec{p}}{|\vec{p}|} \cdot dS \tag{4.2}$$

In order to divide the charge among the traversed pads, the intersection points of the particle's trajectory and pad borders have to be found. The energy is divided among the pads

according to the distance x_i traveled in each of the pads crossed by the particle. The response of the pad is calculated according to Equation 4.3, where $\mathrm{ADC_{RAW}}$ is the response in ADC counts and $f_{MPV} = \frac{450}{80\ keV}$ is the energy to ADC recalculation factor [143]. The channel gain g is read from the calibration database and is applied to model the running conditions, which may change from run to run.

$$\mathrm{ADC} = \frac{dE}{dS} x_i f_{MPV} g^{-1} \tag{4.3}$$

The charge diffusion between the neighboring pads is not modeled and is negligible compared to the pad dimensions [144] of $600\ \mu m \times 6000\ \mu\mathrm{m}$. Furthermore, the design of the pads causes the most signal to be contained in $1-2$ pads. To identify a particle in the simulation an $\mathrm{IdTruth}$ value from the corresponding GEANT MC hit is saved for each pad. The $\mathrm{IdTruth}$ is a particle's unique identifier in the simulation and allows to trace the particle. This is later used during the reconstruction stage and is important for the simulation-based efficiency studies. The clustering algorithm in the StIstClusterMaker was also modified to propagate the $\mathrm{IdTruth}$. In case of merging 2 hits the $\mathrm{IdTruth}$ for the hit, the one with the largest ADC value is assumed.

The Figure 4.21 shows results of the IST simulation for both IST raw hits (StIstRawHit, red) and IST reconstructed hits (StIstHit, blue). The reconstructed hits are obtained after running a clustering algorithm, which adds together adjacent raw hits forming a single hit. The distributions presented in the figure are obtained after an incident angle correction, to take into account the distance traveled by a particle in the silicon sensor. A depletion of raw hits for $\mathrm{ADC} < 400$ is caused by the clustering algorithm, because a pad with low-ADC raw hits is typically adjacent to a pad with high-ADC raw hit and only a small fraction of charge was deposited in the other pad. Such raw hits are merged by the clustering algorithm. The reconstructed hit distribution follows a Landau distribution.

The reconstructed hits positions distribution in the STAR global coordinate system from a pure simulation is shown in Figure 4.22. The blank horizontal lines are caused by the sensor spacing, while the blank patches are caused by the masking out of bad or dead channels in the calibration database.

In a pure simulation mode the IST reconstruction chain needs to read the MC hits from GEANT tables, which are presented as MC data in Figure 4.19. In embedding mode, the chain reads both real data in a raw DAQ file format and simulated MC hits from GEANT. The StIstRawHitMaker was adopted to add together hits form the real data and the Slow Simulator.

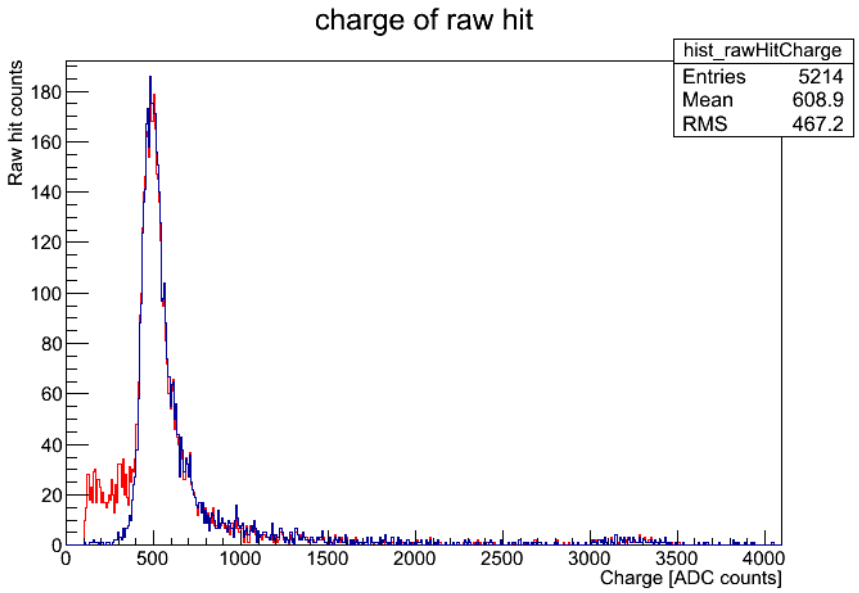

Figure 4.21: ADC distribution obtained from the IST Slow Simulator in the pure simulation mode. The IST raw hits (red) and the IST reconstructed hits (blue) include an incident angle correction, which corrects for the different distance traveled through the sensor by an incident particle.

Finally, the simulator can handle data in either zero suppression mode or non-zero suppression mode.

I developed a helpful visualization software for the output of the IST reconstruction chain to aid in the development of the IST Slow Simulator. It allowed a visual investigation of special cases encountered in the simulation. An example of a primary π^+ causing a knockout of particles from the Pixel detector material (not shown here) is presented in Figure 4.23. Only tracks for particles of interest are drawn.

In summary, the IST Slow Simulator was developed and successfully tested. It has all the needed functionality and performs as expected. Based on the software experience, a series of tutorials for students were prepared [131, 136].

4.4.3 Validation of Pixel detector calibration software for bad pixel masking

Another important service task, in which the author was involved, was the validation of the bad pixel masking code for the Pixel detector. This was a test, if the code works as expected, so the requirements for the masking had already been determined. The software was developed by

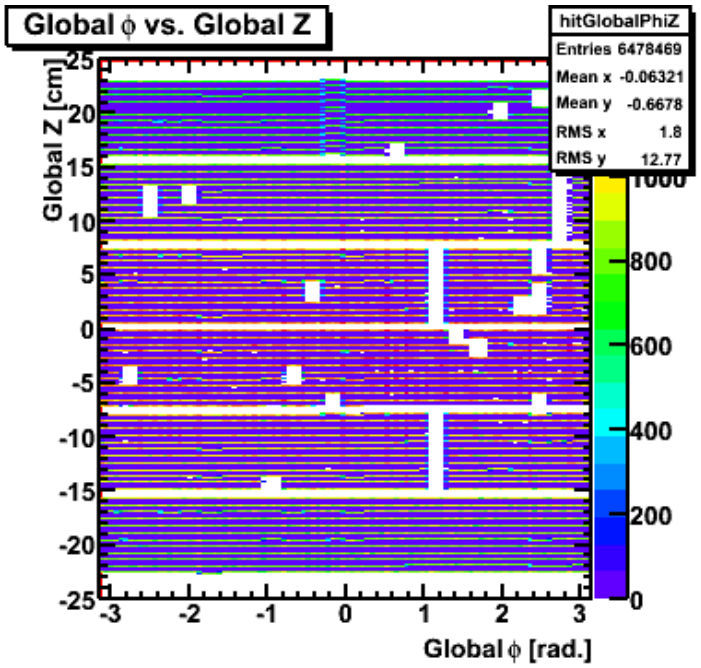

Figure 4.22: Distribution of IST reconstructed hits positions in the STAR global coordinate system produced in embedding mode. The distribution includes data from $Au + Au$ collisions at $\sqrt{s_{NN}} = 200$ GeV collected in 2014 as well as simulated hits created by the IST slow simulator from embedded pions. The blank horizontal lines are due to the sensor spacing. The blank boxes correspond to the bad or dead channels disabled in the calibration database.

Michael Lomnitz and Guannan Xie of the STAR collaboration. There are a few categories of masking for different Pixel detector structures: sensors, pixels, columns and rows.

4.4.3.1 Hot pixels

Hot pixels are defined by a condition set in Equation 4.4 [145], where N is the number of hits in a pixel and N_{ev} is the number of events.

$$\frac{N}{N_{ev}} > 0.1 \tag{4.4}$$

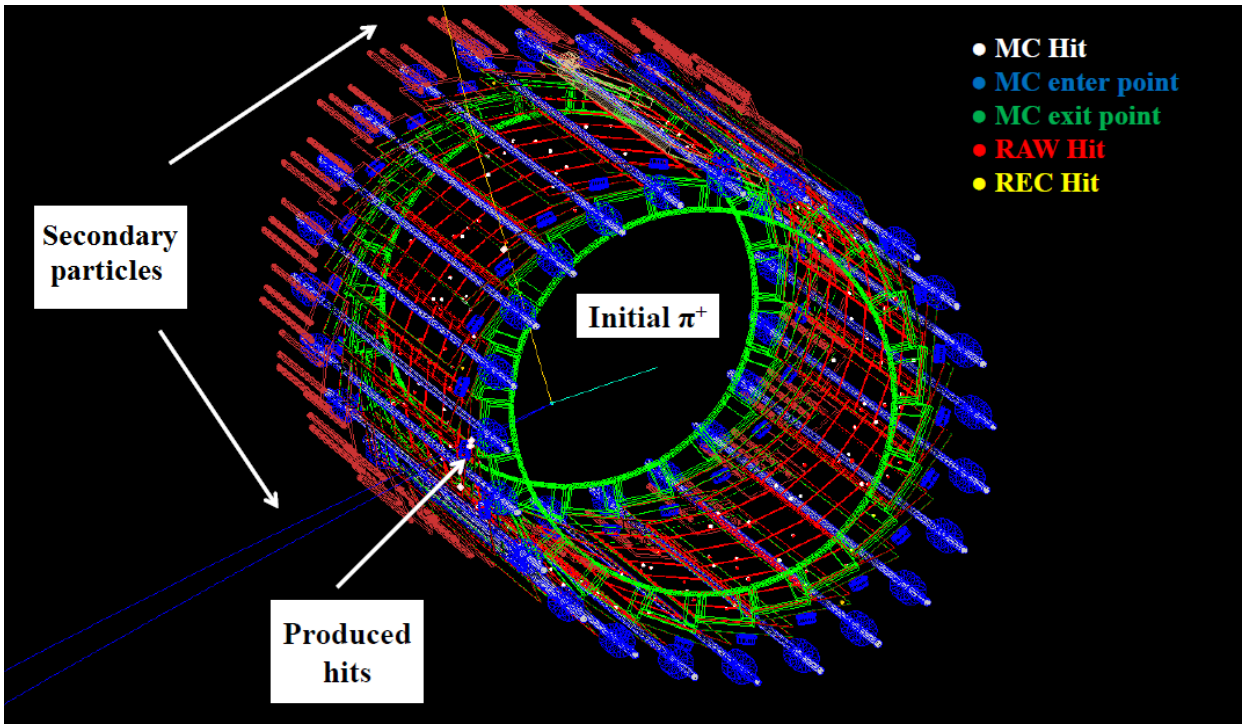

Figure 4.23: A helpful visualization of IST reconstruction chain output with a wireframe view of IST geometry. It shows a simulated event, in which an initial π^+ was absorbed in the Pixel material causing a few knockout particles. Only tracks of particles of interest are drawn here. Different kinds of IST hits are also shown.

4.4.3.2 Bad columns

Columns are marked as bad if they contain more than 200 hot pixels ($\approx$ 20% of a column) according to Equation 4.5 [145]. Here, a number of hot pixels in a column is defined as N_{hotpix}.

$$N_{hotpix} > 200 \tag{4.5}$$

If a number of entries in a column N is $\approx$ 100 times higher than average column entries ($\frac{N_{hits}}{1000}$) in the sensor it is also marked as bad according to Equation 4.6 [145].

$$N > 100\frac{N_{hits}}{1000} \tag{4.6}$$

A column is marked as bad also if the number of entries in a column N is greater than 10 times the average number of hits in columns for a sensor in that layer. This is done with a condition set in Equation 4.7 [145], where N_{hits} is the number of hits in a sensor in the layer

and 1000 is the approximate number of columns. The dead sensors are ignored.

$$N > 10 \sum_{layer=1,2} \frac{N_{hits}}{1000} \tag{4.7}$$

Finally, a block of 50 consecutive columns is marked as bad if the content of each column is lower than 10 times the average entries for a column in that sensor after masking. The described condition is defined with the Equation 4.8 [145], where N^s_{mask} is the number of entries in a sensor after masking.

$$N < 10 \frac{N^s_{mask}}{960 N_S} \tag{4.8}$$

4.4.3.3 Bad rows

Rows are marked as bad if a number of hits N in them is larger than ≈ 100 times the average row content in a sensor. This is defined in Equation 4.9 [145], where N_{hits} is the number of hits in a sensor and 1000 is the approximate number of rows.

$$N > 100 \frac{N_{hits}}{1000} \tag{4.9}$$

Like for columns, the rows are marked as bad if their content is higher than the average number of hits N_{hits} per row in a sensor for that layer. The condition is set by the Equation 4.10 [145], where 928 is the number of rows.

$$N > 10 \sum_{layer=1,2} \frac{N_{hits}}{928 N_S} \tag{4.10}$$

4.4.3.4 Sensor status

The sensor status is defined based on the number of hot or dead pixels as well as bad columns and rows. The sensors are classified according to the categories listed below [145]:

- Good sensor (G), if the number of bad columns and rows is < 5 ($< 0.5\%$ of the sensor).
- Good but hot sensor (H), if the number of bad columns and rows is < 50 ($< 5\%$ of the sensor).
- Non-uniform sensor (U), if the number of bad columns and rows is < 720 ($< 75\%$ of the sensor).

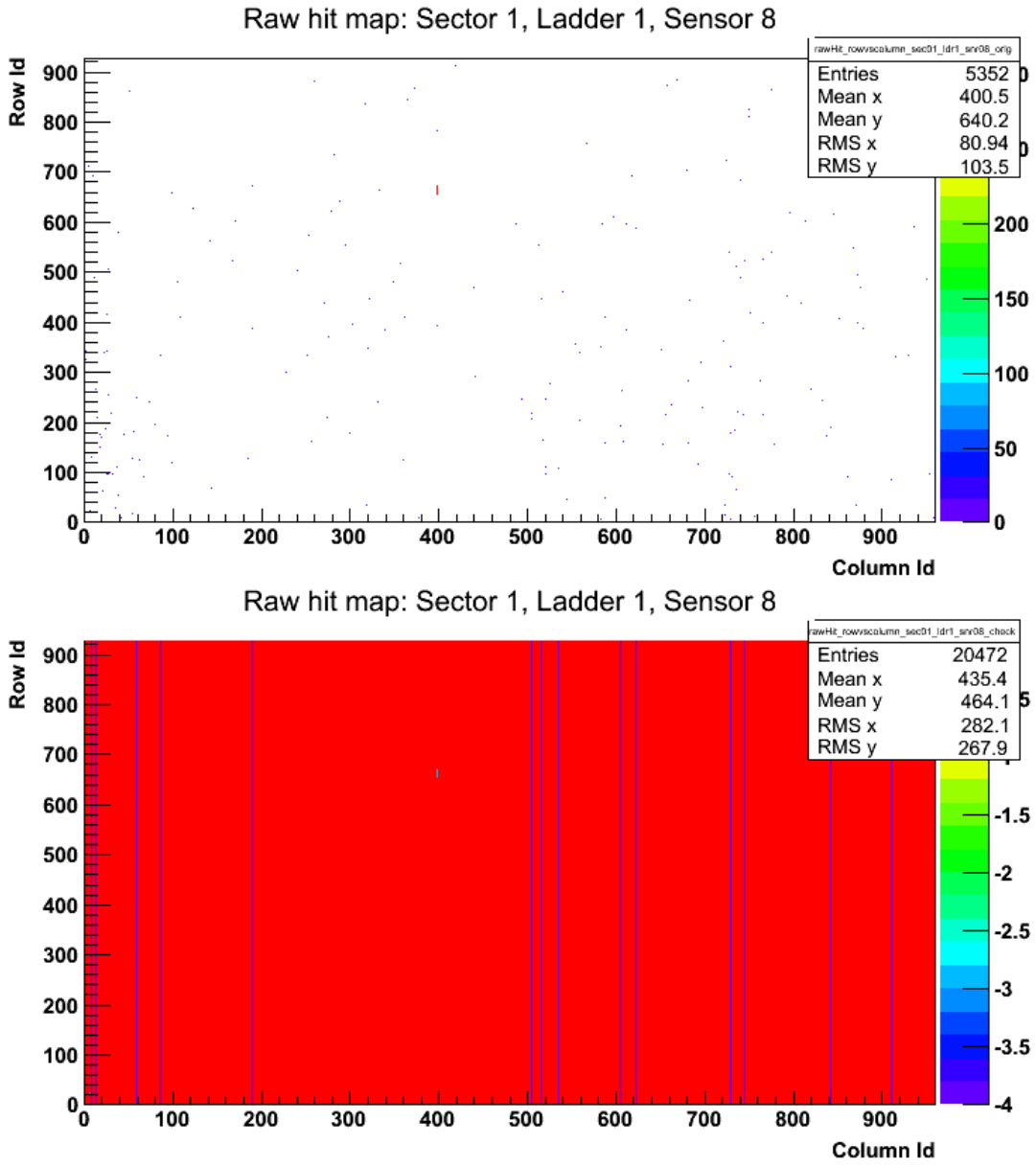

Figure 4.24: Top: An example of a good but hot Pixel sensor before masking. Bottom: A test histogram for the same sensor showing 14 masked out columns and a few hot pixels (blue).

- Low efficiency sensor (L), if the number of entries is < 1 after masking out bad rows and columns.
- Bad sensor (B), if the number of hits per event is > 1000 after masking or number of bad rows and columns is > 720 ($> 75\%$ of the sensor)
- Dead sensor (D), if the number of entries is 0.

The tests were done and small bugs were found independently by me and Michael Lom-

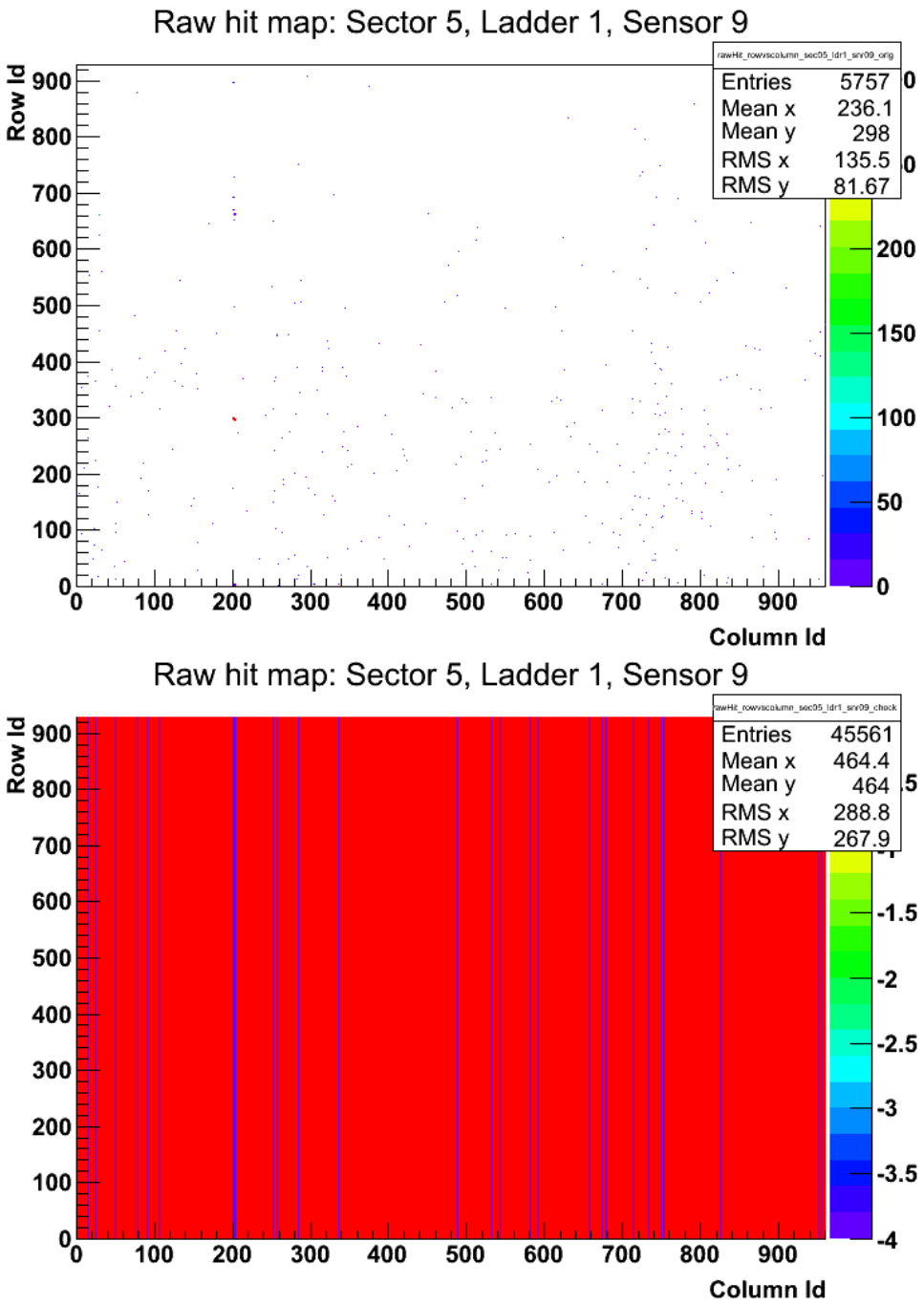

Figure 4.25: Top: An example of a non-uniform Pixel sensor before masking. Bottom: A test histogram for the same sensor. There are more than 50 bad columns and some hot pixels (blue).

nitz [146] and corrected. In order to check if the code works properly a series of test histograms were produced, where a status of the pixels, rows or columns was stored. This was compared to the contents of the produced database tables. A few examples of the test are presented here.

The Figure 4.24 shows an example of a sensor marked as good but hot compared to the test histogram. The masked out columns, rows and pixels are filled with negative values. The sensor

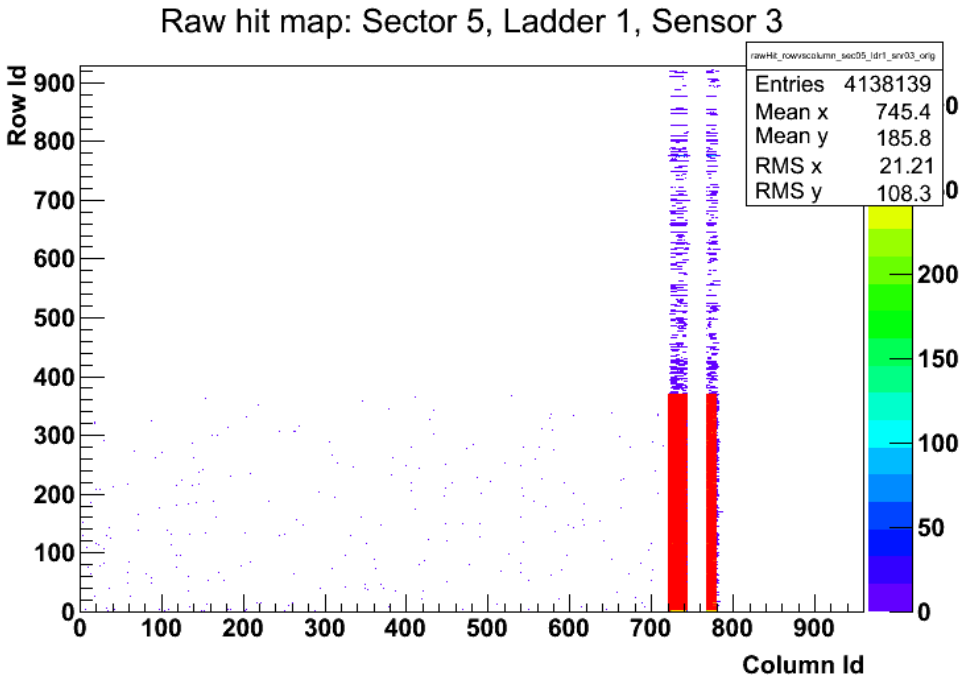

Figure 4.26: An example of a Pixel sensor classified as bad due to a large number of hits per event.

contains 14 bad columns and a few hot pixels. This clearly classifies the sensor as good but hot according to the assumed definition.

An example of a non-uniform sensor is shown in Figure 4.25. There are more than 50 bad columns found in this sensor.

The Figure 4.26 shows a case of a bad sensor. This sensor has been marked as bad, because of high number of hits per event (> 1000).

In summary, the validation of the PXL masking code was done successfully. The software is working properly and was used for Pixel detector calibrations.

4.4.4 Endcap High Tower trigger preparation

The author was also involved in preparation of the EEMC based trigger (so called Endcap High Tower or EHT) for $B \rightarrow J/\psi$ (non-prompt J/ψ) decay studies [147]. The purpose of this trigger was to increase the number of reconstructed J/ψ coming from B meson decays as well as to broaden the y range for these studies from $|y| < 1$ to $-1 < y < 2$. It could also be useful for other studies. To distinguish non-prompt J/ψ from prompt J/ψ a pseudo-proper decay length cut has to be used utilizing the HFT tracking for at least one electron.

An efficiency study using PYTHIA v8.180 [85] event generator was performed to determine

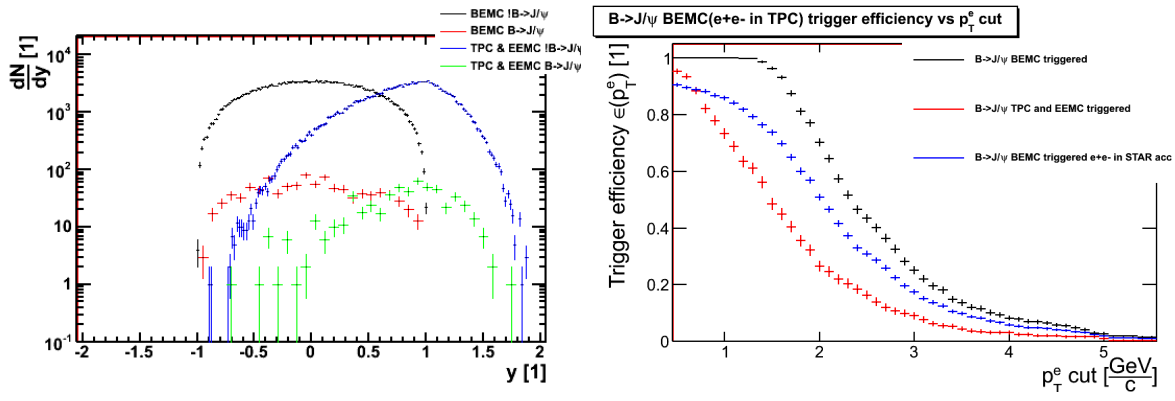

Figure 4.27: Left: J/ψ y distribution from PYTHIA for J/ψ triggered with BEMC: prompt (black) and non-prompt (red) as well as EEMC triggered, with one electron reconstructed with the TPC: prompt (blue) and non-prompt (green). Right: Trigger efficiency estimated with PYTHIA for prompt J/ψ vs. p_T^e cut in 3 cases: BEMC triggered (black), EEMC triggered with one electron reconstructed in the TPC (red) and BEMC triggered with both e^+e^- in the STAR acceptance (blue).

the optimal trigger threshold corresponding to a cut on electron transverse energy E_T^e. The Figure 4.27(left) shows the y distributions of J/ψ from B decays as well as all other J/ψ in two cases: BEMC triggered and EEMC triggered with one of the decay electrons reconstructed in the TPC. A clear gain is visible in the latter case.

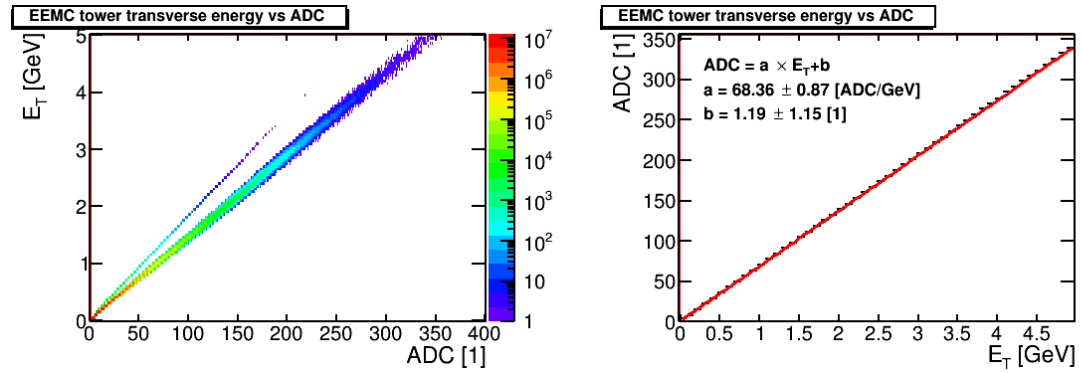

Figure 4.28: Left: A 2D histogram of ADC and E_T obtained from Run10 min-bias $Au+Au$ collisions at $\sqrt{s_{NN}} = 200$ GeV. Right: A profile of the same histogram with a linear fit used to obtain the ADC $\propto E_T$ dependence.

The efficiency was studied as a function of the electron p_T^e cut, which is $p_T^e \approx E_T^e$. It is shown in Figure 4.27(right). A study with the real data allowed to determine the ADC $\propto E_T$ value, to be used as a trigger threshold. This study was done using min-bias $Au+Au$ collisions at $\sqrt{s_{NN}} = 200$GeV collected in 2010. The Figure 4.28(left) presents the 2D histogram of ADC

and E_T. A linear fit is done to the profile of this histogram, which is shown in Figure 4.28(right) to extract the relation between ADC and E_T.

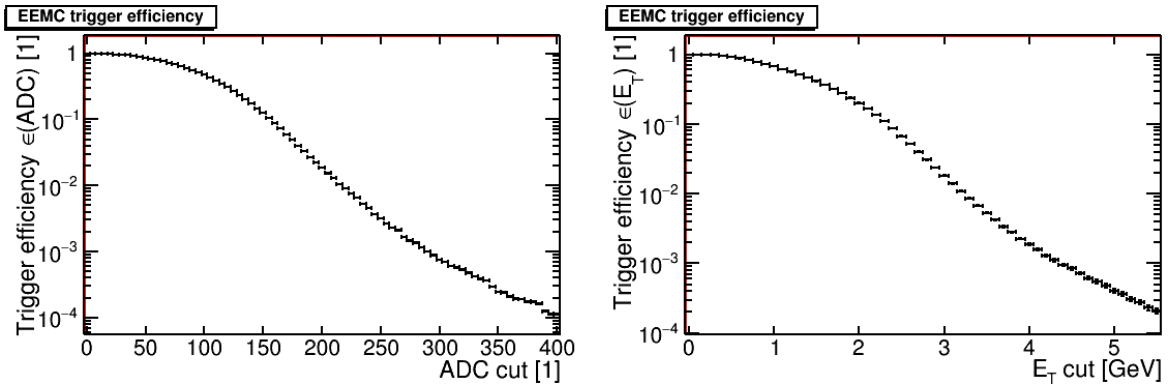

Figure 4.29: Left: Endcap High Tower trigger efficiency vs ADC for $Au + Au$ events at $\sqrt{s_{NN}} = 200\ \mathrm{GeV}$. Right: EHT trigger efficiency vs. E_T.

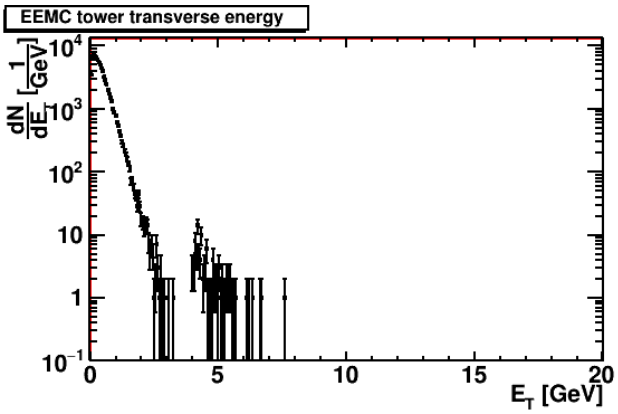

Figure 4.30: E_T distribution of EEMC hits for the data recorded by the EHT trigger. The jump around $E_T > 4\ \mathrm{GeV}$ is related to the EHT trigger effect.

The analysis of the data also allowed to calculate the efficiency for events, when applying an ADC or E_T cut. This is shown in Figure 4.29. It was crucial for estimating the trigger rate. For an E_T threshold of $4\ \mathrm{GeV}$, and assuming the maximum collision rate for $Au + Au$ to be $50\ \mathrm{kHz}$, the trigger rate was estimated to be $93.2 \pm 2.8\ \mathrm{kHz}$ at most. This was deemed acceptable by the STAR trigger board, so an $E_T > 4\,\mathrm{GeV}$ threshold was chosen. It corresponds to the $\mathrm{ADC} = 274.6 \pm 3.7$.

The trigger was successfully implemented and recorded data from $Au + Au$ collisions at $\sqrt{s_{NN}} = 200\,\mathrm{GeV}$. A quick test was done using a fast offline production (reconstruction) of the data, which used a basic set of calibrations. The Figure 4.30 shows an E_T distribution of EEMC

hits for EHT-triggered data. The trigger effect can be seen around $E_T \approx 4\,\mathrm{GeV}$, as the events were required to contain at least one hit in an EEMC tower above this value to be recorded. The values below $E_T \approx 4\,\mathrm{GeV}$ originate from the underlying event.

Chapter 5

Data analysis for Υ production studies

5.1 Software tools

Data analysis is performed using software written in C++ programming language. The analysis codes use the ROOT [135] and root4star data analysis framework and library.

The software had to be developed specifically for this analysis, but some basic parts were available to the members of the STAR Collaboration as part of internal CVS (Concurrent Versions System) [148] repository [149].

5.2 Data set

The data used in the Υ analysis consists of $156\,\mathrm{M}$ $p+p$ events recorded by the STAR experiment using the Barrel High Tower (BHT1) trigger during 2011 run (Run11) at center-of-mass collision energy of $\sqrt{s} = 500\,\mathrm{GeV}$. The trigger required a coincidence of hits in both BBC disks and a high energy hit ($E \approx 4.6$ GeV) in a BEMC tower. It is implemented at the L0 level (lowest level) of trigger electronics. The integrated luminosity for this trigger is $\int \mathcal{L}dt = 22\,\mathrm{pb}^{-1}$. The analysis is performed on the reconstructed data, which size is ≈ 285 TB. The reconstruction procedure includes track, vertex finding, calibrations etc. as described in Section 4.2. It allows to extract the information relevant for the physics analysis from the raw data.

Collision type	$p + p$
Center-of-mass energy	$\sqrt{s} = 500$ GeV
Number of events	156 M
Integrated luminosity	$\int \mathcal{L}dt = 22\,\mathrm{pb}^{-1}$
TriggerId	320501, 330501

Table 5.1: Summary of the Run11 data set used for Υ studies.

5.3 Event selection

Events are selected by requiring the default primary vertex[1], to be within $|V_z| < 40$ cm of the TPC center along the z-axis (beam axis). This ensures uniform acceptance for tracks originating from that vertex. Figure 5.1(left) shows the V_z distribution for all events (black) and those passing $|V_z| < 40$ cm cut (red).

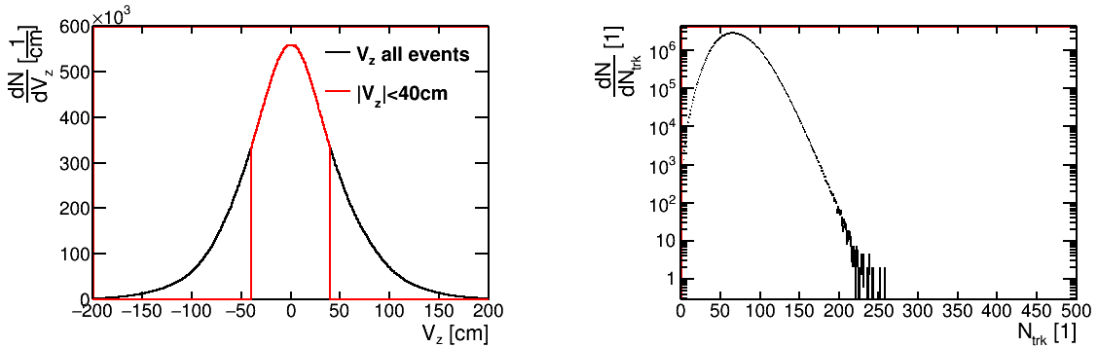

Figure 5.1: Left: Distribution of primary vertex z-position (V_z) for all events (black) and those selected for further analysis (red). Right: Distribution of accepted primary tracks for selected events.

The number of reconstructed primary tracks, passing quality cuts (see Subsection 5.4.1), for selected events is shown in Figure 5.1(right).

cut	value
Events available	156 M
Primary vertex cut	$\|V_z\| < 40$ cm
Events passing cuts	92 M

Table 5.2: Summary of the Run11 event cuts used for Υ analysis.

A summary of the event selection is shown in Table 5.2.

5.4 Track selection

In order to reconstruct Υ candidates, electron and positron tracks have to be selected and combined into pairs. The proper track quality is ensured by the track quality cuts described in

[1]There may be multiple vertices reconstructed in a single event, a default vertex is the highest quality vertex

Subsection 5.4.1. The electron identification cuts are described in Subsection 5.4.2. Moreover, a set of kinematic cuts are applied to reject background. These are described in Section 5.4.3.

5.4.1 Track quality cuts

Track quality cuts are important for the quality of the entire analysis. Badly fit tracks and pile-up effects have to be avoided. Pile-up tracks or vertices are those which are coming from multiple events happening during a single sequence of TPC readout. These are all reconstructed within a single event and are unrelated to the event of interest, which fired the trigger. Pile-up is a problem at high luminosity, with $p+p$ collisions happening at a rate of ≈ 1 MHz. This is in sharp contrast to the typical TPC readout rate of ≈ 1 kHz. Pile-up tracks are removed by a $flag < 1000$ cut. A track flag is assigned as an output of track fitting procedure, performed by the tracking algorithm, and is a basic evaluation of the track quality. Bad fits are rejected with $flag > 0$. Also, $flag = 701, 801, 901$ indicate Forward Time Projection Chamber (FTPC) [150] tracks and beam background tracks.

To reconstruct a good track a sufficient number of points are needed in the helix fit ($nFitPts$). This ensures a good momentum resolution, as $\frac{\sigma p_T}{p_T} \propto \frac{1}{\sqrt{nFitPts}}$. Furthermore, the tracking algorithm may split tracks, which are in fact a single one. By requiring that the ratio of points used in the fit to the maximum possible $\frac{nFitPts}{nFitPtsMax} > 0.52$ such tracks are rejected. In addition a $0 < \frac{dE}{dx} < 6$ keV cut is applied to reject bad or too high $\frac{dE}{dx}$ values, not useful for further analysis. Low-p_T tracks, which barely reach TPC are also rejected with $p_T > 0.2$ GeV/c.

Pile-up may affect the reconstructed Υ signal. In order to check this effect a reference multiplicity ($refMult$) dependence on BBC coincidence rate is plotted in Figure 5.2(left). The reference multiplicity is defined as tracks with $flag > 0$, $nFitPts \geq 10$, $|eta| < 0.5$, $DCA < 3$ cm. A profile of the distribution is drawn (black). It shows a rise of $refMult$ at large values of BBC coincidence rate. The BBC coincidence rate is proportional to collision rate and as its value increases, so does the likelihood of pile-up. This causes the pile-up tracks to be incorrectly reconstructed as originating from the primary vertex. For the multiplicity dependent studies it was required to use TOF matched tracks ($TofMult$) to reduce the influence of pile-up. TOF is a fast detector, and can remove pile-up tracks. This is done by selecting tracks with: $TofMatchFlag > 0$, $nFitPts \geq 15$, $|\eta| < 1$, $p_T > 0.2$, $DCA < 0.5$ cm, where DCA is the distance of closest approach of a track to the primary vertex (P.V.). These values are unified for different measurements in STAR and are summarized in Table 5.4.

Figure 5.2(right) shows the $TofMult$ vs. BBC coincidence rate. A profile (black) shows slight decrease at high BBC rates, because the track reconstruction efficiency drops as the TPC occupancy increases. This is corrected for as described in Section 5.6.

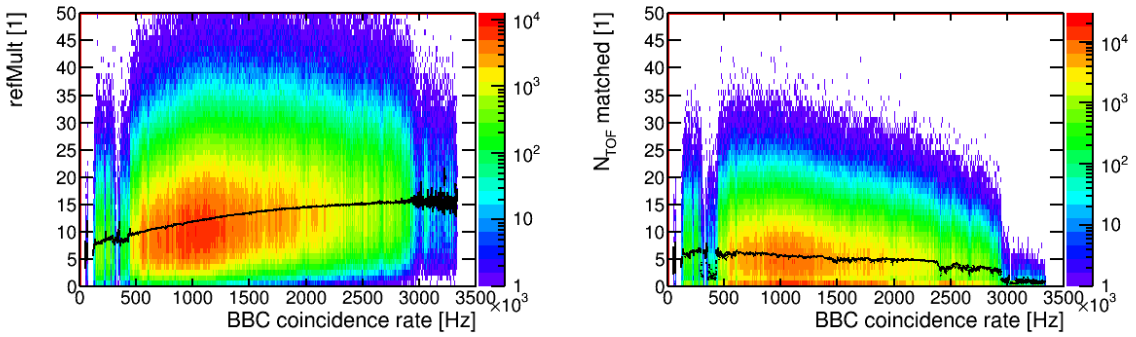

Figure 5.2: Left: Dependence of reference multiplicity ($refMult$) on the BBC coincidence rate. The black line is a profile of the distribution. A rise for large values of BBC rate is due to pile-up tracks wrongly associated to the primary vertex. Right: Dependence of number of tracks matched to TOF ($TofMult$) on the BBC coincidence rate. A profile is plotted in black. It shows a decrease caused by lowering of reconstruction efficiency due to high TPC occupancy.

Pile-up however is very unlikely to affect measured Υ yield, as a production per event is very low, on the order of 10^{-8} [151]. The probability of observing 2 such independent events happening in coincidence would be on the order 10^{-16}. However, a dependence of number of Υ candidates on the BBC rate was also investigated as shown in Figure 5.4. No dependence is observed.

cut	value	purpose
Track flag	$0 < flag < 1000$, $flag \neq 701, 801, 901$	Reject tracks recognized as pile-up, badly fit or non-TPC tracks
Transverse momentum	$p_T > 0.2$ GeV/c	Reject short, low-p_T tracks
Number of fit points	$nFitPts > 20$	Reject tracks with low number of hits used in the fit
Fit points ratio	$\frac{nFitPts}{nFitPtsMax} > 0.52$	Avoid split tracks
Energy loss	$0 < \frac{dE}{dx} < 6$ keV	Reject tracks with bad $\frac{dE}{dx}$ value

Table 5.3: Summary of the track quality cuts used for Υ studies.

A summary of all track quality cuts is shown in Table 5.3.

Transverse momentum	$p_T > 0.2\,\mathrm{GeV/c}$
Pseudorapidity	$\lvert\eta\rvert < 1.0$
Number of fit points	$nFitPts \geq 15$
Distance of closest approach to the P.V.	$DCA < 0.5\,\mathrm{cm}$
TOF matching	$TofMatchFlag > 0$

Table 5.4: Summary of the TOF multiplicity ($TofMult$) definition used for multiplicity-dependent studies.

5.4.2 Electron identification cuts

To identify electrons, information from both TPC and BEMC is used. Electrons can be identified with the TPC $\frac{dE}{dx}$, which is recalculated into $n\sigma_e$ with the Equation 5.1.

$$n\sigma_e = \ln \frac{\frac{dE}{dx}}{\frac{dE}{dx}|^e_{expected}} / \sigma_{TPC} \tag{5.1}$$

Here, the $\frac{dE}{dx}$ is the measured value, while $\frac{dE}{dx}|^e_{expected}$ is the expected value for an electron by the Bichsel function [152, 153]. The σ_{TPC} is the $\frac{dE}{dx}$ resolution of the TPC. Basically, the $n\sigma_e$ value indicates how much, in terms of detector resolution, the measured $\frac{dE}{dx}$ value differs from the expected value. Electrons are selected by requiring $-1.2 < n\sigma_e < 3.0$.

To further improve identification, the tracks are projected to the BEMC to find hit towers and clusters. The energy E_{TOW} is extracted from the tower pointed by a track. In addition, the algorithm looks for the 2 highest energy towers adjacent to the struck tower. The energy of towers in the cluster is added together to form E_{CLU}. Also, a center of the cluster is determined as a weighed average of the tower positions in (η, ϕ), using the tower energy as a weight. This allows to calculate the distance R_{SMD} between the center of a cluster and track projection on SMD layer $(\Delta\eta, \Delta\phi)$ with the Equation 5.2.

$$R_{SMD} = \sqrt{\Delta\eta^2 + \Delta\phi^2} \tag{5.2}$$

Electron selection with the BEMC is done by requiring $R_{SMD} < 0.028$ to remove tracks randomly matched to BEMC signal from π^0, γ. Moreover, a $\frac{E_{TOW}}{E_{CLU}} > 0.5$ cut is used to select electron clusters, which contain a large fraction of E_{CLU} in a single tower. Also, for electrons $\frac{E}{p} \approx 1c$, which leads to selecting $0.55 < \frac{E_{CLU}}{p} < 1.45$, where p is the TPC track momentum.

Electron identification cuts are summarized in the Table 5.5.

cut	value	purpose
Energy loss in the TPC gas	$-1.2 < n\sigma_e < 3.0$	Identify electrons with the TPC
Distance between track projection and center of a cluster	$R_{SMD} < 0.028$	Ensure track matching to the corresponding cluster
Tower energy fraction	$\frac{E_{TOW}}{E_{CLU}} > 0.5$	Select compact towers
Energy to momentum ratio	$0.55 < \frac{E_{CLU}}{p} < 1.45$	Additional rejection of hadrons

Table 5.5: Summary of the electron identification cuts.

5.4.3 Kinematic cuts

The basic purpose of the kinematic cuts is to reject background and streamline analysis. First of all, a track is matched to the BEMC tower, which fired the trigger. The value of $DSMadc$, which is a hit energy converted to a truncated 6-bit ADC value. $DSMadc$ is used by the L0 trigger logic of the BHT1 trigger to decide online whether the event satisfied a threshold of $DSMadc > 18$ ($E \approx 4.6$ GeV). At least one track from each event has to satisfy $DSMadc > 18$ condition. However, during offline analysis the $DSMadc$ is calibrated using more precise offline calibrations instead of the online values. Figure 5.3 shows (η, ϕ) positions of clusters containing a maximum $DSMadc$ L0 tower for an event. Empty areas in the distribution are corresponding to towers that had been masked during calibration or turned off during data taking.

An additional $p_T > 1$ GeV/c cut is applied for a partner track, which forms a pair together with the track, matched to L0 tower. This is done in order to reject background.

cut	value	purpose
$DSMadc$	$DSMadc > 18$	Select track that satisfies the trigger requirements
Partner track p_T	$p_T > 1$ GeV/c	Reduce background

Table 5.6: Summary of the kinematic cuts.

All kinematic cuts are listed in the Table 5.6.

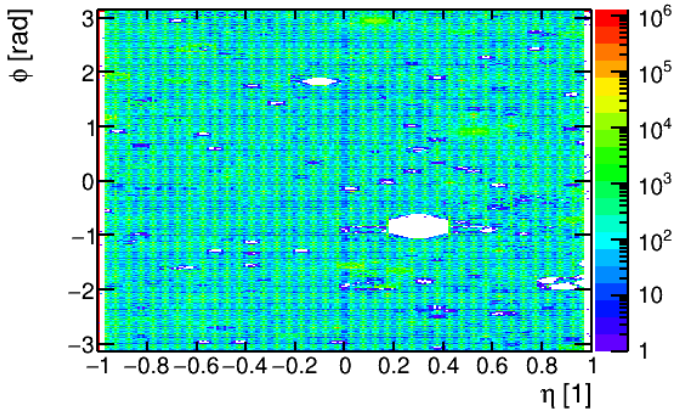

Figure 5.3: Distribution of clusters positions in (η, ϕ), which contain maximum $DSMadc$ L0 tower in an event. The empty patches are due to offline or masked out towers.

5.5 Signal extraction

In order to extract the Υ signal, a resonance peak in an invariant mass of e^+e^- pairs has to be observed. The yield of Υ is determined statistically. The signal is reconstructed by combining trigger and partner track candidates into e^+e^- (unlike-sign) pairs. An invariant mass m_{ee} is calculated for each pair with the Equation 5.3 and a distribution is made. Such a distribution contains Υ signal and 2 types of background: combinatorial and correlated backgrounds. Combinatorial background is estimated by using a sum of like-sign pairs $N_{CB} = N_{e^+e^+} + N_{e^-e^-}$. The correlated background has to be estimated using a fit that includes Drell-Yan ($q\bar{q} \rightarrow e^+e^-$) [154] process and $b\bar{b} \rightarrow B\bar{B} \rightarrow e^+e^- + X$.

$$m_{ee} = \sqrt{(E_1 + E_2)^2 - (\vec{p_1} + \vec{p_2})^2} \tag{5.3}$$

In the above equation, the E_1, E_2 are energies and $\vec{p_1}$, $\vec{p_2}$ and momenta of the particles forming the pair.

The m_{ee} distribution for both unlike-sign (red points) and like-sign (blue points) pairs is presented in Figure 5.5. These distributions are fitted simultaneously using likelihood fits with RooFit [155, 156]. This has an advantage of extracting maximum information from these distributions compared to the background subtraction method. The fit components are described in one of the next paragraphs in detail and are listed below:

- Combinatorial background (CB): $f_{CB} = N_{CB} \cdot exp(\frac{-m_{ee}}{T_{CB}})$

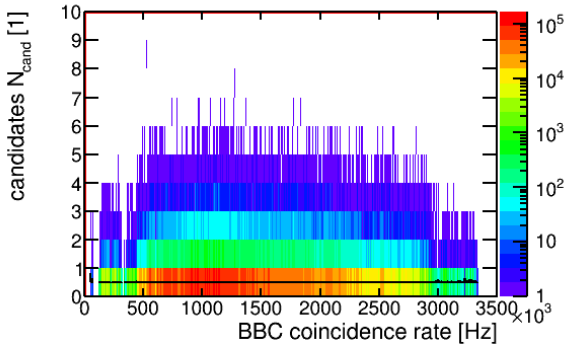

Figure 5.4: Dependence of Υ candidates on BBC coincidence rate. The Υ candidates here were selected by making e^+e^- pairs, which satisfy initial identification cuts for both electrons: $p \geq 1$ GeV/c, $-2 < n\sigma_e < 3$, $\frac{E_{cluster}}{p} \leq 3$, $R_{SMD} \leq 0.04$, a match to the BEMC tower which fired the trigger for at least one of them and an invariant mass cut of $5 \leq m_{ee} \leq 20$ GeV/c^2. The cuts are described in detail in Section 5.4.2.

- Correlated background: Drell-Yan (DY) and $b\bar{b}$: $f_{b\bar{b}+DY} = N_{b\bar{b}+DY} \frac{m_{ee}^A}{(1+\frac{m_{ee}}{B})^C}$
- Signal: $\Upsilon(1S) + \Upsilon(2S) + \Upsilon(3S)$: 3 Crystal Ball functions [157, 158]
- Trigger turn-on (only for $0 < p_T < 2$ GeV/c): $f_{err} = \frac{2}{\sqrt{\pi}} \int_0^{m_{ee}} e^{-t^2} dt$ multiplied by background functions

The fit is done in the invariant mass range $6.6 < m_{ee} < 15.4$ GeV/c^2 in order to use as much information as possible, while keeping the fit not too complicated. The fits are done in 7 p_T bins ($0-10$ GeV/c, $4-10$ GeV/c, $0-2$ GeV/c, $2-4$ GeV/c, $4-6$ GeV/c, $6-8$ GeV/c, $8-10$ GeV/c), 3 y bins ($|y|<1, |y|<0.5, 0.5<|y|<1$) and 5 $TofMult$ bins ($0-100, 0-4, 4-8, 8-12, 12-100$) for a total of 105 fits. The p_T dependence, y dependence and $TofMult$ dependence of Υ signal are presented in Figure 5.6, Figure 5.7 and Figure 5.8 respectively.

The initial parameters for the Drell-Yan and $b\bar{b}$ background are set by fitting the $b\bar{b} \rightarrow B\bar{B} \rightarrow e^+e^-$ invariant mass distributions from a PYTHIA8 simulation [159]. This assumes that Drell-Yan has the same shape as $b\bar{b}$ or has a negligible contribution to the background. A STAR measurement confirms that both cross sections are strongly correlated [160]. The fits are presented in Appendix A. During fitting, the $B = 30$ is fixed, as it simplifies the fit function while providing a good description of the simulations. This parameter is then varied to estimate the systematic uncertainty related to fixing it. For details see Section 5.7.2. In addition, the C

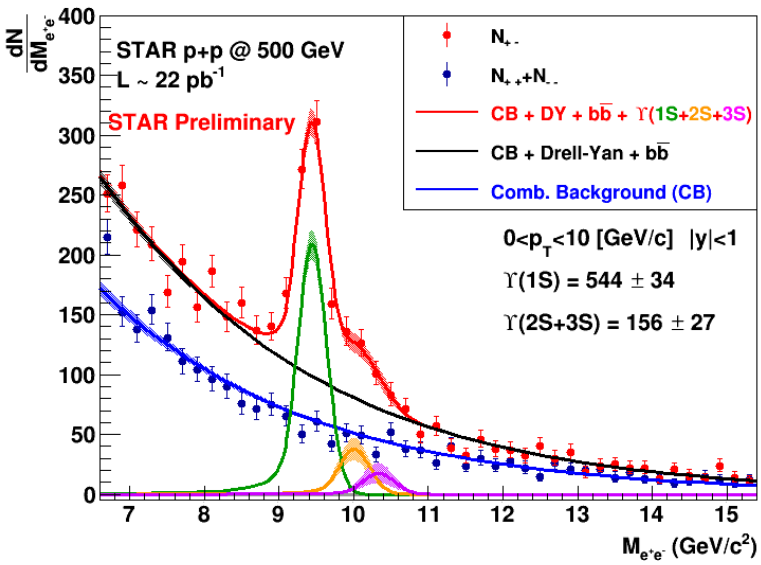

Figure 5.5: Invariant mass m_{ee} distribution for unlike-sign (red points) and like-sign (blue points) pairs. The curves correspond to combinatorial background (blue), correlated background (black), $\Upsilon(1S)$ (green), $\Upsilon(2S)$ (orange), $\Upsilon(3S)$ (purple). The total (red) is a sum of the above components.

parameter is fixed with the value obtained for the p_T-integrated distribution.

The shapes of the Crystal Ball functions are determined from the fit to the simulated $\Upsilon \rightarrow e^+e^-$ decays from embedded into real data. Details of the procedure are described in Section 5.6.6. These include momentum resolution from MC simulation as well as an additional gaussian smearing of the electron p_T. For details see Section 5.6.5 or Appendix C.

Finally, the excited to ground state Υ ratios from fits to the world data are used as starting parameters for ratios between yields of each of the Υ states [82].

After successful fits, the $\Upsilon(1S+2S+3S)$ yield is calculated in the invariant mass range $8.8 < m_{ee} < 11$ GeV/c^2 by integrating unlike-sign counts and subtracting both combinatorial and correlated backgrounds. The yield of $\Upsilon(1S)$ is calculated in the range $8.8 < m_{ee} < 9.8\,\mathrm{GeV/c^2}$, the $\Upsilon(2S)$ in $9.8 < m_{ee} < 10.2\,\mathrm{GeV/c^2}$ and $\Upsilon(3S)$ in $10.2 < m_{ee} < 10.8\,\mathrm{GeV/c^2}$. These yields are corrected for the contribution of other Υ states based on the signal from Crystal Ball fits - a purity correction. Also, an invariant mass cut efficiency correction is applied for each of the states separately and to a combined $\Upsilon(1S+2S+3S)$ yield. The details are described in Section 5.6.6. The extracted yield can be found in the Appendix D.

Finally, the signal from counts and fits as well as ratios of Υ states from counts and from fits are corrected with the reconstruction efficiency for each of the states, which is described

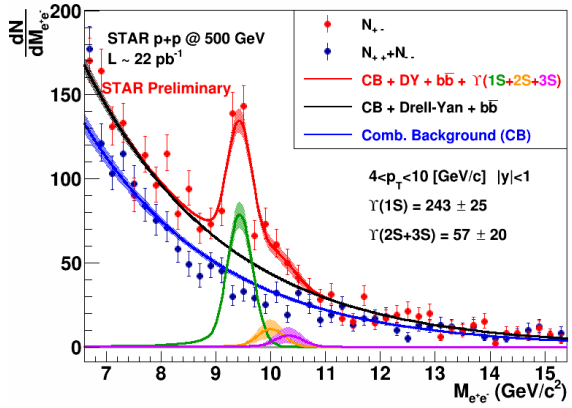

(a) $4 < p_T < 10$ GeV/c

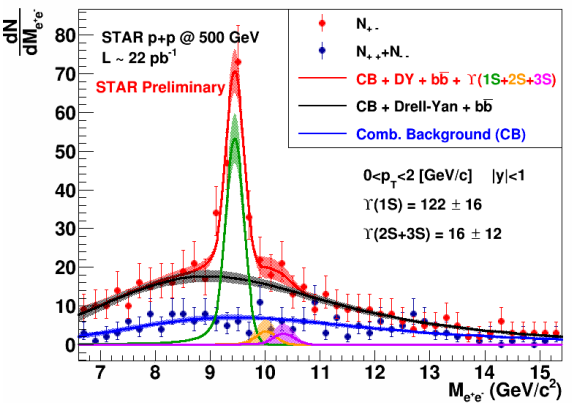

(b) $0 < p_T < 2$ GeV/c

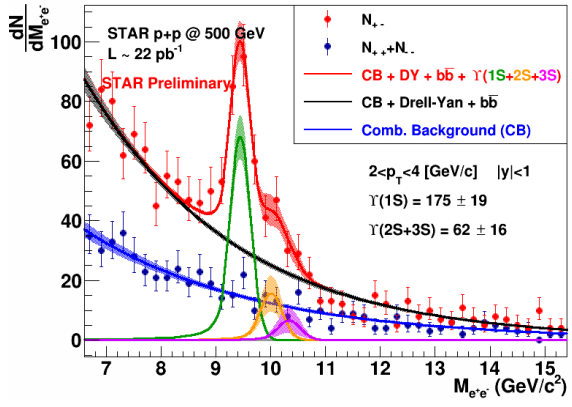

(c) $2 < p_T < 4$ GeV/c

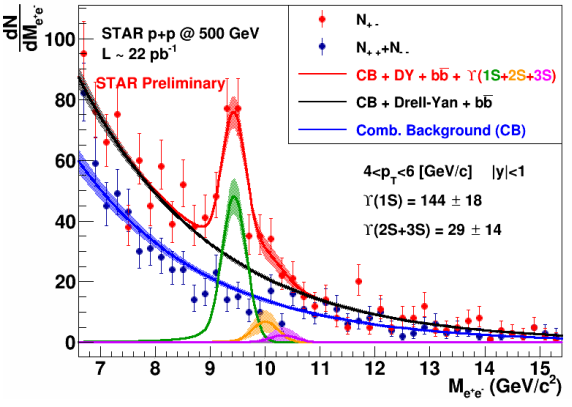

(d) $4 < p_T < 6$ GeV/c

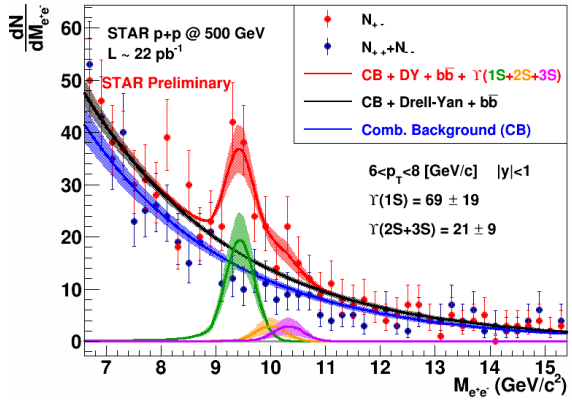

(e) $6 < p_T < 8$ GeV/c

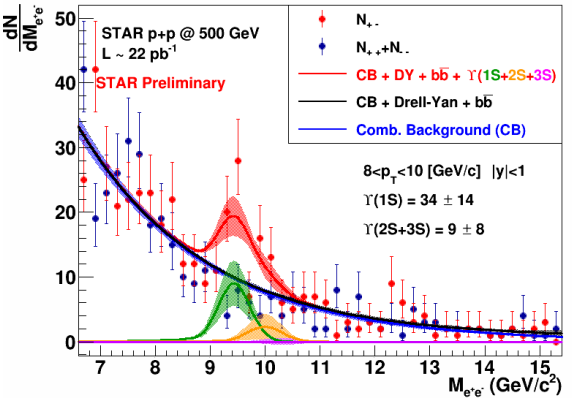

(f) $8 < p_T < 10$ GeV/c

Figure 5.6: Invariant mass distributions $|y| < 1, 0 \leq TofMult < 100$

in Section 5.6.4. Each of the above mentioned steps includes the full uncertainty propagation, taking into account correlations between fit parameters.

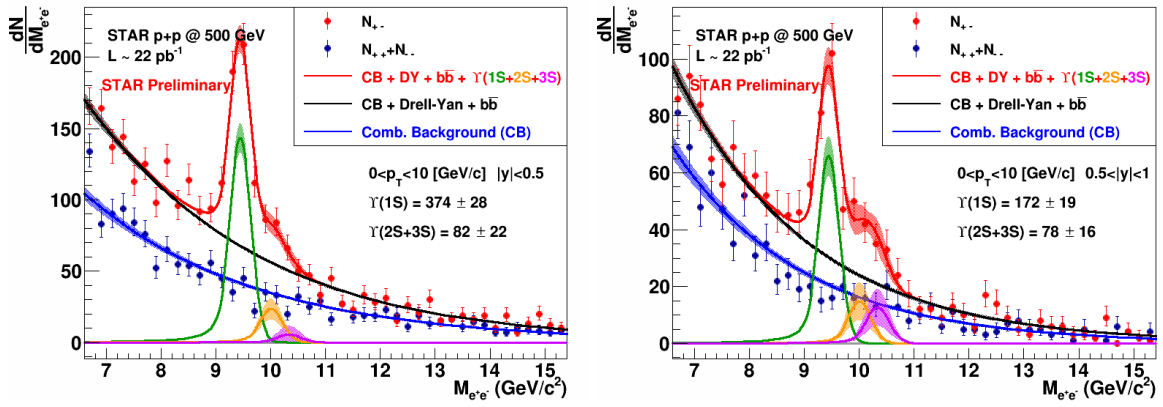

(a) $|y| < 0.5$ **(b)** $0.5 < |y| < 1.0$

Figure 5.7: Invariant mass of e^+e^- pairs for $0 < p_T < 10$ GeV/c, $0 \leq TofMult < 100$

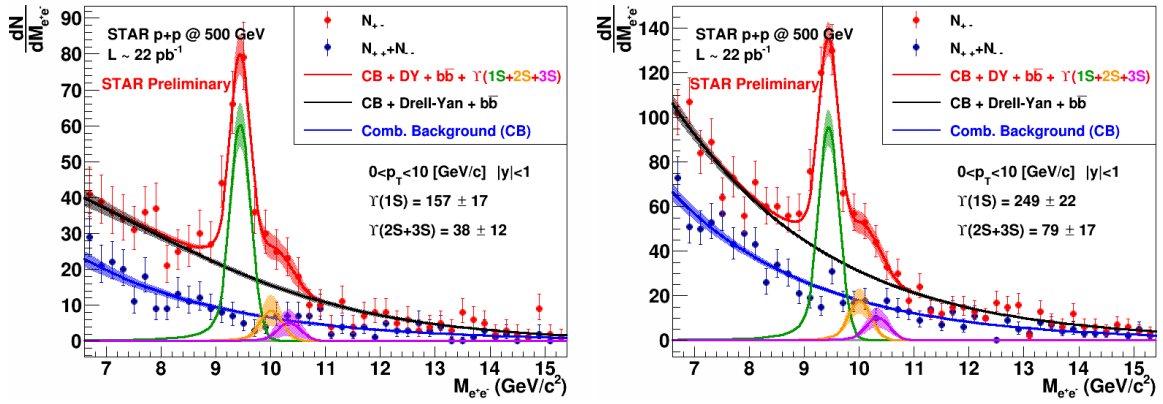

(a) $0 \leq TofMult < 4$ **(b)** $4 \leq TofMult < 8$

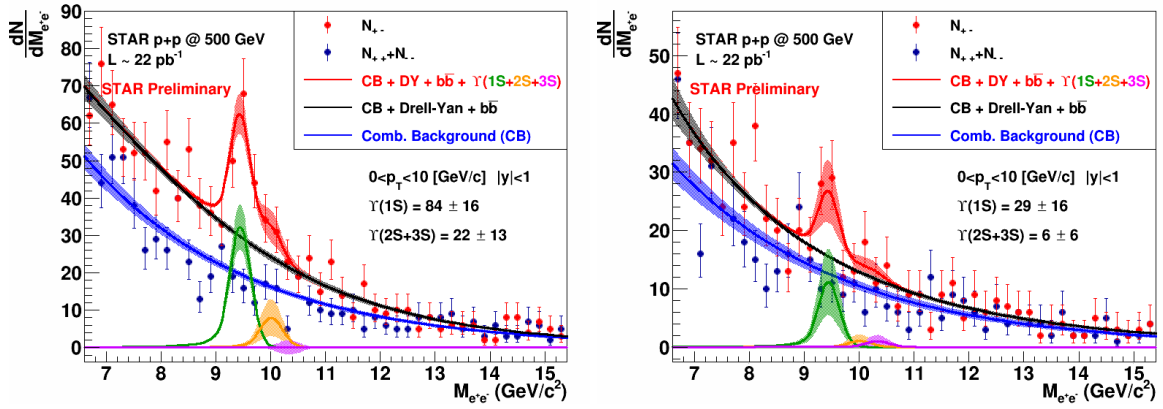

(c) $8 \leq TofMult < 12$ **(d)** $12 \leq TofMult < 100$

Figure 5.8: Invariant mass of e^+e^- pairs for different event TOF multiplicity ranges.

5.6 Efficiency corrections

The results measured by the detector are affected by various effects related to the detector efficiency, acceptance, and data taking conditions. These include effects of the track density,

pile-up, dead channels, etc. All these effects have to be corrected in order to obtain the real, unbiased results. The corrections are determined with the help of Monte Carlo (MC) simulations using embedding technique described in Section 4.3. This technique combines the data and MC simulations. The simulated $\Upsilon(nS) \rightarrow e^+e^-$ decays are embedded [161] in the real data and reconstructed together with the same detector calibrations settings as the real data. In this way, the characteristics of the data taking conditions are reflected in the simulations.

Typically in Monte Carlo studies the efficiencies are calculated as a ratio of MC tracks passing a particular cut to all MC tracks as a function of variable of interest eg. p_T. The uncertainties on the efficiency are calculated using a binomial distribution [162].

5.6.1 Electron identification efficiency

The electron identification efficiency is calculated using a data-driven method. Space charge accumulation in the TPC and $\frac{dE}{dx}$ calibrations affect the $n\sigma_e$ distribution and efficiency. In order to calculate the $n\sigma_e$ cut efficiency a high-purity electron sample has to be obtained. This is done by selecting electrons from $\gamma \rightarrow e^+e^-$ conversions or so called photonic electrons. Such electron pairs have typically low invariant mass of around $m_{ee} < 0.4\ \mathrm{GeV/c^2}$. These also include $\eta \rightarrow e^+e^-$ and $\pi^0 \rightarrow e^+e^-$ decays.

cut	value	purpose
Invariant mass	$m_{ee} < 0.04\ \mathrm{GeV/c^2}$	Select electrons from $\gamma \rightarrow e^+e^-$
Momentum	$p > 1\ \mathrm{GeV/c}$	Reject tracks not used in the analysis
Partner $n\sigma_e$	$\lvert n\sigma_e \rvert < 3$	Increase purity
Cluster to projection distance	$R_{SMD} < 0.028$	Select tracks matched to clusters
Tower energy fraction	$\frac{E_{TOW}}{E_{CLU}} > 0.5$	Select compact towers
Energy to momentum ratio	$0.55 < \frac{E_{CLU}}{p} < 1.45$	Select electrons

Table 5.7: Summary of the cuts used for $n\sigma_e$ cut efficiency studies with $\gamma \rightarrow e^+e^-$.

In the electron identification efficiency analysis, the e^+e^- pairs are selected with the cuts listed in the Table 5.7.

A $n\sigma_e$ electron distribution is made using both electrons from the selected pairs.

A Gaussian is fitted to $n\sigma_e$ distribution for photonic electrons in single electron p bins as

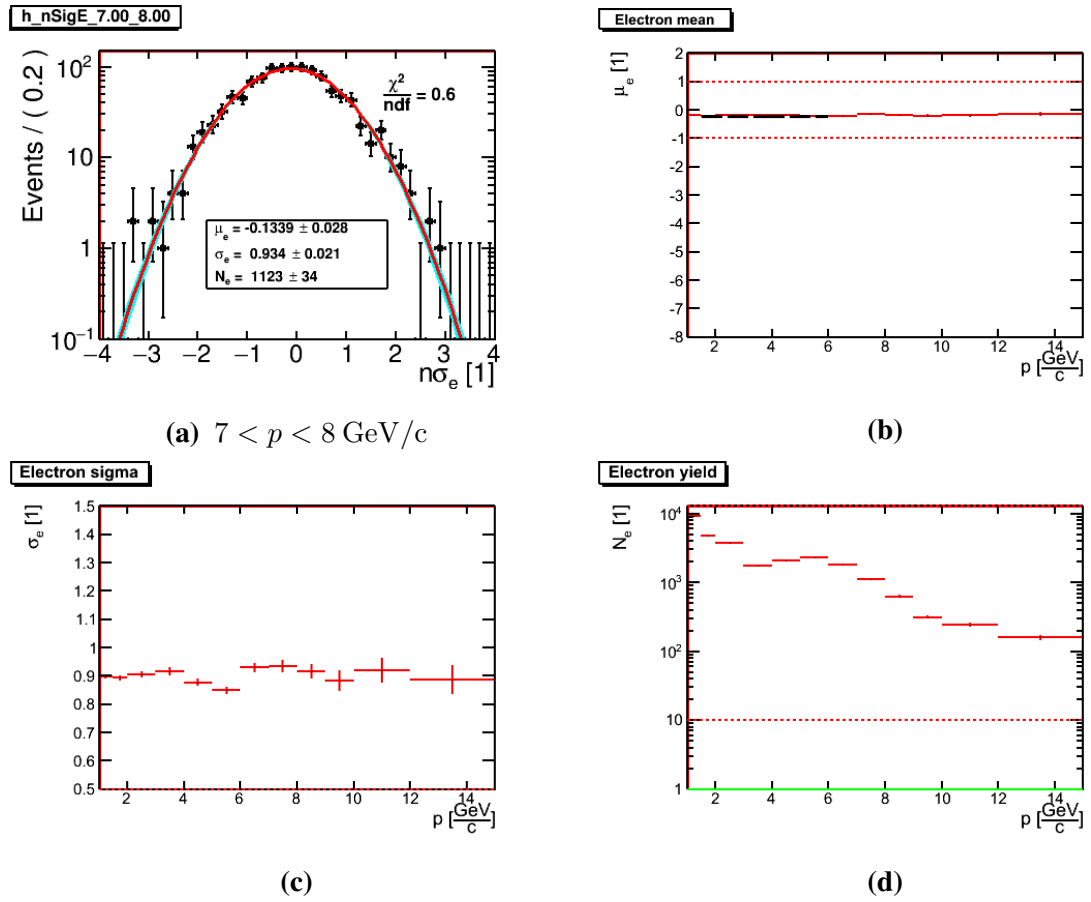

(a) $7 < p < 8$ GeV/c **(b)** **(c)** **(d)**

Figure 5.9: 5.9a: Example of a Gaussian fit (red) to $n\sigma_e$ distribution from photonic electrons (black) with $7 < p < 8$ GeV/c. 5.9b: Mean of a Gaussian from fits to $n\sigma_e$ for photonic electrons (red). Fit constraints (red dashed lines) and a fit to determine the starting parameters (black dashed line) are also shown. 5.9c: Width of a Gaussian from fits to $n\sigma_e$ for photonic electrons (red). 5.9d: Yield from Gaussian fits to $n\sigma_e$ for photonic electrons (red). Also shown are the fit constraints (red dashed lines).

shown in Figure 5.9a. Fits are done with the likelihood method using RooFit [155, 156]. The rest of the fits can be found in the Appendix B. The Figures 5.9b, 5.9c, 5.9d show mean μ_e, width σ_e and yield N_e respectively.

Finally, the efficiency is calculated with the Equation 5.4.

$$\epsilon = \frac{\int_{-1.2}^{3} f_{Gauss}(n\sigma_e) dn\sigma_e}{\int_{-\infty}^{+\infty} f_{Gauss}(n\sigma_e) dn\sigma_e} \tag{5.4}$$

The function f_{Gauss} above is the fitted Gaussian. The uncertainties are calculated using a binomial distribution [162]. A 3σ uncertainty on the fit is included as a systematic uncertainty on the Υ yield, which is described in Section 5.7.10. The resulting efficiency is used to calculate electron and Υ reconstruction efficiency.

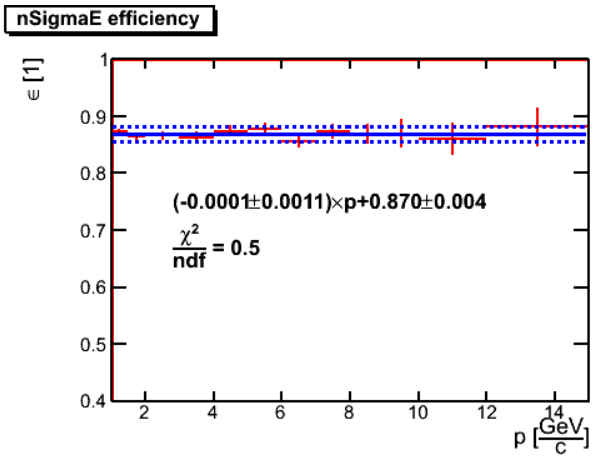

Figure 5.10: Efficiency of $n\sigma_e$ cut (red) calculated from fits to $n\sigma_e$ distributions from photonic electrons. A linear fit to the efficiency (blue solid line) and 3σ uncertainty (dashed blue line) are also presented.

5.6.2 Υ p_T and y spectra in simulation

In embedding, the simulated Υ have flat p_T and y distributions in order to ensure reasonable precision of efficiency calculation for the whole p_T and y range used in the analysis. These distributions are weighed to reflect the realistic spectra using the Equation 5.5.

$$w(p_T, y) = f_{Gauss}(y, \mu = 0, \sigma = 1.45) \cdot \frac{p_T}{e^{p_T/T_{nS}} + 1} \tag{5.5}$$

In the above equation, the $\sigma = 1.45 \pm 0.15$ is determined with PYTHIA8 simulation [163, 164]. The T_{nS} is the slope parameter determined from a fit to CDF data [80] for each of the $\Upsilon(nS)$ states separately. These fits are shown in Figure 5.11a. A logarithmic function $f_{log} = a\ln(\sqrt{s}) + b$ is fitted to the $\sqrt{s}$ dependence of T_{1S} from ISR [79], CDF [80] and CMS [165] as presented in Figure 5.11b. It is used to extrapolate the slope parameters to $\sqrt{s} = 500$ GeV.

The fit was used to extrapolate the obtained values of T_{nS} to $\sqrt{s} = 500$ GeV. This resulted in $T_{1S} = 1.53507$ GeV/c, $T_{2S} = 1.60485$ GeV/c and $T_{3S} = 1.67462$ GeV/c. The weights are applied during the electron and Υ reconstruction efficiencies calculation and lineshape determination.

5.6.3 Electron efficiencies

Single electron and positron reconstruction efficiencies are calculated by applying the same cuts used in the data to the reconstructed tracks in embedding. The Figure 5.12 shows each of the

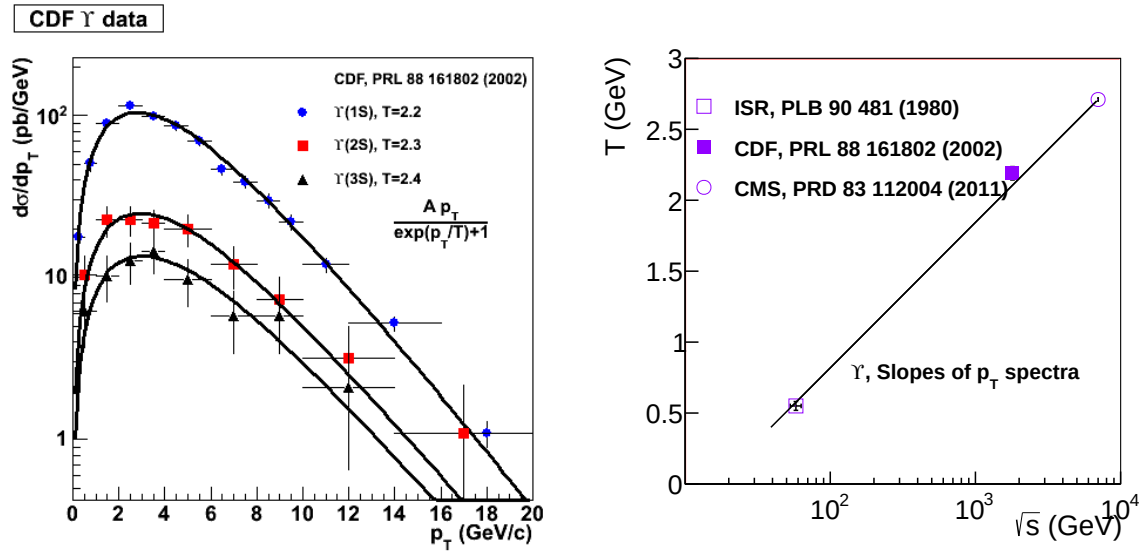

(a) **(b)**

Figure 5.11: 5.11a: The p_T spectrum measured by the CDF [80] for $\Upsilon(1S)$ (blue circles), $\Upsilon(2S)$ (red squares) and $\Upsilon(3S)$ (black triangles) [81]. The lines are exponential functions (black lines) fitted to each of the Υ states. 5.11a: The dependence of slope parameter T_{1S} on $\sqrt{s}$. Presented here are results from ISR [79], CDF [80] and CMS [165] fitted with a logarithmic function f_{log} [81].

efficiency components as successive cuts are applied in order to calculate the reconstruction efficiency (red). Both electron (left) and positron (right) efficiencies are shown. The uncertainties on the efficiency are also calculated using a binomial distribution [162]. An error function and a constant is fitted to the reconstruction efficiency (teal curve).

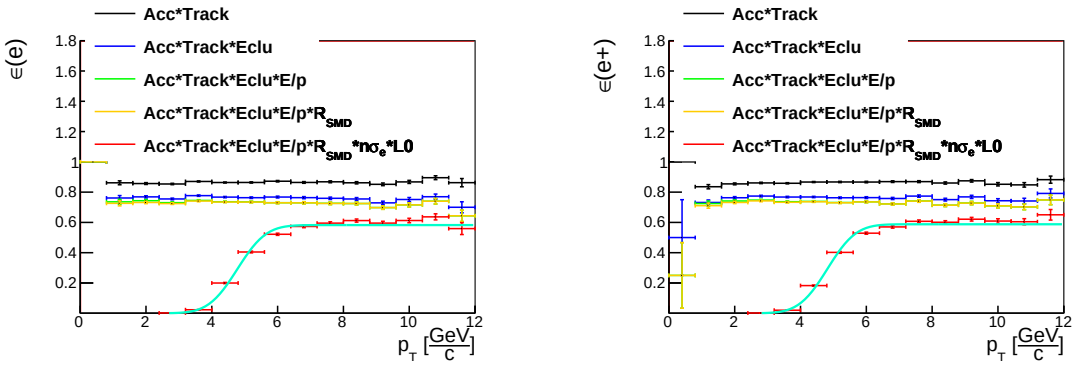

(a) Electrons **(b)** Positrons

Figure 5.12: Electron (left) and positron (right) efficiencies from embedding. It shows electron or positron p_T dependence of efficiency which includes the components: acceptance and tracking (black), $\frac{E_{TOW}}{E_{CLU}}$ cut (blue), $\frac{E_{CLU}}{p}$ cut (green), R_{SMD} cut (orange), $n\sigma_e$ cut and match to L0 tower (red). The total efficiency is fitted with the error function and a constant (teal curve).

5.6.4 Υ efficiencies

Similarly to the single electron efficiency, the Υ reconstruction efficiency is calculated by applying the same set of cuts to the e^+e^- from Υ decays. These efficiencies are calculated separately for $\Upsilon(1S)$, $\Upsilon(2S)$ and $\Upsilon(3S)$ states as shown in Figures 5.13, 5.14, 5.15 respectively. Again, the uncertainties are calculated with the binomial distribution [162].

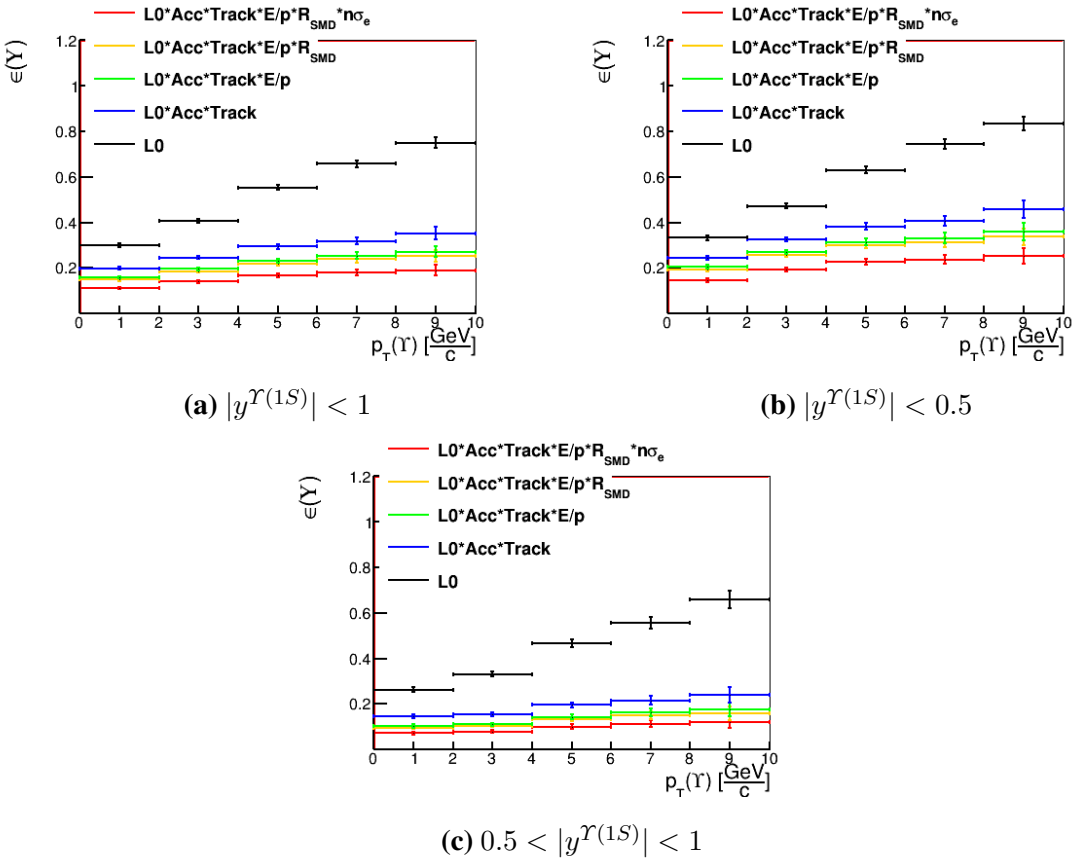

(a) $|y^{\Upsilon(1S)}| < 1$

(b) $|y^{\Upsilon(1S)}| < 0.5$

(c) $0.5 < |y^{\Upsilon(1S)}| < 1$

Figure 5.13: $\Upsilon(1S)$ efficiencies from embedding. Shown above are the p_T-dependent efficiencies which includes components: L0 cut (black), acceptance and tracking (blue), $\frac{E_{TOW}}{E_{CLU}}$ and $\frac{E_{CLU}}{p}$ cuts (green), R_{SMD} cut (orange), $n\sigma_e$ (red).

The p_T dependence and y dependence of the efficiency is investigated. As expected, the efficiency is larger for $|y| < 0.5$ than $0.5 < |y| < 1.0$ due to limited acceptance effects. That is, electrons from Υ decays in $0.5 < |y| < 1.0$ have large p_z, thus being more likely to fall out of acceptance of the TPC than those with $p_z \approx 0$ for Υ with $|y| < 0.5$. Also, the efficiency increases as the Υ p_T increases.

The above efficiencies are used to correct the reconstructed Υ signal.

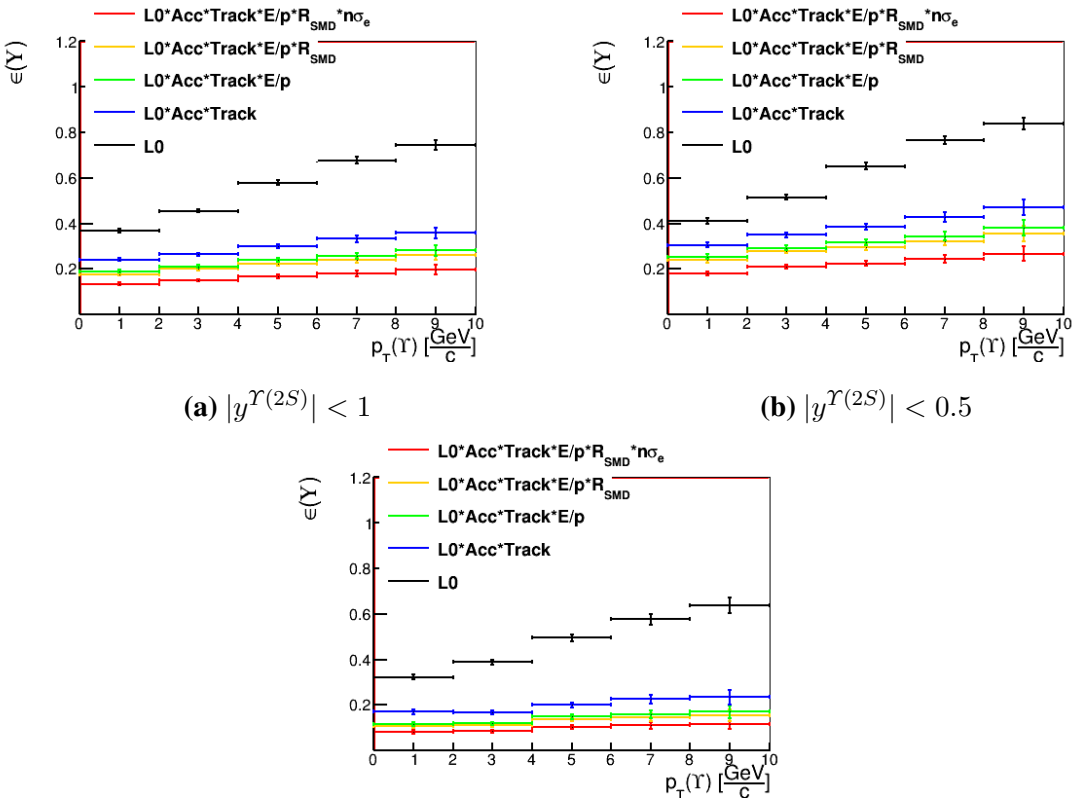

(a) $|y^{\Upsilon(2S)}| < 1$

(b) $|y^{\Upsilon(2S)}| < 0.5$

(c) $0.5 < |y^{\Upsilon(2S)}| < 1$

Figure 5.14: $\Upsilon(2S)$ efficiencies from embedding. Shown above are the p_T-dependent efficiencies which includes components: L0 cut (black), acceptance and tracking (blue), $\frac{E_{TOW}}{E_{CLU}}$ and $\frac{E_{CLU}}{p}$ cuts (green), R_{SMD} cut (orange), $n\sigma_e$ (red).

5.6.5 Addition smearing of electron p_T

The embeddings in STAR result in too narrow lineshapes of Υ and J/ψ compared to the observed signal in the data. This has to be corrected by adding a component to smear the electron momentum resolution. It is done by using a Gaussian smearing of electron p_T. A p_T^{random} is generated from a Gaussian, with a width set to $\frac{\sigma(p_T)}{p_T} = a \cdot p_T$. This is then added to the reconstructed momentum $\vec{p}^{REC}$ to the $\vec{p}^{smear}$ using Equation 5.6.

$$\left\{ \begin{array}{l} p_x^{smear} = p_x^{REC} + p_T^{random} \cdot p_T^{MC} \cdot \cos(\phi^{MC}) \\ p_y^{smear} = p_y^{REC} + p_T^{random} \cdot p_T^{MC} \cdot \sin(\phi^{MC}) \\ p_z^{smear} = p_z^{REC} + p_T^{random} \cdot p_T^{MC} \cdot \sinh(\eta^{MC}) \end{array} \right\} \tag{5.6}$$

Where p_T^{MC} is the p_T of the Monte Carlo track and η^{MC}, ϕ^{MC} are η and ϕ of the Monte Carlo track. The a parameter is determined by performing a χ^2 scan in search for the best fit between smeared J/ψ lineshape from embedding and data [166, 167]. J/ψ is used over Υ

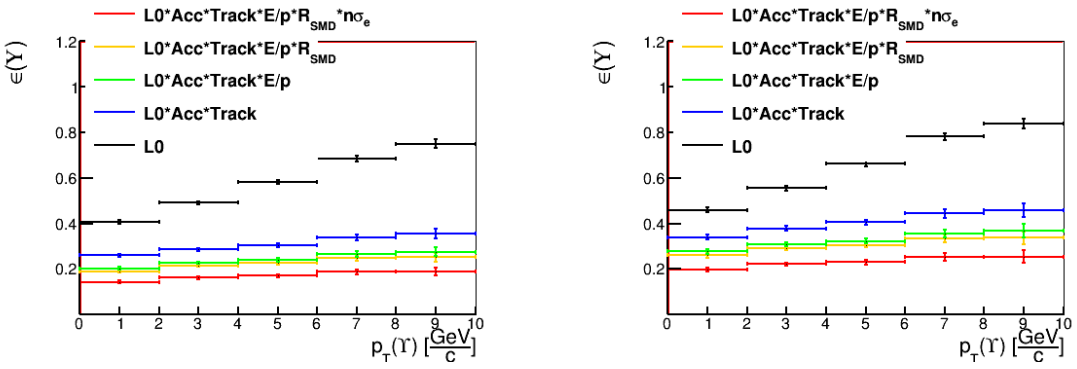

(a) $|y^{\Upsilon(3S)}| < 1$ **(b)** $|y^{\Upsilon(3S)}| < 0.5$

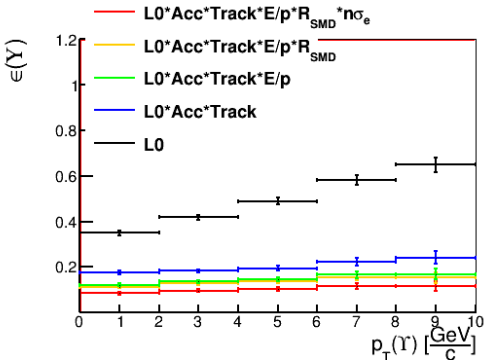

(c) $0.5 < |y^{\Upsilon(3S)}| < 1$

Figure 5.15: $\Upsilon(3S)$ efficiencies from embedding. Shown above are the p_T-dependent efficiencies which includes components: L0 cut (black), acceptance and tracking (blue), $\frac{E_{TOW}}{E_{CLU}}$ and $\frac{E_{CLU}}{p}$ cuts (green), R_{SMD} cut (orange), $n\sigma_e$ (red).

because of larger yields in the data, which can be used to constrain the smearing parameter.. Figure 5.16a shows the comparison of J/ψ widths obtained from Crystal Ball fits to embedding and data. Figure 5.16b presents the dependence of χ^2 on a parameter. The best fit is found to be $a = 0.293^{+0.040}_{-0.045}\%$. The uncertainties on a are included in systematic uncertainty as described in Section 5.7.4.

5.6.6 Υ lineshapes

Lineshapes from embedding are used to help the fitting of the invariant mass distributions in the data. These are modeled by Crystal Ball functions [157, 158]. In order to fix the parameters of Crystal Ball functions for each of the Υ states, the m_{ee} distributions from embedding are fitted separately. Additional smearing of the electron p_T is included in the m_{ee} distributions. The fits are done using likelihood method with RooFit and can be found in the Appendix C. An example fit is shown in Figure 5.17. The lineshape is well described by the Crystal Ball.

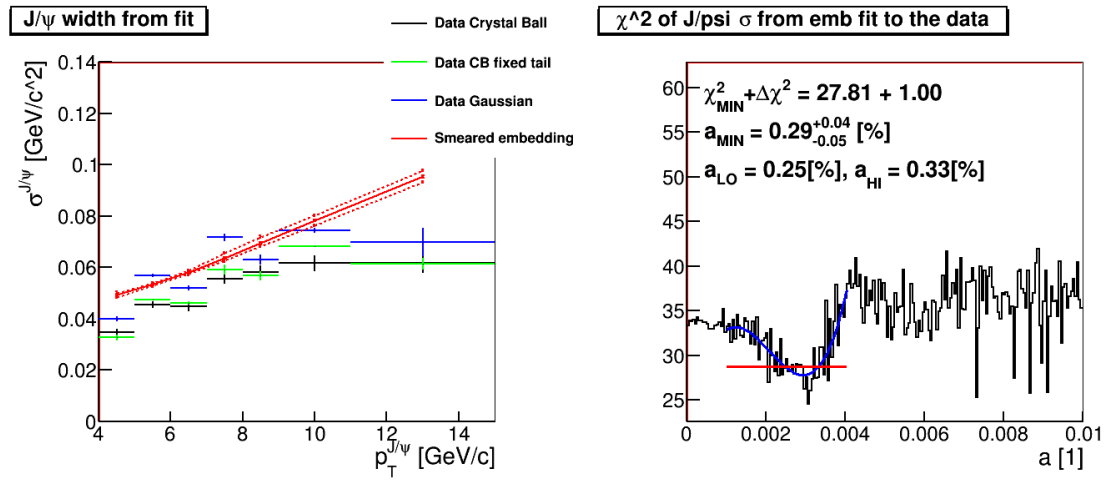

(a) **(b)**

Figure 5.16: Left: Comparison of J/ψ width ($\sigma^{J/\psi}$) from data [166, 167] and embedding. Shown here, are the results of fits to the J/ψ distributions in the data using: Crystal Ball function (black), Crystal Ball with fixed tail parameters (green), Gaussian (blue). This is compared to a Crystal Ball fit to distributions from embedding with additional smearing (red). Right: χ^2 values of fit of the p_T dependence of J/ψ width from smeared embedding and data.

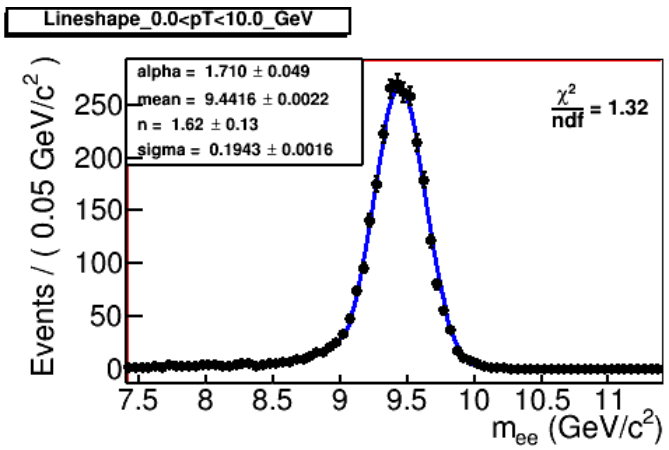

Figure 5.17: Invariant mass distribution for $\Upsilon(1S) \rightarrow e^+e^-$ from smeared embedding (black) fitted with a Crystal Ball function (blue line).

In addition, the fitted functions are used to calculate the invariant mass cut efficiency, which is shown in Figure 5.18. Correlations between fit parameters are included in the uncertainty calculation for the efficiency. The signal calculated by integrating counts in a given range is then corrected for m_{ee} cut efficiency.

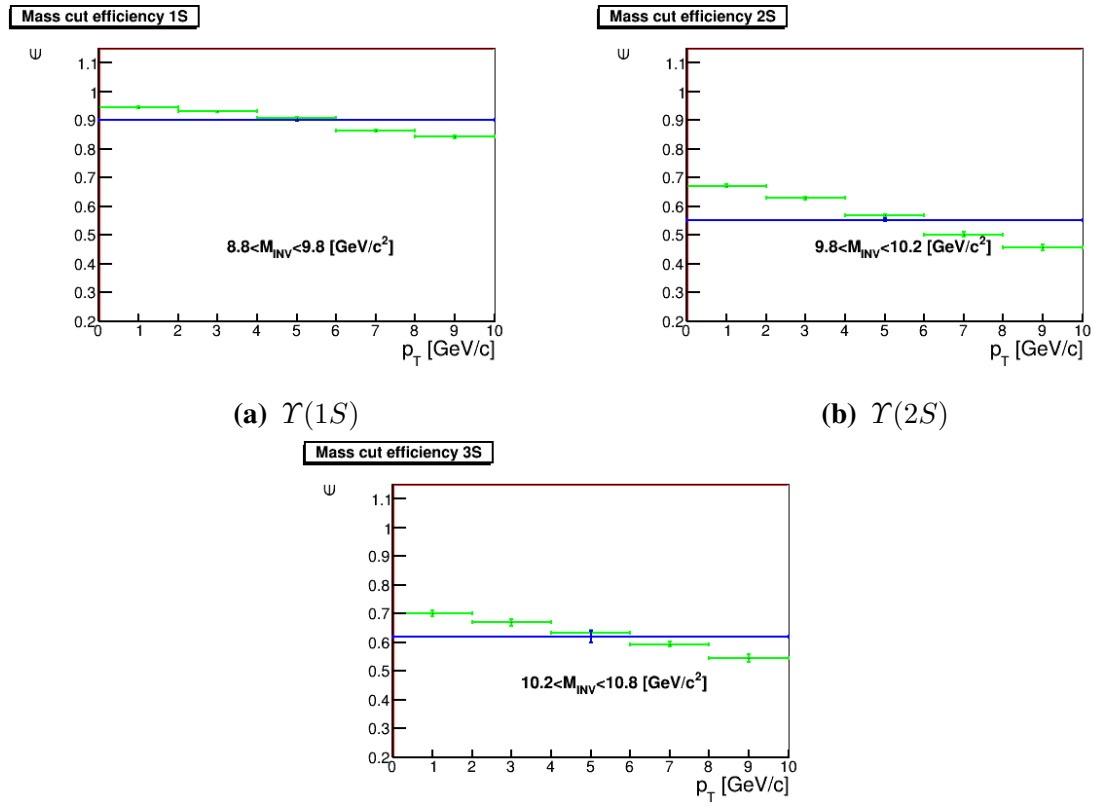

(a) $\Upsilon(1S)$ **(b)** $\Upsilon(2S)$

(c) $\Upsilon(3S)$

Figure 5.18: Mass cut efficiencies for $\Upsilon(1S)$ (5.18a), $\Upsilon(2S)$ (5.18b) and $\Upsilon(3S)$ (5.18c). The p_T dependent (green) and p_T-integrated (blue) efficiency is shown.

5.6.7 Finite bin width correction

To properly present the corrected yield in wide p_T bins, a finite bin width correction has to be applied [168]. This is done by fitting a function (blue), which describes the data, as can be seen in Figure 5.19 to the corrected yield (black). In this case it is a power law function: $f(p_T) = \frac{A \cdot p_T}{e^{p_T/T}+1}$ (blue). The corrected points (red) are placed in p_T^{corr}, which is calculated with Equation 5.7. This is done separately for $\Upsilon(1S+2S+3S)$, $\Upsilon(1S)$ and $\Upsilon(2S+3S)$ yields.

$$f(p_T^{corr}) = \frac{1}{\Delta p_T} \int_{p_T^{lo}}^{p_T^{hi}} f(p_T) dp_T \tag{5.7}$$

5.6.8 Multiplicity efficiency correction

In order to reconstruct the true multiplicity dependence of the Υ production for event activity studies, a reconstruction efficiency and trigger efficiency correction is needed. The reconstruction efficiency correction is done using the Unfolding method with the RooUnfold [169, 170]

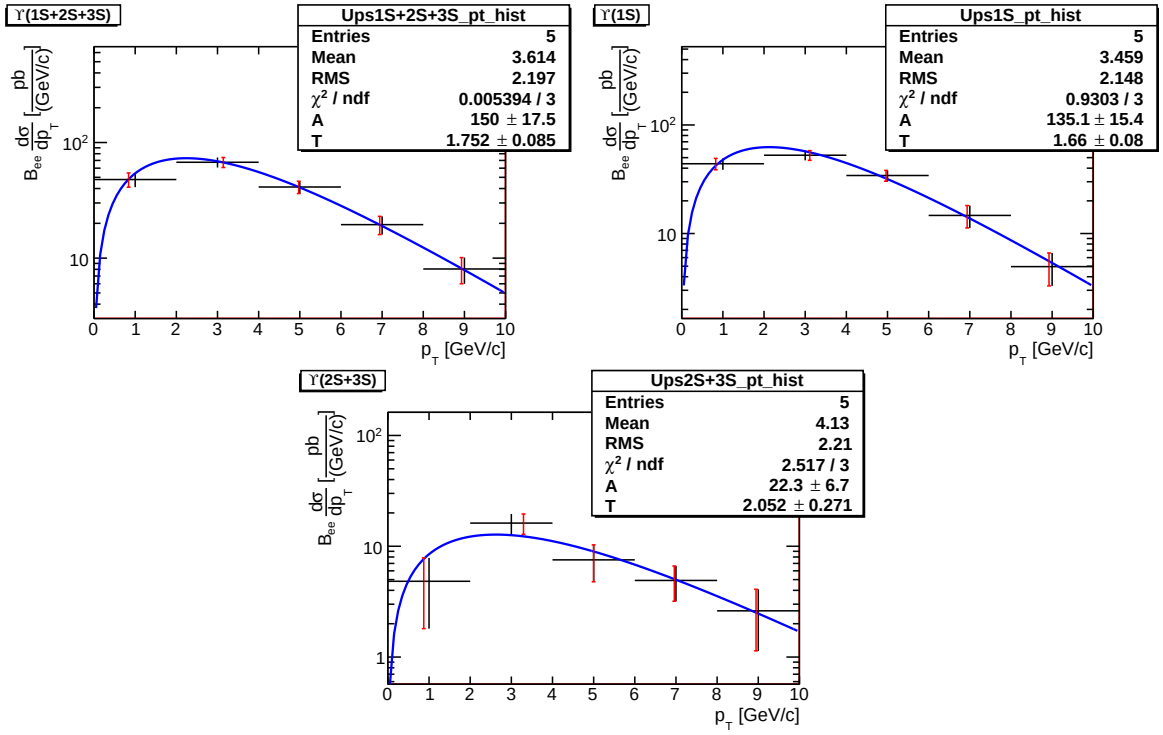

Figure 5.19: Υ corrected yield vs. p_T (black) fitted with at power law function (blue). The points are shifted in p_T to corrected positions (red) based on the fits.

package. It is a method for reconstructing a true distribution T_i of a variable of interest out of a measured distribution M_j using a response matrix R as in Equation 5.8.

$$M_i = R_{ij} T_j \tag{5.8}$$

The response matrix is determined using Monte Carlo simulation and can include the effects of efficiency, bias and resolution. Uncertainties in the measured distribution are taken into account during the unfolding. This is done by using the RooUnfoldBayes algorithm [171], which applies Bayes's Theorem in successive iterations to obtain the true distribution. Here, 4 iterations are used and the dependence of results on number of iterations is studied as part of systematic uncertainty.

In this case, the response matrix maps the measured $TofMult$ distribution into the true N_{ch} distribution. Such a correction is done both for Υ distribution and event $TofMult$ distribution. Because of the high luminosity in the Run11 data, the Run09 Min-Bias data is used instead for the event $TofMult$ distribution in order to minimize the pile-up effect and get the least biased distribution. Low-luminosity data allowed for a $TofMult$ definition with a wider $DCA < 1\text{cm}$ cut compared to Run11 (see Table 5.4). This allows for a more stable event activity measure.

In Run11 a more strict cut was applied to reduce the effect of pile-up.

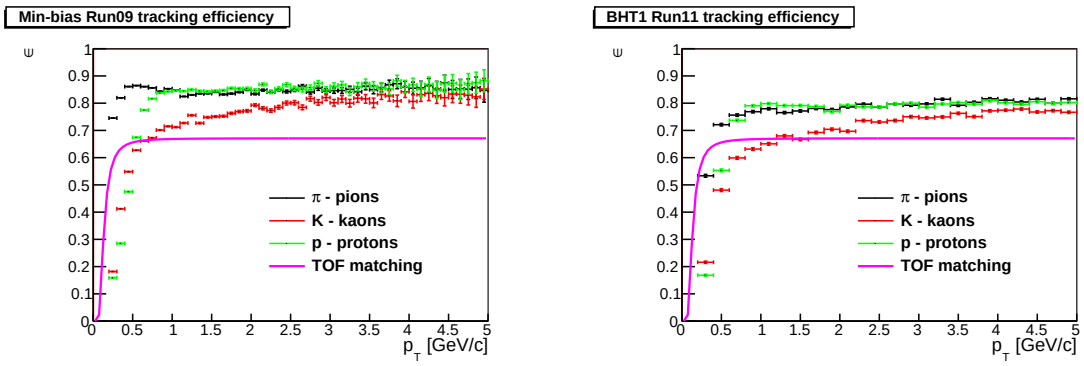

(a) **(b)**

Figure 5.20: Figure 5.20a: Tracking efficiency for pions (black), kaons (red) and protons (green) from Run09 embedding. The purple line is the TOF matching efficiency [167]. Figure 5.20b: Tracking efficiency for pions (black), kaons (red) and protons (green) from Run11 embedding. The purple line is the TOF matching efficiency [167].

The response matrices are determined by using 2 separate PYTHIA8 simulations for Min-Bias Run09 and BHT1 Run11 parts. The latter uses the STAR Heavy Flavor Tune [172] and is set to generate Υ events. Each of the simulations uses pion, kaon and proton tracking efficiencies calculated from embedding as well as TOF matching efficiency [167]. These efficiencies are shown in Figure 5.20. Also, a pile-up correction is applied using efficiency weights vs. number of global tracks [167]. The resulting response matrices are shown in Figure 5.21. For measured Υ distribution, the binning is set to $0-4, 4-8, 8-12, 12-30$, while the unfolded distribution is presented in $0-7, 7-14, 14-21, 21-56, 56-100$. The last bin is discarded, because of very low content. The bins are chosen to be an integer multiple of mean multiplicity in unfolded Min-Bias distribution $\langle N_{ch} \rangle = 7.67$.

The unfolded distributions are corrected with the BBC trigger and vertex reconstruction efficiency, shown in Figure 5.22. These are obtained from PYTHIA8 simulation of the STAR detector response with full reconstruction. For Run11 data, the simulation used STAR Heavy Flavor Tune of Υ production embedded into zero-bias events. The zero-bias events are obtained by registering collisions at a fixed rate, synchronized with a bunch crossing, instead of relying on a trigger. This is in order to avoid any possible trigger bias. However, in case of Run09, there was not enough zero-bias events for embedding, so a pure simulation and reconstruction was done.

The unfolded distributions after BBC trigger and vertex reconstruction efficiency correc-

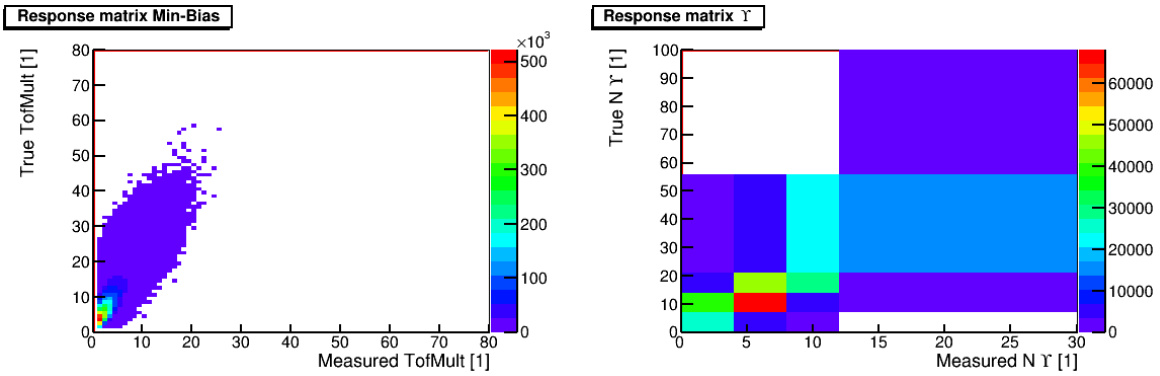

(a) **(b)**

Figure 5.21: Figure 5.21a: Response matrix for Min-Bias events. Figure 5.21b: Response matrix for Υ events.

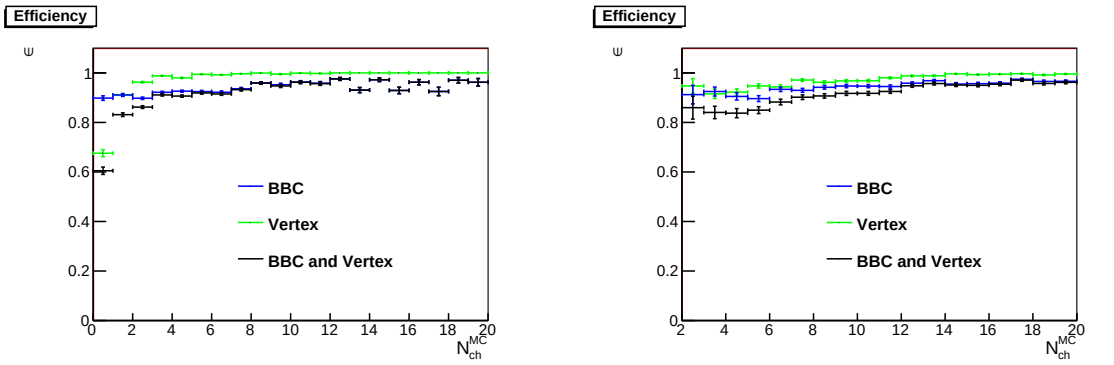

(a) Min-Bias Run09 **(b)** BHT1 Run11 Zero-Bias embedding

Figure 5.22: Figure 5.22a: BBC trigger (blue), vertex (green) reconstruction efficiency and total (black) as a function of number of MC tracks N_{ch}^{MC} from Min-Bias Run09 simulation. Figure 5.22b: BBC trigger (blue), vertex (green) reconstruction efficiency and total (black) as a function of number of MC tracks N_{ch}^{MC} from BHT1 Run11 Zero-Bias embedding.

tions are presented in Figure 5.23.

5.7 Systematic uncertainties

The systematic uncertainties on the Υ cross section measurement are estimated by comparing the central value of the cross section and the one obtained by varying parameters, efficiencies, using different methods, etc. Also, each contribution is symmetrized by assuming maximum deviation [173]. The effects quoted in the description below are on the integrated cross section.

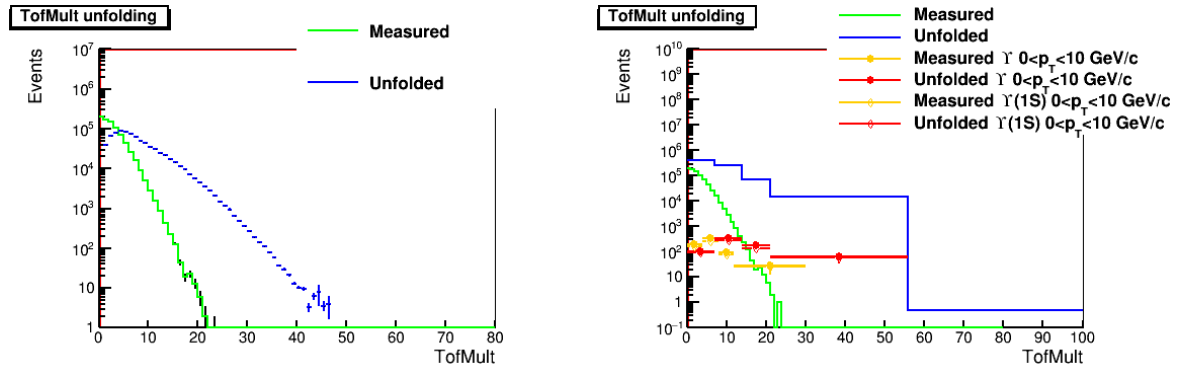

(a) **(b)**

Figure 5.23: Figure 5.23a: Comparison of measured (green) and unfolded (blue) Min-Bias multiplicity distributions. The unfolded distribution also includes BBC and vertex efficiency correction. Figure 5.23b: Comparison of measured (orange) and unfolded (red) Υ (closed diamonds) and $\Upsilon(1S)$ (open diamonds) distributions. The unfolded distributions are corrected for BBC and vertex efficiency. Also shown, are the same Min-Bias distributions from Figure 5.23a, rebinned to match unfolded Υ bins.

5.7.1 Signal extraction from fit

In order to estimate the systematic uncertainty related to the signal extraction method the signal calculated from histogram counts is compared to the value obtained from the fit. The comparison is done, because the signal from counts may be affected by fluctuations in the data, while the lineshapes are affected by imperfections in the simulations. This affects the signal by $\pm 0.1\%$.

5.7.2 Fixing B parameter of correlated background

The B parameter of the correlated background function $f_{b\bar{b}+DY}$ in the fit to invariant mass distribution is fixed to $B = 30$. To estimate the effect of this, the parameter is varied by $B = 30 \pm 15$, resulting in $\pm 1.7\%$ change of the cross section.

5.7.3 Fixing $\frac{\Upsilon(2S)}{\Upsilon(3S)}$ ratio

The ratio $\frac{\Upsilon(2S)}{\Upsilon(3S)}$ is set free in the signal fit. This is sensitive to fluctuations in the data. To check the possible effect of fluctuations, the ratio is fixed to $\frac{\Upsilon(2S)}{\Upsilon(3S)} = 0.679$ [82]. The Υ yield is changed by $\pm 0.02\%$.

5.7.4 Additional smearing uncertainty

The uncertainty connected to the additional smearing of p_T in simulation is estimated by taking the upper limits on the smearing parameter $a = 0.293^{+0.040}_{-0.045}\%$. It changes the cross section by $\pm 0.4\%$.

5.7.5 Tracking efficiency uncertainty

Track reconstruction is affected by the number of clusters in the TPC, which later end up as TPC points. Possible differences in the STAR geometry description in the simulation and reality may introduce systematic effects on the track reconstruction. Also, there may be imperfections in the TPC response simulator, which affect the number of points. These effects are studied by varying a cut $nFitPts \pm 2$ in the simulation, resulting in $\pm 1.3\%$ effect on the Υ cross section.

5.7.6 Υ spin aligment

The Υ spin alignment (also called polarization) affects the decay kinematics and may influence the Υ reconstruction efficiency. If the spin of the Υ is preferentially aligned in some direction with respect to it's momentum, the angular distribution of e^+e^- from Υ will reflect it.

$$w(\theta) = 1 + \lambda cos^2(\theta) \tag{5.9}$$

This is described by Equation 5.9, where w is the weight and θ is the angle between momentum vector of e^+ and momentum vector of Υ. The $cos(\theta)$ distribution in embedding is assumed flat, which is consistent with CDF data [174]. In order to check the effect of this assumption, the λ parameter in Equation 5.9 is varied with the 1σ uncertainty of the CDF data. The value is varied $\lambda = 0 \pm 0.1$ This results in $\pm 0.3\%$ change in the Υ cross section.

5.7.7 Trigger efficiency

The BHT1 trigger efficiency systematic uncertainty is estimated by comparing ADC distributions between embedding and data. A 3% [151] shift is observed, which affects the efficiency by $\pm 8.7\%$. This is the largest source of the systematic uncertainty in this study.

5.7.8 Uncertainty on integrated luminosity

The luminosity is estimated using the BBC. The uncertainty on BBC efficiency affects the integrated luminosity. It is $\pm 8\%$ [175–177] and is included as a global (correlated) uncertainty.

5.7.9 Vertex reconstruction efficiency

Uncertainty on vertex reconstruction efficiency is obtained from a study in Reference [151]. It is found to be $\pm 1\%$ and is categorized as global.

5.7.10 $n\sigma_e$ efficiency uncertainty

The uncertainty connected to $n\sigma_e$ efficiency calculation is estimated by taking the upper and lower limits of 3σ confidence interval of the linear fit to the efficiency obtained from photonic electrons. This is shown in Figure 5.10. The effect is found to be $\pm 3.6\%$ and is treated as a global uncertainty.

5.7.11 Acceptance uncertainty

The acceptance uncertainty is estimated by masking BEMC towers in the simulation. This was taken from the Reference [151]. The effect is $\pm 3\%$ and is treated as global.

5.7.12 Number of iterations for unfolding

The dependence on number of iterations during Bayesian unfolding for multiplicity dependent studies is checked with $3, 6$ and 8 iterations. The effect is on the normalized yield ranges from $0.6 - 1.7\%$ and $0.1 - 0.3\%$ on the normalized multiplicity.

5.7.13 Reconstruction efficiency vs. multiplicity

The Υ reconstruction efficiency from embedding is consistent with being constant in multiplicity. A linear fit is done as shown in Figure 5.24 and the difference between upper limit of 1σ confidence interval from the fit and mean efficiency is propagated through the unfolding procedure. It changes the normalized yield by 0.5% to 2.3%.

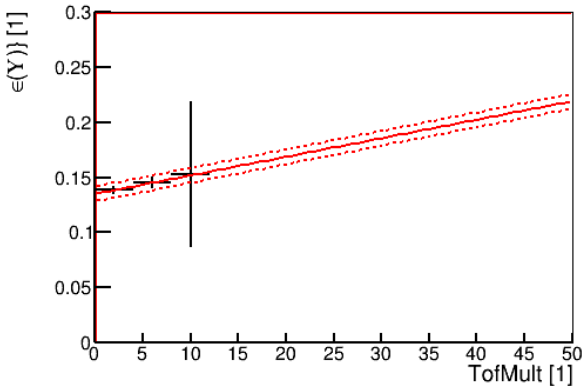

Figure 5.24: $\Upsilon(1S)$ efficiency vs. $TofMult$ (black) fitted with a linear function (red line). A $\pm 1\sigma$ confidence interval is also plotted (red dashed line).

5.7.14 Tracking efficiency in unfolding

The charged particle tracking efficiency in unfolding was varied by $\pm 5\%$ to check the impact on the normalized yield and normalized multiplicity. The effect on the first one is $0.3 - 11.2\%$, while it changes the second by $3.3 - 3.7\%$.

5.7.15 Multiplicity distribution

Possible influence of changes in the multiplicity distribution is investigated, by fitting a negative binomial distribution (NBD). The 1σ upper and lower uncertainty limit is then taken as a true multiplicity distribution, replacing the one obtained from unfolding. This affects the normalized Υ yield by 0.9% to 14.4%, while changing the normalized multiplicity by $2.6 - 4.2\%$.

5.7.16 Dependence on particle production model in PYTHIA8

The model used for multiple parton interactions (MPI) in PYTHIA8 simulation may affect the true N_{ch} distribution and response matrices used for unfolding correction. This is checked by changing the PYTHIA8 settings to 4Cx tune. The impact of this is 0.3% to 1.8% on the normalized Υ yield and $0.3 - 1.8\%$ on the normalized multiplicity.

5.7.17 Summary of systematic uncertainties

All the uncorrelated systematic uncertainties on the $\Upsilon(1S+2S+3S)$ cross section as a function of p_T are presented in Table 5.8. The Table 5.9 contains all the uncorrelated systematic uncer-

tainties for $\Upsilon(1S+2S+3S)$ cross section vs. rapidity. The correlated systematic uncertainties (global) are treated as a separate class and are shown in Table 5.10. Finally, the uncertainties on both the normalized yield of $\frac{N_{\Upsilon(1S+2S+3S)}}{\left\langle N_{\Upsilon(1S+2S+3S)}\right\rangle}$ are presented in Table 5.11 and $\frac{\langle N_{ch}\rangle^{bin}}{\langle N_{ch}\rangle^{all}}$ in Table 5.12.

p_T [GeV/c]						
Uncertainty	$0-10$	$0-2$	$2-4$	$4-6$	$6-8$	$8-10$
Fit	$\pm0.1\%$	$\pm1.2\%$	$\pm1.7\%$	$\pm1.4\%$	$\pm3.3\%$	$\pm15\%$
Fixed $B=15,45$	$\pm1.7\%$	$\pm0.6\%$	$\pm1.3\%$	$\pm1.4\%$	$\pm0.8\%$	$\pm0.2\%$
Fixed $\frac{\Upsilon(2S)}{\Upsilon(3S)}$	$\pm0.02\%$	$\pm0.2\%$	$<0.1\%$	$\pm0.1\%$	$\pm0.8\%$	$\pm0.7\%$
p_T smearing	$\pm0.4\%$	$\pm1.0\%$	$\pm0.6\%$	$\pm0.3\%$	$\pm0.2\%$	$\pm0.3\%$
Tracking	$\pm1.3\%$	$\pm1.4\%$	$\pm1.3\%$	$\pm1.3\%$	$\pm1.4\%$	$\pm1.3\%$
Polarization	$\pm0.3\%$	$\pm1.5\%$	$\pm0.2\%$	$\pm0.4\%$	$\pm0.5\%$	$\pm0.5\%$
Trigger	$\pm8.7\%$	$\pm8.7\%$	$\pm8.7\%$	$\pm8.7\%$	$\pm8.7\%$	$\pm8.7\%$
Total	$\pm13\%$	$\pm9.1\%$	$\pm9.1\%$	$\pm9.0\%$	$\pm9.5\%$	$\pm17\%$

Table 5.8: Summary of systematic uncertainties on the $\Upsilon(1S+2S+3S)$ cross section vs. p_T.

Uncertainty	$\lvert y\rvert<0.5$	$0.5<\lvert y\rvert<1.0$
Fit	$\pm1.5\%$	$\pm3.1\%$
Fixed $B=15,45$	$\pm1.4\%$	$\pm1.1\%$
Fixed $\frac{\Upsilon(2S)}{\Upsilon(3S)}$	$\pm0.2\%$	$\pm0.2\%$
p_T smearing	$\pm0.4\%$	$\pm0.4\%$
Tracking	$\pm1.3\%$	$\pm1.3\%$
Polarization	$\pm0.1\%$	$\pm1.2\%$
Trigger	$\pm8.7\%$	$\pm8.7\%$
Total	$\pm9.1\%$	$\pm9.5\%$

Table 5.9: Summary of systematic uncertainties on the $\Upsilon(1S+2S+3S)$ cross section vs. rapidity.

Uncertainty	Effect
Luminosity	$\pm 8\%$
Vertex	$\pm 1\%$
Acceptance	$\pm 3\%$
$n\sigma_e$ cut	$\pm 3.6\%$

Table 5.10: Summary of global (correlated) systematic uncertainties on the $\Upsilon(1S + 2S + 3S)$ cross section.

Uncertainty	$0 - \langle N_{ch} \rangle$	$\langle N_{ch} \rangle - 2\langle N_{ch} \rangle$	$2\langle N_{ch} \rangle - 3\langle N_{ch} \rangle$	$3\langle N_{ch} \rangle - 8\langle N_{ch} \rangle$
Number of iterations	$\pm 1.7\%$	$\pm 0.6\%$	$\pm 1.5\%$	$\pm 1\%$
Reconstruction efficiency	$\pm 0.5\%$	$\pm 1.4\%$	$\pm 2.3\%$	$\pm 1.9\%$
Tracking	$\pm 12\%$	$\pm 9\%$	$\pm 0.3\%$	$\pm 2.6\%$
N_{ch} from NBD	$\pm 0.9\%$	$\pm 3.9\%$	$\pm 8.4\%$	$\pm 14.4\%$
Fit	$\pm 0.2\%$	$\pm 3.6\%$	$\pm 0.2\%$	$\pm 19\%$
p_T smearing	$\pm 0.6\%$	$\pm 1.9\%$	$\pm 2.1\%$	$\pm 5.4\%$
Fixed $\frac{\Upsilon(2S)}{\Upsilon(3S)}$	$\pm 0.2\%$	$\pm 0.3\%$	$\pm 0.7\%$	$\pm 0.2\%$
Fixed $B = 15, 45$	$\pm 23\%$	$\pm 0.4\%$	$\pm 11\%$	$\pm 11\%$
4Cx tune	$\pm 2.9\%$	$\pm 0.5\%$	$\pm 1.1\%$	$\pm 13\%$
Total	$\pm 26\%$	$\pm 11\%$	$\pm 14\%$	$\pm 30\%$

Table 5.11: Summary of systematic uncertainties on the $\frac{N_{\Upsilon(1S+2S+3S)}}{\langle N_{\Upsilon(1S+2S+3S)} \rangle}$.

Uncertainty	$0 - \langle N_{ch} \rangle$	$\langle N_{ch} \rangle - 2\langle N_{ch} \rangle$	$2\langle N_{ch} \rangle - 3\langle N_{ch} \rangle$	$3\langle N_{ch} \rangle - 8\langle N_{ch} \rangle$
Iterations	$\pm 0.1\%$	$\pm 0.2\%$	$\pm 0.3\%$	$\pm 0.2\%$
Tracking	$\pm 3.3\%$	$\pm 3.5\%$	$\pm 3.7\%$	$\pm 3.3\%$
N_{ch} from NBD	$\pm 4.2\%$	$\pm 2.9\%$	$\pm 2.6\%$	$\pm 3.6\%$
4Cx tune	$\pm 1.8\%$	$\pm 0.4\%$	$\pm 0.5\%$	$\pm 0.3\%$
Total	$\pm 5.6\%$	$\pm 4.6\%$	$\pm 4.6\%$	$\pm 4.9\%$

Table 5.12: Summary of systematic uncertainties on the normalized multiplicity.

Chapter 6

Data analysis for J/ψ production studies

The J/ψ analysis is done in a very similar way to the Υ studies. Results of this analysis were published in Physical Review C [178].

6.1 Data set

The data set used for J/ψ analysis amounts to $312\,\mathrm{M}$ $p+p$ Min-Bias events recorded by STAR during 2009 (Run09) at $\sqrt{s} = 200$ GeV. These events had been registered with the use of VPD-MB trigger, which required a coincidence hits in both east and west VPD.

6.2 Event selection

The event selection is done first, by requiring $\mathrm{TriggerId} = 240020, 240025$ to accept only VPD-MB trigger events. Next, the reconstructed primary vertex V_z has to be within ± 6 cm of the vertex position obtained from time difference between VPD hits V_z^{VPD} as defined by the cut $\left|V_z - V_z^{VPD}\right| < 6$ cm. This removes pile-up vertices and ensures, that the analyzed event is indeed the one, which fired the trigger. In addition, a good quality vertex is selected with $rank(id = 0) > 0$ cut. Finally, to ensure a uniform acceptance and tracking efficiency the $|V_z| < 30$ cm is applied.

Event cuts	Purpose
$\mathrm{TriggerId} = 240020, 240025$	Select VPD-MB trigger events
$rank(id = 0) > 0$	Select a good quality vertex
$\lvert V_z\rvert < 30$ cm	Ensure uniform acceptance and efficiency
$\left\lvert V_z - V_z^{VPD}\right\rvert < 6$ cm	Remove pile-up vertices

Table 6.1: Summary of event selection cuts for J/ψ studies.

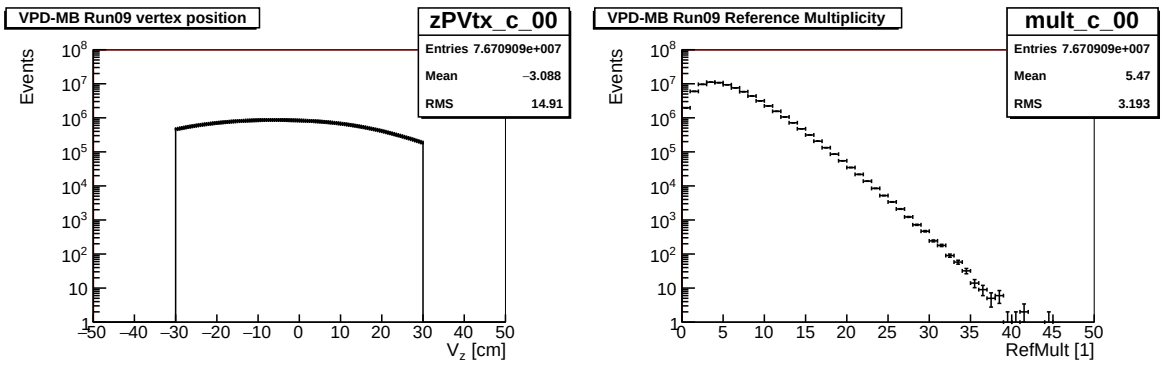

(a) **(b)**

Figure 6.1: Figure 6.1a: Primary vertex V_z distribution after cuts. A Gaussian fit is shown as red line. Figure 6.1b: Reference multiplicity $refMult$ distribution for accepted events.

After applying all the above cuts, which are listed in the Table 6.1, the number of events is 77 M. This is because of low VPD efficiency and vertex quality in Run09. Basic event distributions, like V_z and $refMult$ are shown in Figure 6.1a and Figure 6.1b respectively.

6.3 Track selection

In J/ψ analysis, track selection is done in similar way as for Υ analysis. Track quality cuts are described in Subsection 6.3.1, electron identification cuts are described in Subsection 6.3.2 and kinematic cuts are described in Subsection 6.3.3.

6.3.1 Track quality cuts

Track quality for J/ψ studies is ensured, by requiring charge $|q| = 1$, $|\eta| < 1.0$ and $0 < flag < 1000$. By selecting tracks with $nFitPts > 15$, a good momentum resolution is provided, while $nFitPts/nFitPtsMax > 0.52$ is applied to avoid track splitting. In addition $DCA < 3\text{cm}$ cut is used to select primary tracks with a high probability of originating from the primary vertex. The track quality cuts are Summarized in Table 6.2.

6.3.2 Electron identification cuts

Electron identification cuts for J/ψ reconstruction are selected first with TPC $\frac{dE}{dx}$ by applying $-1 < n\sigma_e < 2$ cut. The distribution of $\frac{dE}{dx}$ vs. p measured by the TPC is shown in Figure 6.2a [178]. In addition TOF is used for hadron rejection at low momentum below

Track QA cut	Purpose
$\|q\| = 1$	Use tracks with charge ± 1
$\|\eta\| < 1.0$	Avoid edges of acceptance
$0 < flag < 1000$	Reject badly reconstructed and pile-up tracks
$DCA < 3\,\mathrm{cm}$	Select primary tracks
$nFitPts > 15$	Assure good momentum resolution
$nFitPts/nFitPtsMax > 0.52$	Reject split tracks

Table 6.2: Summary of track quality cuts for J/ψ studies.

$p < 1.4\mathrm{GeV/c}$. Kaons and protons are well separated from electrons in inverse particle velocity (in the units of speed of light) $\beta^{-1} = \frac{c}{v}$ as can be seen in Figure 6.3 [178] up to $p \approx 1.4\,\mathrm{GeV/c}$. This yields a higher purity electron sample as can be seen for example in Figure 6.2b.

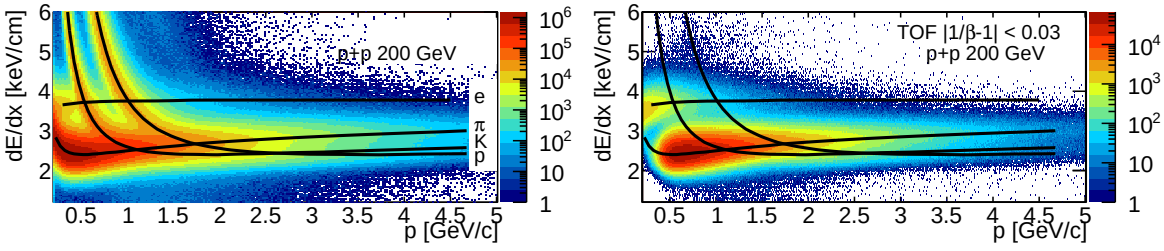

(a) **(b)**

Figure 6.2: TPC $\frac{dE}{dx}$ vs. p before (Figure 6.2a) and after (Figure 6.2b) TOF $|1/\beta - 1| < 0.03$ cut [178]. The lines indicate expected $\frac{dE}{dx}$ for each particle species from Bichsel functions [152, 153].

For momenta $p > 2.0\ \mathrm{GeV/c}$, as hadron bands start to overlap with electrons in $\frac{dE}{dx}$ due to relativistic rise, the BEMC is used. Tracks are matched to BEMC towers with tower energy $E > 0.1\mathrm{GeV}$ to avoid noise. Finally, hadrons are rejected by a tower energy to track momentum ratio $E/p > 0.5$ cut.

Electron identification cuts are summarized in Table 6.3.

6.3.3 Kinematic cuts

Kinematic cuts are applied in order to reduce background. A $p_T > 0.8\ \mathrm{GeV/c}$ cut, rejects low momentum tracks, which have low probability of originating from J/ψ decays. For example, a J/ψ with $p_T \approx 0\ \mathrm{GeV/c}$, will decay into 2 back-to-back electrons, each with $p \approx 1.5\ \mathrm{GeV/c}$.

cut	purpose
$-1 < n\sigma_e < 2$	Identify electrons with TPC
$\lvert 1/\beta - 1\rvert < 0.03$ for $p < 1.4$ GeV/c	Reject hadrons using TOF
$E/p > 0.5$ for $p > 2.0$ GeV/c	Reject hadrons using BEMC

Table 6.3: Summary of the electron identification cuts for J/ψ reconstruction.

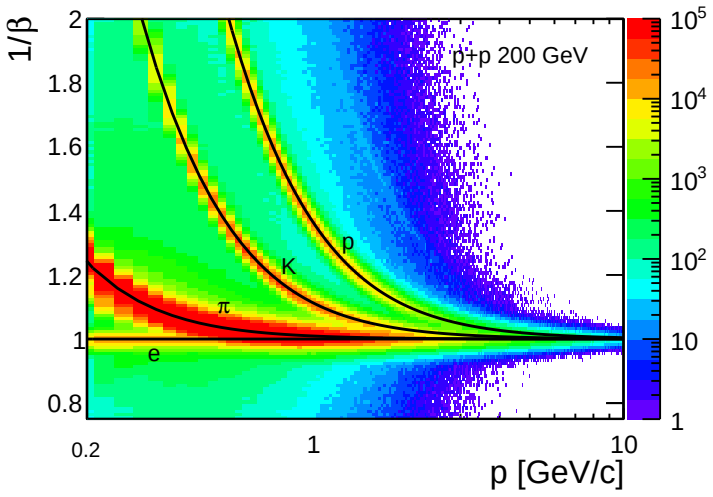

Figure 6.3: Distribution of β^{-1} vs. p for tracks matched to TOF [178]. The lines are the expected values for each particle type.

6.4 Signal extraction

Having selected electron candidates, a J/ψ signal can be reconstructed by combining them into pairs. Similarly to Υ signal reconstruction an invariant mass m_{ee} is calculated with Equation 5.3. An m_{ee} histogram is made for unlike-sign and a sum of like-sign pairs $N_{CB} = N_{e^+e^+} + N_{e^-e^-}$ to estimate combinatorial background. This is shown in Figure 6.4a. Next, combinatorial background is subtracted from the unlike-sign distribution as can be seen in Figure 6.4b. The resulting distribution is fitted with a smeared lineshape from embedding and linear residual background corresponding to $c\bar{c} \to D\bar{D} \to e^+e^- + X$. J/ψ yield is calculated by integrating counts in $2.7 < m_{ee} < 3.2$ GeV/c^2 and subtracting residual background. It is also corrected for mass cut efficiency calculated from the lineshape.

The signal is divided into $0 < p_T < 2$ GeV/c and $2 < p_T < 4$ GeV/c ranges as shown in Figure 6.5.

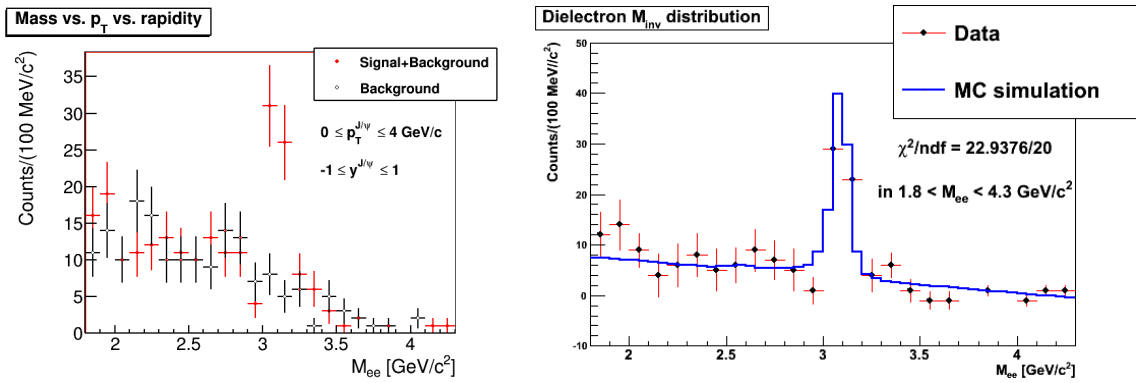

(a) $0 < p_T < 2\,\mathrm{GeV/c}$ **(b)** $2 < p_T < 4\,\mathrm{GeV/c}$

Figure 6.4: Figure 6.4a: Invariant mass distributions for unlike-sign (red points) and like-sign background (black points) for $|y| < 1$ and $0 < p_T < 4\,\mathrm{GeV/c}$. Figure 6.4b: Same distribution after background subtraction (black points) with a MC lineshape and linear residual background fit (blue line).

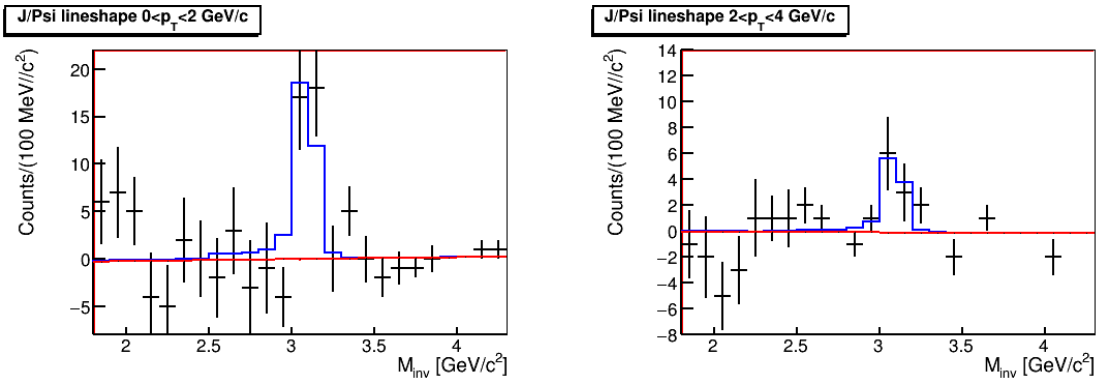

(a) $0 < p_T < 2\,\mathrm{GeV/c}$ **(b)** $2 < p_T < 4\,\mathrm{GeV/c}$

Figure 6.5: Invariant mass distributions after combinatorial background subtraction in $|y| < 1$ for $0 < p_T < 2\,\mathrm{GeV/c}$ (6.5a) and $2 < p_T < 4\,\mathrm{GeV/c}$ (6.5b).

6.5 Efficiency corrections

6.5.1 Electron identification efficiency

Electron identification efficiency is calculated from Gaussian fits to the inclusive particle $n\sigma_e$ distributions from the data. The particles are selected, by applying only TOF and BEMC cuts listed in Table 6.3. This improves electron purity. The parameters for each Gaussian are constrained to the values predicted by Bichsel functions [152, 153] taking the detector resolution into account [179]. The electron Gaussian is constrained using a sample of photonic electrons

selected with $m_{ee} <$ GeV/c^2 and $p > 0.1$ GeV/c. In addition, a $|\beta^{-1} - 1| < 0.03$ cut for $p < 1.5$ GeV/c and $\frac{E}{p} > 0.5$ for $p > 1.5$ GeV/c cuts are applied. A further $|n\sigma_e| < 4$ cut is applied for a partner track, while fits are done for the other track from the pair. A combinatorial background is subtracted using a sum of like-sign pairs as shown if Figure 6.6. An example fit is shown in Figure 6.7a. The resulting fit parameters are presented in Figure 6.7b and are fitted with constants yielding $\sigma_e = 0.814 \pm 0.003$ and $\mu_e = -0.016 \pm 0.004$. The latter are used as constraints for electrons in inclusive particle fits, of which an example is presented in Figure 6.8a [178]. Moreover, the parameters of hadron Gaussians are constrained in the overlap regions with the values obtained from constant fits to parameters p dependence for $p > 2$GeV/c.

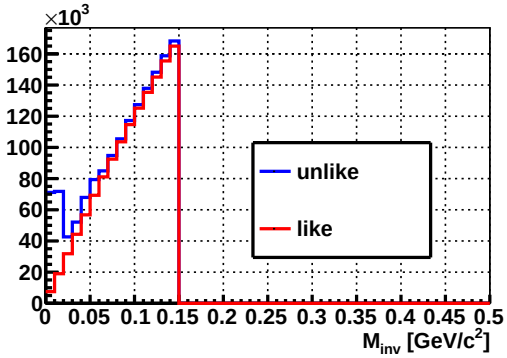

Figure 6.6: Invariant mass distribution for photonic electrons sample. Unlike-sign (blue) and like-sign (red) histograms are both shown.

The efficiency is calculated in a similar way as in Section 5.6.1. This results with the efficiency shown in Figure 6.7b.

6.5.2 TOF matching efficiency

In order to calculate the matching efficiency for a track to a TOF hit, the pp2pp [99] data are used to avoid pile-up effects. These are also VPD-MB trigger data collected in a pp2pp dedicated low-lominosity run. The efficiency is calculated as a function of η and p_T separately. Figure 6.9 shows the p_T-dependent TOF matching efficiency for electrons and hadrons. Electrons are selected with $0 < n\sigma_e < 2$, with hadrons cut out by $-2.5 < n\sigma_\pi < 3$, $|n\sigma_p| < 3$, $|n\sigma_K| < 3$ cuts. Hadrons are on the other hand selected by requiring $|n\sigma_e| > 3$.

The ratio of electron/hadron efficiency is calculated and shown in Figure 6.9b. This is then fitted with a constant for $p_T > 1.8$ GeV/c giving 1.05 ± 0.05, which is used to scale the η dependence of matching efficiency for hadrons as shown in Figure 6.10.

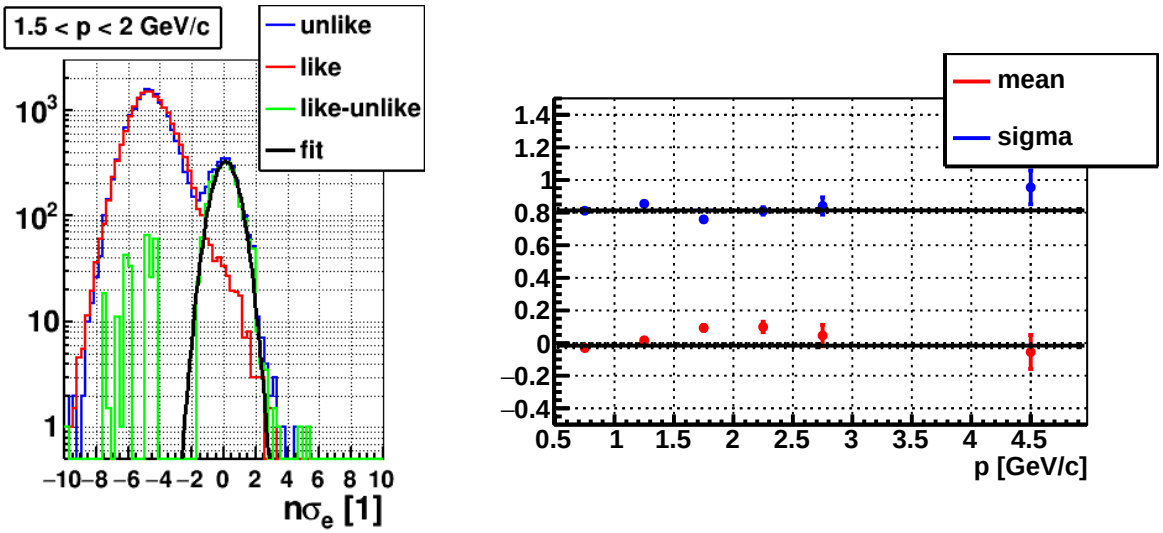

(a) (b)

Figure 6.7: Figure 6.7a: An example fit to the $n\sigma_e$ distribution of photonic electrons with $1.5 < p < 2$ GeV/c. Figure 6.7b: Mean (red) and width (blue) vs. p from Gaussian fits to photonic electrons. The lines are constant fits to the data.

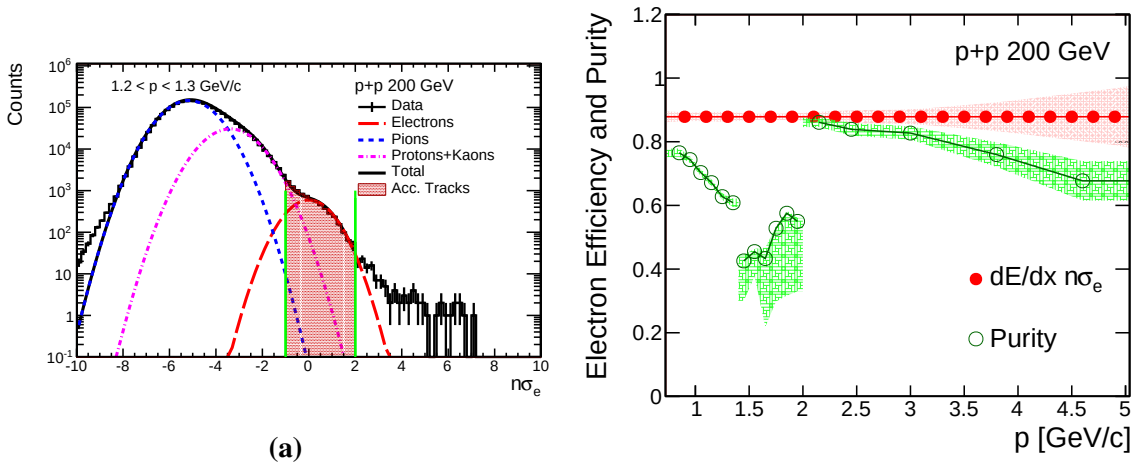

(a) (b)

Figure 6.8: Figure 6.8a: An example fit to the $n\sigma_e$ distribution of inclusive particles with $1.2 < p_T < 1.3$ GeV/c [178]. Figure 6.8b: Efficiency (red) and purity (green) of electrons identified with TPC vs. p from Gaussian fits to single particle distributions. The bands indicate systematic uncertainties.

6.5.3 TOF β^{-1} cut efficiency

In order to calculate the TOF $|1/\beta - 1| < 0.03$ cut efficiency, a photonic electrons sample is used. The electrons are selected with $m_{ee} < 15$ GeV/c^2 and $0 < n\sigma_e < 2$. Figure 6.11 shows the β^{-1} histogram. The efficiency is calculated from a ratio of the counts passing the cut to the

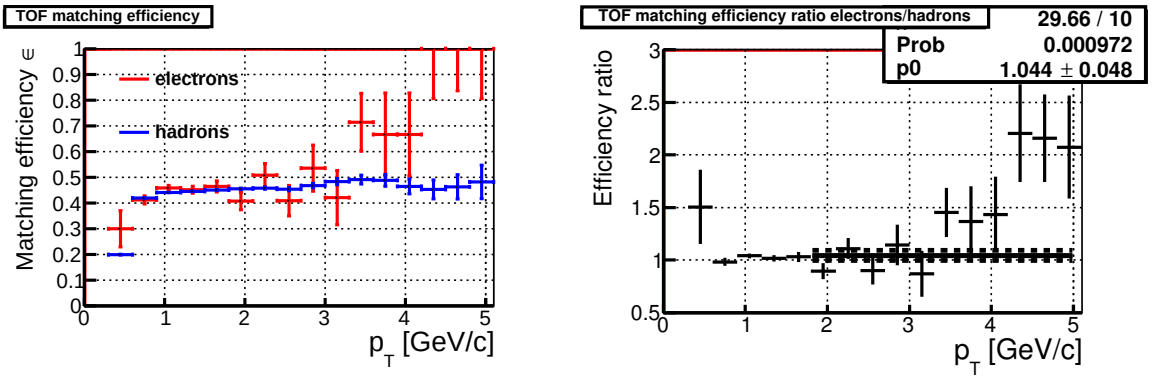

(a) **(b)**

Figure 6.9: Figure 6.9a: TOF matching efficiency vs. p_T for electrons (red) and hadrons (blue). Figure 6.9b: Ratio of electron to hadron of TOF matching efficiency. A constant is fitted for $p_T > 1.8\ \mathrm{GeV/c}$.

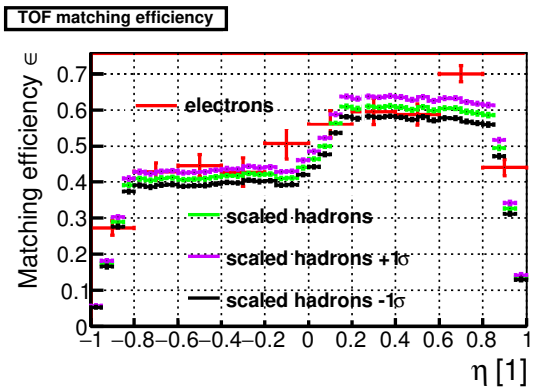

Figure 6.10: Dependence of TOF matching efficiency on eta for electrons (red), and scaled hadrons (green). The efficiency scaled by the upper (purple) and lower (black) limit of uncertainty ratio is also plotted.

total counts in $0.9 < \beta < 1.1$. This avoids the outliers, while the range is much larger than the width $\sigma = 0.013575 \pm 0.000085$ of the fitted Gaussian.

The resulting efficiency is $96.6 \pm 0.7\%$.

6.5.4 BEMC matching efficiency

The efficiency of matching tracks to the BEMC hits is calculated using embedding. A 2 types of tracks are matched: MC tracks and reconstructed ones. The efficiency is calculated with the reconstructed trucks, while the MC tracks are used to estimate the influence of TPC momentum resolution on BEMC matching. Both are shown in Figure 6.12. The difference is included as a

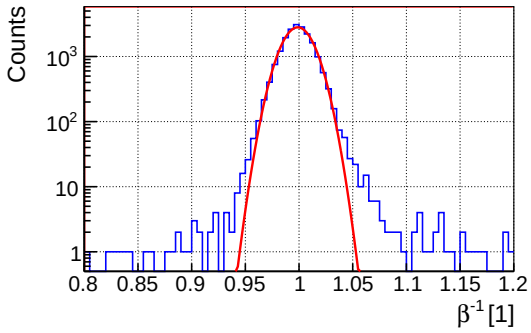

Figure 6.11: TOF β^{-1} distribution for photonic electrons (blue) fitted with a Gaussian (red).

systematic uncertainty.

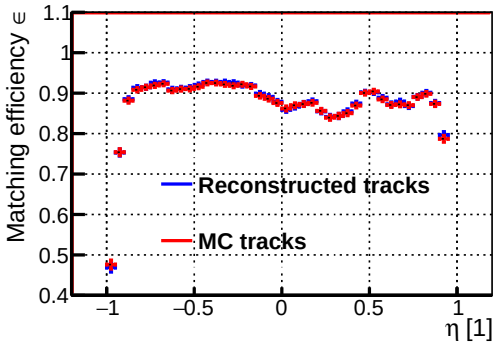

Figure 6.12: The BEMC matching efficiency vs. η for reconstructed (blue) and MC tracks (red).

6.5.5 BEMC $\frac{E}{p}$ cut efficiency

Embedding is also used to calculate the BEMC $\frac{E}{p} > 0.5$ cut efficiency. The Figure 6.13a [178] shows the comparison of $\frac{E}{p}$ distributions between embedding and data obtained from photonic electrons. The data are well described by simulations.

A p dependence of the efficiency is calculated and presented in Figure 6.13b for reconstructed tracks and MC tracks. Again, the difference is included as a systematic uncertainty.

6.5.6 Electron tracking efficiency

Electron tracking efficiency is also calculated with the embedding. The efficiency is calculated as a ratio of number of reconstructed tracks passing track quality and kinematic cuts to the number of all MC tracks. This is done as a function of momentum p and is presented in Figure 6.14 [178].

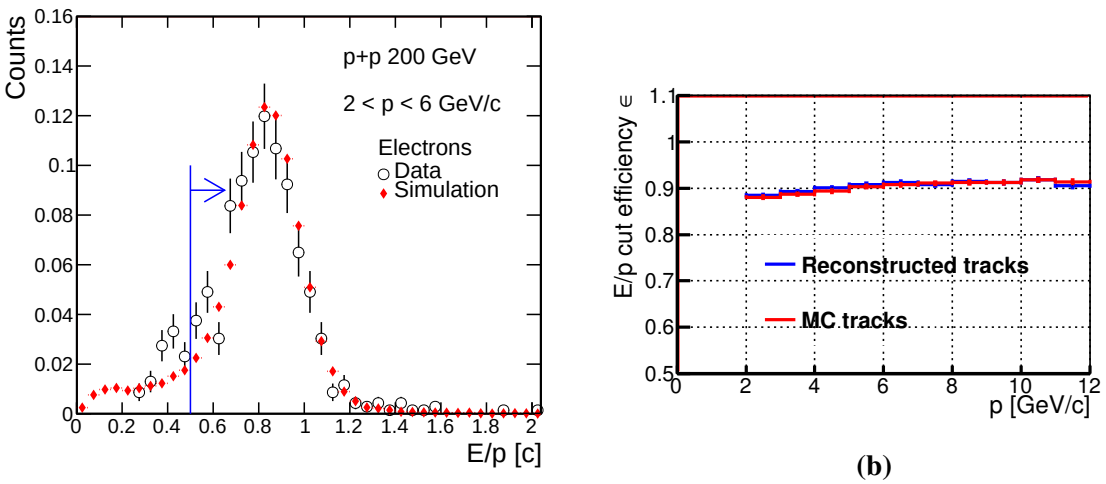

(a) **(b)**

Figure 6.13: Figure 6.13a: Comparison of $\frac{E}{p}$ distributions between embedding (red diamonds) and data (black circles) [178]. Figure 6.13b: $\frac{E}{p}$ cut efficiency vs. p obtained from matching reconstructed tracks (blue) and MC tracks (red) to BEMC towers.

6.5.7 Electron efficiency summary

All electron efficiencies are summarized in the Figure 6.14. The total electron efficiency is calculated with the Equation 6.1.

$$\epsilon_e = \epsilon_{tracking \times acceptance} \times \epsilon_{n\sigma_e} \times \epsilon_{TOF} \times \epsilon_{BEMC} \tag{6.1}$$

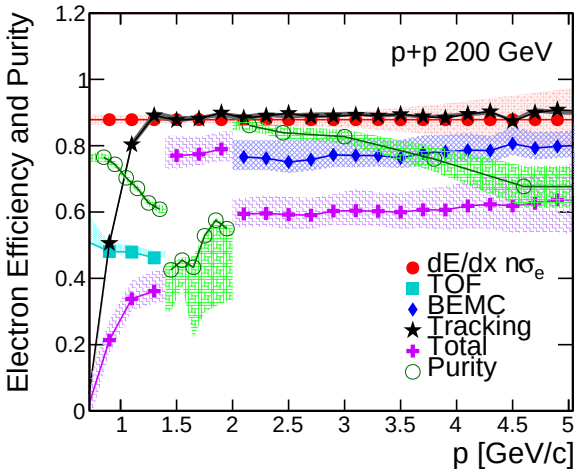

Figure 6.14: Summary plot of electron efficiency and purity vs. p [178]. It shows $\frac{dE}{dx}$ (red closed circles), TOF (teal squares), BEMC (blue diamonds), tracking (black stars) and total efficiency (purple crosses). Purity is also shown (green open circles). The colored bands correspond to systematic uncertainties.

6.5.8 Additional smearing of electron p_T

Similarly to Υ analysis, the width of J/ψ lineshape is narrower in embedding than in the data. Additional Gaussian smearing is applied to electron p_T, where the width of the Gaussian is $\sigma = Ap_T$. The smeared lineshape is fitted to the signal in the data as can be seen for example in Figure 6.4b. This is done for different values of A, so a χ^2 vs. A dependence is obtained. It is shown in Figure 6.15. The best fit is found for $A = 0.71 \pm 0.05$.

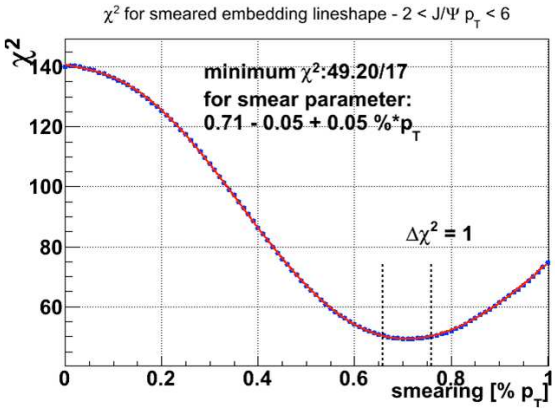

Figure 6.15: Values of χ^2 from fit of J/ψ lineshape from embedding to the data.

6.5.9 J/ψ p_T and y spectra in simulation

In order to reproduce a realistic J/ψ p_T and y spectra. The flat distribution in embedding is weighed with the function found in Equation 6.2.

$$w(p_T, y) = f_{Gauss}(y, \mu = 0, \sigma = 1.416) \cdot Ap_T(1 + (p_T/B)^2)^n \tag{6.2}$$

The function was determined from a fit to STAR [180] and PHENIX [181] J/ψ data. The parameters are $A = 4.239$, $B = 3.699\ \mathrm{GeV/c}$, $n = 5$.

6.5.10 J/ψ reconstruction efficiency

Reconstruction efficiency of J/psi is also calculated using embedding. All the single electron efficiencies are applied in order to obtain the efficiency for J/psi according to the Equation 6.3. An additional $\epsilon_{trigger} = 1/0.7$ correction due to VPD-MB trigger bias towards events containing J/ψ is applied [175]. The Figure 6.16 [178] shows the resulting J/ψ tracking and reconstruc-

tion efficiencies.

$$\epsilon_{J/\psi}(p_T^{J/\psi}) = \epsilon_{trigger} \times \epsilon_{e^+}(p^{e^+}) \times \epsilon_{e^-}(p^{e^-}) \tag{6.3}$$

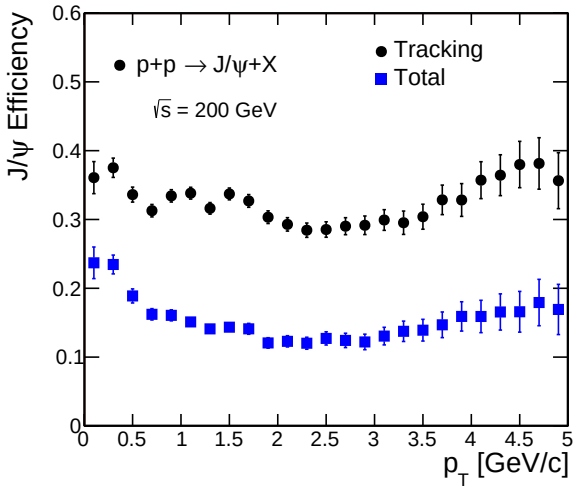

Figure 6.16: J/ψ reconstruction (blue squares) and tracking efficiency (black circles) vs. p_T [178].

6.5.11 Finite bin width correction

Finite bin width correction is calculated in a similar way as for Υ analysis in Section 5.6.7. The correction is done based on power law fit in Equation 6.17 to the J/psi yield vs. p_T for VPD-MB and BHT1 data [180]. The data are corrected with Equation 5.7.

6.17 [180]

$$f(p_T) = Ap_T(1 + (\frac{p_T}{B})^2)^{-6} \tag{6.4}$$

Additional Tsallis q-exponential fit is done to estimate a systeamtic uncertainty, related to the choice of the fit function. The Tsallis function is defined in Equation 6.5.

$$f(p_T) = Ap_T(1 + \frac{m_T}{nT})^{-n} \tag{6.5}$$

Figure 6.17 shows the fits to the J/psi yield vs. p_T. The data are well described by both functions up to $p_T = 8$ GeV/c.

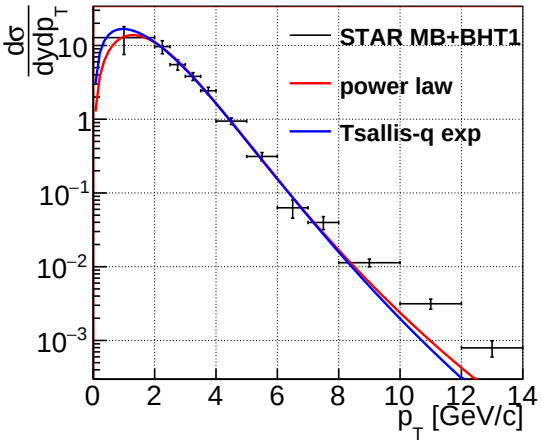

Figure 6.17: J/ψ yield vs. p_T for VPD-MB and BHT1 data [180]. It is fitted with a power law (red) and Tsallis q-exponential (blue) functions.

6.6 Systematic uncertainties

6.6.1 TOF matching efficiency uncertainty

TOF matching efficiency is calculated by using a scaled hadron efficiency as described in Section 6.5.2. It is compared with the upper and lower uncertainty limit on the efficiency and with the efficiency calculated from electron sample. The maximum deviation is chosen as an uncertainty, which affects the results by 1% to 3%.

6.6.2 β^{-1} cut efficiency systematic uncertainty

The β^{-1} cut efficiency is calculated both using photonic electrons and a Gaussian fit to the β^{-1} distribution. The difference is included as a systematic uncertainty and it influences the J/ψ cross section by -4% to 3%.

6.6.3 Additional smearing uncertainty

The uncertainty in the additional smearing parameter $A = 0.71 \pm 0.05\%$ affects the results by $\pm 1\%$.

6.6.4 TPC tracking efficiency

Tracking efficiency uncertainty is calculated by changing $nFitPts \pm 2$. The effect is -4% to 2%.

6.6.5 Shape of J/ψ p_T and rapidity spectra

The influence of the shape of J/ψ p_T and rapidity spectra on J/ψ reconstruction efficiency in embedding is studied by comparing realistic (p_T and y weighed) and flat distributions. The results change by -8% and 5% for p_T and rapidity spectra respectively.

6.6.6 J/ψ spin alignment

The influence of J/ψ spin alignment is investigated by assuming a λ parameter in Equation 5.9 from PHENIX [182] results. The effect is -3%.

6.6.7 $n\sigma_e$ efficiency uncertainty

To check the influence of constraints in the $n\sigma_e$ cut efficiency estimation, the fit range of photonic electrons is changed from $|n\sigma_e| < 3$ to $|n\sigma_e| < 4$. In addition, the constraints are varied by 5σ, because the changes are very small. All these changes affect the results by -8% to 5%.

6.6.8 TPC resolution effect on BEMC matching

The BEMC matching efficiency is calculated by projecting reconstructed and MC tracks to BEMC hits. The difference is taken as a systematic uncertainty and affects the results by 2%.

6.6.9 $\frac{E}{p}$ cut efficiency systematic uncertainty

The uncertainty associated with the $\frac{E}{p}$ cut efficiency calculation is investigated by comparing efficiency from embedding and photonic electrons. The effect is estimated to be -9% to -7%.

6.6.10 Bin width correction uncertainty

The systematic uncertainty connected to the bin width correction is estimated by changing the fit function used to correct the data. The difference between using a power law function in

Equation 6.4 and Tsallis q-exponential from Equation 6.5 is treated as an uncertainty. This affects the results by -3% to 42%.

6.6.11 Signal extraction method

The signal extraction method uncertainty is calculated by comparing signal obtained from histogram counts and fitted lineshape. It is found to be $+35\%$ for $0 < p_T < 2\ \mathrm{GeV/c}$ to $+50\%$ for $2 < p_T < 4\ \mathrm{GeV/c}$.

6.6.12 Invariant mass cut uncertainty

In order to estimate the systematic uncertainty related to invariant mass cut, the $2.7 < m_{ee} < 3.2\ \mathrm{GeV/c^2}$ cut is changed to $2.9 < m_{ee} < 3.2\ \mathrm{GeV/c^2}$. The effect is found to range from $+16\%$ to $+20\%$.

6.6.13 Uncertainty related to radiative decays

Radiative decays $J/\psi \to e^+e^-\gamma$ constitute a fraction of $J/\psi \to e^+e^-$ decays [183]. The energy carried off by γ is missing when reconstructing J/ψ signal using dielectrons. This causes the reconstruction of smaller m_{ee} than $m_{J/\psi}$, thus contributing to the tail in the signal. This effect is not included in STAR simulations, so a systematic uncertainty was estimated using the model in Reference [183] and was found to be 4% [180, 184] for the $2.7 < m_{ee} < 3.2\ \mathrm{GeV/c^2}$ cut.

6.6.14 Uncertainty on integrated luminosity

Similarly to Υ studies in Section 5.7.8, the uncertainty is $\pm 8\%$.

6.6.15 Summary of systematic uncertainties

Table 6.4 lists a sumary of systematic uncertainties on the J/ψ cross section. To show the uncertainty in each category for $0 < p_T < 2\ \mathrm{GeV/c}$, $2 < p_T < 4\ \mathrm{GeV/c}$ and total yield, the maximum deviation is taken and assumed as symmetric.

Systematic uncertainty	$0 < p_T < 4\,\mathrm{GeV/c}$	$0 < p_T < 2\,\mathrm{GeV/c}$	$2 < p_T < 4\,\mathrm{GeV/c}$
TOF efficiency	$\pm 4\%$	$\pm 4\%$	$\pm 3\%$
BEMC efficiency	$\pm 9\%$	$\pm 8\%$	$\pm 12\%$
TPC Tracking efficiency	$\pm 3\%$	$\pm 4\%$	$\pm 2\%$
TPC eID efficiency	$\pm 6\%$	$\pm 6\%$	$\pm 6\%$
Efficiency	$\pm 8\%$	$\pm 9\%$	$\pm 6\%$
Yield extraction	$\pm 44\%$	$\pm 40\%$	$\pm 53\%$
Radiative decay uncertainty	$\pm 4\%$	$\pm 4\%$	$\pm 4\%$
Uncertainty on $\int \mathcal{L}dt$	$\pm 8\%$	$\pm 8\%$	$\pm 8\%$
Total	$\pm 46\%$	$\pm 60\%$	$\pm 55\%$

Table 6.4: Summary of systematic uncertainties on the J/ψ cross section.

Chapter 7

Results

7.1 Υ Results

7.1.1 Integrated cross section

The integrated cross section for $\Upsilon(1S+2S+3S)$ is calculated with the Equation 7.1.

$$B_{ee}\frac{d\sigma_\Upsilon}{dy} = \frac{N_\Upsilon}{\Delta y}\frac{1}{\epsilon_\Upsilon}\frac{N_{ev}^{all}}{N_{ev}\int \mathcal{L}dt} \tag{7.1}$$

Above, B_{ee} is the branching ratio for $\Upsilon \to e^+e^-$, σ_Υ is the Υ cross section, N_Υ is the Υ yield and Δy is the rapidity bin width. Also, the Υ reconstruction efficiency ϵ_Υ is included and integrated luminosity $\int \mathcal{L}dt$ scaled by a fraction of accepted events from all recorded events $\frac{N_{ev}}{N_{ev}^{all}}$.

The integrated cross section results as a function of center-of-mass energy are presented in Figure 7.1 along with Color Evaporation Model (CEM) calculation [185] and world data [80, 151, 165, 186–196]. The results are consistent with the world data trend and the CEM model.

Rapidity	$B_{ee}\frac{d\sigma_\Upsilon}{dy}$ [pb]	stat. [pb]	syst. [pb]
$\lvert y\rvert < 1$	195	12	26
$\lvert y\rvert < 0.5$	186	14	25

Table 7.1: Integrated cross section for $\Upsilon(1S+2S+3S)$.

7.1.2 Transverse momentum spectra

The invariant cross section for Υ is calculated with the Equation 7.2.

$$\frac{B_{ee}}{2\pi p_T}\frac{d\sigma_\Upsilon^2}{dp_T dy} = \frac{1}{2\pi p_T}\frac{N_\Upsilon(p_T)}{\Delta y \Delta p_T}\frac{1}{\epsilon_\Upsilon(p_T)}\frac{N_{ev}^{all}}{N_{ev}\int \mathcal{L}dt} \tag{7.2}$$

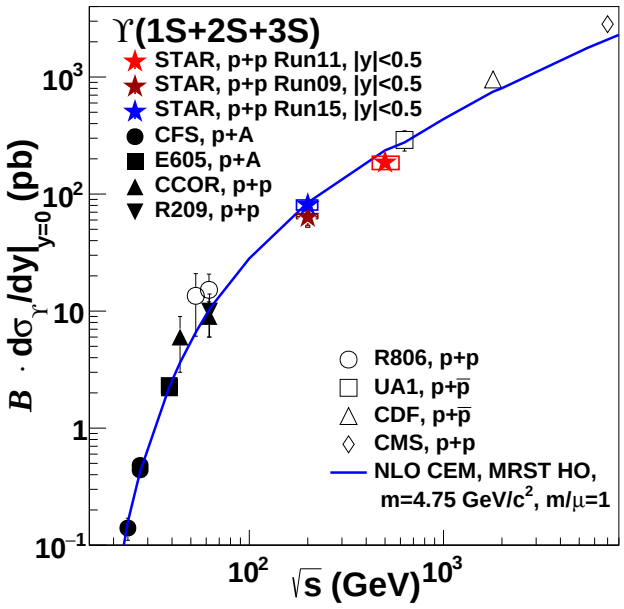

Figure 7.1: Integrated cross section of $\Upsilon(1S + 2S + 3S)$ as a function of $\sqrt{s}$. The STAR data at $\sqrt{s} = 500$ GeV (red star) and $\sqrt{s} = 200$ GeV (blue and brown stars) [151, 196] are compared to measurements by various experiments [80, 165, 186–195] and CEM (blue curve) [185].
These results were shown during Quark Matter 2017 as STAR Preliminary [196], but has since been updated with additional systematic uncertainties.

The results for $\Upsilon(1S + 2S + 3S)$, $\Upsilon(1S)$ and $\Upsilon(2S + 3S)$ are shown in the Figure 7.2. The data are compared to CEM [70, 197] and Color Glass Condensate Non-relativistic QCD (CGC+NRQCD) model calculation [66, 198, 199]. The $\Upsilon(1S)$ yield is consistent with CEM model and $\Upsilon(1S+2S+3S)$ is consistent for $p_T > 4\,\mathrm{GeV/c}$, while $\Upsilon(2S+3S)$ is overestimated by the model, except for $p_T > 6$ GeV/c. In the case of CGC+NRQCD prediction, the $\Upsilon(1S)$ is consistent with the data for $2 < p_T < 8$ GeV/c, while $\Upsilon(1S + 2S + 3S)$ and $\Upsilon(2S + 3S)$ is overestimated. It is important to note, that authors of the model warned [199], that additional corrections are needed in order to describe the cross section at low-p_T. This is however, first such calculation of CGC+NRQCD for Υ. Due to the fact that a NLO+NRQCD calculations require $p_T \gg m_\Upsilon$, they are not available for the $p_T < 10$ GeV/c.

These results were shown during Quark Matter 2017 as STAR Preliminary [196], but have since been updated with additional systematic uncertainties.

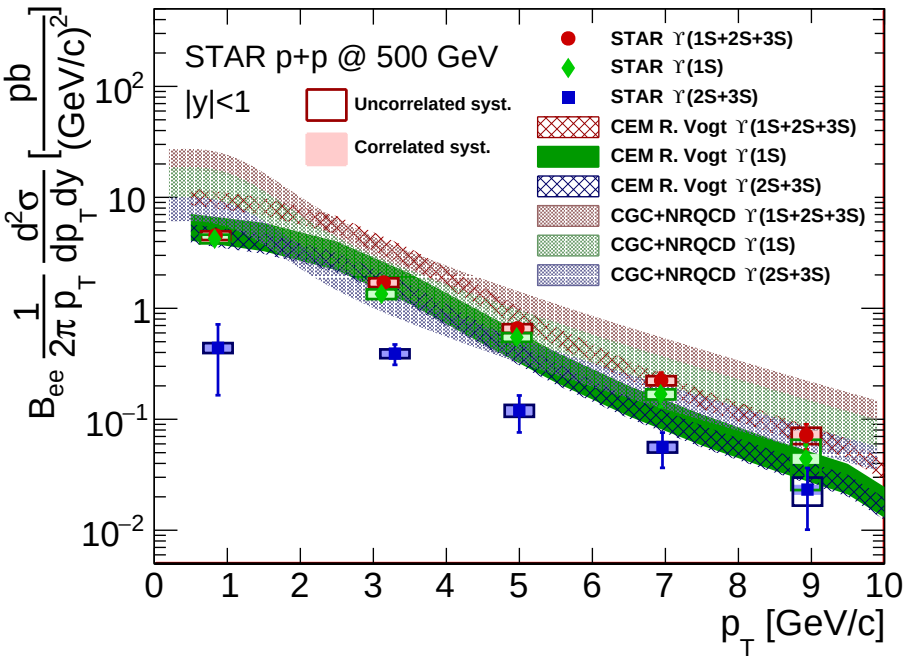

Figure 7.2: Invariant cross section of $\Upsilon(1S+2S+3S)$ (red diamonds), $\Upsilon(1S)$ (green diamonds) and $\Upsilon(2S+3S)$ (blue diamonds) compared to CEM model calculation for $\Upsilon(1S+2S+3S)$ (red checked band), $\Upsilon(1S)$ (green band) and $\Upsilon(2S+3S)$ (blue checked band) [70, 197]. The results are also compared to CGC+NRQCD predictions for $\Upsilon(1S+2S+3S)$ (red shaded area), $\Upsilon(1S)$ (green shaded area) and $\Upsilon(2S+3S)$ (blue shaded area) [66, 198, 199].

7.1.3 Rapidity spectra

A rapidity distribution is obtained in a similar way. The cross section for the $1 < y < -0.5$ and $0.5 < y < 1$ is added together in $0.5 < |y| < 1$ and reflected symmetrically. The rapidity dependence for $\Upsilon(1S+2S+3S)$, $\Upsilon(1S)$ and $\Upsilon(2S+3S)$ is presented in Figure 7.3.

A dip at mid-rapidity ($|y| < 0.5$) is observed in the $\Upsilon(2S+3S)$ cross section, which also contributes to a dip in $\Upsilon(1S+2S+3S)$. This is unexpected, however a smaller yield of $\Upsilon(2S+3S)$ signal is observed already in Figure 5.7a. It may be a downward fluctuation in the $\Upsilon(2S+3S)$ signal or a physical effect. Given the higher Υ reconstruction efficiency at mid-rapidity compared to $0.5 < |y| < 1$, the difference is amplified during efficiency correction.

The data are compared to the CEM [70, 197] and CGC+NRQCD [66, 198, 199] models in Figure 7.3a and Figure 7.3b respectively. CEM calculation for $\Upsilon(1S)$ is consistent with the STAR results. The rest of CEM predictions overestimates the data, however the $\Upsilon(1S+2S+3S)$

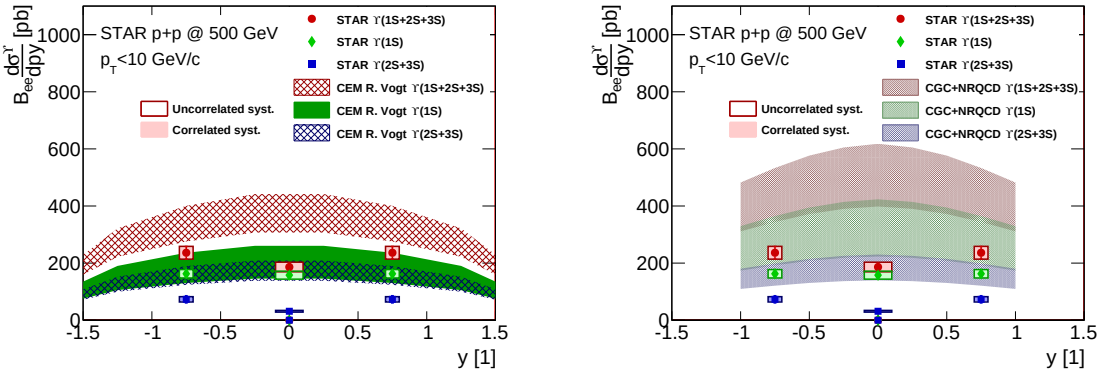

(a) **(b)**

Figure 7.3: Figure 7.3a: Rapidity distribution of $\Upsilon(1S+2S+3S)$ (red diamonds), $\Upsilon(1S)$ (green diamonds) and $\Upsilon(2S+3S)$ (blue diamonds). The data are compared to CEM model predictions for $\Upsilon(1S+2S+3S)$ (red checked band), $\Upsilon(1S)$ (green band) and $\Upsilon(2S+3S)$ (blue checked band) [70, 197] respectively. Furthermore, the data are also compared in Figure 7.3b to CGC+NRQCD model for $\Upsilon(1S+2S+3S)$ (red shaded area), $\Upsilon(1S)$ (green shaded area) and $\Upsilon(2S+3S)$ (blue shaded area) [66, 198, 199].

cross section for $0.5 < |y| < 1$ is within 2σ of the model prediction. The CEM predictions for the $\Upsilon(2S+3S)$, which also contribute to the $\Upsilon(1S+2S+3S)$ are in fact $\Upsilon(1S)$ scaled by the respective ratios, which are constant. These ratios are determined at $\sqrt{s} = 7\,\mathrm{TeV}$ and are found to be $\frac{\Upsilon(2S)}{\Upsilon(1S)} = 0.51$ and $\frac{\Upsilon(3S)}{\Upsilon(1S)} = 0.35$ [197] including branching ratios [15]. These values are much larger than the world data suggest [82].

In the case of CGC+NRQCD, the data are overestimated, however it has to be noted, that additional corrections are needed to describe the data at low-p_T [199]. The excess observed for $p_T < 2\ \mathrm{GeV/c}$ in Figure 7.2 has a large contribution to the integrated cross section and shifts the rapidity distribution to higher values.

The rapidity distribution is flatter, than the one observed by STAR at $\sqrt{s} = 200\ \mathrm{GeV}$ [151, 196], which is qualitatively confirmed by the trend predicted in the models.

7.1.4 Ratios

The data allowed extraction of $\frac{\Upsilon(2S)}{\Upsilon(1S)}$, $\frac{\Upsilon(3S)}{\Upsilon(1S)}$ and $\frac{\Upsilon(2S+3S)}{\Upsilon(1S)}$ ratios. Each ratio is corrected for the mass cut efficiency and reconstruction efficiency. Figure 7.4 shows the STAR data compared to the world data [76, 82, 165, 186, 187, 190, 191, 195, 200–202]. STAR results are within $\approx 2\sigma$ of the constant fits to the world data from Reference [82].

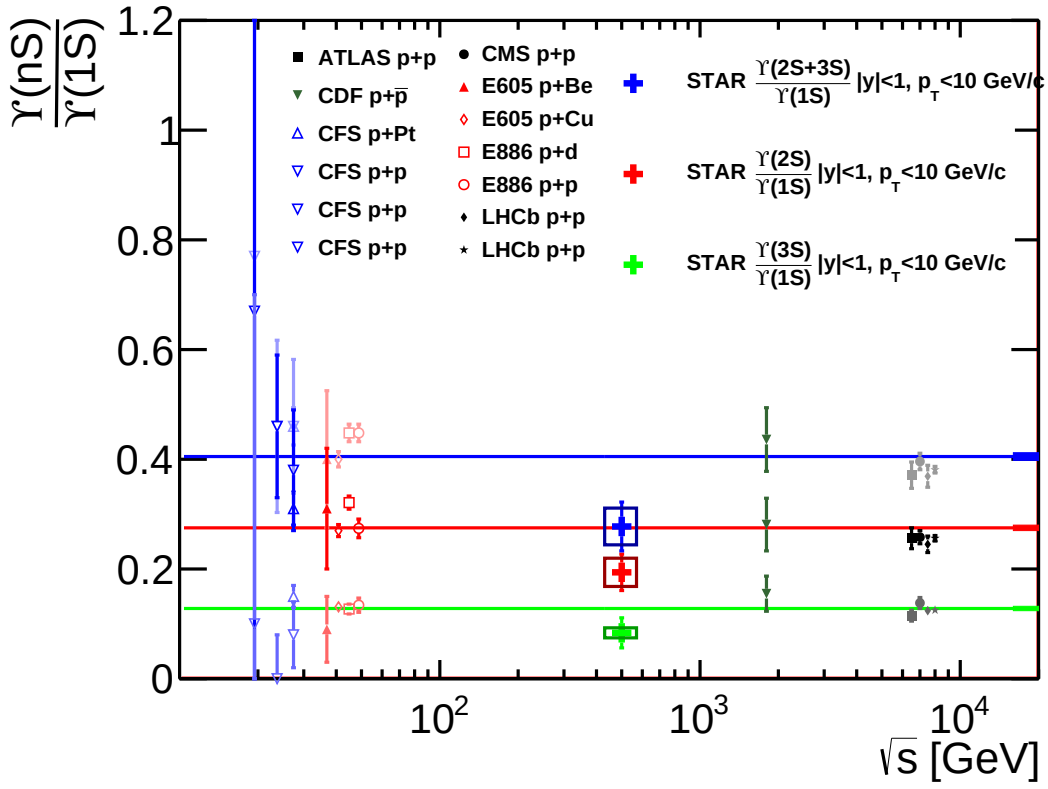

Figure 7.4: $\frac{\Upsilon(nS)}{\Upsilon(1S)}$ ratios as a function of energy [82]. The STAR measured ratios are $\frac{\Upsilon(2S)}{\Upsilon(1S)}$ (red cross), $\frac{\Upsilon(3S)}{\Upsilon(1S)}$ (green cross) and $\frac{\Upsilon(2S+3S)}{\Upsilon(1S)}$ (blue cross) compared to fits to the world data from [82] (red, green and blue lines respectively). The uncertainties on the fits are shown as bands at the end of each line to the right. Ratios measured by CFS experiment in $p+p$ (blue open downward triangles) [186] and $p+Pt$ (blue open upward triangles) [187] collisions are shown. Also plotted are E605 results in $p+Be$ (red closed triangles) [191] and $p+Cu$ (red open diamonds) [190] as well as $p+d$ (red open squares) and $p+p$ (red open circles) [200] by E866 experiment. At higher energies than RHIC are CDF $p+\bar{p}$ (green closed downward triangles) [195] and $p+p$ results from CMS (black closed circles) [165], ATLAS (black closed squares) [76], LHCb at $\sqrt{s} = 7$ TeV (black closed diamonds) [201] and $\sqrt{s} = 8$ TeV (black closed stars) [202].

All the ratios shown are integrated in p_T and rapidity. A p_T dependence of ratios is observed at LHC [75–77, 165, 201, 202]. In fact the ratios increase with increasing p_T, which gives a small contribution to the integrated ratios. The STAR data are more consistent with the values up to $p_T \approx 6\,\mathrm{GeV/c}$. In addition, the smaller $\Upsilon(2S+3S)$ cross section observed at mid-rapidity in Figure 7.3 also affects the ratios.

The dependence of Υ ratios on charged particle multiplicity, represented by $TofMult$ is

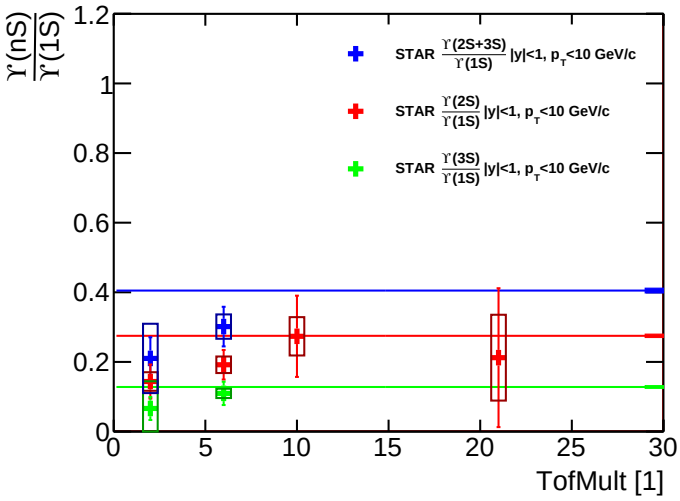

Figure 7.5: Dependence of $\frac{\Upsilon(nS)}{\Upsilon(1S)}$ ratios on charged particle multiplicity $TofMult$. The STAR data for $\frac{\Upsilon(2S+3S)}{\Upsilon(1S)}$ (blue crosses), $\frac{\Upsilon(2S)}{\Upsilon(1S)}$ (red crosses) and $\frac{\Upsilon(3S)}{\Upsilon(1S)}$ (green crosses) are compared to the constant fits to world data from Figure 7.4 (blue, red and green lines).

shown in Figure 7.5. The $\frac{\Upsilon(2S+3S)}{\Upsilon(1S)}$ and $\frac{\Upsilon(2S)}{\Upsilon(1S)}$ ratios are below the world data average for $TofMult < 8$. However, the $\frac{\Upsilon(2S)}{\Upsilon(1S)}$ for $TofMult > 8$ is consistent with the fit to the world data within uncertainties. A good agreement is found between world data fit and $\frac{\Upsilon(3S)}{\Upsilon(1S)}$ ratio. Within available precision, there is no significant change of the rations as function of the charged hadron multiplicity. Thus we do not observe a significant modification of Υ relative yields due to larger hadron density.

7.1.5 Event activity dependence

Using the fully corrected Υ and event multiplicity (a measure of event activity) distributions a normalized Υ yield $\frac{N_\Upsilon}{\langle N_\Upsilon \rangle}$ as a function of normalized multiplicity is calculated with Equation 7.3:

$$\frac{N_\Upsilon}{\langle N_\Upsilon \rangle} = \frac{N_{ev}^{all}}{N_{ev}^{bin}} \frac{N_\Upsilon^{bin}}{N_\Upsilon^{all}} \tag{7.3}$$

Where N_{ev}^{all} is the number of all Min-Bias events and N_{ev}^{bin} is the number of Min-Bias in a given bin. Similarly, N_Υ^{all} is the number of all Υ and N_Υ^{bin} is the number of Υ in a bin. The points are placed according to the Equation 7.4:

$$\frac{N_{ch}}{\langle N_{ch} \rangle} = \frac{\langle N_{ch} \rangle^{bin}}{\langle N_{ch} \rangle^{all}} \tag{7.4}$$

With the $\langle N_{ch} \rangle^{bin}$ being the mean multiplicity in a bin of Min-Bias distribution and $\langle N_{ch} \rangle^{bin}$ a mean of the entire Min-Bias distribution.

The normalized Υ yield $\frac{N_\Upsilon}{\langle N_\Upsilon \rangle}$ is plotted as a function of normalized multiplicity $\frac{\langle N_{ch} \rangle^{bin}}{\langle N_{ch} \rangle^{all}}$ and compared to world data in Figure 7.6 [1, 2, 4] and to the models in Figure 7.7 [5, 6, 172, 203]. The STAR Υ data are consistent with the world data trend and J/ψ data, which exhibit a strong rise with normalized multiplicity. A p_T dependence is observed and is indicated in the shift of central value of the $\Upsilon(1S)$ results for $p_T > 4$ GeV/c with respect to p_T-integrated, but given the uncertainties it is consistent with no dependence.

The STAR Υ are compared to PYTHIA8 calculation using STAR Heavy Flavor (HF) tune [172, 203], which exhibits a stronger rise for $p_T > 4$GeV/c. Both calculations are consistent with the data and suggest influence of multiple parton interactions (MPI) on Υ production. In addition, the String Percolation Model for J/ψ [5, 6] is compared to the data and a good agreement is found. The STAR Υ data are fitted with a quadratic function $f(x) = ax^2$, which is motivated by the String Percolation Model, and a 1σ confidence band is plotted. The data are well described by the fits.

The STAR Υ results suggest similar behavior for Υ and J/ψ. Furthermore, similar behavior is observed at RHIC and LHC energy for both. This gives a hint of collective effects, which may be present at high multiplicity in $p + p$ collisions. Moreover, the behavior may be due to MPI as suggested by ALICE D meson results and PYTHIA8 [3].

7.1.6 x_T dependence

In pQCD, an inclusive invariant cross section σ^{inv} is expected to follow a power law scaling according to Equation 7.5 [204].

$$\sigma^{inv} \equiv E\frac{d^3\sigma}{d^3p} = \frac{F(x_T)}{p_T^{n(x_T,\sqrt{s})}} = \frac{F'(x_T)}{\sqrt{s}^{n(x_T,\sqrt{s})}} \tag{7.5}$$

Here, the $F(x_T)$ and $F'(x_T)$ are functions describing the x_T spectra and $x_T = \frac{2p_T}{\sqrt{s}}$. The $n(x_T, \sqrt{s})$ is the exponent of the power law decrease of the inclusive invariant cross section, which is equal to the number of partons participating in the process. For a $2 \to 2$ process in the parton model $n = 4$, as there are 4 partons taking active role in the process [205]. In general, the $n > 4$ if there are more partons participating in the process [206]. Furthermore, the running of α_s and changes in the PDFs and FFs cause small changes in $n(x_T, \sqrt{s})$, which in turn cause small scaling violations.

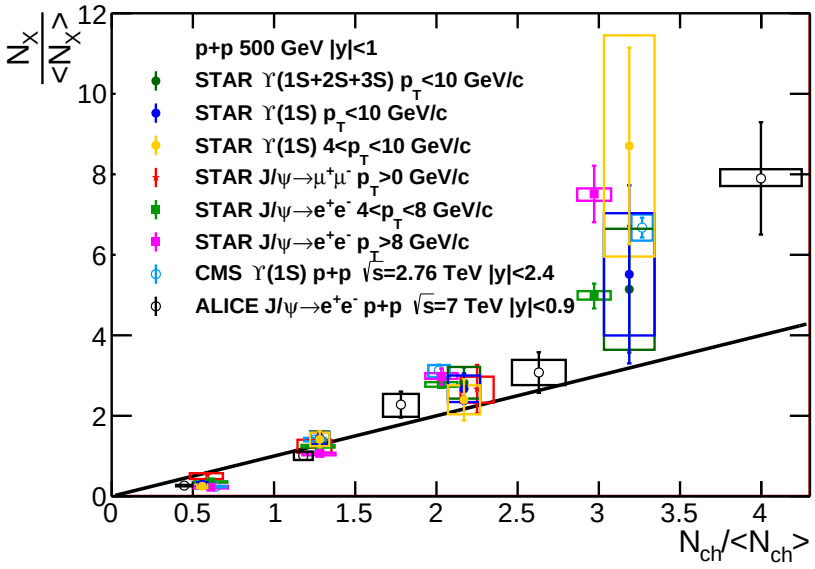

(a)

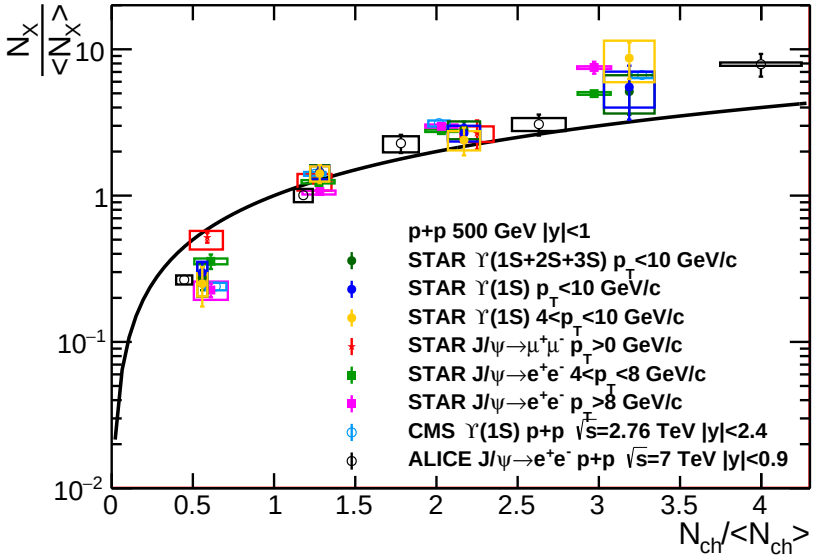

(b)

Figure 7.6: Normalized Υ yield vs. normalized multiplicity. Shown here are the STAR results for $\Upsilon(1S+2S+3S)$ (green closed circles), $\Upsilon(1S)$ (red closed circles), $\Upsilon(1S)$ for $p_T > 4$ GeV/c (orange closed circles). Systematic uncertainties in both $N_{ch}/\langle N_{ch}\rangle$ and $N_\Upsilon/\langle N_\Upsilon\rangle$ are represented by boxes. These are compared to the STAR $J/\psi \to \mu^+\mu^-$ measurements (red stars) and $J/\psi \to e^+e^-$ for $4 < p_T < 8\,\mathrm{GeV/c}$ (green closed squares) and $p_T > 8\,\mathrm{GeV/c}$ (magenta closed squares) [1]. Also shown are ALICE J/ψ results (black open circles) [2] and $\Upsilon(1S)$ from CMS (blue open circles) [4].

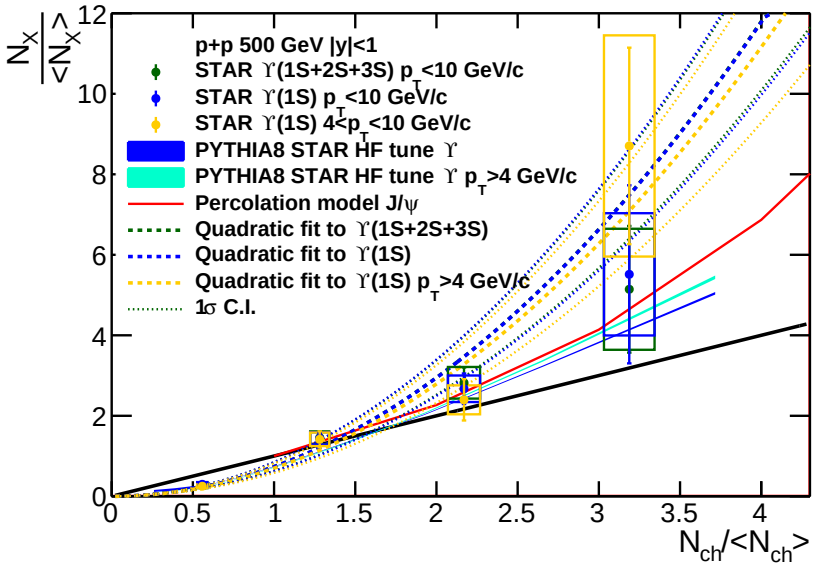

(a)

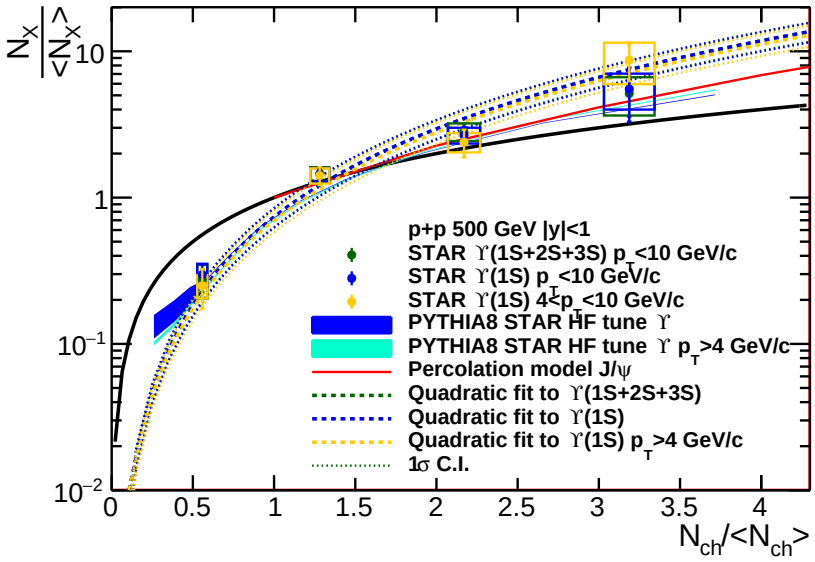

(b)

Figure 7.7: Normalized Υ yield vs. normalized multiplicity. The STAR data are compared to String Percolation Model (red line) [5, 6] and PYTHIA8 with STAR Heavy Flavor (HF) Tune [172, 203] for $p_T > 0\,\mathrm{GeV/c}$ (blue line) and $p_T > 4\,\mathrm{GeV/c}$ (teal line). The data are fitted with a $f(x) = ax^2$ function (dashed lines) and the 1σ uncertainty is plotted (dotted lines). [203].

By testing the x_T scaling of σ^{inv} additional information on the particle production process can be inferred.

A scaling of J/ψ production cross section with x_T was observed [207]. For J/ψ, the expo-

nent was found to be $n = 5.6 \pm 0.2$. Both J/ψ and Υ constituents are produced in a QCD hard process, but a subsequent soft interactions during the formation of a bound state may cause a braking of x_T scaling. A possible scaling for Υ invariant cross section is investigated by plotting the data with $n = 5.6$ vs. x_T. The STAR Υ data are compared to the world data in Figure 7.8. The LHCb results are not shown, because of different rapidity range $y > 4$ [201, 202].

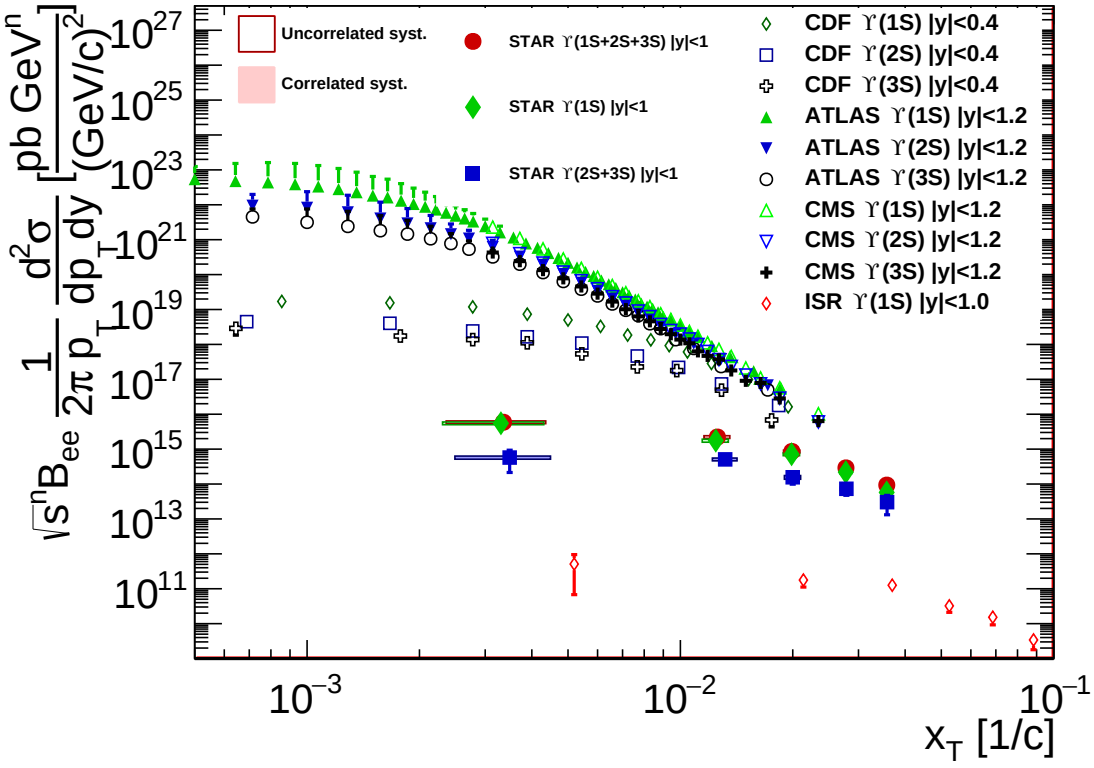

Figure 7.8: Invariant cross section scaled with $\sqrt{s}^n$, where $n = 5.6$ vs. x_T for $\Upsilon(1S + 2S + 3S)$ (red closed circles), $\Upsilon(1S)$ (green closed diamonds) and $\Upsilon(2S + 3S)$ (blue closed squares) measured by STAR. The data are compared with $\Upsilon(1S)$ results from Intersecting Storage Rings (ISR) (red open diamonds) [79] and $\Upsilon(1S)$, $\Upsilon(2S)$, $\Upsilon(3S)$ results measured by CDF (green open diamonds, blue open squares, black open crosses) [80], ATLAS (green closed upward triangles, blue closed downward triangles, black open circles) [76] and CMS (green open upward triangles, blue open downward triangles, black closed crosses) [77].

Besides some indication of scaling between CDF and LHC results, which may need further investigation, no scaling is observed. There is also very little overlap between data at different $\sqrt{s}$.

7.2 J/ψ Results

7.2.1 Integrated cross section

The integrated cross section for J/ψ was calculated in a similar way to Υ integrated cross section using Equation 7.1. In this case, the 2 cases are investigated. In the first one, the STAR results from VPD-MB trigger [178] are used for $p_T < 2\ \mathrm{GeV/c}$ and BHT1 data [180] are used for $2 < p_T < 14\ \mathrm{GeV/c}$. The result is presented in Equation 7.6.

$$B_{ee}\frac{d\sigma_{J/\psi}}{dy} = 38 \pm 11\ \text{(stat.)} \pm 16\ \text{(syst.)}\ \mathrm{nb}. \tag{7.6}$$

In addition, another case is calculated, where STAR VPD-MB results are replaced with PHENIX data [182] for $p_T < 2\ \mathrm{GeV/c}$. This gives the number presented in Equation 7.7.

$$B_{ee}\frac{d\sigma_{J/\psi}}{dy} = 42.5 \pm 1.4\ \text{(stat.)} \pm 4.8\ \text{(syst.)} \pm 3.1\ \text{(glob.)}\ \mathrm{nb}. \tag{7.7}$$

It has to be noted, however, that PHENIX data are limited to $|y| < 0.35$, while STAR data are for $|y| < 1$. Both results are consistent with each other and the STAR preliminary result from Run12 data, which is $B_{ee}\frac{d\sigma_{J/\psi}}{dy} = 47.4 \pm 2.9\ \text{(stat.)} \pm 6.1\ \text{(syst.)} \pm 3.8\ \text{(glob.)}\ \mathrm{nb}$ [63].

7.2.2 Transverse momentum spectrum

The J/ψ invariant cross section vs. p_T is calculated with Equation 7.2. It is shown if Figure 7.9 along with STAR BHT1 [180] and PHENIX data [182].

STAR and PHENIX data are compared to CEM [71], CGC+NRQCD [66] and NLO+NRQCD [60] models. All models describe the data within uncertainties, however, the CGC+NRQCD is slightly above the PHENIX data for $p_T < 1\ \mathrm{GeV/c}$.

7.2.3 Mean square of transverse momentum

A measurement of mean square $\langle p_T^2 \rangle$ of J/ψ can provide information on the origin of the observed yield. Initial J/ψ are expected to have large p_T, while those coming from possible regeneration effect in QGP [208] should have small p_T. One complication however is the Cronin effect [209], which causes the broadening of p_T spectrum due to multiple parton scattering

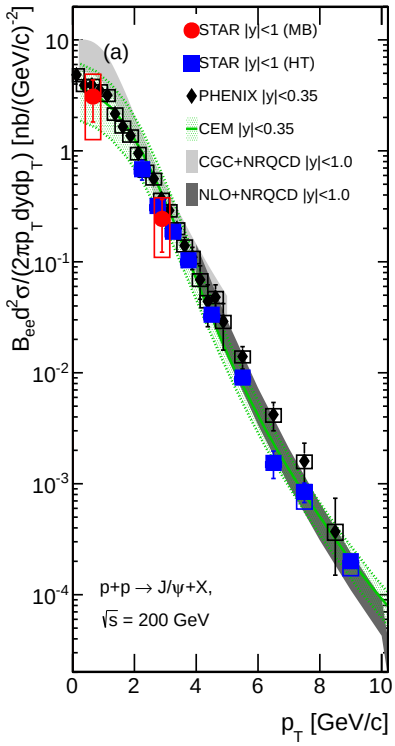

Figure 7.9: J/ψ invariant cross section vs. p_T. STAR data for VPD-MB (red closed circles) [178] are compared to STAR BHT1 data (blue closed squares) [180] and PHENIX results (black closed diamonds) [182]. These are also compared with CEM model (green line and uncertainty band) [71], CGC+NRQCD (light gray) [66] and NLO+NRQCD (dark gray) [60] calculations.

between projectile and target. One of the ways to model this effect is the approach in Equation 7.8 [210, 211].

$$\left\langle p_T^2 \right\rangle_{AA} = \left\langle p_T^2 \right\rangle_{pp} + N_c^{AA} \delta_0 \tag{7.8}$$

The $\left\langle p_T^2 \right\rangle_{AA}$ and $\left\langle p_T^2 \right\rangle_{pp}$ are the $\left\langle p_T^2 \right\rangle$ values for the particles produced in $A + A$ and $p + p$ collisions respectively. The N_c^{AA} is the sum of the average number of collisions for all partons in a projectile and target and δ_0 is the $\left\langle p_T^2 \right\rangle$ acquired by a parton in an individual scattering.

The $\left\langle p_T^2 \right\rangle$ was calculated from the STAR $p + p$ data for $0 < p_T < 14$ and the result is found in Equation 7.9 [178].

$$\left\langle p_T^2 \right\rangle = 3.45 \pm 0.85 \text{ (stat.)} \pm 1.22 \text{ (syst.) } (\text{GeV/c})^2 \tag{7.9}$$

This is also presented in Figure 7.10 and compared to the STAR result in $d + Au$ collisions [178], which also includes PHENIX data for $3 < p_T < 15$ GeV [212].

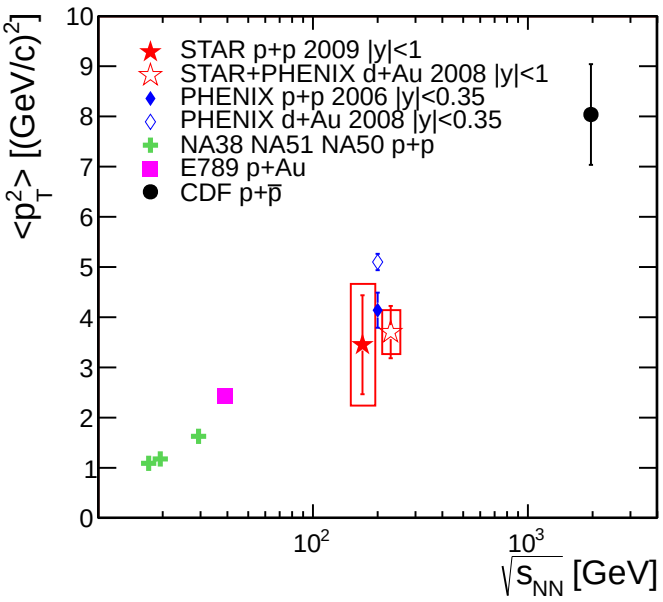

Figure 7.10: J/ψ $\langle p_T^2 \rangle$ vs. $\sqrt{s_{NN}}$ [178]. The STAR $p+p$ data (red closed star) is compared to the STAR+PHENIX combined $d+Au$ data (red open star) [178, 212] as well as PHENIX $p+p$ (blue closed diamond) [181] and $d+Au$ results (blue open diamond) [212]. In addition, the CDF $p\bar{p}$ (black closed circle) [213], E789 $p+Au$ (magenta closed square) and measurements in $p+p$ collisions at SPS (green closed crosses) [214] are also shown. THE STAR results are shifted to the sides in $\sqrt{s}$ for clarity.

Both STAR results are consistent with each other and PHENIX and follow the world data trend. However, PHENIX $d+Au$ result is slightly higher, than STAR+PHENIX $d+Au$ measurement. Also the PHENIX $d+Au$ is above the $p+p$, which may be an indication of Cronin effect [209, 210].

Chapter 8

Summary and conclusions

In this thesis, studies of Υ production in $p+p$ collisions at $\sqrt{s} = 500\,\mathrm{GeV}$ and J/ψ production in $p+p$ collisions at $\sqrt{s} = 200\,\mathrm{GeV}$ have been performed.

The result of Υ studies is the integrated cross section of $\Upsilon(1S+2S+3S)$ production for $p_T < 10\,\mathrm{GeV/c}$ in $|y| < 1$ and $|y| < 0.5$. It is $B_{ee}\frac{d\sigma_\Upsilon}{dy}|_{|y|<1} = 195 \pm 12(stat.) \pm 26(syst.)$ and $B_{ee}\frac{d\sigma_\Upsilon}{dy}|_{|y|<0.5} = 186 \pm 14(stat.) \pm 25(syst.)$, and is consistent with the world data trend vs. $\sqrt{s}$ and Color Evaporation Model (CEM) [185].

In addition, the invariant cross section of $\Upsilon(1S+2S+3S)$, $\Upsilon(1S)$ and $\Upsilon(2S+3S)$ for $p_T < 10\,\mathrm{GeV/c}$ and $|y| < 1$ has been measured. The $\Upsilon(1S)$ data are well described by the CEM model [70, 197]. On the other hand the $\Upsilon(1S+2S+3S)$ and $\Upsilon(2S+3S)$ are overestimated for $p_T < 4\,\mathrm{GeV/c}$ and $p_T < 6\,\mathrm{GeV/c}$ respectively. It has to be noted, however, that the ratios $\frac{\Upsilon(2S)}{\Upsilon(1S)} = 0.51$ and $\frac{\Upsilon(3S)}{\Upsilon(1S)} = 0.35$ [197] obtained from CEM are much higher than the world data [82]. The data are also compared to the Color Glass Condensate Non-relativistic QCD calculation [66, 198, 199]. The model describes the $\Upsilon(1S)$ invariant cross section for $4 < p_T < 10\,\mathrm{GeV/c}$, while the rest is overestimated. In addition the data at $p_T < 2\,\mathrm{GeV/c}$ are overestimated, as the authors mentioned, that more corrections are needed to improve the description there [66, 199]. So far, this is the only measurement of Υ p_T spectrum at RHIC energy range.

The rapidity dependence was also investigated for $\Upsilon(1S+2S+3S)$, $\Upsilon(1S)$ and $\Upsilon(2S+3S)$. A dip for $\Upsilon(1S+2S+3S)$ and $\Upsilon(2S+3S)$ cross section at $|y| < 0.5$ is observed, which may be a downward fluctuation in the data. Besides that, the $\Upsilon(1S)$ results are well described by the CEM model, while the $\Upsilon(1S+2S+3S)$ is slightly above. The CEM fails to describe the data at $\Upsilon(2S+3S)$. The CGC+NRQCD model overestimates the data due to the excess for $p_T < 2\,\mathrm{GeV/c}$, but reproduces the trend qualitatively. In general, a more flat dependence is observed at $\sqrt{s} = 500\,\mathrm{GeV/c}$ than at $\sqrt{s} = 200\,\mathrm{GeV}$ [151, 196].

The $\frac{\Upsilon(nS)}{\Upsilon(1S)}$ ratios was calculated and compared to the measurements at different energies [82].

STAR results are below the fits to the world data, but they are more consistent for $p_T < 6\mathrm{GeV/c}$. In addition a charged particle multiplicity dependence was investigated. The multiplicity is represented by $TofMult$. The results are consistent with other experiments, but the $\frac{\Upsilon(2S+3S)}{\Upsilon(1S)}$ and $\frac{\Upsilon(2S)}{\Upsilon(1S)}$ ratios for $TofMult < 8$ are below. No strong dependence is observed on charged track multiplicity within uncertainties. This suggests no strong Υ interaction with hadrons.

An event activity dependence of Υ production was also investigated. The corrected charged particle multiplicity N_{ch} is used as a measure of event activity. The dependence of $\frac{N_\Upsilon}{\langle N_\Upsilon \rangle}$ on $\frac{\langle N_{ch} \rangle^{bin}}{\langle N_{ch} \rangle^{all}}$ is studied and compared to the world data. STAR results for $\Upsilon(1S+2S+3S)$, $\Upsilon(1S)$ for $p_T < 10$ GeV/c and $4 < p_T < 10$ GeV/c are consistent with the other heavy flavor meson production measured at RHIC and LHC energies. A strong dependence on $\frac{\langle N_{ch} \rangle^{bin}}{\langle N_{ch} \rangle^{all}}$, which is faster than linear is observed. Moreover, the data are consistent with String Percolation Model [5, 6], which may suggest collective behavior in high multiplcity $p+p$ collisions. A PYTHIA8 calculation is also consistent with the data, which indicates that Υ may be produced in multiple parton interactions. More data at higher values of $\frac{\langle N_{ch} \rangle^{bin}}{\langle N_{ch} \rangle^{all}}$ and more p_T differential studies are needed to distinguish the models.

Finally, an x_T dependence is studied to check the scaling behavior predicted by the pQCD. No scaling is observed, however there might be a suggestion of scaling between CDF [80] and LHC data [76, 77].

The result of J/ψ production studies is also an integrated cross section, which is found to be $B_{ee}\frac{d\sigma_{J/\psi}}{dy} = 38 \pm 11$ (stat.) ± 16 (syst.) nb [178]. This is consistent with PHENIX and a new STAR preliminary measurement from Run12 [196].

The J/ψ invariant cross section was also measured and compared to the STAR [180] and PHENIX [182] data. It is consistent with both.

A $\langle p_T^2 \rangle$ was also calculated and compared to the world data [178]. The obtained value is $\langle p_T^2 \rangle = 3.45 \pm 0.85$ (stat.) ± 1.22 (syst.) $(\mathrm{GeV/c})^2$ which is consistent with STAR+PHENIX $d+Au$ [178] and PHENIX $p+p$ [181] and $d+Au$ [212] results. The STAR results follow the same trend observed in the world data. The difference between PHENIX $p+p$ and $d+Au$ measurements may be due to the Cronin effect [209, 210].

Appendices

Appendix A

Fits to $b\bar{b}$ from PYTHIA8

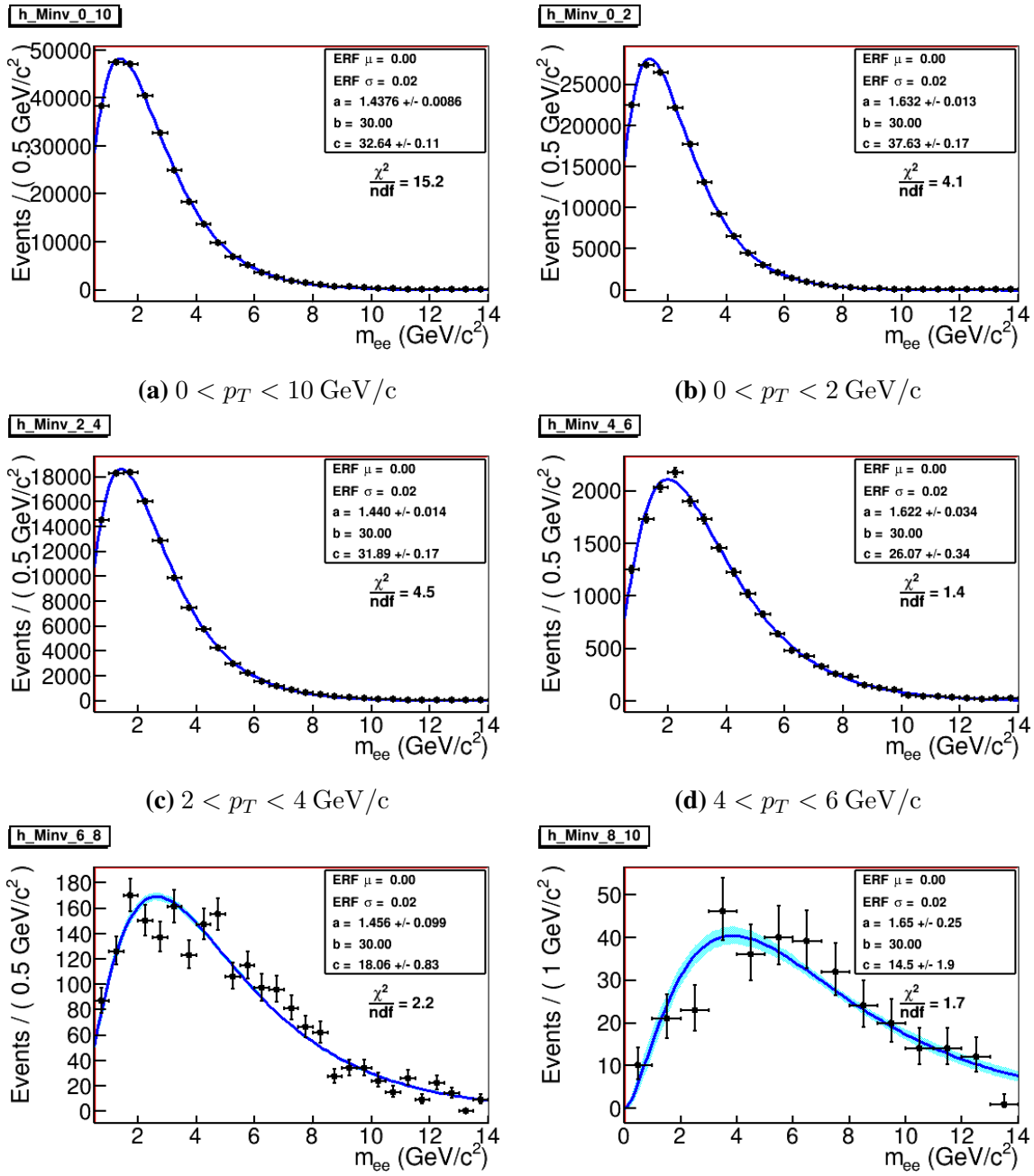

(a) $0 < p_T < 10$ GeV/c

(b) $0 < p_T < 2$ GeV/c

(c) $2 < p_T < 4$ GeV/c

(d) $4 < p_T < 6$ GeV/c

(e) $6 < p_T < 8$ GeV/c

(f) $8 < p_T < 10$ GeV/c

Figure A.1: Power law fits (blue) to invariant mass of $b\bar{b} \to B\bar{B} \to e^+e^- + X$ from PYTHIA8 (black).

Appendix B

Fits to $n\sigma_e$ distributions of photonic electrons

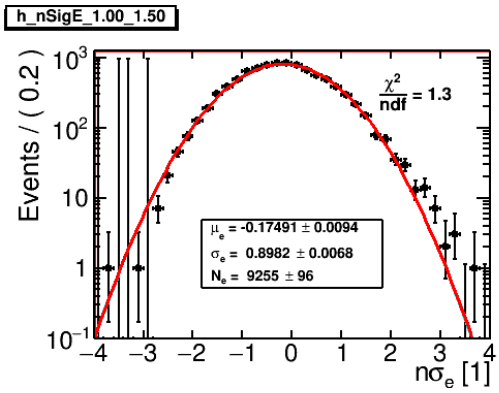

(a) $1 < p < 1.5$ GeV/c

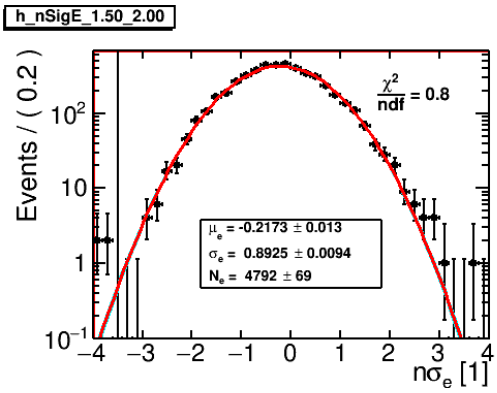

(b) $1.5 < p < 2$ GeV/c

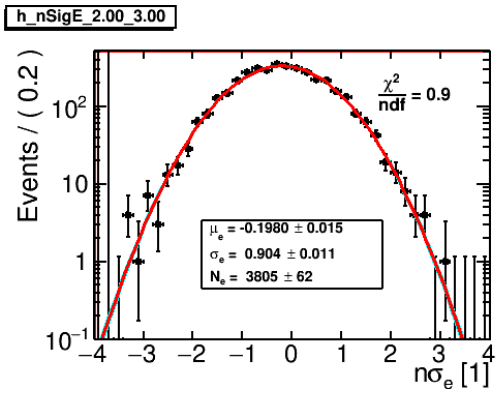

(c) $2 < p < 3$ GeV/c

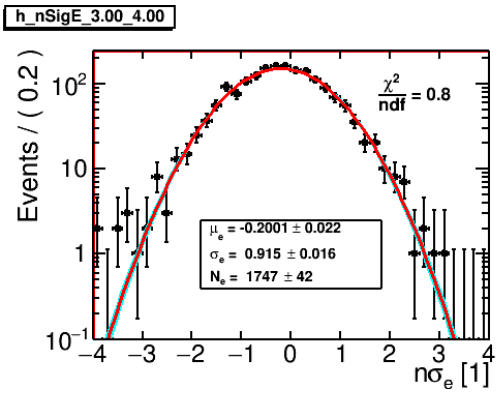

(d) $3 < p < 4$ GeV/c

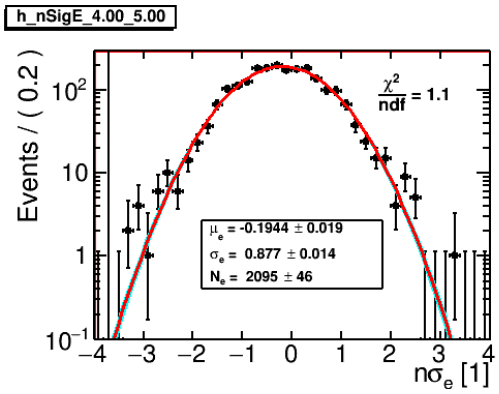

(e) $4 < p < 5$ GeV/c

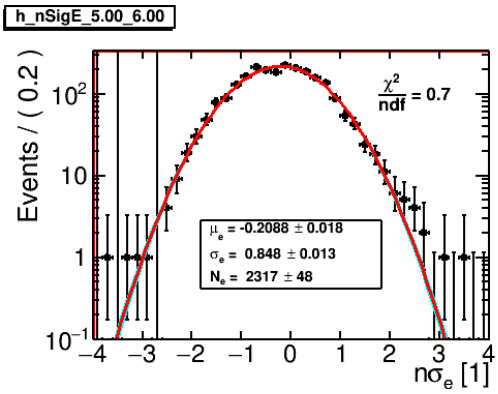

(f) $5 < p < 6$ GeV/c

Figure B.1: Gaussian fits (red) to $n\sigma_e$ distributions from photonic electrons (black).

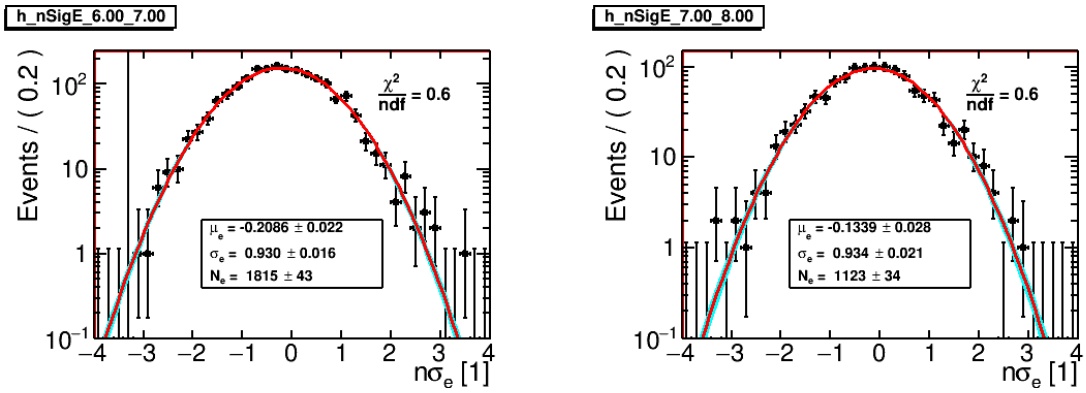

(a) $6 < p < 7$ GeV/c

(b) $7 < p < 8$ GeV/c

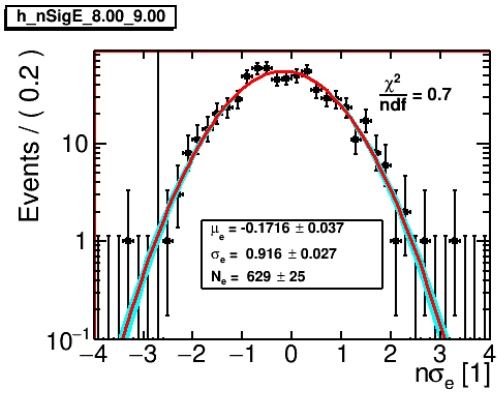

(c) $8 < p < 9$ GeV/c

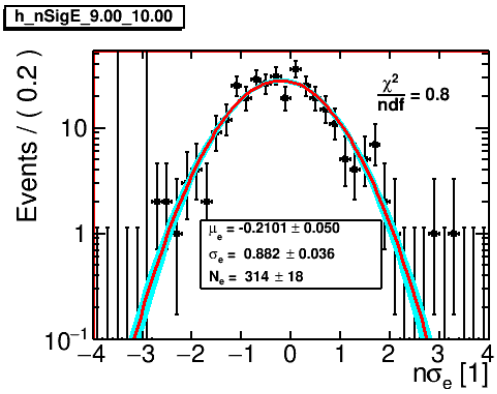

(d) $9 < p < 10$ GeV/c

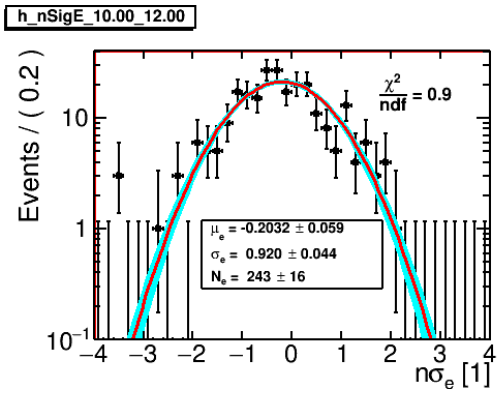

(e) $10 < p < 12$ GeV/c

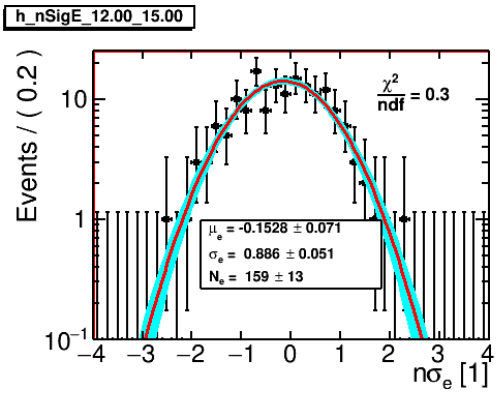

(f) $12 < p < 15$ GeV/c

Figure B.2: Gaussian fits (red) to $n\sigma_e$ distributions from photonic electrons (black).

Appendix C

Fits to Υ lineshapes from embedding simulations

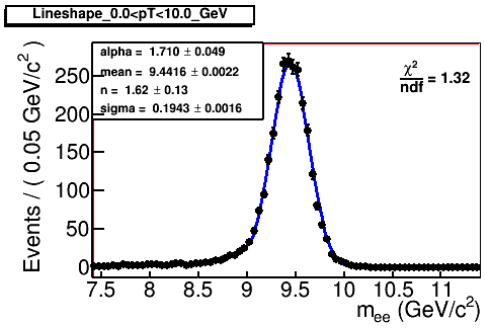

(a) $0 < p_T < 10$ GeV/c

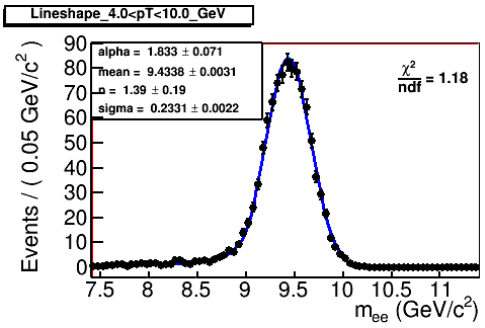

(b) $4 < p_T < 10$ GeV/c

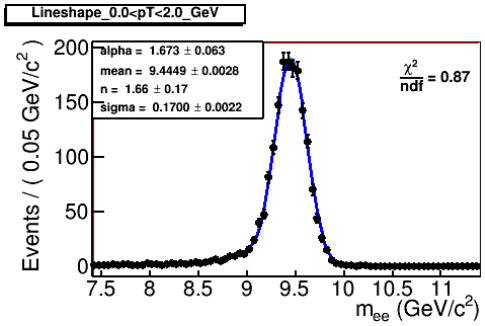

(c) $0 < p_T < 2$ GeV/c

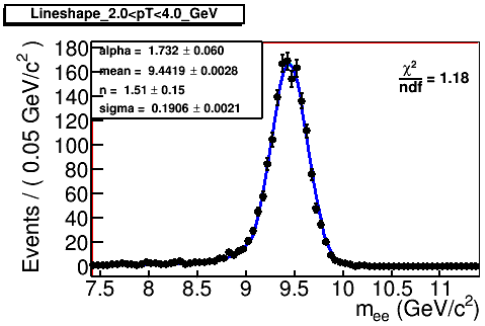

(d) $2 < p_T < 4$ GeV/c

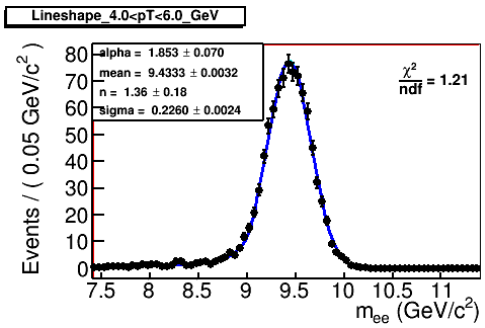

(e) $4 < p_T < 6$ GeV/c

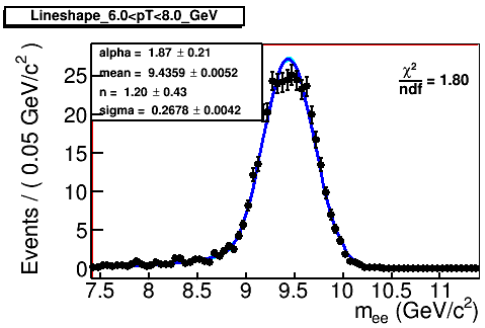

(f) $6 < p_T < 8$ GeV/c

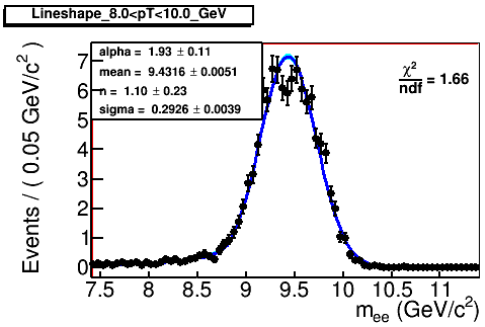

(g) $8 < p_T < 10$ GeV/c

Figure C.1: Crystal Ball function fits (blue) to $\Upsilon(1S)$ lineshapes from embedding (black).

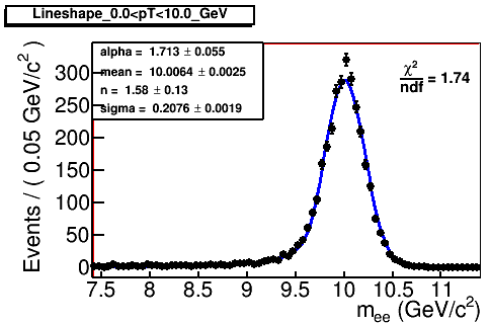

(a) $0 < p_T < 10$ GeV/c

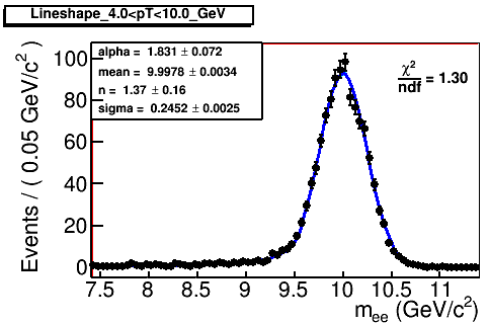

(b) $4 < p_T < 10$ GeV/c

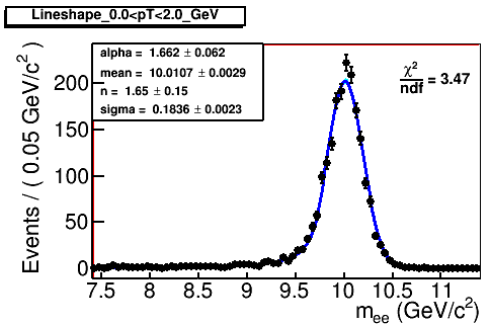

(c) $0 < p_T < 2$ GeV/c

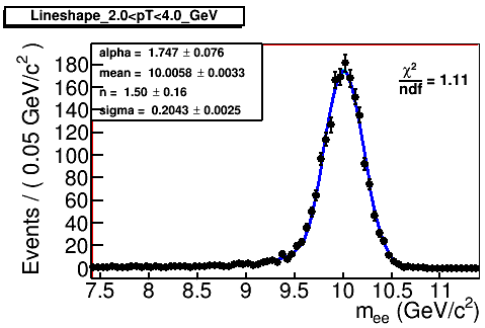

(d) $2 < p_T < 4$ GeV/c

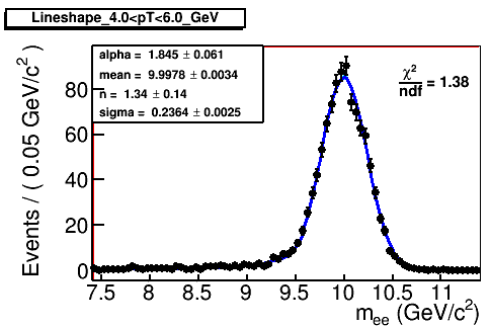

(e) $4 < p_T < 6$ GeV/c

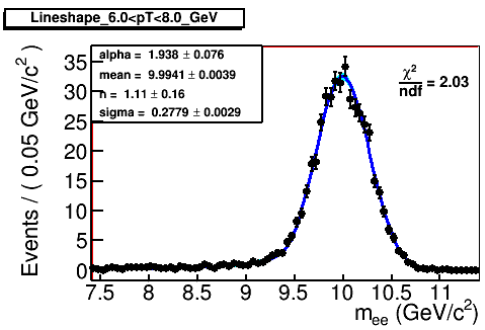

(f) $6 < p_T < 8$ GeV/c

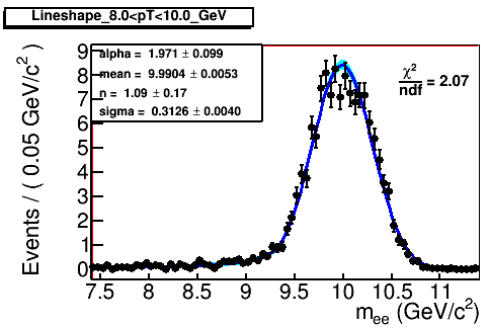

(g) $8 < p_T < 10$ GeV/c

Figure C.2: Crystal Ball function fits (blue) to $\Upsilon(2S)$ lineshapes from embedding (black).

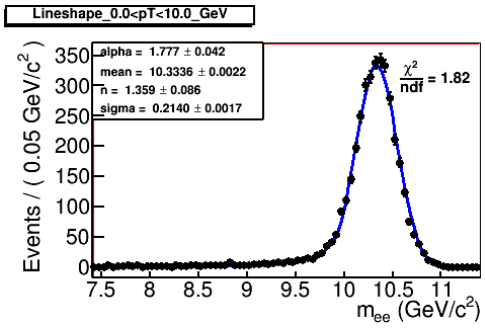

(a) $0 < p_T < 10$ GeV/c

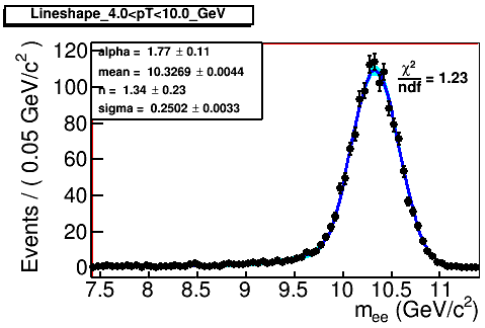

(b) $4 < p_T < 10$ GeV/c

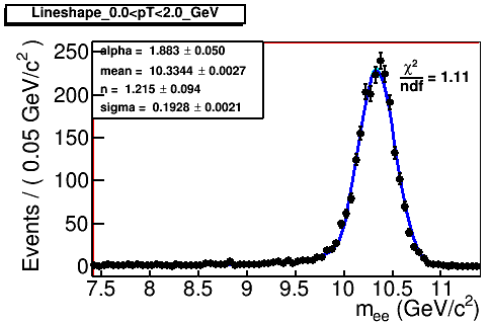

(c) $0 < p_T < 2$ GeV/c

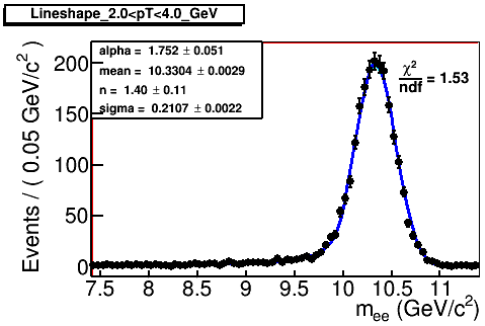

(d) $2 < p_T < 4$ GeV/c

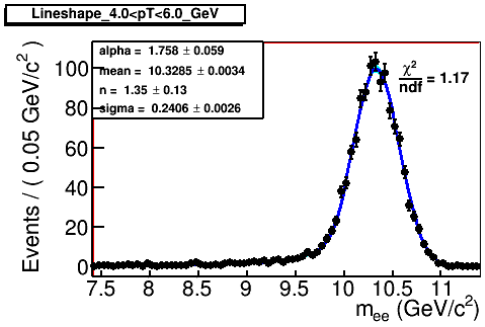

(e) $4 < p_T < 6$ GeV/c

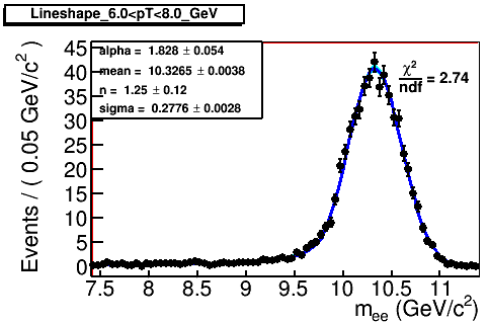

(f) $6 < p_T < 8$ GeV/c

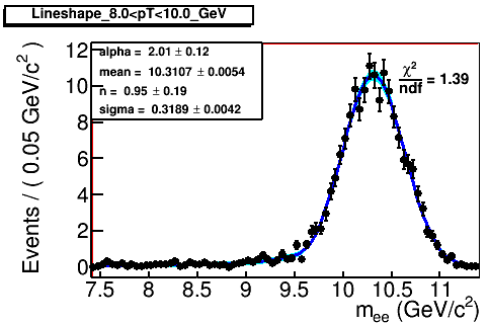

(g) $8 < p_T < 10$ GeV/c

Figure C.3: Crystal Ball function fits (blue) to $\Upsilon(3S)$ lineshapes from embedding (black).

Appendix D

Υ yield tables

p_T [GeV/c]	yield	stat.	syst.	glob.	yield from fit	stat.
$0-10$	701	41	90	-	700	43
$0-2$	136	20	13	13	138	21
$2-4$	240	24	22	23	236	25
$4-6$	171	21	16	16	173	23
$6-8$	88	16	9	9	90	18
$8-10$	38	10	7	4	44	12

Table D.1: $\Upsilon(1S+2S+3S)$ yield vs. p_T, which includes mass cut efficiency correction for contribution of other Υ states. The systematic uncertainty on the p_T-integrated yield includes global systematic uncertainty.

p_T [GeV/c]	yield	stat.	syst.	glob.	yield from fit	stat.
$0-10$	543	32	70	-	544	34
$0-2$	123	15	11	12	122	16
$2-4$	183	19	19	18	175	20
$4-6$	142	17	13	14	144	19
$6-8$	66	16	7	7	69	19
$8-10$	23	8	12	3	34	14

Table D.2: $\Upsilon(1S)$ yield, which includes mass cut efficiency and purity corrections for contribution of other Υ states. The systematic uncertainty on the p_T-integrated yield includes global systematic uncertainty.

p_T [GeV/c]	yield	stat.	syst.	glob.	yield from fit	stat.
$0-10$	115	19	18	-	105	27
$0-2$	7	5	2	1	9	8
$2-4$	45	12	5	5	43	17
$4-6$	30	10	9	3	22	12
$6-8$	0.3	0.1	11	0.1	11	7
$8-10$	22	9	13	3	9	9

Table D.3: $\Upsilon(2S)$ yield vs. p_T, which includes mass cut efficiency and purity corrections for contribution of other Υ states. The systematic uncertainty on the p_T-integrated yield includes global systematic uncertainty.

p_T [GeV/c]	yield	stat.	syst.	glob.	yield from fit	stat.
$0-10$	52	17	8	-	51	25
$0-2$	9	6	3	1	7	7
$2-4$	17	8	3	2	19	12
$4-6$	3	2	6	1	8	9
$6-8$	21	8	11	2	11	7
$8-10$	0	-	7	1	0	3

Table D.4: $\Upsilon(3S)$ yield vs. p_T, which includes mass cut efficiency and purity corrections for contribution of other Υ states. The systematic uncertainty on the p_T-integrated yield includes global systematic uncertainty.

type	y [1]	yield	stat.	syst.	glob.	yield from fit	stat.
$\Upsilon(1S+2S+3S)$	$\|y\| < 0.5$	449	33	41	42	456	35
	$0.5 < \|y\| < 1$	258	25	25	25	250	25
$\Upsilon(1S)$	$\|y\| < 0.5$	373	26	33	35	374	28
	$0.5 < \|y\| < 1$	173	18	16	17	172	19
$\Upsilon(2S)$	$\|y\| < 0.5$	68	14	8	7	66	21
	$0.5 < \|y\| < 1$	48	14	9	5	41	19
$\Upsilon(3S)$	$\|y\| < 0.5$	14	11	4	2	16	18
	$0.5 < \|y\| < 1$	40	14	6	4	37	19

Table D.5: Υ yield vs. rapidity, which includes mass cut efficiency and purity corrections for contribution of other Υ states.

type	$TofMult$ [1]	yield	stat.	syst.	yield from fit	stat.
$\Upsilon(1S+2S+3S)$	$0 < TOfMult < 4$	196	20	75	195	21
	$4 < TOfMult < 8$	333	27	41	328	28
	$8 < TOfMult < 12$	99	18	18	106	20
	$12 < TOfMult < 100$	29	11	9	35	14
$\Upsilon(1S)$	$0 < TOfMult < 4$	159	16	42	157	17
	$4 < TOfMult < 8$	254	21	32	249	23
	$8 < TOfMult < 12$	76	13	15	84	16
	$12 < TOfMult < 100$	26	13	7	29	16
$\Upsilon(2S)$	$0 < TOfMult < 4$	25	8	11	24	13
	$4 < TOfMult < 8$	32	11	8	49	16
	$8 < TOfMult < 12$	23	9	5	23	14
	$12 < TOfMult < 100$	6	4	4	3	3
$\Upsilon(3S)$	$0 < TOfMult < 4$	12	6	21	55	11
	$4 < TOfMult < 8$	32	10	5	30	13
	$8 < TOfMult < 12$	-	-	-	-	-
	$12 < TOfMult < 100$	-	-	-	-	-

Table D.6: Υ yield vs. $TofMult$, which includes mass cut efficiency and purity corrections for contribution of other Υ states. The systematic uncertainties include only those, which affect the yield used as an input to unfolding procedure.

Appendix E

Fits to $n\sigma_e$ distributions of photonic electrons for J/ψ studies

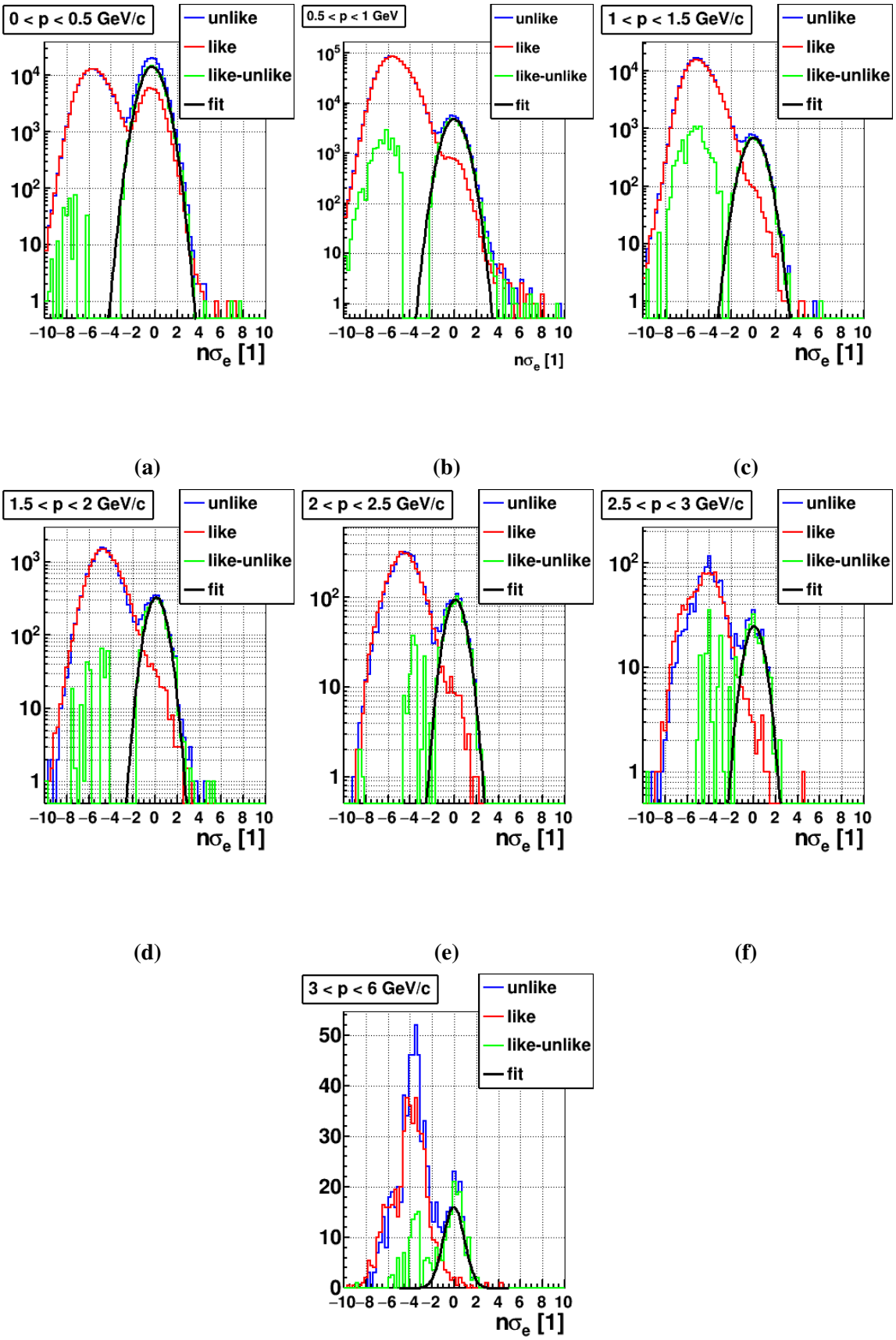

Figure E.1: Gaussian fits to $n\sigma_e$ distributions of photonic electrons for J/ψ studies

Appendix F

Gaussian fits inclusive particle to $n\sigma_e$ distributions for J/ψ studies

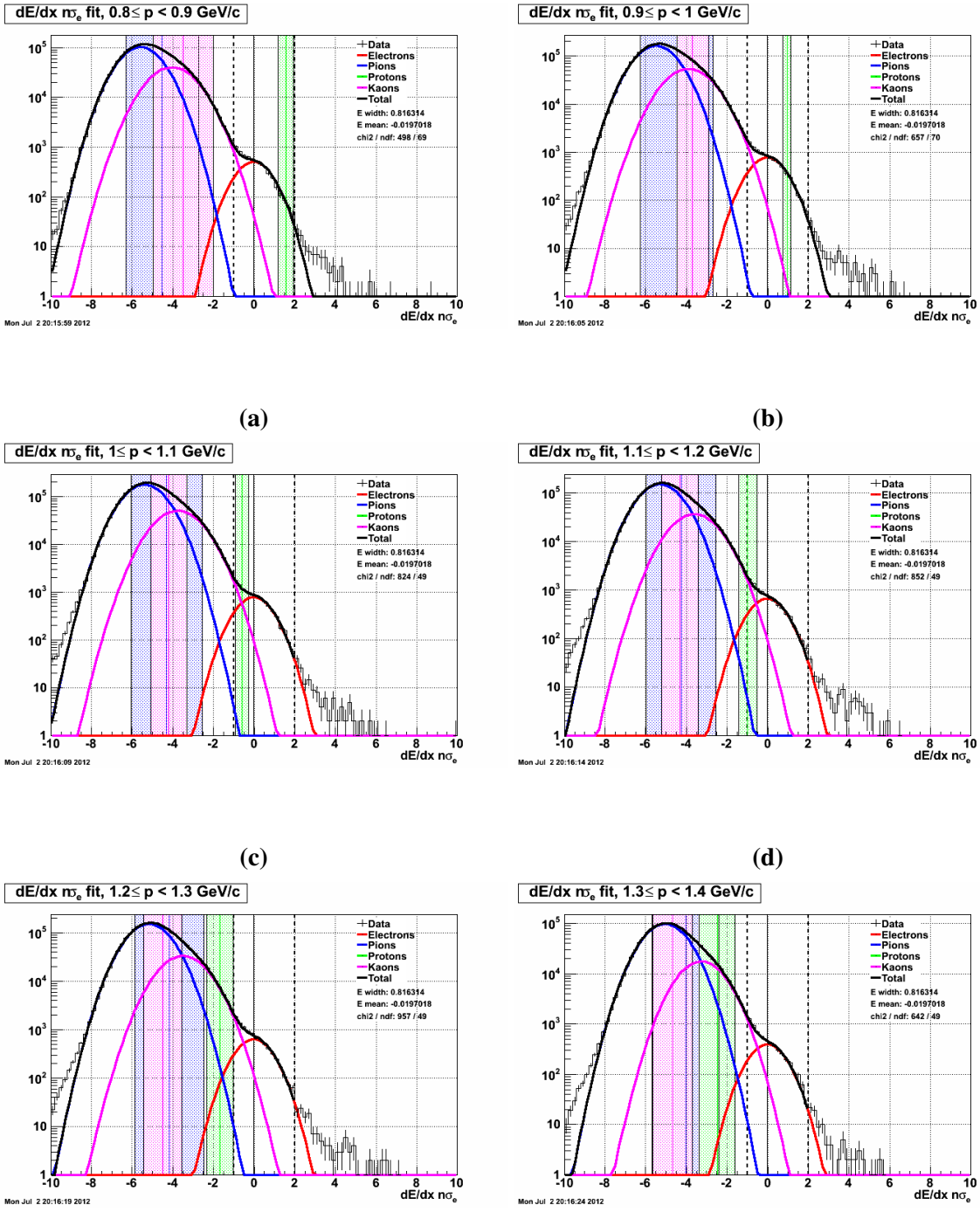

Figure F.1: Gaussian fits to inclusive particle $n\sigma_e$ distributions for J/ψ studies

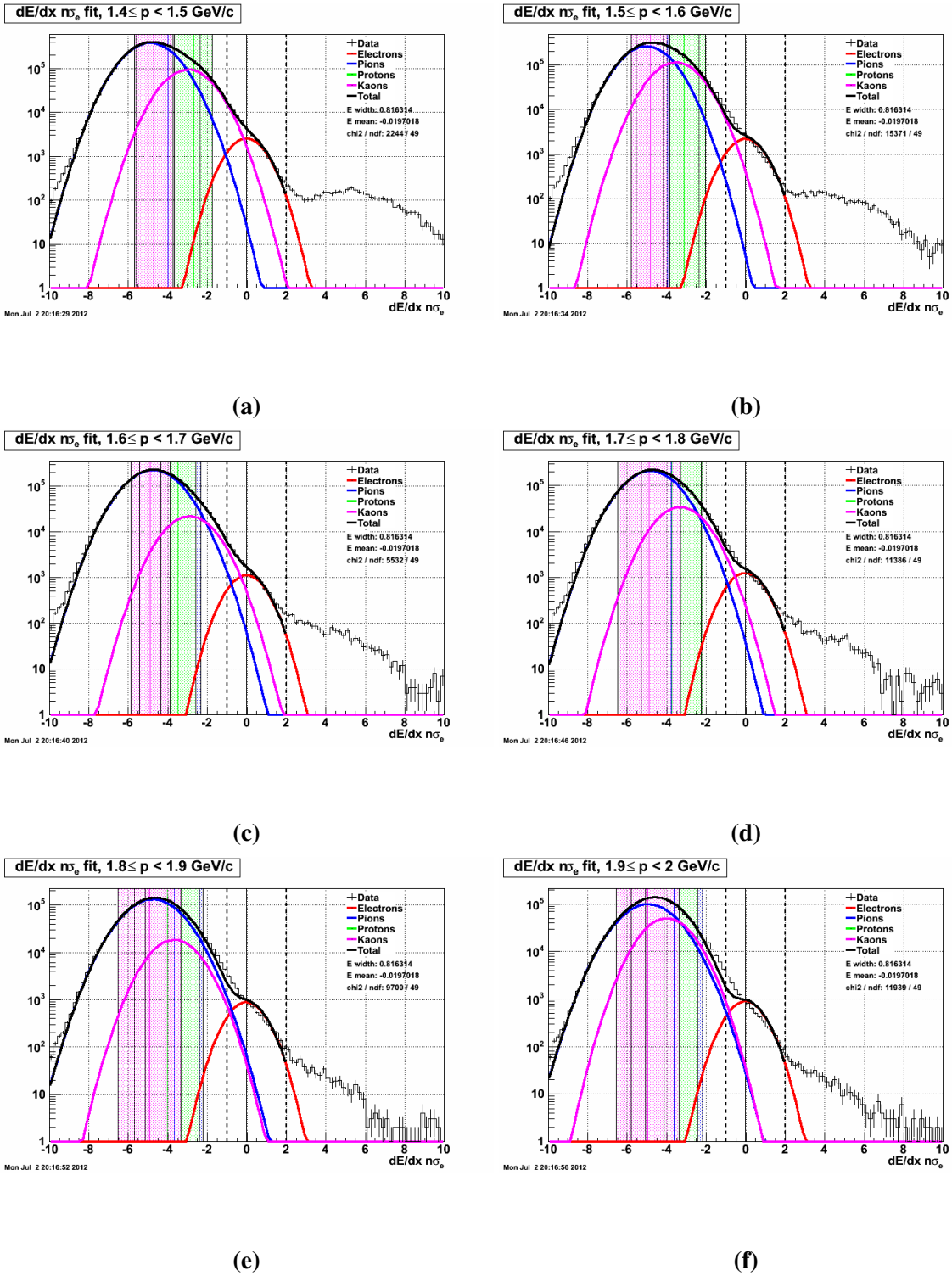

Figure F.2: Gaussian fits to inclusive particle $n\sigma_e$ distributions for J/ψ studies

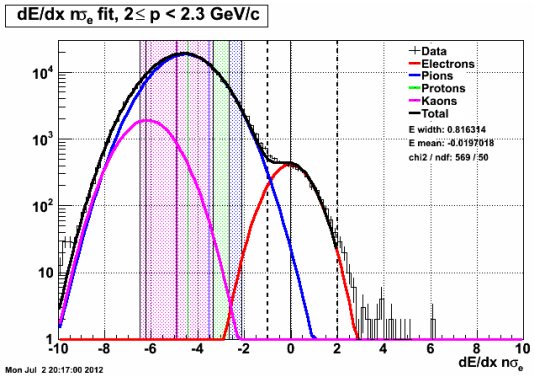

(a)

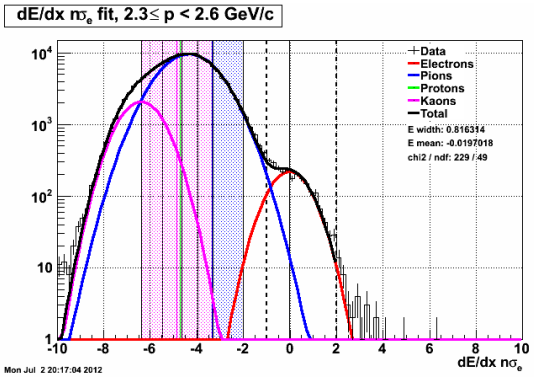

(b)

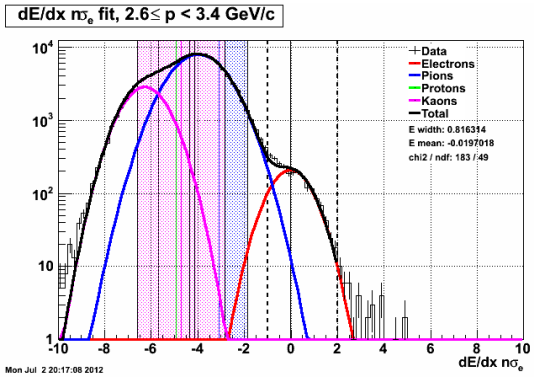

(c)

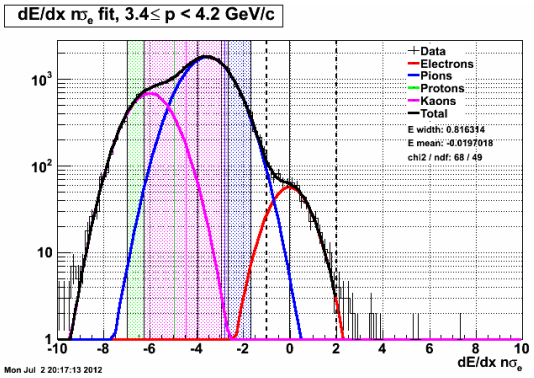

(d)

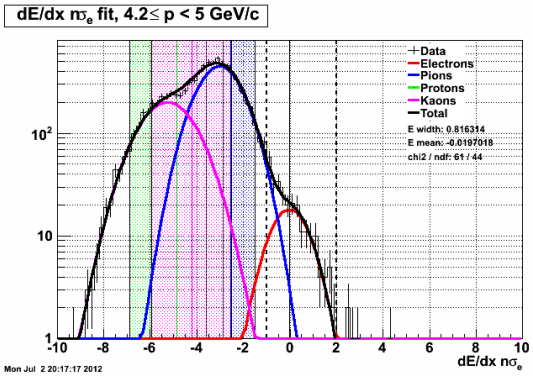

(e)

Figure F.3: Gaussian fits to inclusive particle $n\sigma_e$ distributions for J/ψ studies

Bibliography

[1] R. Ma, *Measurement of J/psi production in p+p collisions at sqrt{s} = 500 GeV at STAR experiment*, Nuclear and Particle Physics Proceedings, vol. 276-278, pp. 261–264, jul 2016, arXiv:1509.06440.

[2] B. Abelev, *et al.*, *J/psi Production as a Function of Charged Particle Multiplicity in pp Collisions at sqrt{s} = 7 TeV*, Physics Letters B, vol. 712, pp. 165–175, jun 2012, arXiv:1202.2816.

[3] J. Adam, *et al.*, *Measurement of charm and beauty production at central rapidity versus charged-particle multiplicity in proton-proton collisions at sqrt(s)=7 TeV*, Journal of High Energy Physics, vol. 2015, p. 148, sep 2015, arXiv:1505.00664 [nucl-ex].

[4] S. Chatrchyan, *et al.*, *Event activity dependence of Y(nS) production in sqrt(s_NN) = 5.02 TeV pPb and sqrt(s) = 2.76 TeV pp collisions*, Journal of High Energy Physics, vol. 2014, p. 103, apr 2014, arXiv:1312.6300.

[5] E. G. Ferreiro - private communications.

[6] E. G. Ferreiro and C. Pajares, *High multiplicity pp events and J/psi production at LHC*, Physical Review C, vol. 86, p. 034903, sep 2012, arXiv:arXiv:1203.5936v1.

[7] C. Aidala, *et al.*, *Measurements of azimuthal anisotropy and charged-particle multiplicity in d+Au collisions at sqrt(s_NN)=200, 62.4, 39, and 19.6 GeV*, aug 2017, arXiv:1708.06983.

[8] C. Aidala, *et al.*, *Measurements of multiparticle correlations in d+Au collisions at 200, 62.4, 39, and 19.6 GeV and p+Au collisions at 200 GeV and implications for collective behavior*, jul 2017, arXiv:1707.06108.

[9] K. Dusling, W. Li, and B. Schenke, *Novel Collective Phenomena in High-Energy Proton-Proton and Proton-Nucleus Collisions*, International Journal of Modern Physics E, vol. 25, p. 1630002, jan 2016, arXiv:1509.07939.

[10] C. Loizides, *Experimental overview on small collision systems at the LHC*, Nuclear Physics A, vol. 956, pp. 200–207, dec 2016, arXiv:1602.09138.

[11] https://drupal.star.bnl.gov/STAR/files/QM15_Upsilon_poster_LK_v3_0.pdf.

[12] https://en.wikipedia.org/wiki/File:Qcd_fields_field_(physics).svg.

[13] http://www.fz-juelich.de/.

[14] D. H. Perkins, *Introduction to high energy physics*, Cambridge University Press, 2000.

[15] K. Olive, *Review of Particle Physics*, Chinese Physics C, vol. 40, p. 100001, oct 2016.

[16] D. J. Gross and F. Wilczek, *Ultraviolet Behavior of Non-Abelian Gauge Theories*, Physical Review Letters, vol. 30, pp. 1343–1346, jun 1973.

[17] H. D. Politzer, *Reliable Perturbative Results for Strong Interactions?*, Physical Review Letters, vol. 30, pp. 1346–1349, jun 1973.

[18] W. Florkowski, *Phenomenology of Ultra-Relativistic Heavy-Ion Collisions*, World Scientific, Singapore, 2010.

[19] J. C. Collins and M. J. Perry, *Superdense Matter: Neutrons or Asymptotically Free Quarks?*, Physical Review Letters, vol. 34, pp. 1353–1356, may 1975.

[20] E. Shuryak, *Quark-gluon plasma and hadronic production of leptons, photons and psions*, Physics Letters B, vol. 78, pp. 150–153, sep 1978.

[21] E. V. Shuryak, *Quantum chromodynamics and the theory of superdense matter*, Physics Reports, vol. 61, pp. 71–158, may 1980.

[22] F. Karsch, *Lattice QCD at High Temperature and Density*, in *Lectures on Quark Matter*, pp. 209–249, Berlin, Heidelberg: Springer Berlin Heidelberg, jun 2001.

[23] J. Rafelski, *Connecting QGP-Heavy Ion Physics to the Early Universe*, Nuclear Physics B - Proceedings Supplements, vol. 243-244, pp. 155–162, oct 2013, arXiv:1306.2471.

[24] J. C. Collins, D. E. Soper, and G. Sterman, *Factorization of Hard Processes in QCD*, arXiv:hep-ph/0409313, sep 2004, arXiv:0409313 [hep-ph].

[25] https://www.bnl.gov/rhic/images/proton-with-gluouns-300px.jpg.

[26] A. D. Martin, *et al.*, *Parton distributions for the LHC*, The European Physical Journal C, vol. 63, pp. 189–285, sep 2009, arXiv:0901.0002.

[27] https://mstwpdf.hepforge.org/.

[28] R. Angeles-Martinez, *et al.*, *Transverse momentum dependent (TMD) parton distribution functions: status and prospects*, jul 2015, arXiv:1507.05267.

[29] M. Diehl, *Generalized parton distributions*, Physics Reports, vol. 388, pp. 41–277, dec 2003, arXiv:0307382 [hep-ph].

[30] T. Sjöstrand, *Multiple Parton-Parton Interactions in Hadronic Events*, FERMILAB-PUB-85-119-T, 1985.

[31] T. Sjöstrand and M. van Zijl, *A multiple-interaction model for the event structure in hadron collisions*, Physical Review D, vol. 36, pp. 2019–2041, oct 1987.

[32] T. Sjöstrand, *The Development of MPI Modelling in PYTHIA*, LU TP 17-22,MCnet-17-10, jun 2017, arXiv:1706.02166.

[33] http://www.desy.de/~jung/multiple-interactions/may06/mi-rick.gif.

[34] L. McLerran, *The Color Glass Condensate and Small x Physics: 4 Lectures*, apr 2001, arXiv:0104285 [hep-ph].

[35] M. Gyulassy and L. McLerran, *New forms of QCD matter discovered at RHIC*, Nuclear Physics A, vol. 750, pp. 30–63, mar 2005, arXiv:0405013 [nucl-th].

[36] F. Gelis, *et al.*, *The Color Glass Condensate*, Annual Review of Nuclear and Particle Science, vol. 60, pp. 463–489, nov 2010, arXiv:1002.0333.

[37] J. Adam, *et al.*, *Enhanced production of multi-strange hadrons in high-multiplicity proton-proton collisions*, Nature Physics, vol. 13, pp. 535–539, apr 2017, arXiv:1606.07424.

[38] W. A. Horowitz, *Probing the Frontiers of QCD*, nov 2010, arXiv:1011.4316.

[39] V. Khachatryan, *et al.*, *Evidence for collectivity in pp collisions at the LHC*, Physics Letters B, vol. 765, pp. 193–220, feb 2017, arXiv:1606.06198.

[40] S. Chatrchyan, *et al.*, *Measurement of the Underlying Event Activity at the LHC with sqrt(s)= 7 TeV and Comparison with sqrt(s) = 0.9 TeV*, Journal of High Energy Physics, vol. 2011, p. 109, sep 2011, arXiv:1107.0330.

[41] V. Khachatryan, *et al.*, *Measurement of the underlying event activity using charged-particle jets in proton-proton collisions at sqrt(s) = 2.76 TeV*, Journal of High Energy Physics, vol. 2015, p. 137, sep 2015, arXiv:1507.07229.

[42] E. G. Ferreiro and C. Pajares, *Open charm production in high multiplicity proton-proton events at the LHC*, pp. 1–7, 2015, arXiv:1501.03381.

[43] G. S. Bali, *QCD forces and heavy quark bound states*, Physics Reports, vol. 343, pp. 1–136, mar 2001, arXiv:0001312 [hep-ph].

[44] T. Matsui and H. Satz, *J/ψ suppression by quark-gluon plasma formation*, Physics Letters B, vol. 178, no. 4, pp. 416–422, 1986.

[45] N. Brambilla, *et al.*, *Heavy quarkonium: progress, puzzles, and opportunities*, The European Physical Journal C, vol. 71, p. 1534, feb 2011, arXiv:1010.5827.

[46] S. Chatrchyan, *et al.*, *Observation of sequential Upsilon suppression in PbPb collisions*, Physical Review Letters, vol. 109, p. 222301, nov 2012, arXiv:1208.2826.

[47] R. Vogt, *Shadowing and absorption effects on J/psi production in d+A collisions*, Physical Review C, vol. 71, p. 054902, may 2005.

[48] J. J. Aubert, *et al.*, *Experimental Observation of a Heavy Particle J*, Physical Review Letters, vol. 33, pp. 1404–1406, dec 1974.

[49] J. E. Augustin, *et al.*, *Discovery of a Narrow Resonance in e+ e Annihilation*, Physical Review Letters, vol. 33, pp. 1406–1408, dec 1974.

[50] S. W. Herb, *et al.*, *Observation of a Dimuon Resonance at 9.5 GeV in 400-GeV Proton-Nucleus Collisions*, Physical Review Letters, vol. 39, pp. 252–255, aug 1977.

[51] B. Trzeciak and STAR Collaboration, *Measurements of Quarkonium Polarization and Production versus Charged-Particle Multiplicity in p+p Collisions at* $\sqrt{s} = 500\,\mathrm{GeV}$ *in the STAR experiment*, vol. Quark Matter 2015, Kobe, 2015.

[52] C. Chao-Hsi, *Hadronic production of J/ψ associated with a gluon*, Nuclear Physics B, vol. 172, pp. 425–434, jan 1980.

[53] R. Baier and R. Rückl, *Hadronic production of J/ψ and γ: Transverse momentum distributions*, Physics Letters B, vol. 102, pp. 364–370, jun 1981.

[54] E. L. Berger and D. Jones, *Inelastic Photoproduction of J/psi and Upsilon by Gluons*, Physical Review D, vol. 23, pp. 1521–1530, apr 1981.

[55] A. Andronic, *et al.*, *Heavy-flavour and quarkonium production in the LHC era: from proton-proton to heavy-ion collisions*, The European Physical Journal C, vol. 76, p. 107, mar 2016, arXiv:1506.03981.

[56] M. Krämer, *Quarkonium production at high-energy colliders*, Progress in Particle and Nuclear Physics, vol. 47, pp. 141–201, jan 2001, arXiv:0106120 [hep-ph].

[57] G. T. Bodwin, *et al.*, *P-wave charmonium production in B-meson decays*, Physical Review D, vol. 46, pp. R3703–R3707, nov 1992.

[58] G. T. Bodwin, E. Braaten, and G. P. Lepage, *Rigorous QCD analysis of inclusive annihilation and production of heavy quarkonium*, Physical Review D, vol. 51, pp. 1125–1171, feb 1995.

[59] G. T. Bodwin, E. Braaten, and G. P. Lepage, *Erratum: Rigorous QCD analysis of inclusive annihilation and production of heavy quarkonium [Phys. Rev. D 51 , 1125 (1995)]*, Physical Review D, vol. 55, pp. 5853–5854, may 1997.

[60] Y.-Q. Ma, K. Wang, and K.-T. Chao, *J/psi (psi') production at the Tevatron and LHC at O(α_s^4v^4) in nonrelativistic QCD*, Physical Review Letters, vol. 106, p. 042002, jan 2011.

[61] K. Wang, Y.-Q. Ma, and K.-T. Chao, *Upsilon(1S) prompt production at the Tevatron and LHC in nonrelativistic QCD*, feb 2012, arXiv:1202.6012.

[62] H.-S. Shao, *et al.*, *Yields and polarizations of prompt J/psi and psi(2S) production in hadronic collisions*, Journal of High Energy Physics, vol. 2015, p. 103, may 2015, arXiv:1411.3300.

[63] https://drupal.star.bnl.gov/STAR/files/yezhenyu_MPI_20161128_v3_0.pdf.

[64] M. Butenschoen and B. A. Kniehl, *World data of Jpsi production consolidate NRQCD factorization at NLO*, Physical Review D, vol. 84, p. 051501, sep 2011, arXiv:1105.0820.

[65] Z.-B. Kang, Y.-Q. Ma, and R. Venugopalan, *Quarkonium production in high energy proton-nucleus collisions: CGC meets NRQCD*, Journal of High Energy Physics, vol. 2014, p. 56, jan 2014, arXiv:1309.7337.

[66] Y.-Q. Ma and R. Venugopalan, *Comprehensive Description of J/psi Production in Proton-Proton Collisions at Collider Energies*, Physical Review Letters, vol. 113, p. 192301, nov 2014, arXiv:1408.4075.

[67] H. Fritzsch, *Producing heavy quark flavors in hadronic collisions-'A test of quantum chromodynamics*, Physics Letters B, vol. 67, pp. 217–221, mar 1977.

[68] V. Barger, W. Keung, and R. Phillips, *On psi and Upsilon production via gluons*, Physics Letters B, vol. 91, pp. 253–258, apr 1980.

[69] V. Barger, W. Y. Keung, and R. J. N. Phillips, *Hadroproduction of ψ and Υ*, Zeitschrift für Physik C Particles and Fields, vol. 6, pp. 169–174, jun 1980.

[70] R. Vogt, *Shadowing effects on J/psi and Upsilon production at energies available at the CERN Large Hadron Collider*, Physical Review C, vol. 92, p. 034909, sep 2015, arXiv:1507.04418.

[71] R. E. Nelson, R. Vogt, and A. D. Frawley, *Narrowing the uncertainty on the total charm cross section and its effect on the J/psi cross section*, Physical Review C, vol. 87, p. 014908, jan 2013, arXiv:1210.4610.

[72] Y.-Q. Ma and R. Vogt, *Quarkonium Production in an Improved Color Evaporation Model*, Physical Review D, vol. 94, p. 114029, dec 2016, arXiv:1609.06042.

[73] J. D. de Deus and C. Pajares, *String percolation and the Glasma*, Physics Letters B, vol. 695, pp. 211–213, jan 2011, arXiv:1011.1099.

[74] L. Kosarzewski, *Quarkonia production vs event activity*, in *Proceedings of SPIE - The International Society for Optical Engineering* (R. S. Romaniuk, ed.), vol. 10031, p. 100313U, sep 2016.

[75] S. Chatrchyan, *et al.*, *Measurement of the Y(1S), Y(2S), and Y(3S) cross sections in pp collisions at sqrt(s) = 7 TeV*, Physics Letters B, vol. 727, pp. 101–125, nov 2013, arXiv:1303.5900.

[76] G. Aad, *et al.*, *Measurement of upsilon production in 7 TeV pp collisions at ATLAS*, Physical Review D - Particles, Fields, Gravitation and Cosmology, vol. 87, nov 2013, arXiv:1211.7255.

[77] V. Khachatryan, *et al.*, *Measurements of the Upsilon(1S), Upsilon(2S), and Upsilon(3S) differential cross sections in pp collisions at sqrt(s) = 7 TeV*, Physics Letters B, vol. 749, pp. 14–34, oct 2015, arXiv:1501.07750.

[78] B. Gong, *et al.*, *Complete next-to-leading-order study on the yield and polarization of Upsilon(1S,2S,3S) at the Tevatron and LHC*, Physical Review Letters, vol. 112, p. 032001, jan 2014, arXiv:1305.0748.

[79] C. Kourkoumelis, *et al.*, *Characteristics of J/psi and Upsilon production at the CERN intersecting storage rings*, Physics Letters B, vol. 91, pp. 481–486, apr 1980.

[80] D. Acosta, *et al.*, *Upsilon production and Polarization in p\bar{p} Collisions at sqrt(s)=1.8TeV*, Physical Review Letters, vol. 88, p. 161802, apr 2002.

[81] https://drupal.star.bnl.gov/STAR/system/files/upsilonppdAuAuAuTechnicalNote-v6.pdf.

[82] W. Zha, *et al.*, *Systematic study of the experimental measurements on ratios of different* Υ *states*, Physical Review C, vol. 88, p. 067901, dec 2013, arXiv:1308.4720.

[83] ATLAS Collaboration, *Observation of a new chi_b state in radiative transitions to Upsilon(1S) and Upsilon(2S) at ATLAS*, Phys. Rev. Lett., vol. 108, p. 152001, dec 2011, arXiv:1112.5154.

[84] R. Aaij, *et al.*, *Study of chi_{b} meson production in pp collisions at sqrt{s}=7 and 8TeV and observation of the decay chi_{b} -> Upsilon(3S) gamma*, The European Physical Journal C, vol. 74, p. 3092, oct 2014, arXiv:1407.7734.

[85] T. Sjöstrand, S. Mrenna, and P. Skands, *A Brief Introduction to PYTHIA 8.1*, oct 2007, arXiv:0710.3820.

[86] T. Huang, *et al.*, *Muon identification with Muon Telescope Detector at the STAR experiment*, Nuclear Instruments and Methods in Physics Research Section A: Accelerators, Spectrometers, Detectors and Associated Equipment, vol. 833, pp. 88–93, oct 2016, arXiv:1601.02910v3.

[87] V. Khachatryan, *et al.*, *Observation of Upsilon(1S) pair production in proton-proton collisions at sqrt(s) = 8 TeV*, Journal of High Energy Physics, vol. 2017, p. 13, may 2017, arXiv:1610.07095.

[88] R. Aaij, *et al.*, *Observation of double charm production involving open charm in pp collisions at sqrt(s)=7 TeV*, Journal of High Energy Physics, vol. 2012, p. 141, jun 2012, arXiv:1205.0975.

[89] R. Maciuła, *et al.*, *New mechanisms for double charmed meson production at the LHCb*, Physics Letters B, vol. 758, pp. 458–464, jul 2016, arXiv:1601.06981.

[90] M. Harrison, T. Ludlam, and S. Ozaki, *RHIC project overview*, Nuclear Instruments and Methods in Physics Research Section A: Accelerators, Spectrometers, Detectors and Associated Equipment, vol. 499, pp. 235–244, mar 2003.

[91] http://www.rhichome.bnl.gov/RHIC/Runs/RhicProjections.pdf.

[92] G. Zschornacka, M. Schmidt, and A. Thorn, *Electron Beam Ion Sources*, oct 2014, arXiv:1410.8014.

[93] K. Adcox, *et al.*, *PHENIX detector overview*, Nuclear Instruments and Methods in Physics Research Section A: Accelerators, Spectrometers, Detectors and Associated Equipment, vol. 499, pp. 469–479, mar 2003.

[94] K. Adcox, *et al.*, *PHENIX central arm tracking detectors*, Nuclear Instruments and Methods in Physics Research Section A: Accelerators, Spectrometers, Detectors and Associated Equipment, vol. 499, pp. 489–507, mar 2003.

[95] M. Aizawa, *et al.*, *PHENIX central arm particle ID detectors*, Nuclear Instruments and Methods in Physics Research Section A: Accelerators, Spectrometers, Detectors and Associated Equipment, vol. 499, pp. 508–520, mar 2003.

[96] L. Aphecetche, *et al.*, *PHENIX calorimeter*, Nuclear Instruments and Methods in Physics Research Section A: Accelerators, Spectrometers, Detectors and Associated Equipment, vol. 499, pp. 521–536, mar 2003.

[97] H. Akikawa, *et al.*, *PHENIX Muon Arms*, Nuclear Instruments and Methods in Physics Research Section A: Accelerators, Spectrometers, Detectors and Associated Equipment, vol. 499, pp. 537–548, mar 2003.

[98] A. Adare, *et al.*, *An Upgrade Proposal from the PHENIX Collaboration*, jan 2015, arXiv:1501.06197.

[99] S. Bültmann, *et al.*, *The PP2PP experiment at RHIC: silicon detectors installed in Roman Pots for forward proton detection close to the beam*, Nuclear Instruments and Methods in Physics Research Section A: Accelerators, Spectrometers, Detectors and Associated Equipment, vol. 535, no. 1, pp. 415–420, 2004.

[100] G. Odyniec, *The RHIC Beam Energy Scan program in STAR and what's next . . .* , Journal of Physics: Conference Series, vol. 455, p. 012037, aug 2013.

[101] K. C. Meehan, *Fixed Target Collisions at STAR*, Nuclear Physics A, vol. 956, pp. 878–881, 2016.

[102] A. Accardi, *et al.*, *Electron Ion Collider: The Next QCD Frontier - Understanding the glue that binds us all*, dec 2012, arXiv:1212.1701.

[103] F. Bergsma, *et al.*, *The STAR detector magnet subsystem*, Nuclear Instruments and Methods in Physics Research Section A: Accelerators, Spectrometers, Detectors and Associated Equipment, vol. 499, pp. 633–639, mar 2003.

[104] https://hep-project-dphep-portal.web.cern.ch/sites/hep-project-dphep-portal.web.cern.ch/files/rhic-map.png.

[105] http://www.star.bnl.gov/protected/heavy/aschmah/STAR_3D/STAR_FINAL_3D.jpg.

[106] M. Anderson, *et al.*, *The STAR time projection chamber: a unique tool for studying high multiplicity events at RHIC*, Nuclear Instruments and Methods in Physics Research Section A: Accelerators, Spectrometers, Detectors and Associated Equipment, vol. 499, pp. 659–678, mar 2003.

[107] L. Kotchenda, *et al.*, *STAR TPC gas system*, Nuclear Instruments and Methods in Physics Research, Section A: Accelerators, Spectrometers, Detectors and Associated Equipment, vol. 499, no. 2-3, pp. 703–712, 2003.

[108] A. Lebedev, *A laser calibration system for the STAR TPC*, Nuclear Instruments and Methods in Physics Research Section A: Accelerators, Spectrometers, Detectors and Associated Equipment, vol. 478, pp. 163–165, feb 2002.

[109] M. Anderson, *et al.*, *A Readout System for the STAR Time Projection Chamber*, Nuclear Instruments and Methods in Physics Research, Section A: Accelerators, Spectrometers, Detectors and Associated Equipment, vol. 499, pp. 679–691, may 2002, arXiv:0205014 [nucl-ex].

[110] K. H. Ackermann, *et al.*, *STAR detector overview*, Nuclear Instruments and Methods in Physics Research, Section A: Accelerators, Spectrometers, Detectors and Associated Equipment, vol. 499, no. 2-3, pp. 624–632, 2003, arXiv:1508.02614.

[111] Z. Xu, *et al.*, *A Heavy Flavor Tracker for STAR*, tech. rep., Lawrence Berkeley National Laboratory (LBNL), Berkeley, CA, mar 2005.

[112] L. Adamczyk, *et al.*, *Measurement of D0 azimuthal anisotropy at mid-rapidity in Au+Au collisions at sqrt(s_NN) = 200GeV*, Physical Review Letters, vol. 118, p. 212301, may 2017, arXiv:1701.06060.

[113] D. Beavis, *et al.*, *The STAR Heavy Flavor Tracker Conceptual Design Report Date : A Heavy Flavor Tracker for STAR*, 2009.

[114] J. Schambach, *et al.*, *The STAR Heavy Flavor Tracker (HFT).*, pp. 659–664, jan 2014.

[115] G. Contin, *The STAR Heavy Flavor Tracker and Upgrade Plan*, Nuclear Physics A, vol. 956, pp. 858–861, 2016.

[116] L. Greiner, *et al.*, *A MAPS based vertex detector for the STAR experiment at RHIC*, Nuclear Instruments and Methods in Physics Research Section A: Accelerators, Spectrometers, Detectors and Associated Equipment, vol. 650, no. 1, pp. 68–72, 2011.

[117] https://drupal.star.bnl.gov/STAR/system/files/HFT%20numbering%20scheme_v7_1.pdf.

[118] L. Arnold, *et al.*, *The STAR silicon strip detector (SSD)*, Nuclear Instruments and Methods in Physics Research Section A: Accelerators, Spectrometers, Detectors and Associated Equipment, vol. 499, pp. 652–658, nov 2002, arXiv:0211083 [physics].

[119] https://drupal.star.bnl.gov/STAR/files/HFT_QM_GContin_2.pdf.

[120] M. Beddo, *et al.*, *The STAR barrel electromagnetic calorimeter*, Nuclear Instruments and Methods in Physics Research, Section A: Accelerators, Spectrometers, Detectors and Associated Equipment, vol. 499, no. 2-3, pp. 725–739, 2003.

[121] https://drupal.star.bnl.gov/STAR/public/img/SketchUpSTAR.

[122] C. E. Allgower, *et al.*, *The STAR endcap electromagnetic calorimeter*, Nuclear Instruments and Methods in Physics Research, Section A: Accelerators, Spectrometers, Detectors and Associated Equipment, vol. 499, no. 2-3, pp. 740–750, 2003.

[123] STAR TOF Collaboration, *Proposal for a Large Area Time of Flight System for STAR*, Science And Technology, 2003.

[124] B. Bonner, *et al.*, *A single Time-of-Flight tray based on multigap resistive plate chambers for the STAR experiment at RHIC*, Nuclear Instruments and Methods in Physics Research Section A: Accelerators, Spectrometers, Detectors and Associated Equipment, vol. 508, no. 1, pp. 181–184, 2003.

[125] Y. Sun, *et al.*, *New prototype multi-gap resistive plate chambers with long strips*, Nuclear Instruments and Methods in Physics Research Section A: Accelerators, Spectrometers, Detectors and Associated Equipment, vol. 593, no. 3, pp. 307–313, 2008.

[126] W. J. Llope, *The STAR Time-of-Flight System*, Proceedings of the 24th Winder Workshop on Nuclear Dynamics, vol. 7, pp. 1–6, 2008.

[127] W. J. Llope, *et al.*, *The TOFp/pVPD Time of Flight System for STAR*, aug 2003, arXiv:0308022 [nucl-ex].

[128] J. Kiryluk and f. t. S. Collaboration, *Local Polarimetry for Proton Beams with the STAR Beam Beam Counters*, Spin 2004, pp. 718–721, jan 2005, arXiv:0501072 [hep-ex].

[129] C. A. Whitten, *et al.*, *The Beam-Beam Counter: A Local Polarimeter at STAR*, in *AIP Conference Proceedings*, vol. 980, pp. 390–396, AIP, 2008.

[130] J. Kiryluk, *Relative Luminosity Measurement in STAR and Implications for Spin Asymmetry Determinations*, in *AIP Conference Proceedings*, vol. 675, pp. 424–428, AIP, 2003.

[131] https://drupal.star.bnl.gov/STAR/system/files/BFC_HQPC_LK_2015_2_12.pdf.

[132] http://www.star.bnl.gov/webdata/dox/html/classStBFChain.html.

[133] R. E. Kalman, *A New Approach to Linear Filtering and Prediction Problems*, Journal of Basic Engineering, vol. 82, no. 1, p. 35, 1960.

[134] F. S. Bieser, *et al.*, *The STAR trigger*, Nuclear Instruments and Methods in Physics Research, Section A: Accelerators, Spectrometers, Detectors and Associated Equipment, vol. 499, no. 2-3, pp. 766–777, 2003.

[135] https://root.cern.ch/.

[136] http://nsww.org/projects/bnl/star/docs/STAR_soft_BNL_LK_2015_6_1.pdf.

[137] R. Brun, *et al.*, *GEANT Detector Description and Simulation Tool*, pp. CERN–W5013, CERN–W–5013, W5013, W–5013, 1994.

[138] http://www.star.bnl.gov/~jwebb/AgML_doc/AgML.html.

[139] J. Webb, J. Lauret, and V. Perevoztchikov, *The abstract geometry modeling language (AgML): experience and road map toward eRHIC*, Journal of Physics: Conference Series, vol. 513, p. 022036, jun 2014.

[140] J. C. Webb, J. Lauret, and V. Perevoztchikov, *Planning for Evolution in a Production Environment: Migration from a Legacy Geometry Code to an Abstract Geometry Modeling Language in STAR*, Journal of Physics: Conference Series, vol. 396, p. 022058, dec 2012.

[141] https://drupal.star.bnl.gov/STAR/comp/general/meet/reviews/2011-sti-ca-and-stv-tracking-component-review.

[142] http://www.star.bnl.gov/webdata/dox/html/classStIstSlowSimMaker.html.

[143] Yaping Wang, private communication.

[144] Gerrit van Nieuwenhuizen, private communication.

[145] M. Lomnitz, *PXL Detector Masking procedures*, Oct 2014.

[146] Michael Lomnitz, private communications.

[147] L. Kosarzewski, *Prospects for $B \to J/\psi$ measurements using Endcap Electromagnetic Calorimeter*, Heavy Ion Reaction Group seminar, Warsaw University of Technology, Jan 2014. http://hirg.if.pw.edu.pl/hirg2/components/com_chronocontact/uploads/pracownia/20140128001321_pythiaB_HIRG_LK_2014_1_27.pdf.

[148] http://cvs.nongnu.org/.

[149] http://www.star.bnl.gov/cgi-bin/protected/cvsweb.cgi/.

[150] K. Ackermann, *et al.*, *The forward time projection chamber in STAR*, Nuclear Instruments and Methods in Physics Research Section A: Accelerators, Spectrometers, Detectors and Associated Equipment, vol. 499, pp. 713–719, mar 2003.

[151] L. Adamczyk, *et al.*, *Suppression of Upsilon Production in d+Au and Au+Au Collisions at sqrt(s_NN) = 200 GeV*, Physics Letters B, vol. 735, pp. 127–137, jul 2014.

[152] H. Bichsel, *Comparison of Bethe-Bloch and Bichsel Functions*, https://drupal.star.bnl.gov/STAR/starnotes/public/sn0439, 2001.

[153] H. Bichsel, *A method to improve tracking and particle identification in TPCs and silicon detectors*, Nuclear Instruments and Methods in Physics Research Section A: Accelerators, Spectrometers, Detectors and Associated Equipment, vol. 562, pp. 154–197, jun 2006.

[154] S. D. Drell and T.-M. Yan, *Massive Lepton-Pair Production in Hadron-Hadron Collisions at High Energies*, Physical Review Letters, vol. 25, pp. 316–320, aug 1970.

[155] W. Verkerke and D. Kirkby, *RooFit Users Manual*, ROOT Documentation, pp. 1–134, 2008.

[156] W. Verkerke, *RooFit Quickstart 3.00*,

[157] J. E. Gaiser, *Charmonium Spectroscopy From Radiative Decays of the J/psi and psi'*, pp. SLAC–R–0255, http://inspirehep.net/record/183554, 1982.

[158] T. Skwarnicki, *A study of the radiative CASCADE transitions between the Upsilon-Prime and Upsilon resonances*, DESY-F31-86-02, DESY-F-31-86-02.

[159] S. Harotoonian - private communications.

[160] B. I. Abelev, *et al.*, *Upsilon cross section in p+p collisions at sqrt(s) = 200 GeV*, Physical Review D, vol. 82, p. 012004, jul 2010, arXiv:1001.2745.

[161] https://drupal.star.bnl.gov/STAR/starsimrequests/2013/jul/16/upsilon1s2s3s-pp-500-gev-run-11.

[162] T. Ullrich and Z. Xu, *Treatment of Errors in Efficiency Calculations*, jan 2007, arXiv:0701199 [physics].

[163] http://www.star.bnl.gov/HyperNews-star/protected/get/heavy/4231/1/1/2/1/1/1.html.

[164] R. Vertesi - private communications.

[165] V. Khachatryan, *et al.*, *Measurement of the Inclusive Upsilon production cross section in pp collisions at sqrt(s)=7 TeV*, Physical Review D, vol. 83, p. 112004, jun 2011, arXiv:1012.5545.

[166] http://www.star.bnl.gov/protected/heavy/tc88qy/pp500/event_Act/extraJpsi/.

[167] Q. Yang - private communications.

[168] G. Lafferty and T. Wyatt, *Where to stick your data points: The treatment of measurements within wide bins*, Nuclear Instruments and Methods in Physics Research Section A: Accelerators, Spectrometers, Detectors and Associated Equipment, vol. 355, pp. 541–547, feb 1995.

[169] T. Adye, *Unfolding algorithms and tests using RooUnfold*, arXiv:1105.1160 [physics.data-an], p. 6, may 2011, arXiv:1105.1160.

[170] http://hepunx.rl.ac.uk/~adye/software/unfold/RooUnfold.html.

[171] G. D'Agostini, *A multidimensional unfolding method based on Bayes' theorem*, Nuclear Instruments and Methods in Physics Research Section A: Accelerators, Spectrometers, Detectors and Associated Equipment, vol. 362, pp. 487–498, aug 1995.

[172] http://www.star.bnl.gov/protected/heavy/ullrich/pythia8/.

[173] R. Barlow, *Asymmetric Systematic Errors*, Current Practice, p. 12, 2003, arXiv:0306138 [physics].

[174] CDF Collaboration, *Measurement of Upsilon(1S) Polarization*, https://www-cdf.fnal.gov/physics/new/bottom/090903.blessed-Upsilon1S-polarization/cdf9966_ups_1s_pol_public.pdf, 2009.

[175] L. Adamczyk, *et al.*, *Measurements of D^{0} and D^{*} Production in p+p Collisions at sqrt{s} = 200 GeV*, Physical Review D, vol. 86, p. 072013, oct 2012, arXiv:1204.4244.

[176] J. Adams, *et al.*, *Transverse momentum and collision energy dependence of high p_T hadron suppression in Au+Au collisions at ultrarelativistic energies*, Physical Review Letters, vol. 91, p. 172302, oct 2003, arXiv:0305015 [nucl-ex].

[177] B. I. Abelev, *et al.*, *Longitudinal double-spin asymmetry and cross section for inclusive jet production in polarized proton collisions at sqrt(s) = 200 GeV*, Physical Review Letters, vol. 97, p. 252001, dec 2006, arXiv:0608030 [hep-ex].

[178] L. Adamczyk, *et al.*, *J/psi production at low transverse momentum in p+p and d+Au collisions at sqrt(S_{NN}) = 200 GeV*, Physical Review C, vol. 93, p. 064904, jun 2016, arXiv:1602.02212.

[179] P. Huck - private communications.

[180] L. Adamczyk, *et al.*, *J/ψ production at high transverse momenta in p+p and Au + Au collisions at sNN=200 GeV*, 2013.

[181] A. Adare, *et al.*, *J/psi Production versus Transverse Momentum and Rapidity in p+p Collisions at sqrt(s)=200 GeV*, Physical Review Letters, vol. 98, p. 232002, jun 2007, arXiv:0611020 [hep-ex].

[182] A. Adare, *et al.*, *Transverse momentum dependence of J/psi polarization at midrapidity in p+p collisions at sqrt(s)=200 GeV*, Physical Review D, vol. 82, p. 012001, jul 2010, arXiv:0912.2082.

[183] A. Spiridonov, *Bremsstrahlung in Leptonic Onia Decays: Effects on Mass Spectra*, oct 2005, arXiv:0510076 [hep-ex].

[184] http://www.star.bnl.gov/protected/heavy/zbtang/web/highPtJpsiRun9_10/notes/highpT_Jpsi_run9_run10_note_0208_2012.pdf.

[185] A. D. Frawley, T. Ullrich, and R. Vogt, *Heavy flavor in heavy-ion collisions at RHIC and RHIC II*, Physics Reports, vol. 462, pp. 125–175, jun 2008, arXiv:0806.1013.

[186] J. K. Yoh, *et al.*, *Study of Scaling in Hadronic Production of Dimuons*, Physical Review Letters, vol. 41, pp. 684–687, sep 1978.

[187] K. Ueno, *et al.*, *Evidence for the Upsilon" and a Search for New Narrow Resonances*, Physical Review Letters, vol. 42, pp. 486–489, feb 1979.

[188] S. Childress, *et al.*, *Production Dynamics of the Upsilon in Proton-Nucleon Interactions*, Physical Review Letters, vol. 55, pp. 1962–1964, nov 1985.

[189] W. R. Innes, *et al.*, *Observation of structure in the Upsilon region*, Physical Review Letters, vol. 39, pp. 1240–1242, nov 1977.

[190] G. Moreno, *et al.*, *Dimuon production in proton-copper collisions at s = 38.8 GeV*, Physical Review D, vol. 43, pp. 2815–2835, may 1991.

[191] T. Yoshida *et al.*, ((E605 Collab.)) Phys. Rev. D, vol. 39, p. 3516, 1989.

[192] H. A. E. L. Camilleri, in: T.B.W. Kirk Proc. 1979 Int. Symp. on Lepton and Photon Interactions at High Energies, Fermilab, Illinois, USA, p. 232, 1979.

[193] A. Angelis, *et al.*, *A measurement of the production of massive e+e- pairs in proton-proton collisions at sqrt(s) = 62.4 GeV*, Physics Letters B, vol. 87, pp. 398–402, nov 1979.

[194] C. Albajar, *et al.*, *Beauty production at the CERN proton-antiproton collider*, Physics Letters B, vol. 186, pp. 237–246, mar 1987.

[195] F. Abe, *et al.*, *Upsilon Production in p\bar{p} Collisions at sqrt(s)= 1.8 TeV*, Physical Review Letters, vol. 75, pp. 4358–4363, dec 1995.

[196] Z. Ye, *Upsilon measurements in p+p, p+Au and Au+Au collisions at sqrt(s_{NN})=200 GeV with the STAR experiment*, Nuclear Physics A, vol. 967, pp. 600–603, nov 2017.

[197] R. Vogt - private communications.

[198] H. Han, *et al.*, *Upsilon(nS) and chi^{b}(nP) production at hadron colliders in nonrelativistic QCD*, Physical Review D, vol. 94, p. 014028, jul 2016.

[199] Y-Q. Ma - private communications.

[200] L. Y. Zhu, *et al.*, *Measurement of Upsilon Production for p+p and p+d Interactions at 800 GeV*, Physical Review Letters, vol. 100, p. 062301, feb 2008, arXiv:0710.2344.

[201] R. Aaij, *et al.*, *Measurement of Upsilon production in pp collisions at sqrt{s} = 7 TeV*, The European Physical Journal C, vol. 72, p. 2025, jun 2012, arXiv:1202.6579.

[202] R. Aaij, *et al.*, *Production of J/psi and Upsilon mesons in pp collisions at sqrt(s) = 8 TeV*, Journal of High Energy Physics, vol. 2013, p. 64, jun 2013, arXiv:1304.6977.

[203] A. Dorsett - private communications.

[204] F. Arleo, D. D'Enterria, and A. S. Yoon, *Single-inclusive production of large-pT charged particles in hadronic collisions at TeV energies and perturbative QCD predictions*, Journal of High Energy Physics, vol. 2010, p. 35, jun 2010, arXiv:1003.2963.

[205] S. M. Berman, J. D. Bjorken, and J. B. Kogut, *Inclusive Processes at High Transverse Momentum*, Physical Review D, vol. 4, pp. 3388–3418, dec 1971.

[206] F. Arleo, *et al.*, *Higher-Twist Dynamics in Large Transverse Momentum Hadron Production*, Physical Review Letters, vol. 105, p. 062002, aug 2010, arXiv:0911.4604.

[207] B. I. Abelev, *et al.*, *J/psi production at high transverse momentum in p+p and Cu+Cu collisions at sqrt(s_NN)=200GeV*, Physical Review C, vol. 80, p. 041902, oct 2009, arXiv:0904.0439.

[208] R. L. Thews and M. L. Mangano, *Momentum spectra of charmonium produced in a quark-gluon plasma*, Physical Review C, vol. 73, p. 014904, jan 2006, arXiv:0505055 [nucl-th].

[209] J. W. Cronin, *et al.*, *Production of hadrons at large transverse momentum at 200, 300, and 400 GeV*, Physical Review D, vol. 11, pp. 3105–3123, jun 1975.

[210] D. Kharzeev, M. Nardi, and H. Satz, *The Transverse Momentum Dependence of Anomalous J/psi Suppression*, Physics Letters B, vol. 405, pp. 14–19, jul 1997, arXiv:9702273 [hep-ph].

[211] F. Karsch, D. Kharzeev, and H. Satz, *Sequential charmonium dissociation*, Physics Letters B, vol. 637, pp. 75–80, jun 2006, arXiv:0512239 [hep-ph].

[212] A. Adare, *et al.*, *Transverse-Momentum Dependence of the J/psi Nuclear Modification in d+Au Collisions at sqrt(s_NN)=200 GeV*, Physical Review C, vol. 87, p. 034904, mar 2013, arXiv:1204.0777.

[213] D. Acosta, *et al.*, *Measurement of the J/psi meson and b-hadron production cross sections in ppbar collisions at sqrt(s) = 1960 GeV*, Physical Review D, vol. 71, p. 032001, feb 2005.

[214] O. Drapier, *Etude des distributions en impulsion transverse des dimuons produits dans les collisions noyau-noyau aupres du SPS du CERN*, PhD thesis, 1998. http://na50.web.cern.ch/NA50/theses.html.